

MECHANISTIC STUDIES OF BUBBLE
EVOLUTION

Thesis submitted for the degree of
Doctor of Philosophy
at the University of Leicester

by

Sarah Lucy Gilbert BSc (Leicester)
Department of Chemistry
University of Leicester

August 2000

UMI Number: U129393

All rights reserved

INFORMATION TO ALL USERS

The quality of this reproduction is dependent upon the quality of the copy submitted.

In the unlikely event that the author did not send a complete manuscript and there are missing pages, these will be noted. Also, if material had to be removed, a note will indicate the deletion.



UMI U129393

Published by ProQuest LLC 2013. Copyright in the Dissertation held by the Author.
Microform Edition © ProQuest LLC.

All rights reserved. This work is protected against
unauthorized copying under Title 17, United States Code.



ProQuest LLC
789 East Eisenhower Parkway
P.O. Box 1346
Ann Arbor, MI 48106-1346

ABSTRACT

This thesis describes a study of the bubble evolution mechanisms of four systems; $\text{H}_2/\text{HClO}_4/\text{Au}$, $\text{H}_2/\text{HClO}_4/\text{Pt}$, $\text{Cl}_2/\text{NaCl}/\text{RTO}$ and $\text{Cl}_2/\text{NaCl}/\text{Ti}$ as a function of current density, surface composition (RTO) and morphology. Three experimental techniques have been used, fast frame video (FFV), electrochemical quartz crystal microbalance (EQCM) and the pressure release bubble nucleation technique (PRBN). The three complementary techniques were utilised to provide a comprehensive study of bubble behaviour. The FFV was used to study individual bubbles, the EQCM to measure the detachment rate integrated over the nucleating surface area, and the PRBN technique was used to measure the bubble nucleation rate integrated over space and time.

In the current density range $3\text{-}44\text{ mA cm}^{-2}$ nucleation of individual hydrogen bubbles was found to be rapid at vertical gold and platinum electrodes. For both electrode materials, the detachment radius decreased as a function of current density, but the average bubble size on detachment was approximately 50% smaller on the platinum electrode. The detachment rate and number of active nucleation sites both increased as a function of current density, and the dominant detachment mechanism was coalescence between closely paired neighbouring bubbles. EQCM analysis of the overall detachment rates at the electrodes confirmed the visual observations; novel Fast Fourier Transform analysis of the frequency response from the gold electrode showed that the detachment frequency increased with current density, but there was little change in the volume of gas resident on the electrode. On the platinum electrode small bubbles detached rapidly and were characterised by small fluctuations in the EQCM resonant frequency response.

Using the FFV technique, nucleation was found to be the rate-limiting step for chlorine bubble evolution at an RTO electrode in the current density range $18\text{-}56\text{ mA cm}^{-2}$. The large number of active nucleation sites at the surface site were characterised by a high surface coverage of bubbles, which detached mainly due to buoyancy and collision with rising bubbles. Using the PRBN technique, these nucleation sites were found to have a distribution of activities. Comparable results for titanium surfaces showed that the roughness of the substrate contributed significantly to the nucleation activity of RTO electrodes. EQCM analysis of RTO showed that the coupled mass of the electrode increased during bubble evolution, possibly caused by the porous surface being flooded.

An important result that emerged as a common theme from each experimental technique was the distribution of site energetics observed at all of the surfaces. Different nucleation site characteristics were found to be active under different conditions. This feature of heterogeneous bubble evolution establishes that any mechanistic study must be carried out under different operating conditions to establish the relevant bubble activity at the surface.

This thesis is dedicated to the memory of my father

I, Sarah Lucy Gilbert, state that all of the work presented within this thesis is original, unless otherwise acknowledged in the text or by references. The results were obtained during the period October 1995 to August 1999. None of the work has been submitted for any other degree at this, or any other University.

A handwritten signature in black ink that reads "S. Gilbert". The letters are cursive and fluid, with a large initial "S" and a stylized "G".

S. L. Gilbert

ACKNOWLEDGEMENTS

First and foremost I would like to thank my supervisor, Rob Hillman, for his guidance, support and wealth of knowledge. The industrial collaboration with ICI was managed with great expertise by Dave Hodgson whom I would like to thank for his practical advice, infectious enthusiasm and generous hospitality. Finally thanks to my second supervisor Andy Abbott for his many helpful suggestions and objective opinions.

I am grateful to many people for their technical assistance, especially, Dave Hodgson's colleagues at ICI's Electrochemical Technology Business laboratories in Runcorn and members of Leicester University's Chemistry workshops, Gerry, Phil, Roy and Keith.

My sincerest thanks to my colleagues in Professor Hillman's group for the endless hours of arguments, tantrums and more than a few laughs, that must have contributed somehow. Many thanks to Lee, Angela, Hendo, Mark, Little Rob, Helen, Lou, Sally, Paul, Sara, Silvana, Claudia, Miguel, Magda, and fondest memories of Lorraine.

Finally, thanks to my family and friends for making allowances.

CONTENTS

CHAPTER 1 Introduction	1
1.1 Introduction	1
1.1.1 Bubble evolution	2
1.1.2 Gas-liquid dispersions	2
1.1.3 Area of research	3
1.2 Chlor-alkali industry	3
1.2.1 Cell design	4
1.2.1.1 Mercury cell	4
1.2.1.2 Diaphragm cell	5
1.2.1.3 Membrane cell	6
1.2.2 Electrolytic bubble formation	8
1.3 Mechanism of spontaneous bubble formation	9
1.3.1 Classical nucleation theory	9
1.3.2 Bubble nucleation	11
1.3.2.1 Heterogeneous nucleation	11
1.3.3 Non-classical nucleation theory	14
1.3.4 Pre-existing nuclei	15
1.3.5 Bubble growth	15
1.3.6 Bubble coalescence	16
1.3.7 Bubble detachment	17
1.4 Measurement of bubble evolution rate	18
1.4.1 Applied bubble nucleation kinetics	20
1.4.2 Nucleating geometry	20
1.4.2.1 Nucleation at a single site	21
1.4.3 Surface modifications	21
1.4.3.1 Effect of electrolyte composition	22
1.5 Cell voltage	22
1.5.1 Ohmic losses	23
1.5.2 Overpotential	23
1.5.3 Mass transfer at electrodes	23
1.6 Electrocatalysis of gas evolving reactions	24
1.6.1.1 Hydrogen evolution reaction	25
1.6.1.2 Chlorine evolution mechanism	25
1.6.2 Structure of electrocatalyst	26
1.6.3 Surface and system modifications	27
1.6.3.1 Effect of bubbles	27
1.6.4 Surface characterisation	29
1.7 Project objectives	29
1.7.1 Experimental techniques	30
1.7.2 The use of video to monitor bubbles	30
1.7.3 The use of EQCM to monitor bubble formation	30
1.7.4 PRBN as bubble monitoring device	32
1.7.5 Thesis outline	32
CHAPTER 2 Theory	38
2.1 Bubble Formation	38
2.1.1 Supersaturation	38
2.1.2 Nucleation	39
2.1.3 Homogeneous nucleation	39
2.1.4 Bubble nucleation in a unary liquid	43

2.1.5	Bubble nucleation in dissolved gas solutions	44
2.1.6	Heterogeneous nucleation	45
2.1.6.1	Nucleation at a planar surface	45
2.1.6.2	Nucleation at a non-planar surface	46
2.1.7	Bubble Growth	47
2.1.8	Bubble detachment	48
2.2	EQCM Theory	50
2.2.1	Introduction	50
2.2.2	Piezoelectric effect	50
2.2.3	The EQCM as a mass sensing device	50
2.2.4	Mass to frequency relationship	52
2.2.5	Application: effect of a liquid on oscillation	54
2.3	Measurement of bubble evolution	54
2.3.1	Detecting bubbles	55
2.3.2	Fourier analysis	56
2.4	Rate of electrochemical reactions	59
2.4.1	Cell potential	59
2.4.2	Relationship between current and rate	60
2.4.2.1	Kinetically controlled current	60
2.4.2.2	Diffusion limited current	61
2.4.3	Cyclic voltammetry	61
2.4.4	Chronoamperometry	62
2.5	PRBN Theory	63
2.5.1	Measurement of Bubble Evolution by Pressure Rise	63
2.5.1.1	Supersaturation	63
2.5.1.2	Adiabatic expansion	64
2.5.2	Nucleation rate measurement	64
2.6	Direct visual observation	65
CHAPTER 3 Experimental		68
3.1	Introduction	68
3.2	Electrochemical Quartz Crystal Microbalance (EQCM)	68
3.2.1	Crystal specification	68
3.2.2	Three electrode cell	69
3.2.3	Metal oxide coating	71
3.2.4	Data Acquisition	71
3.2.5	Data Analysis	73
3.2.5.1	Novel Analysis of EQCM data using FFT	73
3.3	Pressure Release Bubble Nucleation (PRBN) Technique	74
3.3.1	Standard Experimental procedure	75
3.3.2	Gradient Measurement	76
3.4	Fast Frame video	76
3.5	Chemicals	77
CHAPTER 4 FFV		78
4.1	Introduction	78
4.1.1	Objectives	79
4.2	Theoretical aspects of bubble evolution	81
4.2.1	Bubble growth	81
4.2.2	Bubble nucleation	83

4.2.3	Definition of experimental parameters	84
4.3	Methodology of data analysis from visual observation	85
4.3.1	Induction time	86
4.3.2	Detachment rate	87
4.3.3	Specific sites for further study	88
4.3.3.1	Detachment mechanism	90
4.3.3.2	Growth mechanism	91
4.3.3.3	Bubble growth for non-adjacent bubbles	92
4.3.3.4	Growth at adjacent nucleation sites	94
4.3.4	Summary of methodology	96
4.3.4.1	Nucleation	96
4.3.4.2	Growth mechanism	96
4.4	Hydrogen evolution on gold	97
4.4.1	Results for low current density	97
4.4.2	Results for moderate current density	100
4.4.3	Results for high current density	102
4.4.4	Bubble behaviour as a function of current density	104
4.4.5	Conclusions	107
4.4.5.1	Nucleation	107
4.4.5.2	Growth and detachment	108
4.5	Hydrogen evolution on platinum	109
4.5.1	Specific nucleation sites for further study	109
4.5.2	Results for a low current density	111
4.5.3	Results for a moderate current density	113
4.5.4	Results for a high current density	116
4.5.5	Bubble behaviour as a function of current density	119
4.5.6	Conclusions	122
4.5.6.1	Nucleation	122
4.5.6.2	Growth and detachment	123
4.6	Chlorine evolution on RTO	124
4.6.1	Distribution of nucleation sites	124
4.6.2	Chlorine evolution as a function of current density	125
4.6.3	Nucleation	127
4.6.4	Growth and Detachment	128
4.6.5	Chlorine evolution on RTO; conclusions	132
4.7	Conclusions: Bubble evolution at different electrode surfaces	132
4.7.1	Nucleation	132
4.7.2	Growth	134
4.7.3	Detachment	134
4.8	Future work	135
CHAPTER 5 EQCM		138
5.1	Introduction	138
5.1.1	Principle of EQCM frequency response analysis	139
5.2	Objectives	140
5.3	EQCM Data Analysis	141
5.3.1	Surface Structure	142
5.3.2	Model of coupled mass response due to bubble evolution	143
5.3.3	Data analysis in the time domain	145
5.3.4	Fast Fourier Transform (FFT)	146
5.3.5	Summary	149
5.4	Bubble evolution using cyclic voltammetry	149
5.4.1	Single voltammetry scan	149
5.4.2	Electrode surface properties	151

5.4.3	Multiple voltammetry scans	152
5.4.3.1	Hydrogen evolution at gold	153
5.4.3.2	Hydrogen evolution at platinum	156
5.4.3.3	Chlorine evolution at RTO	157
5.4.4	Conclusions	158
5.5	Time domain and Fourier analysis of EQCM data	159
5.5.1	Acquisition rate	159
5.5.2	Conversion of time domain to frequency domain	161
5.5.3	Appearance of EQCM frequency response features in FFT spectra	163
5.5.3.1	Change in mechanism	164
5.5.3.2	Change in activity	166
5.6	FFT as a function of surface properties and current density	167
5.6.1	Low surface activity: Hydrogen evolution at polished gold	167
5.6.2	High surface activity	171
5.6.2.1	Hydrogen evolution at platinum	171
5.6.2.2	Chlorine evolution at RTO	173
5.6.3	Electrode orientation	174
5.7	Conclusions	178
5.7.1	Surface properties	179
5.7.2	FFT as a diagnostic tool	180
5.8	Future Work	181

CHAPTER 6 PRBN 183

6.1	Introduction	183
6.1.1	Objectives	184
6.2	Principles of PRBN analysis	186
6.2.1	Nucleation rate measurement	186
6.2.2	The two site model	186
6.2.3	Novel methodology	187
6.3	Data analysis technique	188
6.3.1	Calibration	188
6.3.2	Adiabatic Expansion	189
6.3.3	Diffusion	190
6.3.4	Gradient Measurement	190
6.4	Results for RTO as a function of surface composition	192
6.4.1	Results for a single experiment	195
6.5	Results for titanium as a function of surface roughness	198
6.6	Effect of oxide coating on nucleation rate	200
6.7	Conclusions	201
6.7.1	Future work	201

CHAPTER 7 CONCLUSIONS 204

LIST OF SYMBOLS AND ABBREVIATIONS

A	Area
A^*	Surface area of critical nucleus
B	Pre-exponential coefficient for nucleation
c_2	Concentration of gas in solution
c_{2e}	Equilibrium concentration of gas over a flat surface
D	Diffusion coefficient
DSA	Dimensionally stable anode
E	Electrode potential
e	Electronic charge
E_e	Equilibrium cell potential
EQCM	Electrochemical quartz crystal microbalance
$f(\theta)$	Correction factor for heterogeneous nucleation
f_0	Fundamental frequency
F_b	Buoyancy force
$\Delta f_{\text{bubble layer}}$	Change in resonant frequency due to displacement of coupled liquid layer by bubbles
$f_{cc}(\theta)$	Correction factor nucleation in a conical cavity
F_d	Drag force
f_{exp}	Measured EQCM frequency response
FFT	Fast Fourier Transform
FFV	Fast frame video
F_i	Liquid inertia
$\Delta f_{\text{liquid layer}}$	Change in resonant frequency due to coupled liquid layer
F_p	Force due to excess vapour pressure
F_s	Surface tension
ΔG^*	Free energy of formation of critical nucleus
ΔG_v	Free energy per unit volume of liquid phase
HER	Hydrogen evolution reaction
i	Current
J	Nucleation rate
j	Flux of charge

J_a	Nucleation rate of nucleation site type a
J_b	Nucleation rate of nucleation site type b
k	Rate constant
k	Boltzmann constant
L	Quartz crystal modulation layer thickness
m	Molecular mass
m	Mass
n^*	Number of critical sized nuclei
Nafion	Perflourinated ionomer membrane
NHE	Normal hydrogen electrode
p	Supersaturated vapour pressure
p	Vapour pressure
P	Hydrostatic pressure
p_b	Vapour pressure inside a bubble nucleus
p_e	Equilibrium vapour pressure
PRBN	Pressure release bubble nucleation
PTFE	Polyflourotetraethylene
R	Resistance
r	Radius
R	Gas constant
r^*	Critical radius
RTO	Mixed ruthenium titanium oxide electrode
SCE	Saturated calomel electrode
T	Absolute temperature
v_q	Wave velocity of quartz oscillation
Z	Zeldovich non-equilibrium factor
α	Saturation ratio/transfer coefficient
α_c	Condensation coefficient
β	Half angle subtended at the base of a conical cavity
β_g	Growth coefficient
γ	Interfacial tension
g	Gravitational acceleration
η	Overpotential

φ	Correction term for bubble nucleation in a multi component system
λ_q	Wavelength of quartz oscillation
θ	Three phased contact angle
ρ	Density
σ	Supersaturation
σ_{trans}	Transition supersaturation
ω	Rate of impingement
Ω	Molecular volume of vapour molecules

1.1 Introduction

In any system where gas is dispersed in a liquid, phase separation will occur by the formation of bubbles: boiling occurs due to the temperature-induced elevation of liquid vapour pressure. Cavitation is a phenomenon that occurs when the liquid structure is deformed due to hydrodynamic forces [1]. A gas-liquid dispersion may be formed because of a chemical reaction or by the physical process of gas-liberation from a solution that is supersaturated with dissolved gas. Supersaturation can be caused by liquid depressurisation, a process employed in carbonated beverages. Electrochemical gas evolution causes the electrolyte to become supersaturated with respect to the dissolved gas. This chapter covers the fundamental processes governing bubble formation and behaviour within the context of modern chlor-alkali technology. Chlor-alkali is the name given to the electrochemical process of simultaneous production of hydrogen and chlorine gases from aqueous solutions of caustic soda and sodium chloride.

1.1.1 Bubble evolution

Bubbles form in a liquid via two different processes (defined respectively as causing a decrease or increase in free energy of the system) [2,3]. Firstly, spontaneous bubble evolution occurs by desupersaturation of a solution of the gas, or by decomposition of a component of the liquid (analogous to a boiling process). Secondly, non-spontaneous bubble evolution occurs by direct introduction of gas into the liquid by a bubbler (sparger) or by mechanical entrainment (or break up of large bubbles).

The introduction of gas into the liquid described by the latter case is used in processes such as particle flotation [4] and fluidised beds [5]. Bubbles cause mixing and enable separation of the product from other impurities. However, complete phase separation is not a requirement of these processes. The former case of bubble formation is more complex. In any system, it is vital to predict the conditions giving rise to spontaneous bubbles and especially to establish where in the system bubbles will appear. The mechanism of formation of gas bubbles, their size and distribution, and their subsequent behaviour are functions of the physical and chemical properties of the system such as temperature,

pressure, the dispersion composition and the nature of any solid/liquid interface where reactions occur. These parameters are used to define the system under study and hence predict expected bubble behaviour. Jackson [6] showed the size and number of bubbles produced by a rapid pressure drop of a flowing supersaturated solution depends on the degree of supersaturation and the energy available for formation (most of which is required for the formation of the bubble/liquid interface). Nucleation in clean water requires high energy and results in a small number of large bubbles, whereas the presence of impurities, such as surface-active agents, induces bubble formation at a lower energy, where smaller bubbles are produced in larger numbers. Using a higher pressure to produce the flow, compared to the pressure used for saturation can facilitate control of bubble size and number.

1.1.2 Gas-liquid dispersions

A two-phase gas-liquid dispersion can exist in different states depending on the population density of gas bubbles (or volume of gas) per unit volume of liquid, a property known as the void fraction [2].

Low void fraction

A bubble is a small volume of gas surrounded by a continuous mass (or thin film) of liquid. Bubbles dispersed in low concentration in a liquid form an unstable dispersion. Those formed by mechanical (rather than chemical) methods tend to contain larger bubbles. Complete phase separation occurs by gravitational means: the buoyancy of bubbles causes them to rise and coalesce with other rising bubbles or the bulk liquid/air interface.

High void fraction

Foam consists of a number of bubbles separated by a thin film. Foams have a finite static life, but if dynamically maintained can be very stable. Froth is a highly concentrated dispersion of bubbles in a liquid. Foams or froths form stable dispersions where complete phase separation is very difficult. Pure two-component systems cannot form a stable dispersion: foam formation requires the presence of a third surface-active species adsorbed at the interface.

1.1.3 *Area of research*

The rate of gas liberation in the form of bubbles is dependent on the rate of gas evolution. In an electrochemical cell, this is enhanced by the use of electrocatalysts. The activity and properties of these have been covered extensively in the literature, and are summarised in section 1.6. The behaviour of high void fraction systems, such as two-phase flow, is a suitable model for the behaviour of bubbles swarms during electrochemical gas evolution on an industrial scale. A major economic concern is the detrimental effect on the efficiency of industrial electrochemical cells of the presence of large numbers of bubbles; these decrease efficiency and hence increase energy consumption. Consequently, the effect of the two-phase flow on electrochemical parameters has also received much attention.

An important area of research that lies between these two areas in terms of the bubble evolution process, and which is less widely studied, is the kinetics of the bubble evolution at the electrocatalytic surface, from the nucleation of microscopic bubbles to their departure from the electrode. The focus of this literature review concerning gas evolution concentrates mostly on research carried out on individual bubble formation in an unstable gas-liquid dispersion where foam formation (and therefore phase separation) is not considered a significant problem.

1.2 **Chlor-alkali industry**

The combined manufacturing output of the chlor-alkali industry makes it the world's largest electrolytic process. Although the technology used varies, the principal chemical reactions do not differ. Chlorine is produced by the electrochemical oxidation of chloride at the anode using brine produced from natural salt deposits [7,8]. A simultaneous cathodic reduction reaction produces caustic soda and hydrogen. The overall reaction is typically



Both chlorine and caustic soda are considered main products and are used primarily within the chemical industry e.g. synthesis of organic compounds, pulp and paper manufacture, manufacture of PVC (Cl_2) and detergent production (NaOH). The size and operation of

plants varies significantly depending on the specifications required from the products. The physical conditions under which the products are formed vary according to the type of cell technology used; these differences are discussed in the next section. Common features in cell operation are the low pH of the anolyte, which prevents the hydrolysis of chlorine to hypochlorite and minimizes the competing oxygen evolution reaction. All the cells are run at elevated temperatures (60-90°C) to improve the kinetics of the electrode reactions [9,10].

1.2.1 Cell design

Chemical methods of chlorine production were superseded by electrolytic methods in the 1930s. Two dominant production methods used either mercury or diaphragm cells. Although technological developments enabled lower energy consumption, the use of carbon anodes was a major inefficiency. The advent of titanium based electrode materials was a breakthrough, due to their enhanced durability; they were named dimensionally stable anodes (DSA®). Invented in 1967 by Beer [10], DSA® are electrocatalytic compounds containing a mixture of ruthenium and titanium oxides, coated onto titanium substrates. By the 1970s, all new cells used metal anodes, and carbon anodes were gradually replaced in existing cells. Although the mercury and diaphragm cells comprise very different designs, the most significant distinction is that the diaphragm cell sacrifices the high purity product of the mercury cells in favour of higher power efficiency [11].

A significant development that has occurred over the last twenty years is in the product separation technology. The use of Nafion® membranes improves product quality over the diaphragm cell and avoids the operational and environmental concerns of the mercury cell. Economic pressures such as rising electricity prices drive continued research to improve production efficiency [12]. Three common cell designs are described below; their operation and output are compared in Table 1.1.

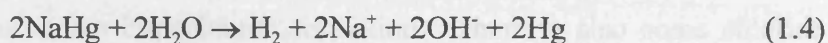
1.2.1.1 Mercury cell

The mercury cell uses a flowing mercury cathode and a DSA® coating on a Ti mesh substrate anode (see Fig 1.1). The two electrode reactions are given below [9].



where E_e is the equilibrium potential for the electrode reactions vs. NHE at pH 4 and 298 K.

The sodium amalgam is hydrolysed in a separate reactor vessel called a denuder.



The reversible cell potential is -3.16V, but the cell operates at approximately -4.50V. The difference arises because an additional driving force is required to pass current through the mercury-DSA[®] gap, the electrodes and the external circuit. However, because the anode and cathode products are in different phases, no physical barrier is required to separate them.

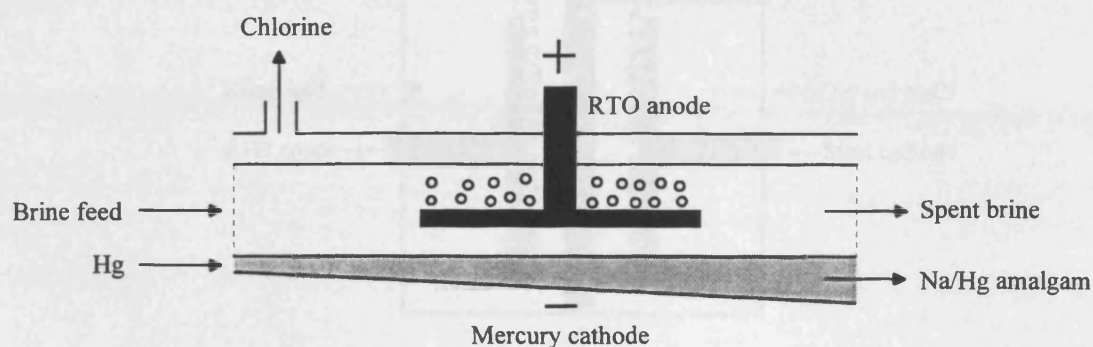
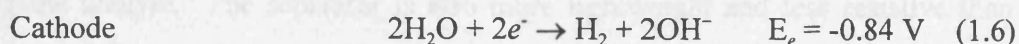
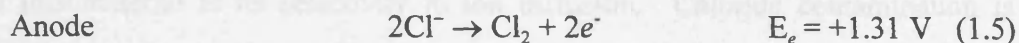


Figure 1.1 Schematic diagram of mercury cell

1.2.1.2 Diaphragm cell

The same anode materials are used in a diaphragm cell, but the mercury cathode is replaced by a hydrogen evolving steel cathode, often coated with a catalyst such as nickel, to produce a high surface area and reduce the overpotential for the hydrogen evolution reaction.



where E_e is the equilibrium potential for the electrode reactions vs. NHE at pH 4 (anode), pH 14 (cathode) and 298 K.

As chlorine, caustic soda and hydrogen are produced simultaneously, a separator is required to prevent cross-contamination of the products (see figure 1.2). The separator, fabricated from asbestos, merely forms a physical barrier; the transport of ions is possible. This limits the concentration of caustic soda that can be produced, as diffusion of hydroxide ions from the catholyte to the anolyte causes hypochlorite formation. There is also some chloride contamination of the caustic soda. The pH of the catholyte is approximately 14 due to OH^- formation. The reversible cell potential is -2.15V. However, the operating potential is approximately -3.50V, due mainly to the separator.

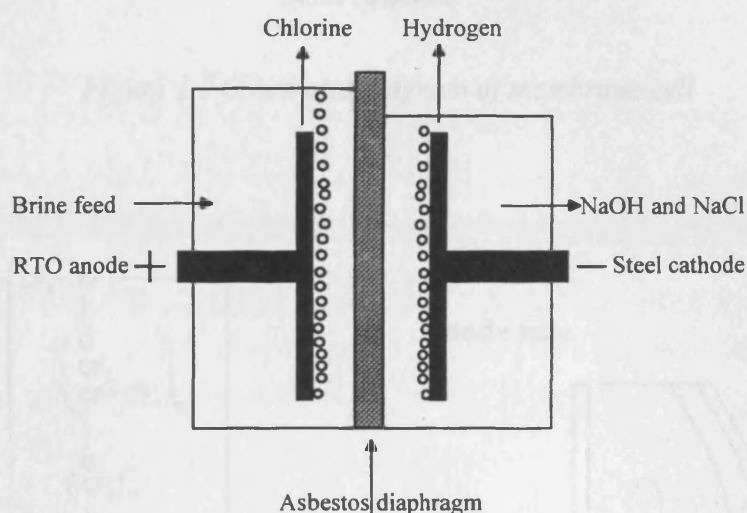


Figure 1.2 Schematic diagram of diaphragm cell

1.2.1.3 Membrane cell

The membrane cell uses the same design and electrodes as the diaphragm cell (see figure 1.3); the only difference is the separator material. A cation-permeable membrane, commonly a PTFE copolymer, Nafion[®], replaces the asbestos (see figure 1.4). The advantage of this material is its selectivity to ion diffusion. Chloride contamination is minimised, and a higher concentration of caustic soda can be produced without contaminating the anolyte. The separator is also more lightweight and less resistive than asbestos, which enables the cell to be run at higher current densities. The ion-selectivity of

the membrane also allows the use of electrocatalysts on the cathode, which reduces the overpotential for hydrogen evolution (the electrocatalysts would be poisoned by trace impurities in the diaphragm cell).

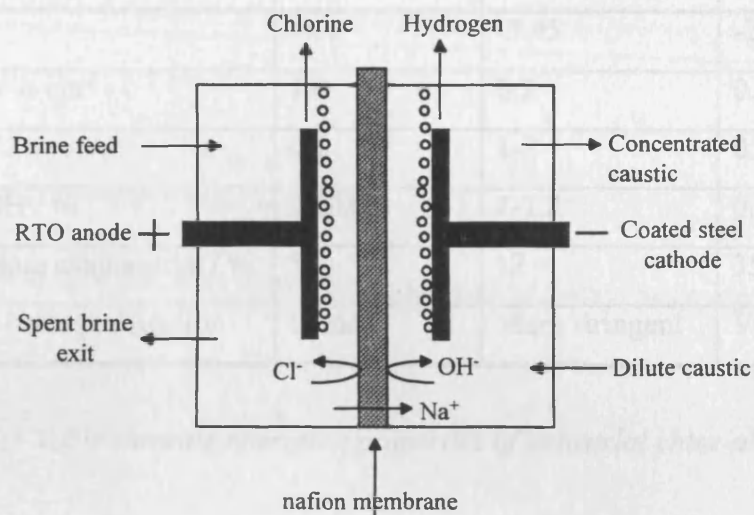


Figure 1.3 Schematic diagram of membrane cell

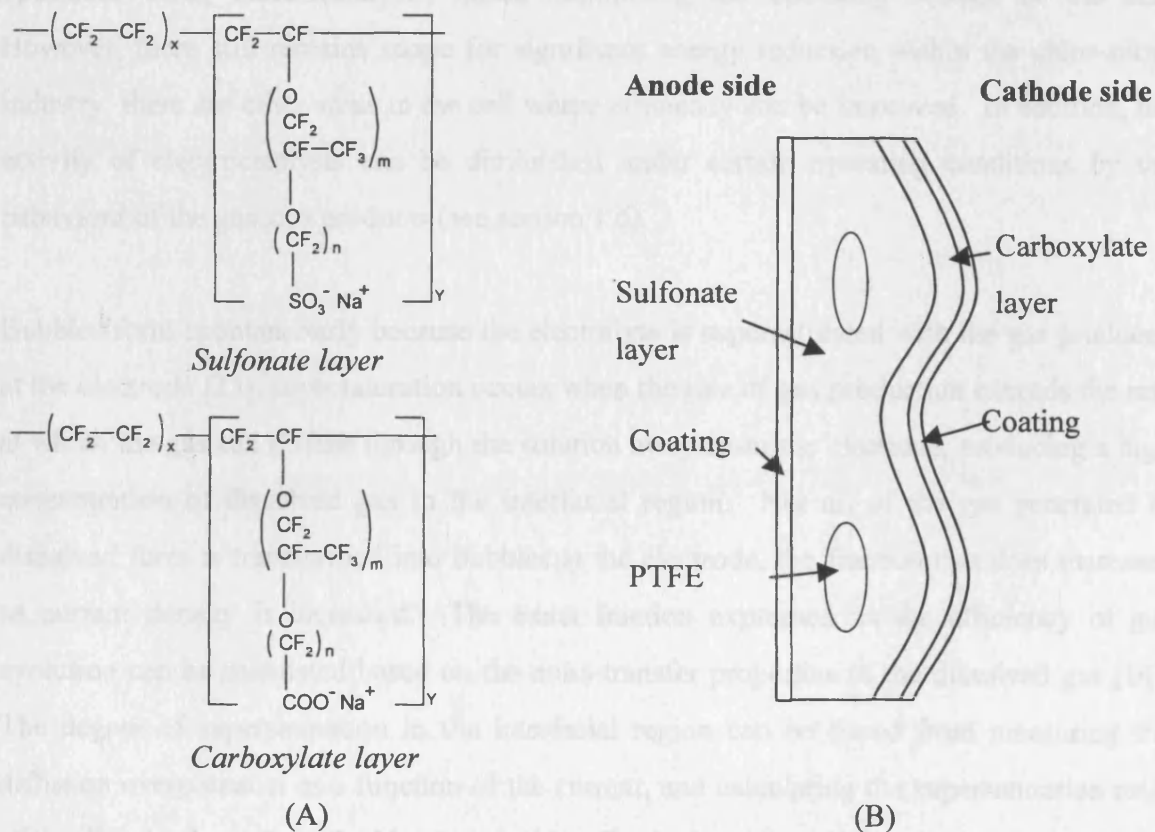


Figure 1.4 Polymeric structure (A) and cross-section of the membrane (B) of Nafion®

The table below summarises the characteristics of the three cell technologies [9]

	Mercury cell	Diaphragm cell	Membrane cell
cell voltage /V	-4.4	-3.45	-2.95
current density / A cm ⁻²	1.0	0.2	0.4
O ₂ in Cl ₂ / %	0.1	1-2	0.3
Cl ⁻ in 50% NaOH / %	0.003	1-1.2	0.005
NaOH conc. before evaporation / %	50	12	35
requirement for brine purification	Some	More stringent	Very extensive

Table 1.1 Table showing operating properties of industrial chlor-alkali cells

1.2.2 Electrolytic bubble formation

The kinetics and thermodynamics of the chlorine-producing electrode reactions have been optimised using electrocatalysts, hence minimising the operating voltage of the cell. However, there still remains scope for significant energy reduction within the chlor-alkali industry; there are other areas in the cell where efficiency can be improved. In addition, the activity of electrocatalysts can be diminished under certain operating conditions by the behaviour of the gaseous products (see section 1.6).

Bubbles form spontaneously because the electrolyte is supersaturated with the gas produced at the electrode [13]; supersaturation occurs when the rate of gas production exceeds the rate at which the gas can diffuse through the solution away from the electrode, producing a high concentration of dissolved gas in the interfacial region. Not all of the gas generated in dissolved form is transformed into bubbles at the electrode, the fraction that does increase as current density is increased. The exact fraction expressed as the efficiency of gas evolution can be calculated based on the mass transfer properties of the dissolved gas [14]. The degree of supersaturation in the interfacial region can be found from measuring the diffusion overpotential as a function of the current, and calculating the supersaturation ratio of the dissolved gas from the Nernst equation. For hydrogen evolution from 0.5M sulphuric acid, supersaturation is approximately 100 at high current density, the value for chlorine evolved from concentrated NaCl is much lower, approximately 30 [15].

The presence of bubbles in the electrolyser increases the ohmic drop. Bubbles adhered to the electrode not only block the surface, preventing further product formation, but also disturb the potential and current distribution at the surface, thereby increasing the overpotential for chlorine evolution (see section 1.5) [16]. A comprehensive review by Sides [17] covers all aspects of electrolytic bubble evolution. The mechanism of bubble formation at the electrode surface is described below. The rate of bubble formation is dependent on the current density and electrode morphology and pre-treatment. Because bubble evolution is a surface process, small amount of impurities can have a large affect on the interaction of the electrode and electrolyte and the electrode potential dependence of both. This in turn effects the rate of bubble formation and the rate at which bubbles detach from the surface. The presence of bubbles in the electrochemical cell obstructs the current, decreasing the effective conductivity of the electrolyte; however bubbles stir the electrolyte and increase mass transfer to the electrode. All of these issues are covered in the following sections.

1.3 Mechanism of spontaneous bubble formation

The theory of individual bubble evolution can be separated into different functionally independent processes of nucleation, growth and detachment (for a bubble formed at a solid interface). If bubbles are formed in bulk liquid, they rise under buoyancy and burst at the surface. Each process in the mechanism of bubble formation is treated separately below. The relevant literature in each area is reviewed. Theoretical treatments are described briefly, and indications given where the theory is described in further detail in Chapter 2. A summary of the methods applied to bubble evolution is given in section 1.4.

1.3.1 Classical nucleation theory

Nucleation is a process by which a new phase is formed from an existing one, a change that requires a thermodynamic driving force. Hence, at ambient pressure, water bubbles nucleate spontaneously in boiling water, but not in water at room temperature. In an electrochemical cell the electrolyte becomes supersaturated with the product gas; a new gaseous phase is thermodynamically more stable than the supersaturated electrolyte, thus providing the driving force for nucleation.

The formation of bubbles in a supersaturated liquid is analogous to the condensation of liquid droplets from a supersaturated vapour. The droplet model is used as the basis for a description of homogeneous nucleation theory [6,18,19], which can be modified to account for the presence of a nucleating surface [20], or the nucleation of bubbles [21]. A supersaturated medium exists in a metastable state; thermodynamic fluctuations can cause the formation of molecular clusters, and these grow by accretion to form macroscopic nuclei. The nuclei themselves are unstable, with equal tendency to grow further or re-dissolve. They can only grow into macroscopic sized droplets (or bubbles) once they have achieved a specific size. Once this threshold is surpassed, the nuclei grow rapidly. Nuclei attaining this threshold are termed critical sized nuclei. As described below, the rate of formation of critical sized nuclei is the basis of nucleation theory.

Classical nucleation theory was developed early in the twentieth century [22] and is based on the kinetic treatment of nucleation rate in terms of the rate of impingement of molecules on the equilibrium concentration of critical sized nuclei.

$$J = A\omega n^* \quad (1.7)$$

where A^* is the surface area of the critical sized nucleus, ω is the frequency of molecular impingement per unit area per unit time, n^* is the equilibrium number of critical nuclei. Becker and Doring [23], and Zeldovich [24] added another term into equation 1.7 which accounted for the loss of nuclei by dissolution into the supersaturated phase and so provided a steady-state concentration of critical nuclei. J can be expressed in a general form as

$$J = C \exp\left(-\frac{\Delta G^*}{kT}\right) \quad (1.8)$$

A detailed derivation of equation 1.8 is given in section 2.1.3; however, a brief explanation of the terms is given here. ΔG^* is the change in Gibbs energy for nucleation, and can be described as the activation energy for formation of a critical sized nucleus. The Gibbs function can be expressed as

$$\Delta G^* = 16\pi\gamma^3\Omega^2/3k^2 T^2 \ln^2 \alpha \quad (1.9)$$

where γ is interfacial tension and α is the saturation ratio. The pre-exponential term C is not a constant, but slowly dependent on variables found in the exponential term such as interfacial tension and supersaturation. The dimension of a critical sized nucleus can be calculated from the nucleation work with respect to the supersaturation [25] and is approximately 8 Å (containing 90 molecules) for a water nucleus forming in supersaturated water [26]. A criticism of classical nucleation theory is that the activation energy given in equation 1.9 is defined by macroscopic properties such as surface tension, vapour pressure and liquid density, whereas in fact critical sized nuclei are composed of only a few molecules. This inconsistency is discussed in section 1.3.3.

1.3.2 Bubble nucleation

Classical nucleation theory was expanded to the theory of bubble formation in boiling liquids [27,28], and supersaturated solutions [29,30]. A mechanism for electrolytic bubble evolution was proposed by Nevedov for the formation of hydrogen bubbles at an electrode during the electrolysis of water where non-polar gas molecules arrange themselves between the water molecules, increasing the distance between water molecules, so weakening hydrogen bonds and allowing formation of the new phase. The value of supersaturation required for this mechanism is 30 for oxygen evolution and 50 for hydrogen evolution [31]. The current state of understanding and experiments was reviewed by Lubetkin [3].

1.3.2.1 Heterogeneous nucleation

One of the most important considerations in the application of nucleation theory to an experimental system is whether nucleation is homogeneous or heterogeneous. Heterogeneous nucleation, where the bubble forms at a solid/liquid interface, is thermodynamically favourable, because the energy barrier to nucleation, ΔG^* is decreased. Therefore, in almost every application, heterogeneous nucleation will be the dominant mechanism [32]. The two cases are depicted in Figure 1.5.

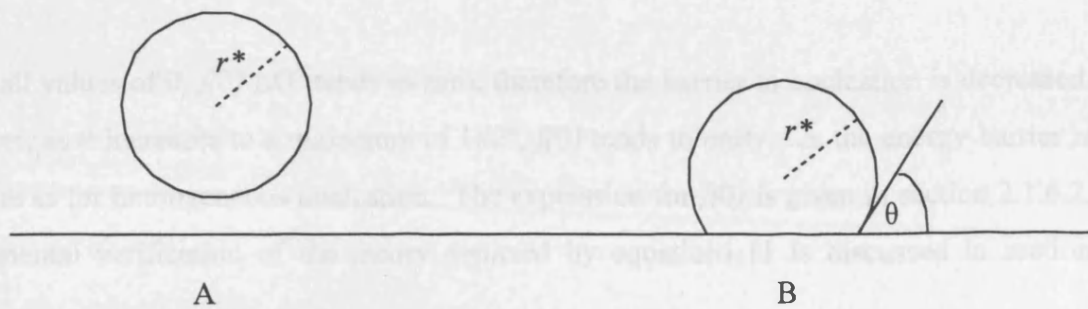


Figure 1.5 A) homogenous nucleation near a planar surface B) heterogeneous nucleation at a planar surface

The size of the critical nucleus, as defined by the critical radius r^* , is a function of the supersaturation of the solution, and the chemical composition of the surface (which affects the contact angle). The contact angle is determined by the balance of forces at the interface. The relationship between the surface tension at the point of contact and the three phase contact angle is shown in figure 1.6 and given by Young's equation [26].

$$\gamma_{SL} - \gamma_{SG} + \gamma_{LG} \cos\theta = 0 \quad (1.10)$$

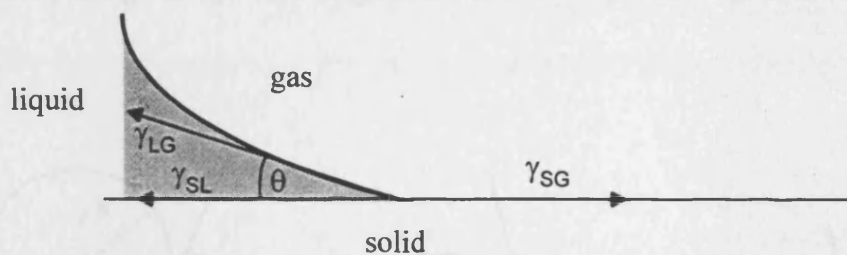


Figure 1.6 Schematic diagram showing the balance of forces resulting in contact angle θ

Fewer molecules are required to form the same critical sized bubble heterogeneously compared to homogeneously, as defined by the same critical bubble radius r^* . The fraction of the volume of the spherical critical nucleus required is a function of the contact angle, θ and is denoted $f(\theta)$. Equation 1.9 can be modified to include this term. The nucleation rate J for heterogeneous nucleation can be expressed as

$$J = C' \exp\left(-f(\theta)\frac{\Delta G^*}{kT}\right) \quad (1.11)$$

For small values of θ , $f(\theta)$ ΔG^* tends to zero, therefore the barrier to nucleation is decreased. However, as θ increases to a maximum of 180° , $f(\theta)$ tends to unity, i.e. the energy barrier is the same as for homogeneous nucleation. The expression for $f(\theta)$ is given in section 2.1.6.2. Experimental verification of the theory depicted by equation 1.11 is discussed in section 1.4.1.

Surface effects complicate this model especially since any real surface is not “flat” or chemically homogeneous when considered on the (submicron) scale of nuclei of the new phase [20]. Heterogeneous nucleation is favoured in most systems where a nucleating surface is present and consequently is a function of the properties of that surface. This is demonstrated in Figure 1.7, which introduces the idea of catalytic surface features for nucleation. Figure 1.7(A) shows a bubble where the contact angle is small and therefore the volume of gas required for a given radius of bubble to form is large. Figure 1.7(B) shows the converse case where the contact angle is large. Figure 1.7(C) shows the same chemical conditions as A), however, the formation of the bubble in the cavity means the volume of gas required is smaller than for case A). The conditions under which a bubble will form in a conical cavity are given by Ward [33]; these ideas are explored in greater depth in Chapter 2.

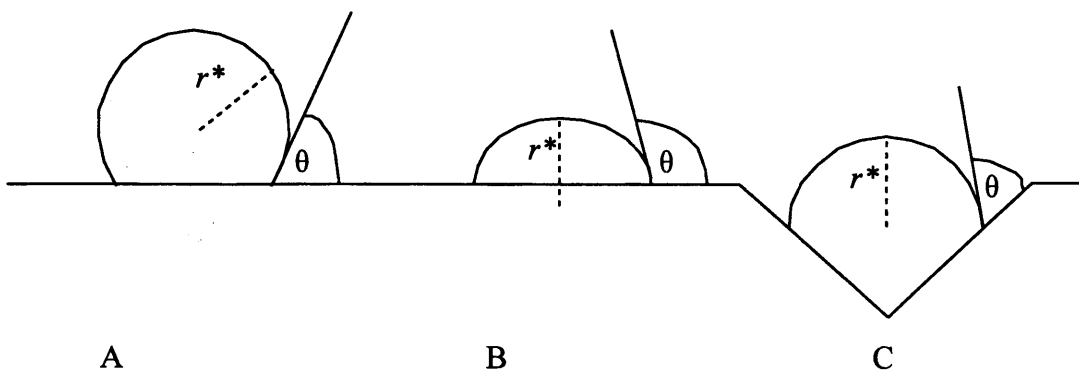


*Figure 1.7 Schematic diagram demonstrating the effect of a nucleating surface structure on the volume of gas molecules required to form a critical sized nucleus of radius r^**

A summary of bubble nucleation theory and a description of the kinetics of the initial stage of isothermal bubble formation including the rate of bubble growth is given by Kashiev [34]. Recent developments in nucleation theory have sought to quantify the terms in the general

nucleation rate equation 1.11. Increased use of computational power [35] and the development of new experimental techniques has enabled the definition of variables such as surface tension and contact angle not as macroscopic properties, but as displaying a functional variation on droplet (bubble) size [36]. The statistical mechanical or “non-classical” approach to the definition of the thermodynamic variables in the rate equation is outlined in the following section.

1.3.3 *Non-classical nucleation theory*

A significant departure from the classical theory has been caused by disagreement over the use of standard thermodynamic variables in the original theory. It is assumed bubbles form from pre-bubble clusters of molecules, which grow by stepwise addition of further molecules to the cluster. The point at which bubble nucleation occurs is defined by the formation of the gas-liquid interface. The energy required to form the interface is defined using the surface tension of the liquid (a macroscopic property of the system). It has been argued that this value cannot be attributed to microscopic bubbles containing tens or hundreds of molecules. A study of the dependence of surface tension on droplet size shows that curvature corrections to the surface tension may be important in the quantitative determination of the Gibbs function for surface formation. However, qualitatively the classical theory is valid [37].

Two factors can account for the difference between theoretical contact angles for homogeneous macroscopic planar surfaces and the actual contact angles relevant to the formation of a bubble nucleus. It has been shown using experimental, [38] and theoretical [39] techniques, that contact angle is affected by surface roughness. Drelich used sessile-drop and captive-bubble techniques to measure the three-phase contact angles between water, air and thiol monolayers at three different surfaces (gold, methylated quartz and roughened polymer). As the roughness is increased, the difference is more pronounced for the receding rather than advancing contact angles. Another factor that effects contact angles is the dimensions of the solid surface. A systematic difference occurs between the contact angle of a small spherical particle and a planar surface, (a decrease of 10° is seen for a hydrophobic particle compared to a planar surface) [36,40].

Non-classical theory utilises a statistical thermodynamic approach to define the metastable solution of clusters of dissolved gas and so does not require the inclusion of macroscopic

thermodynamic values. Experiments have shown classical nucleation theory to be in error in predicting nucleation rates in cases of extreme superheating where the liquid is close to the critical point. However, a comparison the theories [41] has shown the errors in using the classical model to be small in most systems. A review of recent developments in the theory is given by Oxtoby [42]. An alternative mechanism of nucleation proposed by Martinez, the conventional thermodynamic approach where molecules overcome the energy barrier to nucleation (see figure 2.1), is replaced with a tunnelling mechanism [43].

1.3.4 Pre-existing nuclei

It is possible for the nuclei from which bubbles grow to be permanently present at the surface. The presence of these nuclei was first described by Harvey; hence, they are often termed “Harvey nuclei” [44]. The fact that the reported nucleation threshold is lower than expected for homogeneous nucleation theory, can be explained by the presence of the pre-existing Harvey nuclei stabilized in the liquid. Stabilisation could also be the result of impurities such as solid particles and Ward and Tikuisis proved that stability could also arise from the presence of microbubbles in the bulk liquid [45].

1.3.5 Bubble growth

The rate of growth of a critical sized bubble is zero, because it is in a chemical and mechanical equilibrium with the surrounding liquid. A small increase in the radius initiates growth by allowing the internal pressure to overcome the opposing forces of curvature and background pressure. The initial stage of growth is by expansion of the bubble due to high internal pressure and by mass transport to the gas liquid interface, determined by a number of factors such as the pressure inside the bubbles, the ambient pressure, liquid inertia, liquid viscosity, surface tension and the transport properties of the gas through the liquid. The mechanism for the development of a bubble is outlined by Sides [17]. Expansion due to high internal pressure will continue until the supply of new molecules limits the growth rate and mass transfer determines the final stage. Frank provided a solution of diffusion for spherical symmetry [46]. Based on this work, again assuming the growing bubble to be a spherical cavity, Scriven provided an equation for the diffusion-controlled growth of a

bubble from critical size until the point where it detaches or coalesces with another bubble [47]. The growth rate is

$$r(t) = \beta_g (Dt)^{0.5} \quad (1.12)$$

where β_g is the growth coefficient characterised by the level of supersaturation, r is the radius, D is the diffusion coefficient.

Sides later stated that the error in assuming the entire process is governed by mass transfer is small. This assumption is validated by the experiments of Westwater et al [48,49,50] for the growth rates of oxygen, chlorine, carbon dioxide and hydrogen from various materials. The diameters of bubbles evolved on a microelectrode were measured using high-speed photography. Plots of $\ln r$ vs. $\ln t$ yield a straight line of slope 0.5, consistent with equation 1.12 for individual bubbles but the behaviour of multiple bubble formation was found to be more complex.

More recently, this technique has been developed to identify another mode of growth of bubbles from microelectrodes. Brandon and Kelsall proposed a direct injection method of growth for bubbles larger than the electrode diameter where bubble radius, r , is proportional to $t^{1/3}$ and showed the growth coefficient was strongly dependent on current density but independent of pH, type of gas, and electrode material [51]. Further developments in the high speed photography technique, again using a single nucleation site, have proved the importance of monitoring repetitive growth from a single nucleation site in order to determine its activity [52].

1.3.6 *Bubble coalescence*

Coalescence is a fundamental factor in determining the size distribution of bubbles dispersed in a liquid. Coalescence occurs when two bubbles collide, and the liquid film between them drains, becoming thinner and unstable until it ruptures at around 100 nm thickness producing one large bubble. The rate of coalescence depends on the rate at which the liquid drains from the film. Addition of a surface-active species can prevent coalescence, enabling the

formation of a stable foam [21,53]. Surfactants inhibit coalescence by providing resistance to film thinning or increasing the elasticity of the thin film, which prevents rupture [54]. An increase in the film elasticity means that when the film is stretched, regions of low surfactant concentration and high surface tension are generated, so providing an opposing force to film thinning [26]. Accounting for these factors, the rate of coalescence can be modelled and is in good agreement with experiment [55].

The effect of addition of electrolytes on the mechanism of coalescence is complex. Electrolytes negatively adsorb at the liquid/ vapour interface so increasing the surface tension. They would also be expected to reduce any electrostatic repulsion produced by charge build up on the bubble surface. Based on these properties, the presence of electrolytes should facilitate bubble coalescence. However, it has been found that many electrolytes inhibit bubble coalescence if present at a sufficient concentration (>20mM). This mechanism has been explained in terms of a reduction in hydrophobic attraction between bubbles [53]. Further insight has suggested that the cause of the attractive forces between bubbles operating over short distances arises from a perturbation of the structure of water. The attraction between bubbles operates via bridging microscopic bubbles. The effect of electrolyte is to decrease dissolved gas concentration. That in turn decreases the concentration of the bridging microbubbles and hence decreases the strength of attraction between bubbles so inhibiting coalescence [56].

Several modes of bubble coalescence have been identified. A characteristic behaviour of oxygen in alkaline electrolyte is “specific radial coalescence” [57], where a large bubble attracts and consumes smaller ones surrounding it. This effect was later explained as a thermocapillary phenomenon [58], where the motion of neighbouring bubbles is controlled by thermocapillary migration (arising from the temperature dependent surface tension) in the temperature gradient created by the collector bubble.

1.3.7 Bubble detachment

Bubbles detach from a surface once they have grown to a specific volume that is determined by the dynamics of the surrounding solution, the buoyancy, pressure and adhesion forces. Detachment occurs when the surface adhesion related to contact angle can no longer

overcome the buoyancy. This force balance is given by Karri [59] and covered in detail in section 2.1.8. For hydrogen bubbles evolved by the oxidation of formaldehyde at a small vertical copper electrode (diameter 0.4 mm), it was found that the contact angle decreases sharply with increasing bubble diameter for small bubbles (20 to 60 μm) and remains relatively constant for larger bubbles. This effect was attributed to the slow growth of the contact region compared to the growth of the bubble. As the bubbles grow, the difference between the upper and lower contact angles, θ_u and θ_l , changes with time (see figure 1.8). As the concentration of surfactant (sodium dodecyl benzene sulfate) increases, the bubbles grow more uniformly with a larger population density and smaller detachment diameter. However, the contact angle for an individual bubble was not significantly affected by the presence of the surfactant [60].

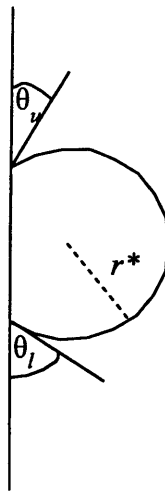


Figure 1.8 Schematic diagram showing side view of bubble attached to a vertical surface

The electrostatic interaction between a bubble and an electrode strongly influences the size of the bubble detaching. Interfacial electrical properties of hydrogen, oxygen and chlorine bubbles, as measured by electrophoresis, has shown the bubble charge is a function of the pH of the electrolyte [61]. All bubbles displayed a point of zero charge at pH 2-3. They were negatively charged at a higher pH and positively charged at a lower pH.

1.4 Measurement of bubble evolution rate

Bubble evolution at an electrode is commonly measured by recording the fluctuation of electrochemical parameters such as current, potential or electrolyte conductivity that occur as a result of the continuous movement of bubbles at the interface [62]. Although methods of fluctuation analysis differ, the common theme is to establish the time dependence of the fluctuations in order to obtain kinetic information. A statistical approach was used by Gabrielli to extract characteristic bubble parameters such as nucleation rate and bubble lifetime for hydrogen bubbles forming in sulphuric acid at a corroding iron electrode [63, 64] and the evolution of hydrogen and oxygen at a platinum electrode [65]. A linear-growth model of voltage fluctuations was used, shown in figure 1.9.

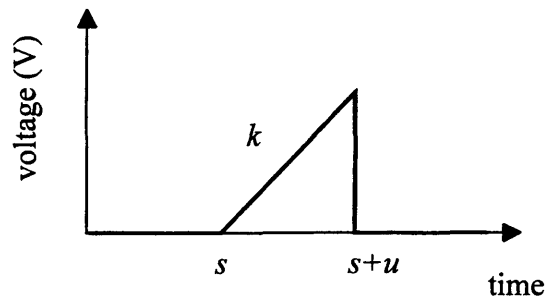


Figure 1.9 Model of elementary linear voltage transient

where s is the nucleation time, u is the bubble lifetime, and k is the rate of voltage increase. The recorded voltage fluctuation is considered the sum of elementary transients; s and u are random quantities, whose probability is given by a homogeneous Poisson law of intensity. Their values are determined from the asymptotic values of the power spectral density (PSD.; an FFT spectrum of the autocorrelated voltage signal). This analysis is useful for obtaining characteristic bubble evolution parameters. However, the model used is phenomenological and does not take into account other events such as coalescence.

Hodgson used Fourier analysis as a qualitative treatment of current noise fluctuations due to bubble evolution. It was noted that the most prominent features occur at less than 2 Hz [66]. The distribution of bubble sizes can be established from photography, although this technique only provides the distribution at a specific cross-section. Acoustic detection of bubbles is well established; a comprehensive review of various acoustic techniques highlights the complex analysis involved [67]. A simpler, alternative technique based on the

same principles as sedimentation size analysis has been developed by Sasaki [68]. Bubbles rising in a column cause the volume of the liquid to change. If the drop in meniscus height is measured as a function of time after bubble evolution has ceased, the bubble size distribution can be calculated from the variation in the rising bubble velocity.

1.4.1 Applied bubble nucleation kinetics

Lubetkin provides the conditions for which the Wilt equation (equations 1.11 and 2.34) is valid [69], specifically where Harvey nuclei may be present. The conclusion drawn from this study is that nucleation may not be the rate-limiting step in the evolution process at hydrophobic surfaces. Further departure from the validity of equation 1.11 for the measurement of the bubble nucleation rate at a physically inhomogeneous surface has been identified [70]. The nucleation of carbon dioxide at a Pyrex surface was measured using the pressure release bubble nucleation (PRBN) technique [71]. The deviation from theory was accounted for by the concept of nucleation rate dispersion, when plotting the natural log of the nucleation rate (J) as a function of supersaturation (σ); the measured nucleation rate is in fact a composite of the rate of nucleation of each type of site at the surface. If the activity of these sites varies significantly, the distribution of rates gives rise to curve when $\ln J$ is plotted vs. $(\sigma P)^2$, not the straight line predicted by the theory.

1.4.2 Nucleating geometry

The geometry of active sites for nucleate boiling of ether and pentane on zinc and nickel has been determined by high-speed photography [72]. It was found that pits with diameters of 5 μm were very active nucleation sites. However, there was no difference in activity for different crystal faces of zinc, and no bubbles formed at grain boundaries. The degree of gas entrapment that occurs as a liquid wets a rough surface depends on the steepness and the height of the cavities, as more gas entrapment occurs in a steeper walled cavity. These gas filled cavities initiate bubble formation by providing a Harvey nucleus [73].

Judd and Chopra review the theory and experiment relating to the interaction of nucleation processes occurring at adjacent nucleation sites. Using a system where dichloromethane bubbles are nucleated at a heated glass surface in a sealed vessel (bubble departure diameter

being controlled by the pressure in the vessel), they concluded that site activation/deactivation is the mechanism responsible for nucleation site interaction. If the geometry of a cavity is such that it does not retain a nucleus of gas upon the detachment of a bubble from it, bubble formation can only occur if a bubble growing at an adjacent site covers it and so deposits a nucleus in it. Hence, its activity will be enhanced by its proximity to the adjacent active site [74].

1.4.2.1 Nucleation at a single site

Single nucleation sites have been manufactured, with one proposed application being a surface tension sensor [75]. The artificial site is created in the working electrode (a silicon wafer; (100) crystal orientation, coated with a Ti/Au/Ti sandwich) by isotropic etching of the silicon. Mouth diameters between 2 and 10 μm have been fabricated. Hydrogen was evolved at the exposed silicon and on the bulk electrode. The gas produced at the working electrode does not give rise to nucleation but rather diffuses to the nucleation site containing a Harvey nucleus. As successive bubbles evolved at the microcavity, simultaneous measurement of the overpotential and impedance fluctuations gave rise to a periodic signal [76]. This phenomenon is discussed in section 2.3.1.

1.4.3 Surface modifications

It has been found that chemical modification of porous silica microspheres dramatically changes the number of bubbles evolved from water supersaturated with N_2 at 5, 15 and 50 atmospheres [77]. The pores (described as deep channels) had diameters ranging from 80-300 \AA . At low supersaturations, the particles with the smallest pore size produce the greatest number of bubbles. Coating the particles with a hydrophobic layer causes a significant increase in the number of bubbles. Hydrostatic pressurization prior to the experiment, to remove any gas trapped in the pores, suppresses bubble activity. This work confirms that the presence of Harvey nuclei enhances bubble evolution activity by removing the energy barrier to bubble formation.

Modification of porous graphite electrodes with Pt decreases the overpotential required to achieve a specific current density for hydrogen evolution from flowing KOH electrolyte. This effect is consistent up to a threshold of 200 mA cm^{-2} ; after this value the polarization required is significantly higher than predicted. At higher current densities, it is believed

hydrogen gas bubbles become trapped in the porous graphite, increasing gas void fraction (and hence resistivity) and decreasing effective electrode area [78].

1.4.3.1 Effect of electrolyte composition

The effect of electrolyte composition has been shown to have a significant effect on the dynamics of hydrogen bubble evolution at a copper microelectrode. In unmodified acid electrolyte, the energy barrier to nucleation was sufficiently high that only one nucleation site was active. The addition of an inorganic salt to the electrolyte facilitated nucleation and inhibited coalescence, causing a larger number of smaller bubbles to be evolved [79].

1.5 Cell voltage

It was shown in Table 1.1 that all three chlor-alkali cells run at a higher potential (E_{cell}) than the thermodynamic cell potential E_{rev} . This increased power consumption can be explained by looking at the factors contributing to E_{cell} .

$$E_{cell} = E_e^C - E_e^R - |\eta_A| - |\eta_C| - iR_{cell} - iR_{circuit} \quad (1.13)$$

Originally, the mercury cell operated at 5V, whereas the modern membrane cell operates at only 3.1V. A large overvoltage is needed to operate a chlor-alkali cell. The overall effect of increasing the operating potential is to increase running costs. This problem arises due to ohmic losses (electrical energy is dissipated as heat) in the electrodes, and the electrolyte that contains bubbles and in the cell separator. There is also a contribution from anodic and cathodic overpotentials needed to achieve the required current densities at the electrodes. The minimisation of the cell voltage is achieved by operating the cell at a high temperature, pressure and electrolyte conductivity, decreasing the inter-electrode gap and the use of highly active electrode materials. Bubbles dispersed in the bulk electrolyte increase the ohmic losses in the cell, and affect the macroscopic current distribution. Bubbles attached to the electrode (or located very near to it) alter the microscopic current distribution, effectively physically blocking the catalytic surface by covering active sites. The supersaturation is also affected which influences the concentration overpotential of the electrode.

1.5.1 Ohmic losses

In vertical cells, the bubble resistance is determined by the bubble void fraction in the inter-electrode region. Because of the high dispersion of bubbles in the cell, the average void fraction can be obtained by measuring the change in height of electrolyte, before and during electrolysis. However, this method is impractical for cells with horizontal electrodes. It has been shown that for oxygen bubbles evolved at the underside of a horizontal electrode, bubble resistivity for a given inter-electrode gap for both carbon and graphite anodes is linearly proportional to the bubble coverage (a parameter calculated from visual observation of the electrode) [80,81].

1.5.2 Overpotential

The various components of the overpotential due to an attached bubble on the surface can be separated [82]. The overpotential η is the sum of activation (kinetic) and concentration overpotentials. The concentration of product gas dissolved in the electrolyte in immediate contact with electrode determines the average concentration overpotential that can be calculated using equations for the chemical potential of the gas [17]. Ignoring activity coefficients, the concentration overpotential (η_c) may be estimated as shown in equation 1.14.

$$\eta_c = \left(\frac{RT}{4} \right) \ln(\alpha) \quad (1.14)$$

where α is the supersaturation ratio.

1.5.3 Mass transfer at electrodes

Although the presence of bubbles in the electrolyte increases the effective current density on the electrode, resulting in an increase in the ohmic drop, bubbles also enhance mass transport at the electrode, by causing mixing between the electrolyte at the surface and in the bulk. Dissolved gas in the boundary layer undergoes two superimposed methods of mass transfer, which increase the mass transfer coefficient for dissolved gas. One controls the flux of

dissolved gas from the electrode to the bulk electrolyte; the other controls the flux from the supersaturated electrolyte to the bubble surface [83]. As bubbles grow, their surfaces expand, and upon detachment, fresh electrolyte flows to fill the vacancy. Measurement of interfacial re-equilibration during hydrogen bubble evolution shows large numbers of bubbles coalescing at the surface improves mass transport properties [84]. Although the contribution of individual bubbles is unknown [85], two parallel hydrogen streams create greater mass transport enhancement than the equivalent-volume single stream [86]. Increases in the mass transfer coefficient of more than 100% can be obtained by modifying the macroscopic geometry of the electrode. For example, performance is enhanced significantly by the use of an electrode fabricated from an expanded metallic mesh rather than a planar sheet [87].

1.6 Electrocatalysis of gas evolving reactions

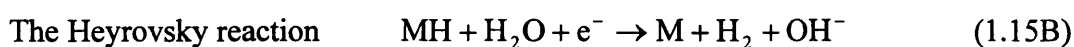
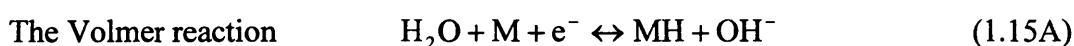
Many electrode reactions only occur at a significant rate by the application of a high potential, hence the need for catalytic electrode materials as described in Section 1.2. Electrocatalysts enable the electrode reaction, and hence the formation of products to occur at a lower overpotential. The reaction is often catalysed by desorption of a species from the electrode, hence, the activity of an electrocatalyst is affected by its structure and morphology. The material must possess a high surface area, and good mechanical strength and durability to resist corrosion. As well as catalysing the required reaction, the material must inhibit any competing reactions, e.g. in a chlor-alkali cell, the oxygen evolution reaction is thermodynamically more feasible than chlorine evolution, so the anode material must kinetically favour chlorine evolution. Prediction of the reaction mechanism arises from the measurement of the kinetics of the electrode reactions using Tafel analysis. An important parameter is the surface area determined by voltammetric charge.

If the efficiency of the reaction at the electrodes is promoted by using electrocatalysts, there is a possibility of shifting the kinetic bottleneck away from the chlorine evolution step towards bubble evolution. The rate-limiting step would become the phase change that occurs in the cell, i.e. from dissolved gas molecules in solution to the formation of gas bubbles at the electrode, this issue is discussed in section 1.6.3.

1.6.1.1 Hydrogen evolution reaction

The hydrogen evolution reaction (HER) is very well characterised in the literature. Hydrogen is a significant product formed in the chlor-alkali process and water electrolysis. Studies of the hydrogen evolution reaction (HER) at single crystal gold surfaces in perchloric acid have shown that the reaction mechanism is independent of the surface structure. However, the rate of the elementary steps is influenced and there is a large dependence of the kinetics of the HER with the crystallographic orientation of the electrode. The catalytic activity increases with the atomic density of the surface [88].

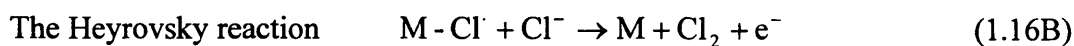
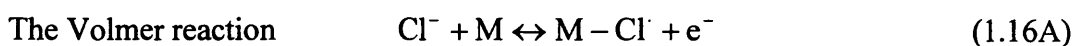
In alkaline solution, the HER may proceed by three possible reactions given below

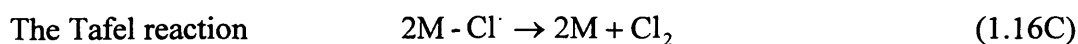


Equations 1.15B and 1.15C show the different rate limiting steps for the Heyrovsky and Tafel mechanisms [89]. A comprehensive study of the HER on a variety of electrode materials has shown the mechanism to proceed according to Volmer-Heyrovsky, with electrodes containing noble metals being the most electrocatalytic [90].

1.6.1.2 Chlorine evolution mechanism

Analogous to hydrogen evolution, the chlorine evolution reaction is generally thought to proceed via either of the two mechanisms given above. The electrode reactions are given below





It is known that electrocatalytic activity of the electrode is enhanced by changing the surface composition i.e. making the surface rich in RuO₂. An alternative recombination reaction at a RuO₂ electrode was proposed by Krishtalik



For chlorine evolved at a mixed RuO₂/TiO₂ electrode, the Volmer-Heyrovsky mechanism was found to be dominant [91]. A study of various mechanisms has been proposed for chlorine evolution on the RTO surface and the subject is under debate [92].

1.6.2 *Structure of electrode coating*

One of the electrocatalysts used for the evolution of oxygen in the electrogalvanizing of steel is an iridium-based anode IrO₂-Ta₂O₅. Prepared by thermal decomposition, the coating has a heterogeneous “mud-cracked” morphology. IrO₂ particles form on the flat areas and in the cracks. The surface morphology is strongly dependent on the pre-treatment of the substrate and the painting method of the coating solution. It has been found that presence of fine particles formed on the flat areas are important in the electrocatalysis of oxygen evolution, whereas clusters of the particles, the flat areas, or particles formed in the cracks have little effect on catalytic activity [93]. Porous Raney-nickel coatings, prepared from NiZn_x, NiAl_y, or NiS_z precursors are the latest technological innovation for hydrogen evolving cathodes used in chlor-alkali electrolyzers. Typical pore diameter is 20 Å and evolving hydrogen from KOH it has been found that the effective catalytic activity of porous electrodes is dependent on the morphology of catalytic particles. The activity is limited by the penetration of the current into the nanoporous matrix [94,95]. This problem can be overcome by using Teflon bonded electrodes [96], which facilitates the removal of gas bubbles from the pores, so increasing the area of electrocatalyst exposed to the electrolyte.

1.6.3 *Surface and system modifications*

The properties of RuO₂ + TiO₂ (RTO)-based DSA[®] used for industrial applications can be modified by the addition of a third component to optimise activity, selectivity and stability. A study on the effect of substituting Ce for Ti highlights the subtle balance required between activity and durability that is required by an electrocatalytic compound [97]. Substitution by Ce increases the activity for chlorine evolution, shown by the increased current density at a fixed potential. However, the current depends on both electronic and geometric factors. By measuring the true surface area from the charge, the current can be normalised. It transpires that in fact CeO₂ is less active than TiO₂, as its surface area is higher. The smaller particle size of CeO₂ + RuO₂ also means the surface is less stable to mechanical erosion from Cl₂ evolution.

The kinetics of gas evolution at electrocatalysts can be further enhanced by the use of ultrasound [98]. For the evolution of hydrogen and chlorine at platinized platinum, the rate-limiting step of these reversible processes is the removal of the gaseous product from the electrode surface. Irradiation with ultrasound significantly enhances this process, but its effect is less significant for oxygen evolution, an irreversible process where surface oxidised species are involved in the electron transfer. A similar effect is seen when the surface roughness and temperature are increased [99]. Increasing the porosity of the electrode and the temperature can increase the rate of an irreversible gas evolution process. For a reversible process, the small pores are not effective if the overvoltage is determined by the supersaturation.

1.6.3.1 *Effect of bubbles*

Chirkov identified the distribution of gas and electrolyte within a porous electrode to be fundamental in the determination of the mechanism of bubble evolution [100]. The kinetics of hydrogen evolution on platinum from HCl, are found to be subject to a passivation mechanism due to the inhibition the electron transfer reaction caused by the formation of hydrogen bubbles. The ohmic resistance increases with increases in bubble population and reaches a constant value associated with the size and number of bubbles leaving the electrode [101]. The overpotential for H₂, O₂ and Cl₂ evolution at platinized platinum was shown to decrease by the addition of PTFE sites (of 0.5mm diameter) to the electrode surface [102].

The overpotential of the H_2 and Cl_2 evolution is essentially a concentration overpotential, its value being determined by the supersaturation as shown in equation 1.14. The PTFE sites act as collectors of gas bubbles, so removing them from the electrochemically active part of the electrode. The bubbles form at the PTFE/Pt interface and adhere to the PTFE sites. This increases mass transport of the gas to the bubble, hence reducing supersaturation, simultaneously increasing the electrocatalytic area of the electrode compared to an unmodified sample. The behaviour of bubbles, in terms of their tendency to either adhere to the electrode or detach, has been investigated for both an unmodified RuO_2 electrode and one modified with PTFE [103]. By comparing the charge for oxygen evolution to the charge for oxygen reduction, measured by cyclic voltammetry, parameters such as bubble collection, escape and dissolution efficiency were used to characterise the electrode. The increased hydrophobicity of the modified electrode resulted in large bubbles adhering to the electrode and therefore blocking active RuO_2 sites to further oxygen evolution. This effect is demonstrated in figure 1.10.

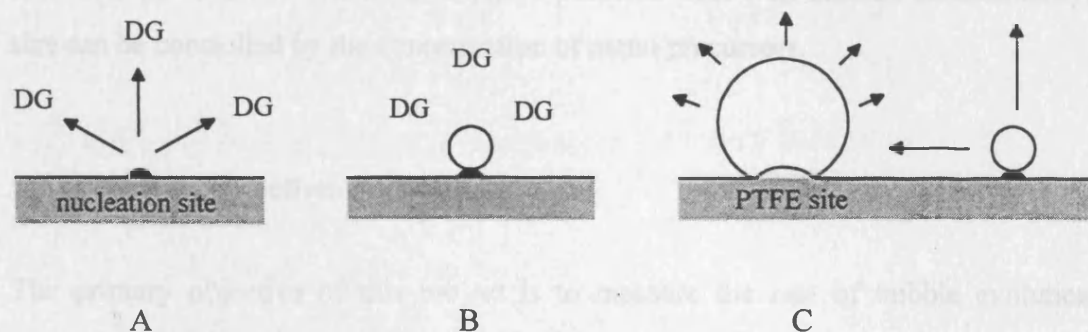


Figure 1.10 Schematic diagram of a chemically modified electrode

- A) The active nucleation site produces that dissolved gas (DG) in the electrolyte.
 B) The bubble grows at the site by diffusion C) The bubble detaches or collects at a hydrophobic site (PTFE) where it can grow to a larger size.*

The presence of surfactants in the electrolyte can modify the overpotential by affecting bubble evolution characteristics such as detachment diameter and population density of bubbles. The influence of various surfactants on the kinetics of hydrogen evolution from sulphuric acid at a gold electrode has been investigated [104]. The formation of hydrogen bubbles increases the electrolyte resistance due to a screening effect; the extent of screening

that occurs in the presence of a surfactant depends on its molecular structure. Maximum screening occurs for cationic surfactants, minimum screening for non-ionic surfactants.

1.6.4 Surface characterisation

The surface morphology and microstructure of DSA[®] are not homogeneous and are greatly influenced by the preparation conditions. The properties of the coatings can be defined by the surface composition, as measured by techniques such as x-ray photoelectron spectroscopy (XPS), x-ray diffraction analysis (XRD), electrochemical techniques and thermal desorption spectrometry (TDS). It has been found that TDS and electrochemical techniques are particularly useful for analysis of the upper surface and the inner surface (including pores) whereas XPS cannot give information on the hidden part of a concave surface [105]. The sol-gel process is a method that has been utilised as an alternative to the thermal decomposition method in order to prepare a more homogeneous surface [106]. The ultra fine mixed oxide particles are prepared by the hydrolysis and condensation of the metal alkoxides in ethanol. The method yields particles with well-defined stoichiometry, whose size can be controlled by the concentration of metal precursors.

1.7 Project objectives

The primary objective of this project is to measure the rate of bubble evolution at the interface between a solid electrode and an aqueous solution. The concern is only with bubble evolution dynamics whilst the bubbles are attached to the electrode. Three techniques are used to monitor bubble behaviour in order to characterise the system from which they are evolved. Using this information, the fundamental processes of bubble evolution can be related to the physical and chemical properties of the system. These properties are essentially microscopic, e.g. the microscopic electrode surface geometry is relevant to bubble behaviour at the electrode. However, the effect of the macroscopic electrode geometry, in terms of its shape or dimension, on two-phase flow in the electrochemical cell is beyond the scope of this project.

1.7.1 *Experimental techniques*

Gas bubbles were evolved using two different methods of solution supersaturation. The EQCM and FFV techniques monitored gas bubbles produced electrochemically. Gas molecules generated by electrolysis saturate the solution in the immediate vicinity of the electrode. A large current density is applied to supersaturate the electrolyte. The major advantage of the electrolytic method is that it allows effective control over the kinetics and thermodynamics of nucleation and growth by manipulation of the current and overvoltage. The PRBN technique causes the solution to become supersaturated by a mechanical process. The solution is saturated with the gas at an elevated pressure in a sealed vessel, by diffusion across the gas/liquid interface. When the gas pressure inside the vessel is reduced, bubbles form spontaneously in the now supersaturated solution.

Using these electrochemical techniques, bubble nucleation, growth and detachment processes are studied under varied conditions of temperature and pressure, and as a function of the electrode surface characteristics, such as chemical composition and morphology and physical orientation, different electrode material and electrolyte used to evolve the gas. A complete picture of bubble evolution at the surface is achieved by the use a complementary technique (PRBN) where bubbles are evolved in a purely chemical environment

1.7.2 *The use of video to monitor bubbles*

This technique of direct visual observation is well established. The use of computer software to capture images greatly enhances the scope of the technique in terms of the number of images that can be analysed. Fast frame video (FFV) analysis has been used to monitor bubble evolution at a macroelectrode. Also all previous work has been carried out on microelectrodes, where the number of active nucleation sites, and hence the interaction between neighbouring bubbles, is limited.

1.7.3 *The use of EQCM to monitor bubble formation*

The use of the EQCM for bubble detection is a relatively novel application; all previous studies have been empirical in nature, using two different approaches. Firstly, the feasibility

of the EQCM for detecting the nucleation of bubbles in the vicinity of the electrode was established [107]. Hydrogen bubbles were evolved at a gold electrode from 0.1M HClO₄. The onset of bubble nucleation causes the frequency of the quartz crystal to increase, indicating a mass decrease at the electrode interface. It was proposed that the magnitude of this increase was dependent on the three phase contact angle. For a 300µm bubble, the expected frequency change was 0.08Hz when the contact angle was 0°, compared to 80Hz when the contact angle was 90° (see section 2.3.1). This work was extended to the study of hydrogen and chlorine bubble evolution on platinum electrodes [108]. It was demonstrated that hydrogen bubbles detached at a smaller size than chlorine bubbles and it was suggested that bubble phenomena would be best studied under potentiostatic control. This was later confirmed by a simultaneous gravimetric and chronoamperometric study of chlorine on platinum where individual bubbles produced frequency changes of 2-10Hz [109].

An alternative approach was the use of spectral analysis of the “mass” fluctuations arising from successive bubble detachment events [110]. This technique had been used previously to extract statistical data about bubble nucleation from the analysis of potential fluctuations as described in section 1.4.1. While this work validated the use of Fourier analysis, no attempt was made to resolve individual components of the frequency spectrum or characterise the shape of the mass transient produced. The dependence of the size of mass fluctuation on current density was not resolved.

The aim of the EQCM study is to utilise both techniques to establish the dependence of bubble behaviour on surface properties. A fast Fourier transform (FFT) [111] of the frequency data obtained from a quartz crystal surface should yield trends in the frequency signal which can be attributed to bubbles nucleating and detaching from specific sites on the electrode. In principle, the technique could be used to obtain the rate constant for the rate-limiting step and to determine the distribution of bubble sizes (size of bubbles on detachment as affected by surface properties). Bubble evolution can be categorised in terms of the shape of the EQCM frequency response as a function of overpotential, under different modes of evolution, e.g. cyclic voltammetry and chronoamperometry, surface roughness and electrocatalytic properties. The behaviour of two different gases, hydrogen and chlorine will be compared, as will the position of the electrode, in either an upward-facing horizontal, or vertical position.

1.7.4 PRBN as a bubble monitoring device

This technique monitors bubble nucleation by detecting the elevation of pressure in the headspace above the solution in the pressure vessel arising from bubble nucleation. The PRBN system is a technique that can provide evidence for whether nucleation or growth is rate limiting [30]. Where nucleation is the rate limiting step, i.e. on hydrophilic surfaces, the nucleation rate can be determined directly from the slope of the rising pressure transient.

The PRBN method comprises a pressure vessel that is used to saturate a liquid (here, brine) with a gas (here, chlorine) at an elevated pressure. After equilibration, the vessel is decompressed, so that the solution is supersaturated to an extent determined by the initial and final pressures. Once the final target pressure is established, the vessel is resealed. The subsequent evolution of gas from the supersaturated solution can then be measured via the associated pressure rise in the headspace above the solution (after application of a correction for the effects of adiabatic cooling).

1.7.5 Thesis outline

The theory required to extract quantitative information from each technique is given in Chapter 2. The experimental procedures used are described in Chapter 3. The results are separated into three chapters, 4-6, one for each of the experimental techniques. Chapters 4-6 are each written as self-contained studies, including a brief introduction and discussion of the results. Conclusions and ideas for future work are given in Chapter 7.

1. Shima, A., *Shock Waves*, **1997**, 7, 33-42.
2. *Chemical Engineer's Handbook*; 6th Edition; Perry, R.H.; Green, D.W. and Maloney, J.O., Ed.; McGraw-Hill: New York, 1984.
3. Lubetkin, S.D., *Chemical Society Reviews*, **1995**, 24, 243.
4. Zhou, Z. A.; Xu, Z.; Finch, J. A., *Minerals Engineering*, **1994**, 7, 1073-1084.
5. Ponter, A.B.; Surati, A.I., *Chem. Eng. Technol.*, **1997**, 20, 85-89.
6. Jackson, M.L., *Industrial & Engineering Chemistry Research*, **1994**, 33, 929-933.
7. Brooks, W.N., *Chemistry in Britain*, **1986**, 22, 1095-1098.
8. Mahmood, M.N.; Turner, A.K.; Man, M.C.M.; Fogarty, P.O., *Chemistry & Industry*, **1984**, 50-54.
9. Pletcher, D.P.; Walsh, F.C., *Industrial Electrochemistry*; 2nd ed.; Chapman and Hall: London, 1990.
10. Hine, F.; Tilak, B. V.; Viswanathan, K., "Chemistry and the chlor-alkali industry" in *Comprehensive Treatise of Electrochemistry*; Plenum: New York, 1986; Vol. 18; pp 249-302.
11. Kelham, S., "Chlor-alkali products" in *An introduction to Industrial chemistry*; 3rd ed.; Heaton, A., Ed.; Chapman and Hall: New York, 1996.
12. Tseung, A. C. C.; Antonian, J. A.; Hibbert, D. B., *Chemistry & Industry* **1984**, 54-59.
13. Chirkov, Y. G.; Pshenichnikov, A. G., *Soviet Electrochemistry* **1985**, 21, 114-117.
14. Vogt, H., *Electrochimica Acta* **1984**, 29, 167-173.
15. Vogt, H., *J. Appl. Electrochem.* **1993**, 23, 1323-1325.
16. Nevedov, V.G.; Serebritskii, V.M. and Ksenzhek, O.S., *Elektrokhimiya*, **1992**, 29, 534-536.
17. Sides, P. J., "Phenomena and effects of Electrolytic gas evolution" in *Modern Aspects of Electrochemistry*; White, R. E., Bockris, J.O'M., Conway, B.E., Ed.; Plenum: New York, 1986; Vol. 18; pp 303-354.
18. Dunning, W. J., "Theory of crystal nucleation from vapour, liquid and solid systems" in *Chemistry of the solid state*; Garner, W. E., Ed.; Butterworth: London, 1955.
19. Frenkel, J. *Kinetic Theory of Liquids*; Dover: New York, 1955.
20. Wilt, P.M., *J. Coll. Int. Sci.*, **1986**, 112, 530-538.
21. Lubetkin, S. D., "Bubble nucleation and growth" in *Controlled particle, droplet and bubble formation*; Welock, D. J., Ed.; Butterworth-Heinemann: Oxford, **1994**; pp 159-190.

22. Volmer, M., *Kinetik der Phasenbildung*; Steinkopff Verlag: Dresden, 1939.
23. Becker, R.; Doring, W., *Ann. Phys.*, 1935, 24, 719.
24. Zeldovich, J., *J. Exp. Theor. Phys.*, 1942, 12, 525.
25. Kashchiev, D., *J. Chem. Phys.*, 1982, 76, 5098-5102.
26. Adamson, A. W., *Physical chemistry of surfaces*; 5th ed.; John Wiley and Sons, Inc.: New York, 1990.
27. Cole, R., *Advances in Heat Transfer*, 1974, 19, 85-166.
28. Blander, M.; Katz, J. L., *A. I. Ch. E. Journal*, 1975, 21, 833-847.
29. Ward, C. A.; Balakrishnan, A.; Hooper, F. C., *Journal of Basic Engineering*, 1970, 85, 695-704.
30. Lubetkin, S.; Blackwell, M., *J. Coll. Int. Sci.*, 1988, 126, 610-615.
31. Nefedov, V. G., *Russian Journal of Electrochem.*, 1995, 33, 815-818.
32. Chirkov, Y. G.; Pshenichnikov, A. G., *Soviet Electrochem.*, 1986, 22, 580-584.
33. Ward, C. A.; Johnson, W. R.; Venter, R. D.; Ho, S., *J. Appl. Phys.*, 1983, 54, 1833-1843.
34. Kaschiev, D.; Firoozabadi, A., *J. Chem. Phys.*, 1993, 98, 4690-4699.
35. Bravina, L. V.; Zabrodin, E. E., *Physics Letters A*, 1995, 202, 61-67.
36. Preuss, M. A.; Butt, H. J., *J. Coll. Int. Sci.*, 1998, 208, 468-477.
37. Schmeltzer, J. W. P.; Gutzow, I.; Schmeltzer, J. J., *J. Col. Int. Sci.*, 1996, 178, 657-665.
38. Drelich, J.; Miller, J. D.; Good, R. J., *J. Coll. Int. Sci.*, 1996, 179, 37-50.
39. Swain, P. S.; Lipowsky, R., *Langmuir*, 1998, 14, 6772-6780.
40. Drelich, J., *Journal of Adhesion*, 1997, 63, 31-51.
41. McClurg, R. B.; Flagan, R. C., *J. Coll. Int. Sci.*, 1998, 201, 194-199.
42. Zeng, X. C.; Oxtoby, D. W., *J. Chem. Phys.*, 1990, 94, 4472-4478.
43. Martinez, J. C., *J. Coll. Int. Sci.*, 1998, 205, 476-481.
44. Harvey, E. N.; McElroy, W. D.; Whiteley, A. H., *J. Appl. Phys.*, 1947, 18, 162-172.
45. Ward, C. A.; Tikuisis, P.; Venter, R. D., *J. Appl. Phys.*, 1982, 53, 6076-6084.
46. Frank, F. C., *Proc. Roy. Soc.*, 1950, A201, 586-599.
47. Scriven, L. E., *Chem. Eng. Sci.*, 1959, 10, 1-13.
48. Buehl, W. M. and Westwater, J. W., *A. I. Ch. E. Journal*, 1966, 12, 571-576.
49. Westerheide, D. E.; Westwater, J. W., *A. I. Ch. E. Journal*, 1961, 7, 357-362.
50. Glas, J. P.; Westwater, J. W., *Int. J. Heat Mass Trans.*, 1964, 7, 1427-1443.
51. Brandon, N. P.; Kelsall, G. H., *J. Appl. Electrochem.*, 1985, 15, 475-484.

52. Carr, M. W.; Harris, L. A.; Hillman, A. R., *J. Electroanal. Chem.*, **1994**, 367, 251-254.
53. Craig, V. S. J.; Ninham, B. W.; Pashley, R. M., *J. Phys. Chem.*, **1993**, 97, 10192-10197.
54. Pashley, R. M.; Craig, V. S. J., *Langmuir*, **1997**, 13, 4772-4774.
55. Li, D., *J. Coll. Int. Sci.*, **1996**, 181, 34-44.
56. Weissenborn, P. K.; Pugh, R. J., *J. Coll. Int. Sci.*, **1996**, 184, 550-563.
57. Sides, P. J.; Tobias, C. W., *J. Electrochem. Soc.*, **1985**, 132, 583-587.
58. Guelcher, S. A.; Solomentsev, Y. E.; Sides, P. J.; Anderson, J. L., *J. Electrochem. Soc.*, **1998**, 145, 1848-1855.
59. Karri, S. B. R., *Chem. Eng. Comm.*, **1988**, 70, 127-135.
60. Trieu, H.H., *J. Electrochem. Soc.*, **1989**, 136, 2218-2223.
61. Brandon, N. P.; Kelsall, G. H.; Levine, S.; Smith, A. L., *J. Appl. Electrochem.*, **1995**, 15, 485-493.
62. Gabrielli, C.; Huet, F., *J. Appl. Electrochem.* **1994**, 24, 593-601.
63. Gabrielli, C.; Huet, F.; Keddam, M., *J. Electrochem. Soc.*, **1991**, 138, L82-84.
64. Gabrielli, C.; Huet, F.; Keddam, M., *J. Appl. Electrochem.*, **1985**, 15, 503-508.
65. Gabrielli, C.; Huet, F.; Keddam, M.; Sahar, A., *J. Appl. Electrochem.*, **1989**, 19, 683-696.
66. Hodgson, D. R., *Electrochimica Acta*, **1996**, 41, 605-609
67. Leighton, T. G.; Ramble, D. G.; Phelps, A. D., *J. Acoust. Soc. Am.*, **1997**, 101, 2626-2635.
68. Sasaki, H.; Matsukawa, H.; Usui, S.; Matijevic, E., *J. Coll. Int. Sci.* **1986**, 113, 500-503.
69. Lubetkin, S. D., *J. Chem. Soc., Faraday Trans. 1*, **1989**, 85(7), 1753-1764
70. Carr, M. W.; Hillman, A. R.; Lubetkin, S. D., *J. Coll. Int. Sci.*, **1995**, 169, 135-142.
71. Lubetkin, S. D., *J. Appl. Electrochem.*, **1989**, 19, 668-676.
72. Clarke, H. B.; Strenge, P. S.; Westwater, J. W., *Chem. Eng. Progr. Symp.*, **1959**, 55, 103-110.
73. Bankoff, S. G., *A. I. Ch. E. Journal*, **1958**, 4, 24-26.
74. Judd, R.L.; Chopra, A., *J. Heat Transfer-Trans. of the A. S. M. E.*, **1994**, 115, 955-962.
75. Volanschi, A.; Olthuis, W.; Bergveld, P., *Sensors and Actuators A-Physical*, **1996**, 52, 18-22.
76. Volanschi, A.; Nijman, J.G.H.; Olthuis, W.; Bergveld, P., *Sensors and materials*, **1997**, 9, 223-240.

77. Ryan, W. L.; Hemmingsen, E. A., *J. Coll. Int. Sci.*, **1998**, *197*, 101-107.
78. El-Deab, M. S.; El-Sharke, M. E.; El-Anadouli, B. E.; Ateya, B. G., *J. Appl. Electrochem.*, **1996**, *26*, 1133-1137.
79. Kristof, P.; Pritzker, M., *J. Appl. Electrochem.*, **1997**, *27*, 255-265.
80. Qian, K.; Chen, J. J. J.; Matheou, N., *J. Appl. Electrochem.*, **1997**, *27*, 434-440.
81. Qian, K.; Chen, Z. D.; Chen, J. J. J., *J. Appl. Electrochem.*, **1998**, *28*, 1141-1145.
82. Gabrielli, C.; Huet, F.; Keddam, M.; Macias, A.; Sahar, A., *J. Appl. Electrochem.*, **1989**, *19*, 617-629.
83. Vogt, H., *J. Appl. Electrochem.*, **1989**, *19*, 713-719.
84. Egan, E. W.; Tobias, C. W., *J. Electrochem. Soc.*, **1994**, *141*, 1118-1126.
85. Dees, D. W.; Tobias, C. W., *J. Electrochem. Soc.*, **1987**, *134*, 1702-1713.
86. Sutija, D. P.; Tobias, C. W., *J. Electrochem. Soc.*, **1994**, *141*, 2599-2607.
87. Piovano, S.; Cavatora, O. N.; Bohm, U., *J. Appl. Electrochem.*, **1988**, *18*, 128-133.
88. Perez, J.; Gonzalez, E. R. and Villullas, H. M., *J. Phys. Chem. B*, **1998**, *102*, 10931-10935.
89. Lasia, A., *J. Electroanal. Chem.*, **1998**, *454*, 115-121.
90. Borodzinski, J. J.; Lasia, A., *Int. J. Hydrogen Energy*, **1993**, *18*, 985-994.
91. Tomcsanyi, L.; DeBattisti, A.; Hirschberg, G.; Varga, K.; Liszi, J., *Electrochimica Acta*, **1999**, *44*, 2463-2472.
92. *Modern Chlor-alkali technology*; Sealey, S. A., Ed.; The Royal Society of Chemistry: Cambridge, 1998; Vol. 7.
93. Otagawa, R.; Morimitsu, M.; Matsunaga, M., *Electrochimica Acta*, **1998**, *44*, 1509-1513.
94. Wendt, H., *Electrochimica Acta*, **1998**, *39*, 1749-1756.
95. Raushch, S.; Wendt, H., *J. Electrochem. Soc.*, **1996**, *143*, 2852-2862.
96. Tseung, A. C. C., *J. Appl. Electrochem.*, **1985**, *15*, 575-580.
97. DeFaria, L. A.; Boodts, J. F. C.; Trasatti, S., *Electrochimica Acta*, **1997**, *42*, 3525-3530.
98. Walton, D. J.; Burke, L. D.; Murphy, M. M., *Electrochimica Acta*, **1996**, *41*, 2747-2751.
99. Heidrich, H. J.; Muller, L.; Podlovchenko, B. I., *J. Appl. Electrochem.*, **1990**, *20*, 686-691.
100. Chirkov, Y. U.; Pshenichnikov, A. G., *Elektrokhimiya*, **1991**, *26*, 1545-1549.
101. Harrison, J. A.; Kuhn, A. T., *Surface Technology*, **1983**, *19*, 249-259

102. Heidrich, H. J.; Muller, L., *Electrochimica Acta*, **1990**, *35*, 1089-1093.
103. Shieh, D. T.; Hwang, B. J., *J. Electroanal. Chem.*, **1995**, *391*, 77-91.
104. Cachet, C.; Keddam, M.; Mariotte, V.; Wiart, R., *Electrochimica Acta* **1994**, *39*, 2743-2750.
105. Kameyama, K.; Tsukada, K.; Yahikozawa, K.; Takasu, Y., *J. Electrochem. Soc.*, **1994**, *141*, 643-647.
106. Kameyama, K.; Shohji, S.; Onoue, S.; Nishimura, K.; Yahikozawa, K.; Takasu, Y., *J. Electrochem. Soc.*, **1993**, *140*, 1034-1037.
107. Carr, M. W.; Hillman, A. R.; Lubetkin, S. D.; Swann, M. J., *J. Electroanal. Chem.*, **1989**, *267*, 313-320.
108. Li, F.; Hillman, A. R.; Lubetkin, S. D.; Roberts, D. J., *J. Electroanal. Chem.*, **1992**, *335*, 345-362.
109. Li, F.; Lubetkin, S. D.; Roberts, D. J.; Hillman, A. R., *J. Chem. Soc. Chem. Comm.*, **1994**, 159-160.
110. Gabrielli, C.; Huet, F.; Keddam, M.; Torresi, R., *J. Electroanal. Chem.*, **1991**, *297*, 515-522.
111. Wayne, R. P., *Chemistry in Britain*, **1987**, *23*, 440-446.

This chapter provides a summary of nucleation, growth and detachment rate equations for bubbles forming spontaneously in a liquid supersaturated with gas. Also outlined is a description of the theory governing quantitative analysis of experimental PRBN, EQCM and video data. A more detailed description is given to the novel analysis of FFT treatment of EQCM mass transients.

2.1 Bubble Formation

The theory described below is relevant to bubble formation from supersaturated solutions where the value of supersaturation is a similar order of magnitude to that found during electrolytic gas evolution.

2.1.1 Supersaturation

Supersaturation is a measure of a system's deviation from equilibrium. Equilibrium is defined as the saturation of the medium with a second dissolved component at a given temperature and pressure. The absence or removal of a suitable pathway to release energy can achieve supersaturation. The converse of this argument, i.e. the ability to supply the system with a suitable low energy pathway to achieve new phase formation (e.g. bubbles) at low supersaturation is the general problem addressed by this research. Supersaturation (σ) is defined as

$$\sigma = 1 - \alpha \quad (2.1)$$

where for a supersaturated gas solution the saturation ratio (α) is expressed as

$$\alpha = c_2 / c_{2e} \quad (2.2)$$

where c_2 is the concentration of gas in solution and c_{2e} is the equilibrium concentration of gas over a flat surface [1].

2.1.2 Nucleation

Nucleation is a process by which a new phase is formed in an existing one. The process requires a thermodynamic driving force. In a unary liquid the driving force will exist if the chemical potential of the liquid phase exceeds that of the vapour. The appearance of vapour bubbles will reduce the free energy of the system and is therefore a spontaneous process. Generally there are two causes of this phenomenon (the stabilisation of the vapour phase compared to the liquid), either the elevation of temperature or reduction of pressure.

In a two-component system (e.g. Cl₂/brine solution) bubbles can form spontaneously at room temperature. The supersaturated Cl₂ solution is thermodynamically less stable than the Cl₂ gaseous phase and therefore has a higher chemical potential. Production of the new phase by bubble nucleation causes the free energy of the system to decrease due to the increased stability of the supersaturated phase. Obviously under the conditions of temperature elevation behaviour will be similar to that of a unary liquid.

2.1.3 Homogeneous nucleation

A system where a new phase is nucleated can be described using standard thermodynamic variables. A supersaturated medium is in a metastable state, thermodynamic fluctuations can cause the formation of molecular clusters, and these grow by accretion to form macroscopic nuclei. Consider an analogous system; the formation of spherical liquid droplets from a supersaturated vapour. In the absence of surface tension the free energy difference (ΔG_v) per unit volume of new (liquid) phase is given by the free energy required to transfer molecules from the vapour to the liquid phase [1,2,3].

$$\Delta G_v = -\left(\frac{RT}{v}\right) \ln\left(\frac{p}{p_e}\right) \quad (2.3)$$

where v is the molar volume of the new phase, p is the supersaturated vapour pressure and p_e the equilibrium vapour pressure of the liquid. The free energy contribution from the creation of a spherical droplet (ΔG_{bulk}) is given by

$$\Delta G_{bulk} = \frac{4\pi r^3 \Delta G_v}{3} \quad (2.4)$$

However, a significant degree of supersaturation is required before new phase is formed, once that threshold is reached, the new phase is formed rapidly. However, there is impedance to the formation of new phase due to the high surface energy requirement of small clusters. The free energy (ΔG_s) required to form the new surface is given by

$$\Delta G_s = 4\pi r^2 \gamma \quad (2.5)$$

where r is the droplet radius, γ is interfacial tension. The overall change in free energy (ΔG_{total}) is expressed in equation 2.6 and shown schematically in Figure 2.1.

$$\Delta G_{total} = 4\pi r^2 \gamma + 4\pi r^3 \Delta G_v / 3 \quad (2.6)$$

The maximum free energy value (ΔG^*) is equivalent to the activation energy for the formation of nuclei. The droplet radius at ΔG^* is termed the critical radius (For water at 0°C and saturation ratio 4, $r^* \approx 8\text{\AA}$ and the critical clusters contain approximately 90 molecules).

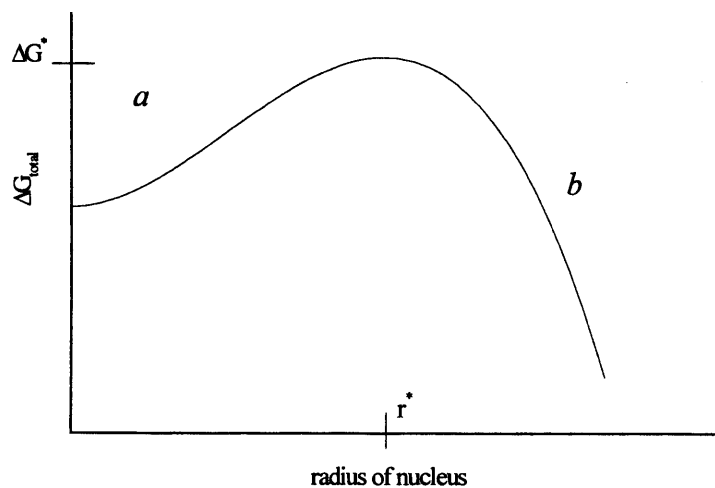


Figure 2.1 Schematic plot of free energy vs. droplet radius. Slope “a” shows ΔG_{total} is proportional to r^2 (the surface term dominates) and slope “b” shows ΔG_{total} is proportional to $-r^3$ (bulk term dominates)

At the critical radius r^* , $\frac{d\Delta G_{total}}{dr} = 0$, so setting equation 2.6 to zero, an expression for ΔG_v is obtained

$$\Delta G_v = \frac{2\gamma}{r^*} \quad (2.7)$$

Equation 2.7 is the Kelvin equation, which relates the vapour pressure of a droplet (relative to the vapour pressure over a flat surface) to its radius of curvature $1/r^*$. A critical size droplet exists in a metastable state; loss of a molecule will cause it to evaporate, because its radius of curvature will be greater than $1/r^*$ so increasing its vapour pressure. Conversely, the addition of a single gas molecule to a droplet of this radius will cause its vapour pressure to be reduced below the ambient supersaturated vapour, so the droplet will grow freely. The Kelvin equation can be expressed in terms of r^* and substituting ΔG_v in equation 2.3 gives

$$r^* = 2\Omega\gamma / kT \ln\alpha \quad (2.8)$$

where Ω is the molecular volume and α denotes (p/p_e) , the saturation ratio. Substituting this expression for r^* into equation 2.6 gives an expression for the activation energy ΔG^*

$$\Delta G^* = \frac{4\pi r^{*2}\gamma}{3} = \frac{16\pi\gamma^3}{3(\Delta G_v)^2} \quad (2.9)$$

Equation 2.9 shows that ΔG^* is equal to a third of the surface free energy of the critical nucleus. Further substitution of ΔG_v into equation 2.3 gives

$$\Delta G^* = 16\pi\gamma^3\Omega^2 / 3k^2 T^2 \ln^2\alpha \quad (2.10)$$

Classical nucleation theory developed by Volmer and Weber [4] is based on the kinetic treatment of nucleation rate as described by the rate of impingement of molecules on the equilibrium concentration of critical sized nuclei.

Nucleation rate (J) is given by

$$J = \omega n_i \quad (2.11)$$

where ω is the rate of impingement from the Hertz-Knudsen equation, given by

$$\omega = \frac{\alpha_c p A^*}{(2\pi m k T)^{1/2}} \quad (2.12)$$

where α_c is the condensation coefficient, A^* is the surface area of the critical nucleus, n_i^* is the equilibrium number of nuclei containing i molecules (where i is the number of molecules in a critical nucleus), n_i^* is given by

$$n_i^* = n_1 \exp(-\Delta G^*/kT) \quad (2.13)$$

where n_1 is the equilibrium concentration of molecules and ΔG^* is the activation energy for the formation of a critical nucleus given in equation 2.11.

This term was modified by Becker and Doring [5] and Zeldovich [6] giving the steady-state concentration of nuclei, by accounting for the loss of critical sized nuclei. The so-called Zeldovich factor (Z) is given below

$$Z = (\Delta G^*/3\pi k T i^{*2})^{1/2} = \frac{\Delta G_v^2 \Omega}{8\pi\gamma} \left(\frac{1}{\gamma k T} \right)^{1/2} \quad (2.14)$$

The modified rate equation becomes

$$J = Z\omega n_i \quad (2.15)$$

Substituting in equations 2.10 and 2.13 gives

$$J = B_d \exp(-16\pi\gamma^3 \Omega^2 / 3k^3 T^3 \ln^2 \alpha) \quad (2.16)$$

where B_d is given by

$$B_d = \frac{Z\alpha_c 4\pi r^{*2} \rho}{(2\pi m k T)^{1/2}} \quad (2.17)$$

2.1.4 Bubble nucleation in a unary liquid

Equation 2.16 requires modification to account for the nucleation of bubbles from a liquid. In a boiling liquid, the hydrostatic pressure of the liquid, as well as the size of the nucleus determine the number of molecules in the nucleus. Blander and Katz [7] defined the critical bubble radius as the point at which the bubble is in chemical and mechanical equilibrium with the surrounding liquid. This is expressed using the Laplace equation given in equation 2.18.

$$r^* = \frac{2\gamma}{(p_b^* - P)} \quad (2.18)$$

where p_b^* is the vapour pressure inside the nucleus, P is the applied (hydrostatic) pressure. The net reversible work of formation (ΔG_b) of a gas nucleus under applied pressure P is given by

$$\Delta G_b = 4\pi r^2 \gamma - \frac{4}{3}\pi r^3 (p_b - P) \quad (2.19)$$

The last term accounts for the work required to create a nucleus against the ambient pressure P and the work gained by filling the nucleus with gas at pressure p_b . At the critical radius, equation 2.18 is substituted into equation 2.19 to give the net reversible work of formation of a critical bubble (ΔG_b^*)

$$\Delta G_b^* = \frac{16\pi\gamma^3}{3(p_b^* - P)^2} \quad (2.20)$$

Analogous to droplet nucleation, the rate of bubble nucleation (J) in a boiling unary liquid is given as [7]

$$J = \left(\frac{2\gamma}{\pi m B} \right)^{1/2} n_1 \exp \left(- \frac{16\pi\gamma^3}{3kT(p_b^* - P)^2} \right) \quad (2.21)$$

where m is the molecular mass, and B is given by

$$B = 1 - \frac{(1 - P/p_b^*)}{3} \quad (2.22)$$

2.1.5 Bubble nucleation in dissolved gas solutions

Further modifications are required for a multi-component system. The surface tension varies as a function of the dissolved gas concentration, and the vapour pressure inside the bubble is the sum of the partial pressures of the solvent vapour (p_s) and the dissolved gas (p_v), shown below.

$$p_b^* = p_s + p_v \quad (2.23)$$

For dilute solutions of gases, it can be shown that [8]

$$\frac{p_s}{P} = \frac{c_2}{c_{2e}} \quad (2.24)$$

and

$$p_v = \phi p_{vap} \quad (2.25)$$

where ϕ is given by

$$\phi = \exp\left(\frac{\Omega(P - p_{vap})}{kT - c_2/c_1}\right) \quad (2.26)$$

where Ω is the molecular volume of the solvent and c_1 is the solvent concentration in moles per unit volume. Substituting these values into equation 2.21 gives an expression for the nucleation rate (J)

$$J = B_b \exp\left[\frac{-16\pi\gamma^3}{3kT((P c_2/c_{2e} + \phi p_{vap}) - P)^2}\right] \quad (2.27)$$

where B_b is the pre-exponential term given in equation 2.21. It has been shown [9] that equation can be simplified by assuming p_v is small compared to p_s , therefore the dominator in the exponential term becomes $3kT((c_2/c_{2e} - 1)P)^2$. Substituting in equations 2.1 and 2.2 gives a simplified expression for the nucleation rate (J)

$$J = B_b \exp\left(-16\pi\gamma^3/3kT(\sigma P)^2\right) \quad (2.28)$$

2.1.6 Heterogeneous nucleation

Distinction between homogeneous nucleation where the new phase is formed within the bulk of the existing phase and heterogeneous nucleation where the new phase is formed at a surface is important. Less work is required if the new phase forms at an existing interface (heterogeneously), such as the surface of a vessel or a dust particle.

If the bubbles are formed at a solid interface, the volume of gas required to form a critical nucleus is smaller than that required for homogeneous nucleation. This difference appears in the rate equation as a difference in the free energy of formation [10].

$$\Delta G_{hetero}^* = f(\theta)\Delta G_{homo}^* \quad (2.29)$$

where θ is the three-phase contact angle.

2.1.6.1 Nucleation at a planar surface

As explained in section 1.3.2.1, the fractional reduction of the volume ($f(\theta)$) is given by

$$f(\theta) = (1 - \cos\theta)^2(2 + \cos\theta)/4 \quad (2.30)$$

for droplets, $f(\theta)=1$, when $\theta = 180^\circ$, $f(\theta)=0$, when $\theta = 0^\circ$. For bubbles

$$f(\theta) = (1 + \cos\theta)^2(2 - \cos\theta)/4 \quad (2.31)$$

and $f(\theta)=0$, when $\theta = 180^\circ$, $f(\theta)=1$, when $\theta = 0^\circ$.

The modified rate equation for bubbles forming at a planar surface is

$$J = \left(\frac{2\gamma}{\pi m B f(\theta)} \right)^{1/2} S \exp \left(- \frac{16\pi\gamma^3 f(\theta)}{3kT(\sigma P)^2} \right) \quad (2.32)$$

where the term S accounts for the fact that each solution molecule in contact with the solid planar surface is considered a to be a potential nucleation site [11]. S is given by

$$S = n_1^{2/3} (1 + \cos\theta) / 2 \quad (2.33)$$

2.1.6.2 Nucleation at a non-planar surface

If bubbles nucleation at a non-planar surface, the term $f(\theta)$ is a function of the geometry of the nucleation site. The function for a conical cavity (thought the most suitable model for a nucleation site) is given below [11]

$$f_{cc}(\theta) = \frac{1}{4} \left(2 - 2\sin(\theta - \beta) + \frac{\cos\theta \cos^2(\theta - \beta)}{\sin\beta} \right) \quad (2.34)$$

where β is the half angle subtended at the base of the cavity, as shown in figure 2.2. An additional function appears in the pre-exponential term

$$f'_{cc}(\theta) = \frac{1 - \sin(\theta - \beta)}{2} \quad (2.35)$$

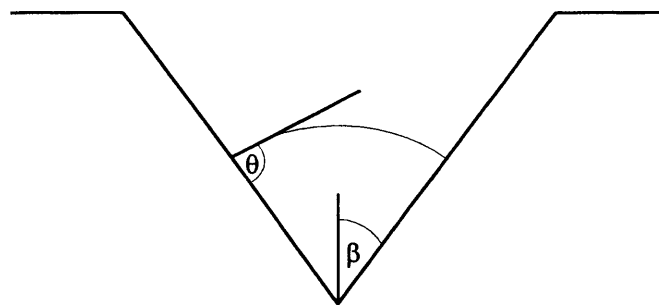


Figure 2.2. Schematic diagram of a gas nucleus in a conical cavity of half angle β with three-phase contact angle θ .

The rate equation for the nucleation of a bubble at a conical cavity (J) is given as

$$J = f'_{cc} \left(\frac{2\gamma}{\pi m B f(\theta)} \right)^{1/2} S \exp \left(- \frac{16\pi\gamma^3 f_{cc}(\theta)}{3kT(\sigma P)^2} \right) \quad (2.36)$$

Plotting $\ln J$ vs. $(\sigma P)^2$ should give a straight line of gradient

$$d \ln J / d(\sigma P)^2 = -16\pi\gamma^3 f_{cc}(\theta) / 3kT \quad (2.37)$$

However, it has been found experimentally [12] that plotting $\ln J$ vs. $(\sigma P)^2$ for the nucleation of CO_2 from H_2O , gives a curve. This has been attributed to a distribution in nucleation site energetics, each nucleation site with a particular rate equation. The overall measured nucleation rate is a combination of several different rates, so a curve is obtained. This concept will be explored further in Chapter 6.

2.1.7 Bubble Growth

Once a bubble has reached a supercritical size it is expected to become free growing (provided the solution is sufficiently supersaturated to supply the new phase). The rate of growth is determined by a number of factors but the most important is the supersaturation. In the very early stages of bubble growth (typically the first 10 ms) inertial and surface tension forces are dominant and the limiting factor is the rate of supply of new phase across the interface. The time-dependence of the bubble radius, r , is given by

$$r_{(t)} = At \quad (2.38)$$

where A is a constant. Growth is controlled by surface tension, viscosity and pressure [9]. In later stages growth is diffusion controlled, the further growth of a bubble is determined by the rate of mass transport of dissolved gas to the expanding liquid/gas interface. The growth rate is given by Scriven [13], based on earlier work on spherically symmetrical phase growth calculated by Frank [14]. Solution of the diffusion equations, with appropriate boundary conditions provide the Scriven equation below

$$r_{(t)} = 2\beta (Dt)^{1/2} \quad (2.39)$$

where β is the growth coefficient (dependent on the supersaturation) and D is the diffusion coefficient. Equation 2.39 shows the radius grows, with $t^{1/2}$ dependence, where the surface area increases linearly with time.

A third growth regime has been identified for the growth of bubbles at microelectrodes [15], where the bubbles grow by “direct injection” of gas into the bubble.

$$r_{(t)} = Ct^{1/3} \quad (2.40)$$

where C is a constant and the bubble volume increases linearly with time.

2.1.8 Bubble detachment

The detachment of a bubble resident at a surface is governed by a balance of buoyancy forces (F_b) caused by the density difference between the gas and liquid, and surface tension (F_s) causing the bubble to remain attached to the surface (see figure 2.3). The force balance at the bubble detachment radius as stated by Karri [16] is given below. It is calculated from the relationship between the bubble radius, the bubble base radius and the rate of bubble growth and the contact angle.

$$F_d + F_s = F_i + F_p + F_b \quad (2.41)$$

where F_d is the drag force, F_i is the liquid inertia and F_p is the pressure force (arising from the dynamic excess vapour pressure inside the bubble). The condition for bubble departure is assumed to be the point at which the net force goes from negative to positive. The bubble shape is governed by the three phase contact angle and the detachment radius is governed by the growth rate. F_d , F_i and F_p are dynamic forces; F_s and F_b are static forces.

A similar model proposed by Lubetkin [17] provides an estimate of the detachment time τ_d . The volume of the detaching bubble (V) is given below

$$V = \frac{\pi r^3 \psi(\theta)}{3} \quad (2.41)$$

where $\psi(\theta) = 4f(\theta)$ (see equation 2.31). The buoyancy force (F_b) is given by

$$F_b = V(\rho_l - \rho_g)g \quad (2.42)$$

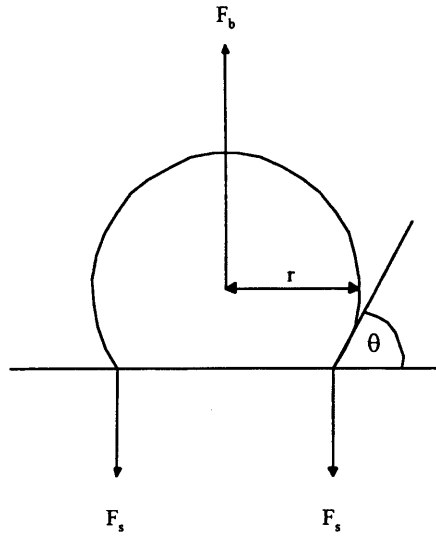


Figure 2.3. Schematic diagram of the forces acting on a growing bubble at a planar surface (Lubetkin model)

The downward force is given by the vertical component of the surface tension (F_s).

$$F_s = 2\pi r \gamma \sin^2(\theta) \quad (2.43)$$

Balancing these forces gives the radius on detachment (r_d)

$$r_d^2 = \frac{6\gamma \sin^2(\theta)}{\psi(\theta) \Delta \rho g} \quad (2.44)$$

Assuming that growth of the bubble to the detachment size is diffusion controlled (see equation 2.39), the detachment time (τ_d) is given below

$$\tau_d = \frac{\psi(\theta)r_d}{2\lambda(1 + \cos\theta)} \quad (2.45)$$

where λ is the linear growth rate. Substituting equation 2.44 into equation 2.45 gives

$$\tau_d = \frac{\sin\theta}{2\lambda} \left(\frac{6\gamma(2 - \cos\theta)}{g\Delta\rho} \right)^{1/2} \quad (2.46)$$

2.2 EQCM Theory

2.2.1 Introduction

The quartz crystal microbalance (QCM) is a very sensitive mass sensor capable of monitoring nanogram mass changes. QCM is a generic term covering many mass-sensing acoustic wave devices each comprising an oscillating piezoelectric quartz crystal. The electrochemical quartz crystal microbalance (EQCM) utilises one face of the coated crystal as a working electrode in a standard three-electrode cell and hence allows simultaneous analysis via conventional electrochemical methods coupled with a microbalance or viscosity monitor. The equations governing the quantitative analysis of in-situ EQCM data are derived below.

2.2.2 Piezoelectric effect

The word "piezo" is derived from the Greek word meaning "pressure." Therefore a material may be described as possessing piezoelectric properties by the creation of polarisation of the crystal faces through the application of mechanical pressure, conversely an electric field imposed on a piezoelectric crystal should result in a strain being induced in the material.

2.2.3 The EQCM as a mass sensing device

Piezoelectricity is a property of non-symmetrical ionic crystalline solids whose structures have no centre of inversion. Application of electrical potential to the crystal provides an electrostatic force that displaces ions in the unit cell, causing reorientation of the dipoles and

so induces strain in the lattice structure of the crystal. If the applied electric field is made to alternate, the strain induced in the crystal will also alternate (oscillate) at the frequency of the applied field, changing sign with the change in electrical polarity. Oscillator resonance occurs when the crystal thickness is an odd multiple of half the acoustic wavelength. The EQCM utilises this effect by placing the crystal in the feedback network of a closed loop system containing an amplifier [18, 19].

The QCM comprises a quartz wafer sandwiched between two electrodes across which the alternating potential is applied. A quartz crystal may have different modes of oscillation depending upon the axes from which it was cut. The QCM comprises an AT-cut crystal (figure 2.4A), which resonates in the high frequency, thickness shear mode (figure 2.4B), a simple one-dimensional oscillation that is very sensitive to mass deposition.

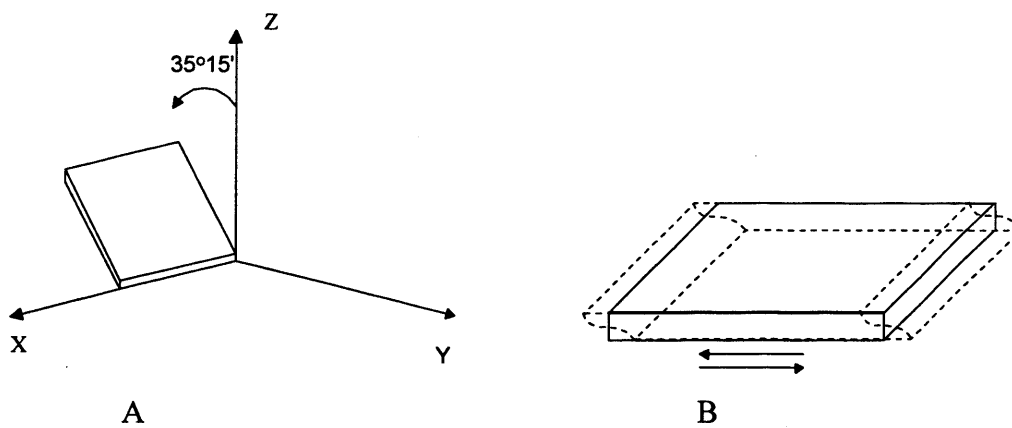


Figure 2.4 Schematic diagram showing A) the angle of the AT-cut quartz crystal, B) the thickness-shear mode of oscillation

Quartz crystal resonators are ideal for determining very small mass changes, due to several properties. Their resonance bandwidth is narrow, allowing resonant frequency to be determined very accurately. Using an AT-cut quartz crystal minimises the influence of environmental factors such as electric or magnetic field and temperature changes.

2.2.4 Mass to frequency relationship

Addition of a rigid coupled mass Δm to one of the crystal faces causes a decrease in the resonant frequency of the crystal Δf . The linear relationship between Δm and Δf derived by Sauerbrey [20] is given below. We will consider only the fundamental frequency of oscillation. At resonance, a standing wave is set up within the crystal.

A wave equation can be written for this.

$$v_q = f_o \lambda_q \quad (2.48)$$

where v_q is the wave velocity, f_o is the wave frequency and λ_q is the wavelength where the thickness of the crystal (t_q) is given by

$$t_q = \frac{\lambda_q}{2} \quad (2.49)$$

From this it can be deduced that an increase in thickness (t_q) causes a decrease in fundamental resonance frequency (f_o).

Thickness can also be expressed in terms of mass

$$t_q = \frac{M}{\rho_q A} \quad (2.50)$$

where M is the mass of quartz in the oscillating region (the piezoactive area A) between the two electrodes. ρ_q is the density of quartz. Substituting equations 2.49 and 2.50 into equation 2.48 gives

$$f_o = \frac{v_q \rho_q A}{2M} \quad (2.51)$$

$$\text{Areal density } (m) = \frac{M}{A}$$

$$f_o = \frac{\rho_q v_q}{2m} \quad (2.52)$$

Equation 2.53 shows that the frequency of oscillation f_o , is dependent on the mass per unit area of the quartz between the two electrodes. A rigid film is considered to be one that is completely adhered to the entire surface of one of the electrodes. It moves synchronously with the crystal as it oscillates, therefore it has the effect of increasing the mass of the crystal by an amount δm . Equation 2.53 can be rewritten to account for the increased mass.

$$(f_o + \delta f) = \frac{\rho_q v_q}{2(m + \delta m)} \quad (2.53)$$

This is rearranged to

$$\delta f = - \left(\frac{2f_o^2}{\rho_q v_q} \right) \left(\frac{\delta m}{1 + \delta m/m} \right) \quad (2.54)$$

In most cases $m \gg \delta m$. Simplification of equation 2.55 gives the Sauerbrey equation [20]

$$\Delta f = \left(\frac{2f_o^2}{\rho_q v_q} \right) (\Delta m) \quad (2.55)$$

For AT cut quartz crystals, $\rho = 2.65 \text{ g cm}^{-3}$, $v = 334000 \text{ cm s}^{-1}$, giving the following relationship

$$\Delta f = -2.26 \times 10^{-6} f_o^2 \Delta m \quad (2.56)$$

The QCM is very sensitive. For a 10MHz crystal, with an electrode area of 0.25 cm^2 , increasing the mass by 1.1ng produces a frequency decrease of 1Hz. The Sauerbrey equation is valid for rigidly coupled solids of small mass (up to $20 \mu\text{g cm}^{-2}$).

2.2.5 Application: effect of a liquid on oscillation

It was originally thought that immersing the crystal in a liquid would cause excessive energy loss to the solution and therefore prevent oscillation. This theory was disproved by Nomura [21] leading to a new application, the electrochemical quartz crystal microbalance (EQCM). If one face of the crystal is exposed to a liquid, the thickness-shear mode oscillation couples to the solution by a hydrodynamic effect [22], as shown in figure 2.5. As a result of the coupling, a liquid layer (ca. 300 nm for a 10 MHz AT cut crystal in an aqueous solution) oscillates at the same frequency as the crystal but the amplitude of modulation decreases with distance from the surface [23]. This modulation layer causes a decrease in the resonant frequency of the crystal (ca. 2 kHz for a 10 MHz crystal in an aqueous solution at room temperature) the magnitude of which is a function of the liquid's viscosity and density [24, 25]. Hence any chemical process, which perturbs the viscosity or density of the liquid within the modulation layer, will cause a change in the resonant frequency of the crystal. The presence of a bubble within the modulation layer decreases the density of the coupled liquid layer and therefore causes an increase in the resonant frequency.

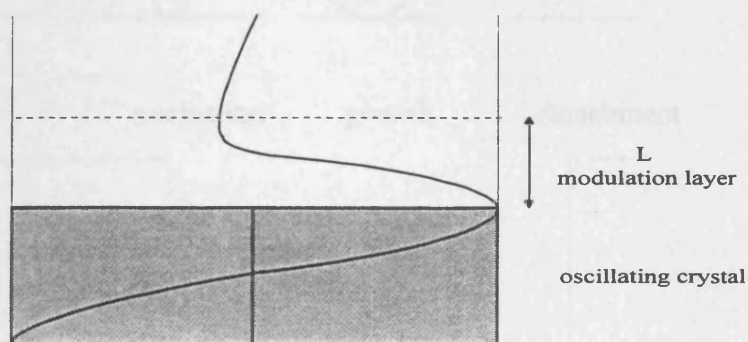


Figure 2.5 Diagram showing propagation of the acoustic standing wave into a liquid

2.3 Measurement of bubble evolution

As discussed in section 1.7.3, the use of the EQCM for bubble detection is a relatively novel application. In this section the fundamental properties of Fourier analysis [26] are applied to an accepted model of an EQCM mass transient arising from bubble evolution [27, 28]. The time dependence of these frequency signals can provide kinetic information on bubble evolution. The principles of this analysis are explained in section 2.3.2. The comparison of

the ideal mass transient model with real data is entirely novel and so requires greater discussion than is possible in the context of this chapter and is covered in chapter 5 where the method of data analysis that has been developed for experimental EQCM data in order to utilise the properties of Fourier analysis is described fully.

2.3.1 Detecting bubbles

Bubbles forming in the modulation layer adjacent to the electrode cause changes in the resonant frequency of the crystal. Discontinuities in the frequency arise from bubble nucleation or detachment; steady frequency increases signal bubble growth. This can be explained using a model in which frequency changes are accounted for by displacement of liquid by gas bubbles in the modulation layer, as shown in the figure below. The volume of liquid displaced by the gas is determined by the three phase contact angle (see figure 2.7).

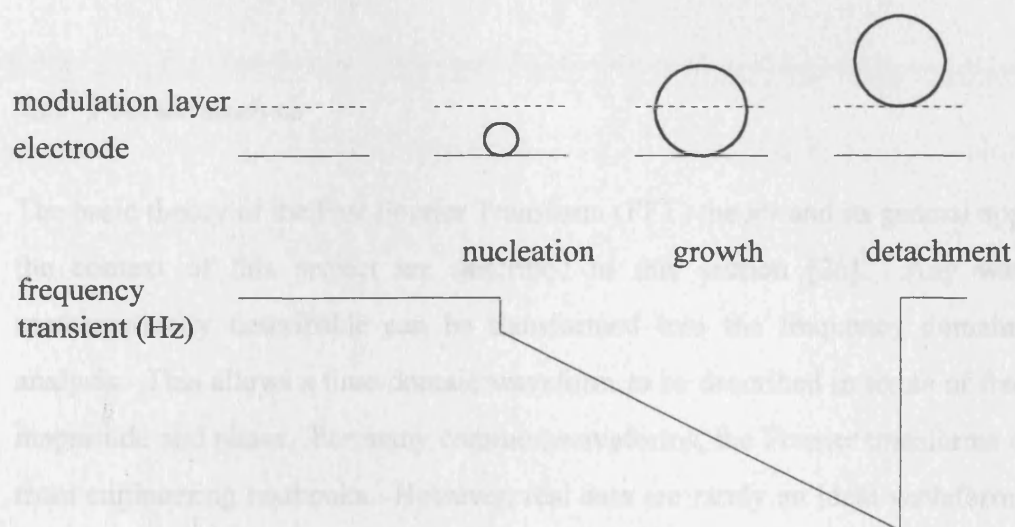


Figure 2.6 Model of an EQCM frequency transient for bubble evolution

It is convenient to visualise the changes that occur in the resonant frequency as “mass” changes, although as the liquid film is not rigidly coupled to the crystal, the Sauerbrey equation cannot be applied. However, for clarity the term “coupled mass” is used in some contexts in chapter 5. The volume of liquid displaced by a bubble depends on the three phase contact angle (θ).

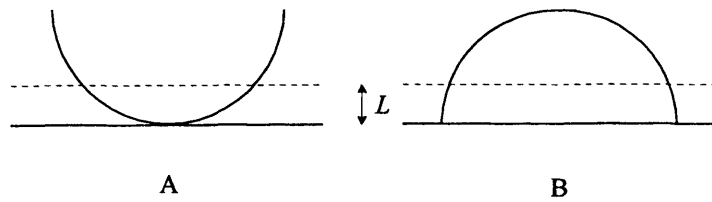


Figure 2.7 Schematic diagram of the removal of liquid from the oscillating boundary layer (L) by a bubble A) $\theta = 0^\circ$ and B) $\theta = 90^\circ$.

The volume of liquid displaced by the bubble (V_{disp}) for the two limiting cases shown above can be calculated.

$$\text{When } \theta = 0^\circ \quad V_{\text{disp}} = \pi L^2(r-L/3) \quad (2.57)$$

$$\text{When } \theta = 90^\circ \quad V_{\text{disp}} = \pi r^2 L \quad (2.58)$$

where r is the bubble radius.

2.3.2 Fourier analysis

The basic theory of the Fast Fourier Transform (FFT) theory and its general application within the context of this project are described in this section [26]. Any waveform that is mathematically describable can be transformed into the frequency domain using Fourier analysis. This allows a time-domain waveform to be described in terms of frequency domain magnitude and phase. For many common waveforms, the Fourier transforms can be obtained from engineering textbooks. However, real data are rarely an ideal waveform. If the data to be analysed cannot be expressed by a mathematical formula, classical Fourier techniques cannot be used. The waveform must be sampled and digitised in order to use a discrete Fourier transform (DFT) which can be used to perform the transform. The fast Fourier transform (FFT) is the commonly used algorithm for evaluating the DFT. The FFT effectively converts a time-based spectrum to a frequency-based one. The DFT is derived from the Fourier integral. An example of a Fourier transform is given below

A sinusoidal wave $x(t)$ can be expressed mathematically

$$x(t) = a_0 + b_0(\sin \omega_0 t) \quad (2.59)$$

where b_0 is the amplitude, $\omega_0 = 2\pi f_0$, where f_0 is the frequency and a_0 is the mean y value of the waveform and so corresponds to the shift of the waveform along the y-axis. The waveform can also be displayed graphically as shown below.

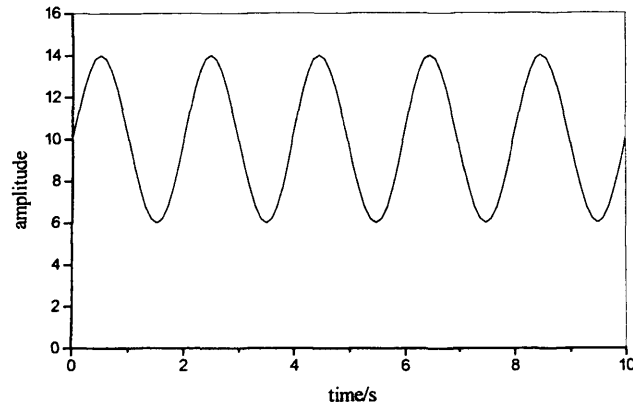


Figure 2.8 Plot of a sinusoidal waveform where $a_0 = 10$, $b_0 = 4$, $f_0 = 0.5\text{Hz}$

This waveform can be transformed into the frequency domain, using the Fourier integral

$$X(f) = \int_{-\infty}^{+\infty} x(t) e^{-j2\pi t} dt \quad (2.60)$$

The frequency spectrum obtained from operating a Fast Fourier Transform on the sinusoid shown in figure 2.8 is given below.

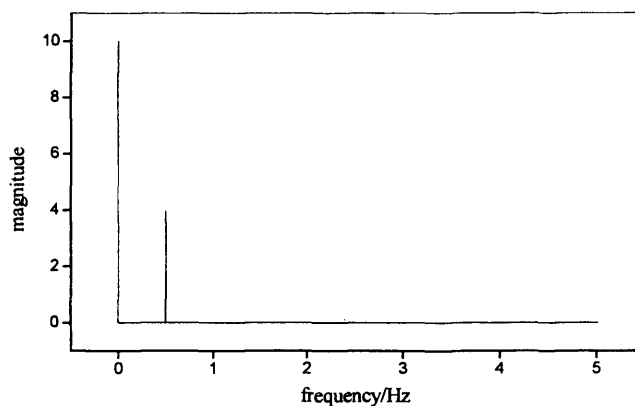


Figure 2.9 Frequency spectrum of a sinusoid waveform

The peak at 0Hz corresponds to a_0 , the offset or D.C. value. Due to the presence of this peak experimental data are corrected so its mean value is zero before performing the FFT. The peak at 0.5Hz corresponds to the frequency of the sine wave, its magnitude being equal to the waveform's amplitude. In principle, any waveform can be constructed from a combination of sine waves, once transformed into the frequency domain, each separate element will be identified by its corresponding peak on the frequency axis see figures 2.10 and 2.11 below.

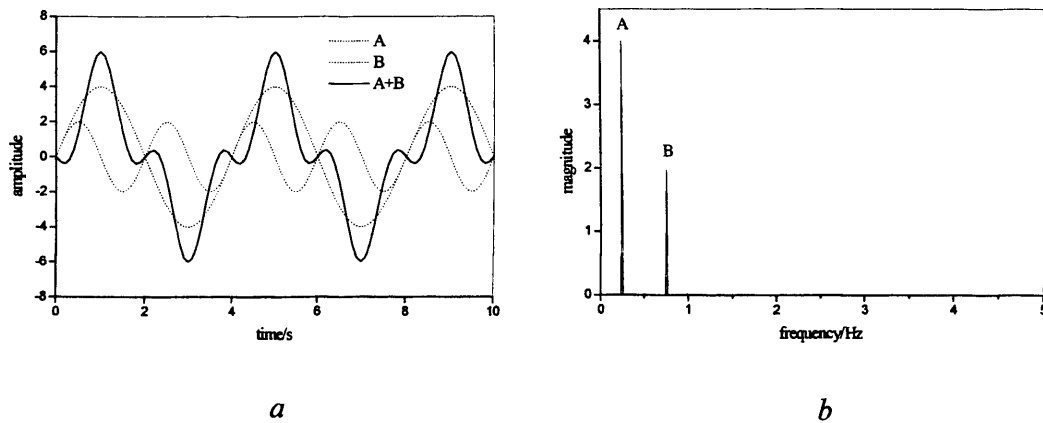


Figure 2.10 a) Waveform created from combining two sine waves b) Frequency spectrum obtained from the FFT of the composite waveform

As shown in figure 2.6, the mass transient produced by a detaching bubble, can be modelled using a sawtooth waveform. The following figure shows a sawtooth wave; $V = \pi/2$, $f_0 = 0.5\text{Hz}$.

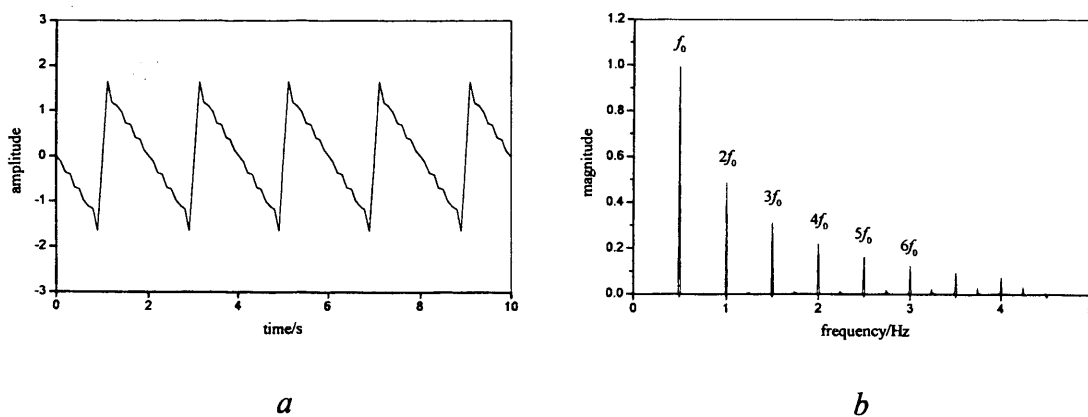


Figure 2.11 A) Sawtooth waveform B) corresponding frequency spectrum

This waveform can be constructed from the following Fourier series

$$x(t) = \frac{2V}{\pi} \left[\sin \omega_0 t - \frac{1}{2} (\sin 2\omega_0 t) + \frac{1}{3} (\sin 3\omega_0 t) - \frac{1}{4} (\sin 4\omega_0 t) + \dots \right] \quad (2.61)$$

where V is the amplitude of the sawtooth waveform.

The peaks on the frequency spectrum correspond to the fundamental frequency f_0 and the harmonics as defined in equation 2.34. The important feature of this spectrum is that the magnitude of the harmonics decays according to the equation $y = 1/x$. If bubble evolution occurs at one isolated nucleation site, increasing the kinetics of bubble evolution causes the mass transient to be modified. The type of modification is dependent on the rate-limiting step of the mechanism, and is shown in figure 5.3 in chapter 5.

2.4 Rate of electrochemical reactions

This section covers the established theory of the electrochemical techniques used to generate dissolved gas in the electrolyte, the subsequent current generated is the parameter that is measured simultaneously with the frequency in EQCM analysis. A more in-depth account of general electrochemistry can be found on the literature [29,30].

2.4.1 Cell potential

The cell potential of an electrochemical cell is calculated from the electrode potentials of the respective half reactions and is given by

$$E_{cell} = E_{right} - E_{left} \quad (2.62)$$

where E_{right} and E_{left} are the half-cell potentials for reduction and oxidation, obtained from the Nernst equation. For the electrode reaction



The Nernst equation is defined as

$$E = E^0 + \frac{RT}{nF} \ln \left(\frac{[O]_s}{[R]_s} \right) \quad (2.64)$$

where $[O]_s$ and $[R]_s$ are the surface concentrations of the species O and R . E^0 is the standard electrode potential of the cell defined with respect to a standard hydrogen electrode and n is the number of electrons transferred. $E - E^0$ is defined as the overpotential.

2.4.2 Relationship between current and rate

2.4.2.1 Kinetically controlled current

As a small overpotential is applied, the current is limited by the rate of electron transfer and the reaction rate is dependent on the reaction kinetics and the overpotential. Using equation 2.63 as an example, the net reaction flux, j_{net} can be represented in terms of the forward and back reaction fluxes (j_f and j_b)

$$j_{net} = j_f - j_b \quad (2.65)$$

The current, i , is given by

$$i = nFA(j_f - j_b) = nFA(k_f'[O]_s - k_b'[R]_s) \quad (2.66)$$

where A is the electrode area. The current is a function of the rate constants, k_f and k_b and the concentration of reactants. There is an exponential relationship between current and overpotential, given by the Butler-Volmer equation:

$$i = nFAk_0' \left[\left([O]_s \exp \left(\frac{-\alpha nF(E - E^0)}{RT} \right) \right) - \left([R]_s \exp \left(\frac{(1-\alpha)nF(E - E^0)}{RT} \right) \right) \right] \quad (2.67)$$

where α is the transfer coefficient for the reaction and k_0' is the standard rate constant. If a high overpotential is applied and the vessel is stirred, one of the terms in equation 2.67

becomes negligible and the equation is simplified to the Tafel equation. At large negative overpotentials the Tafel equation is expressed by

$$\ln i = \ln(nFAk_0[O]_s) - \frac{\alpha nF(E - E^0)}{RT} \quad (2.68)$$

2.4.2.2 Diffusion limited current

Diffusion is the movement of charged or neutral species down a concentration gradient and occurs whenever there is a chemical change at the electrode. It will be the dominant mechanism of mass transport at high overpotentials. As the electron transfer rates increase, the concentration of species O depletes to zero. This species must diffuse from the bulk solution to the electrode surface in order for the electron transfer to occur; therefore diffusion is the rate-limiting step. At this point the current is proportional to the concentration gradient at the surface and is given by Fick's First Law.

$$i = nFAD \left(\frac{dc}{dx} \right)_{x=0} \quad (2.69)$$

where D is the diffusion coefficient and x is the distance from the electrode surface. The limiting diffusion current can be expressed as a function of time by the Cottrell equation

$$i = nFAC_{bulk} \left(\frac{D}{\pi t} \right)^{1/2} \quad (2.70)$$

the diffusion coefficient can be obtained from the slope of a plot of i vs. $t^{1/2}$.

2.4.3 Cyclic voltammetry

The cyclic voltammetry technique involves the application of an electrode potential to the working electrode that varies continuously with time. This causes oxidation and reduction reactions of the electroactive species in the solution (faradaic reactions), possible adsorption

and a capacitive current due to charging of the double layer immediately adjacent to the electrode. The shape of the recorded current response can be explained as follows. As the potential reaches a point where the electrode reaction begins, a current will flow. As the electroactive species is consumed, a concentration gradient is created and just before the maximum value of the current (the peak current), the supply of electroactive species begins to diminish. Due to this depletion, the current begins to decay, proportionally to $t^{-1/2}$.

The use of cyclic voltammetry for the evolution of bubbles produces a unique curve whose shape is determined by the activity of the bubbles, rather than the diffusion of the electroactive species. There is a high concentration of the electroactive species, and the formation of bubbles effectively mixes the solution, therefore the current does not decay according to diffusion. Spikes are seen in the current response upon bubble detachment, which are due to the removal of what is effectively an insulating sphere and its replacement with bulk electrolyte.

2.4.4 Chronoamperometry

Potential Step Chronoamperometry causes a diffusion-limited current by changing the potential applied to the electrode cation from a value where there is no electrode reaction to a value where all the electroactive species that reach the electrode react. This gives rise to a diffusion limited current that decreases with $t^{1/2}$. However, at short timescales (less than 0.1 seconds) there is a capacitive component in the current due to double layer charging. At longer timescales a steady state current is achieved, although there is a contribution from natural convection (after several seconds).

The use of chronoamperometry for bubble evolution produces unique features in the current response. Superimposed on the steady-state current are discontinuities that arise from detaching bubbles. As the bubble detaches there is a sharp increase in the current due to the replacement of the insulating sphere with bulk electrolyte. Also the current fluctuates with the growth of new bubbles, the area of the electrode in contact with the electrolyte decreases as it is effectively blocked by bubbles.

2.5 PRBN Theory

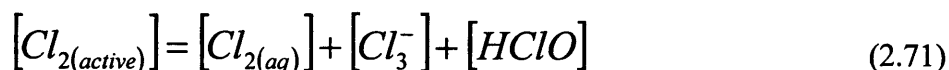
The theoretical basis of the pressure release technique is the measurement of bubbles numbers that allows an indirect measurement of the number of nuclei formed in a system [9]. The rate of pressure rise observed during bubble nucleation is directly related to the rate of nucleation, as described in section 2.1.6, and given in equation 2.36. Two different methods can be used to measure the rate of bubble evolution [31]; the first uses a microphone to record the acoustic event caused by a bubble bursting at the liquid surface, the second measures the pressure rise caused by bubbles evolving in the sealed vessel. The following sections cover the theoretical aspects of the latter method.

2.5.1 Measurement of Bubble Evolution by Pressure Rise

The nucleation rate is measured from the pressure rise occurring following the depressurisation of the vessel. The full experimental procedure is given in section 3.3.1. The sealed vessel contains a supersaturated solution and a nucleating surface; bubbles form spontaneously at the nucleating surface, thus causing the pressure inside the vessel to rise. The measurements taken relate to nucleation events integrated over time and space, the method does not allow for the measurement of individual nucleation events; however, the rate of nucleation occurring at the surface can be obtained. The following sections explain the theoretical aspects of the PRBN technique.

2.5.1.1 Supersaturation

The supersaturation is controlled by changing the initial and target pressures the solution is exposed to according to equations, 2.1 and 2.2, where $c_2 \propto P_{initial}$ and $c_{2e} \propto P_{target}$. The equilibrium concentration of chlorine in brine at a given pressure is calculated from the solubility. Chlorine dissolves in brine to form a solution of hypochlorous acid, molecular chlorine and Cl_3^- ions according to equation 2.71 below.



where $[Cl_{2(active)}]$ is the total quantity of dissolved chlorine. This relationship was used by Yokata to measure the concentration of Cl_2 , Cl_3^- and $HClO$ as a function of pH, temperature, NaCl concentration and Cl_2 partial pressure [32]. It was found that $[HClO]$ was negligible compared to $[Cl_2]+[Cl_3^-]$. An expression for the concentration of these two components is given below

$$[Cl_{2(aq)}] + [Cl_3^-] = P(2.21 - 0.00389N) \times 10^{-5} \times 10^{1000/T} \quad (2.72)$$

where P is the partial pressure of chlorine in atm, T is the temperature in Kelvin, N is the concentration of NaCl in $g\ l^{-1}$.

2.5.1.2 *Adiabatic expansion*

In a thermally isolated system, a release of pressure against a lower external pressure requires work to be done by the system (unless the external pressure is zero). This effect is manifested in the headspace of the pressure vessel after decompression. The work required by the system causes the temperature of the expanding (escaping) gas to decrease. Upon resealing the vessel, the temperature of the residual gas in the headspace rapidly re-equilibrates with the ambient temperature of the pressure vessel. This reheating causes a pressure rise in the headspace that occurs simultaneously with bubble nucleation, it affects the initial gradient of the pressure vs. time curve and therefore must be accounted for. It has been proved that the reheating process is Newtonian; defined by the exponential rise in temperature and common time constant of the temperature vs. time curve regardless of the degree of cooling. Due to the reproducibility of the measured pressure rise arising from the reheating of the headspace gas, it has been found that this component can be directly subtracted from the experimentally measured pressure [33]. The reheating component is removed from the measured pressure vs. time curve prior to the calculation of nucleation rate enabling the bubble evolution kinetics to be separated from adiabatic effects. This procedure is described in section 3.3.2.

2.5.2 *Nucleation rate measurement*

The rate of the pressure rise (corrected for adiabatic reheating) is linearly related to the rate of bubble nucleation [9]. Assuming the bubbles reaching the surface are of equal radius, containing n moles of gas, then

$$\frac{dP}{dn} = \frac{RT}{V} \quad (2.73)$$

where V is the volume of the vessel headspace. The number of moles of gas released into the headspace during a given time interval is given by the number of bubbles generated per unit time. It has been shown that the pressure rise is related to the nucleation rate by the following equation

$$\frac{dP}{dt} = \frac{RT}{V} nJ(t) \quad (2.74)$$

where J is the bubble nucleation rate defined in equation 2.36.

2.6 Direct visual observation

Bubbles can be observed visually using a variety of photographic methods. A fast frame video (FFV) coupled to an optical microscope, as used for this study, allows the images to be captured digitally; the bubble diameter is recorded as a function of time. These data can be correlated with electrochemical data such as potential noise measurements [34]. The method allows direct visual observation of individual bubble events such as coalescence and detachment, by recording the bubble radius at regular time intervals; equations 2.38-2.40 can be used to identify the growth mechanism. It is possible to measure a bubble's detachment size and the induction time between detachment and subsequent nucleation. By recording the coordinates of a nucleation site on an electrode surface, nucleation activity can be determined as a function of current density. Although direct visual observation does not provide an integrated measurement of bubble behaviour at a surface, by repeating measurements for a number of nucleation sites on an electrode surface, it is a powerful technique for identifying the various patterns of behaviour that are unique to a given surface.

1. Lubetkin, S. D., "Bubble nucleation and growth" in *Controlled particle, droplet and bubble formation*; Wedlock, D., Ed.; Butterworth-Heinemann: Oxford, 1994; pp 159-190.
2. Adamson, A. W., *Physical chemistry of surfaces*; 5th ed.; John Wiley and Sons, Inc.: New York, 1990.
3. Cole, R., *Advances in Heat Transfer*, **1974**, *19*, 85-166.
4. Volmer, M., *Kinetik der phasenbildung*; Steinkopff Verlag: Dresden, 1939.
5. Becker, R.; Doring, W., *Ann.Phys.*, **1935**, *24*, 719.
6. Zeldovich, J., *J. Exp. Theor. Phys.*, **1942**, *12*, 525.
7. Blander, M.; Katz, J. L., *A. I. Ch. E. Journal*, **1975**, *21*, 833-847.
8. Ward, C. A.; Balakrishnan, A.; Hooper, F. C., *Journal of Basic Engineering*, **1970**, *85*, 695-704.
9. Lubetkin, S. D; Blackwell, M., *J. Coll. Int. Sci.*, **1988**, *126*, 610-615.
10. Dunning, W. J., "Theory of crystal nucleation from vapour, liquid and solid systems" in *Chemistry of the solid state*; Garner, W. E., Ed.; Butterworth: London, 1955; pp 159-183.
11. Wilt, P. M., *J. Coll. Int. Sci.*, **1986**, *112*, 530-538.
12. Carr, M. W.; Hillman, A. R.; Lubetkin, S. D., *J. Coll. Int. Sci.*, **1995**, *169*, 135-142.
13. Scriven, L. E., *Chem. Eng. Sci.*, **1959**, *10*, 1-13.
14. Frank, F. C., *Proc. Roy. Soc.*, **1950**, *A201*, 586-599.
15. Brandon, N. P.; Kelsall, G. H., *J. Appl. Electrochem.*, **1985**, *15*, 475-484.
16. Karri, S. B. R. *Chem. Eng. Comm.*, **1988**, *70*, 127-135.
17. Lubetkin, S. D., *J. Chem. Soc., Faraday Trans. 1*, **1989**, *85(7)*, 1753-1764.
18. Lu, C.; Chanderna, W. A., *Applications of piezoelectric quartz crystal microbalances*; Elsevier: Oxford, 1984.
19. Buttry, D. A.; Ward, M. D., *Chemical Reviews*, **1992**.
20. Sauerbrey, G., *Zeitschrift fur Physik*, **1959**, *155*, 206-222.
21. Nomura, T.; Minemura, A., *Nippon Kagaku Kaishi*, **1980**, 1261.
22. Hillman, A. R.; Bruckenstein, S., in *The Handbook of Surface Imaging and Visualisation*; Hubbard, A. T., Ed.; 1995.
23. Kanazawa, K. K.; Gordon, J. G., *Anal.Chem.*, **1985**, *57*, 1770.
24. Bruckenstein, S.; Shay, M., *Electrochimica Acta*, **1985**, *30*, 1295.
25. Weil, K. G., *Ber. Bunsenges. Phys. Chem.*, **1988**, *92*, 1363-1368.

-
26. Ramirez, R. W., *The FFT, fundamentals and concepts*; Prentice-Hall, Inc.: Englewood Cliffs, 1985.
 27. Li, F.; Lubetkin, S. D.; Roberts, D. J.; Hillman, A. R., *J. Chem. Soc. Chem. Comm.*, **1994**, 159-160.
 28. Gabrielli, C.; Huet, F.; Keddam, M.; Torresi, R., *Journal of Electroanalytical Chemistry*, **1991**, 297, 515-522.
 29. The Southampton Electrochemistry Group, *Instrumental Methods in Electrochemistry*; Ellis Horwood, 1985.
 30. Brett, C. M. A.; Brett, A. M. O., *Electrochemistry, principles, methods and applications*, Oxford Science Publications: Oxford, 1993.
 31. Lubetkin, S. D., *J. Appl. Electrochem.*, **1989**, 19, 668-676.
 32. Yokota, N., *Nagaku Kogaku*, **1958**, 22, 476-4821.
 33. Carr, M. W., Ph. D. Thesis; University of Bristol, 1993.
 34. Hodgson, D. R., *Electrochimica Acta*, **1996**, 41, 605-609.

G

3.1 Introduction

This chapter provides a description of the EQCM, PRBN and FFV instrumentation, and the experimental procedures and methods of data analysis, including the novel data analysis of EQCM mass and current transients by the use of fast Fourier transform (FFT) analysis.

3.2 Electrochemical Quartz Crystal Microbalance (EQCM)

The use of the EQCM as an in situ mass balance has been described elsewhere [1]. An EQCM was assembled based on a Bruckenstein circuit design [2]. Simultaneous mass and current measurements are made possible by using one face of the oscillating crystal as the working electrode in a standard three electrode cell [3] as shown in figure 3.2.

3.2.1 Crystal specification

10 MHz AT-cut quartz crystals were supplied by the International Crystal Manufacturing (ICM) Company, Oklahoma City, USA. Crystals cut along the axis $35^{\circ}15'$ to the crystal face (so called AT-cut) oscillate in a mode which is particularly sensitive to addition of mass. The crystals comprise a thin quartz slice of diameter 13mm and approximate thickness 0.2 mm and are supplied with a $5\mu\text{m}$ finish. Each face is coated with a 900\AA keyhole shaped layer of gold or platinum as shown in figure 3.1. Additionally, crystals polished to a $1\mu\text{m}$ finish and coated with an underlayer of titanium and top layer of gold were used.

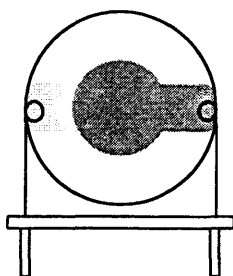


Figure 3.1 Standard mounting for quartz crystals

3.2.2 Three electrode cell

A three-electrode cell was used under potentiostatic control to generate gas at the working electrode. The working electrode was one crystal face, the reference electrode was a saturated calomel electrode (SCE) prepared using calomel and saturated NaCl, and the counter electrode was a high surface area platinum gauze. All experiments were carried out at room temperature using 50ml of aqueous electrolyte.

Two cell designs were used to incorporate the crystals into an electrochemical cell. Initially, the crystals were retained on the mounting shown above, using a glass cell with an 8mm hole at the base. The crystals were glued to this hole forming a seal using a silicone rubber sealant (Dow-Corning 3145 RTV). Figure 3.2 shows the cell for a horizontally mounted upward facing working electrode.

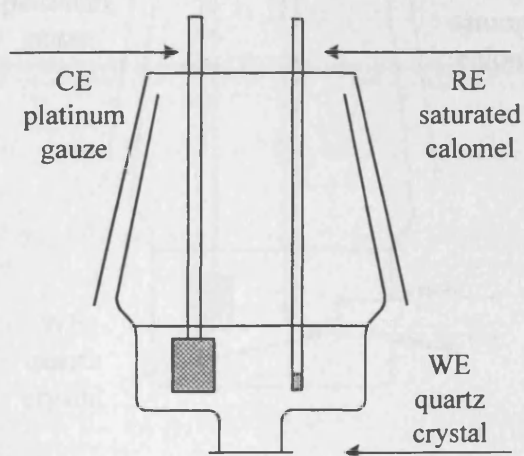


Figure 3.2 Schematic diagram of the electrochemical cell with a horizontal working electrode

In later experiments the standard mounting was modified. The crystal was removed from the mounting and glued to a thin walled glass tube outer diameter 0.52cm² (see figure 3.3). This glass tube was sealed into the side of the glass cell utilising quick-fit glassware. This enabled the same working electrode to be incorporated into the electrochemical cell in a number of orientations.

Figure 3.3 Schematic diagram of the crystal as a working electrode

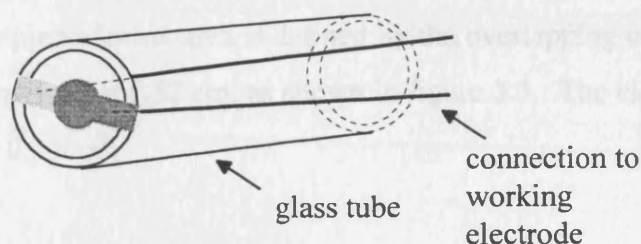


Figure 3.3 Quartz crystal mounted on a glass tube

A glass cell of the same dimensions shown in figure 3.2 was used for experiments where the working electrode was placed vertically, horizontally facing upwards. Figure 3.4 shows a vertically mounted crystal.

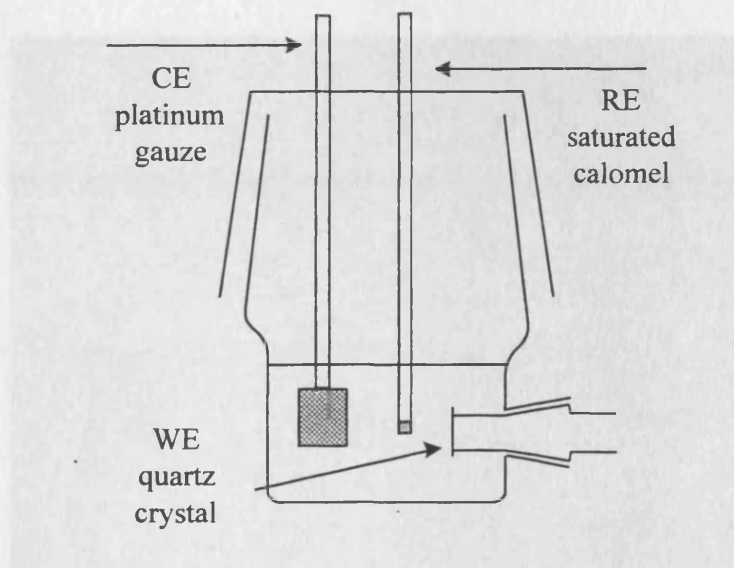


Figure 3.4 Schematic diagram of an electrochemical cell with a vertical working electrode

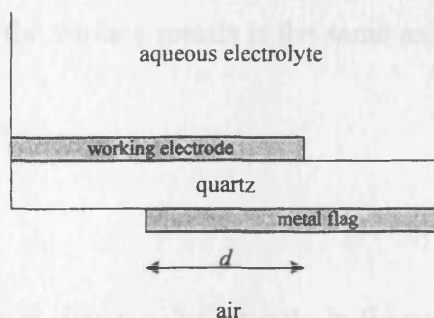


Figure 3.5 Schematic diagram of the crystal as a working electrode

In all electrode orientations, one face of the crystal was exposed to the solution, so becoming the working electrode. The piezoelectric area is defined by the overlapping conducting layer i.e. a 0.21cm^2 circle of diameter $d = 0.52\text{ cm}$, as shown in figure 3.5. The electroactive area of the working electrode is 0.23cm^2 .

3.2.3 *Metal oxide coating*

A thin film of mixed ruthenium and titanium oxides was deposited onto platinum coated crystals using a spray-bake technique where ruthenium and titanium were thermally oxidised [4]. A dilute solution of the metal salts in pentanol was brushed onto the platinum, then fired at 500°C , this procedure was repeated until the required thickness was achieved (typically $1\mu\text{m}$). This coating technique produces a characteristic mud-cracked structure.

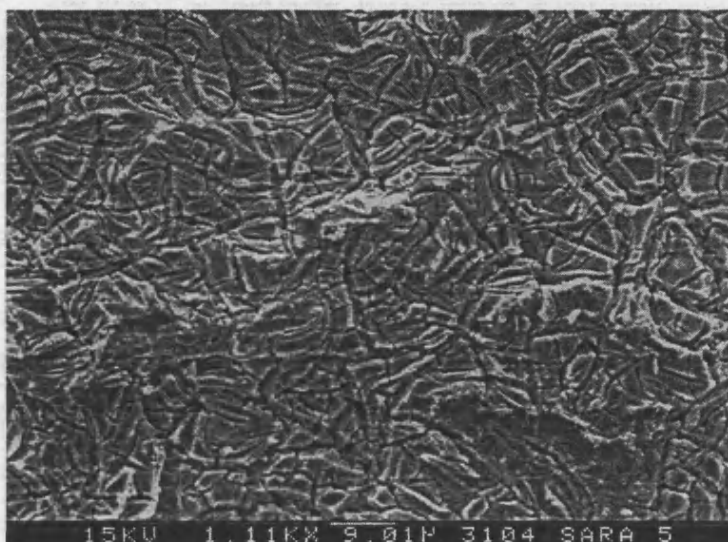


Figure 3.6 SEM of an RTO surface at 1.1×10^3 magnification.

Figure 3.6 shows a SEM image, typical of an RTO coated electrode. EXP data reveals that the surface composition of the surface metals is the same as for the bulk composition of the coating solution.

3.2.4 *Data Acquisition*

The EQCM instrumentation is shown schematically in figure 3.7. The EQCM comprises an oscillator circuit, where the variation in resonant frequency of the working crystal is

compared to the resonant frequency of a reference crystal whose value is fixed throughout the experiment. The output of this circuit is a value equivalent to the difference in frequency between the two crystals. Once the frequency is converted to a voltage its value can be monitored simultaneously with the current as a “second signal” input to the potentiostat. The potentiostat is controlled using a PC, allowing the data to be recorded digitally.

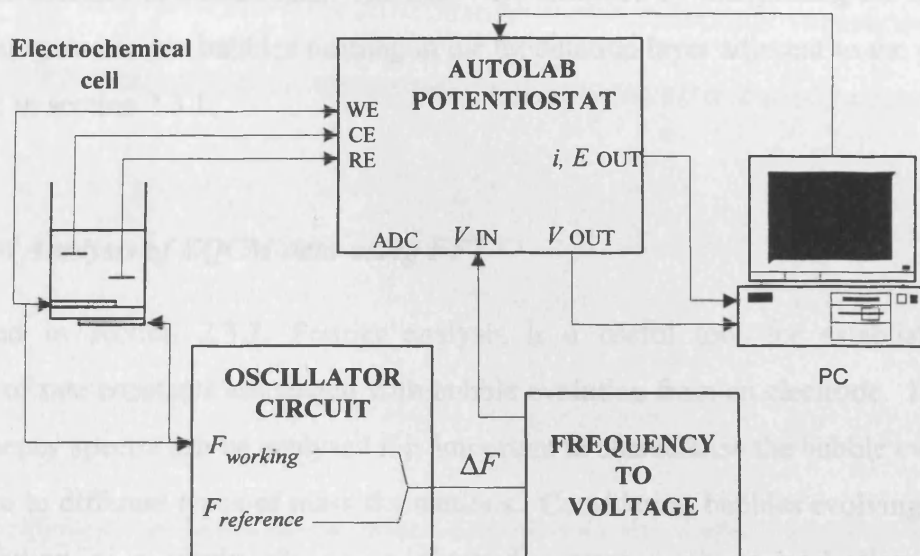


Figure 3.8 Schematic diagram of the EQCM instrumentation

Cyclic voltammetry, chronoamperometry and chronopotentiometry data were recorded. In most experiments current and frequency were measured simultaneously. Gas was evolved by either stepping or sweeping the potential (at a rate of 20 mV s^{-1}) from an electrode potential region where no gas evolution occurred to a region where gas evolution occurred at a significant rate forming gas bubbles. During the chronopotentiometry experiments, electrode potential and frequency were measured simultaneously as the current was increased to a value at which a significant rate of gas evolution was observed.

Experimental parameters were varied systematically to establish the functional behaviour of bubbles in different nucleating environments. Hydrogen bubbles were evolved at gold and platinum electrodes from an aqueous solution of 0.1M HClO_4 . Chlorine bubbles were evolved at RTO electrodes from 5M NaCl containing 0.01M HCl . The electrode was placed in three different orientations as described above.

3.2.5 *Data Analysis*

The frequency was monitored as a voltage, which was converted back to a frequency value using conversion constants obtained from the calibration of the circuit using a waveform generator. All data were recorded as a function of time, either directly in the potentiometry and amperometry experiments or indirectly in the voltammetry experiments where the potential was scanned at a fixed rate. The data were analysed by interpreting the frequency changes arising due to gas bubbles forming in the modulation layer adjacent to the electrode as described in section 2.3.1.

3.2.5.1 *Novel Analysis of EQCM data using FFT*

As described in section 2.3.2, Fourier analysis is a useful tool for establishing the distribution of rate constants associated with bubble evolution from an electrode. However, before frequency spectra can be analysed it is important to characterise the bubble events that will give rise to different types of mass fluctuations. Considering bubbles evolving from an aqueous solution *at a single site* on an electrode, events such as nucleation, growth, detachment and coalescence with bubbles at neighbouring sites determine the shape of the mass transient. Different regimes of bubble evolution display a different functional dependence on factors such as supersaturation and electrode orientation.

Elementary characterisation was achieved by the assessment of raw data in terms of the shape of the frequency transient and the overall mass change. This information correlated with visual observation, and provided reasonable estimates of the number of active nucleation sites on the surface. The number and distribution of activity of nucleation sites on the electrode complicates the appearance of real data, because growth and detachment events associated with different sites occur on a different timescale. However, if there is a fixed detachment rate associated with an individual nucleation site this will appear as a peak on the frequency spectrum, regardless of any “overlap” that occurs in the raw data. In order for the FFT spectra to be unambiguous, the data were truncated to obtain a representative sample and obtain a number of data points equal to 2^n . The data were then normalised to equate the mean value to zero. This procedure enabled high peak resolution in the frequency domain, and will be explained in greater depth in Chapter 5.

3.3 Pressure Release Bubble Nucleation (PRBN) Technique

The use of this technique for the measurement of bubble nucleation rates has been described elsewhere [4, 5]. The apparatus was constructed based on an existing design [6]. Modifications to this design were the inclusion of materials required to withstand the wet chlorine environment, the automation of the method of pressure control, and the shape of the nucleation surface.

Due to the corrosive properties of wet chlorine and the risk associated with its toxicity in the event of a leak, care was taken to minimise the potential hazard. Only two commercially available materials, PTFE (polytetrafluoroethylene) and tantalum metal show long-term resistance to attack from wet chlorine. One other material that shows moderate resistance to corrosion is Monel, an alloy of stainless steel. Taking these factors into account, the pressure vessel was constructed from stainless steel lined with PTFE. The pipe work was PFA (perfluoroalkoxy: a co-polymer of PTFE) and the pipe work connections were made from either PFA or Monel. The vessel was able to withstand pressures up to 10 atmospheres. The pressure inside the vessel was monitored using a pressure transducer (Huba pressure sensor 691.1700100). The pressure transducer used in the apparatus was protected from chlorine gas using a tantalum diaphragm and a silicone oil-filled reservoir. The transducer measured pressure relative to atmosphere and so was calibrated periodically to calculate the voltage vs. pressure relationship.

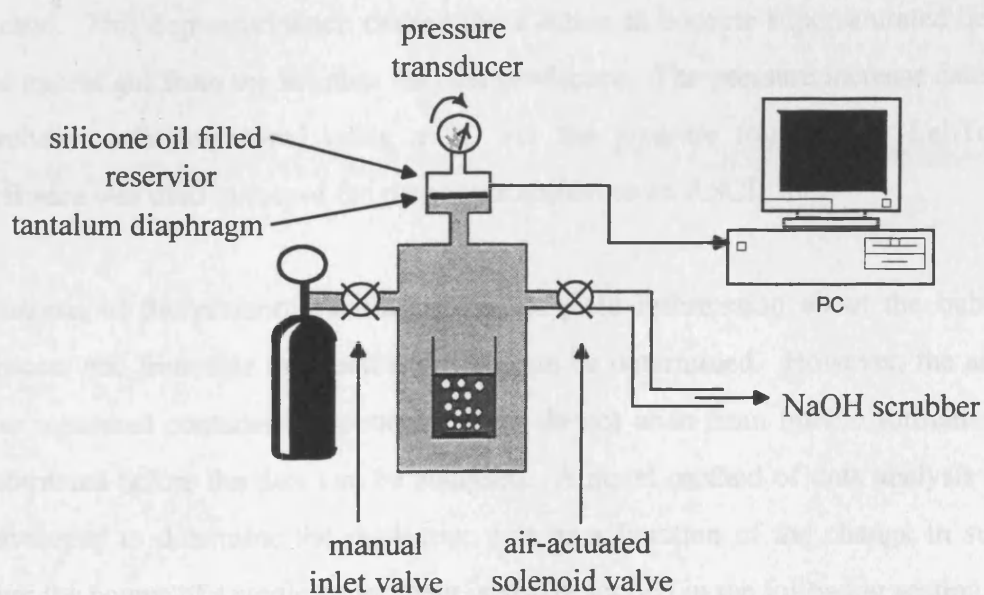


Figure 3.9 A schematic diagram of the PRBN apparatus

A manually operated inlet valve and an air actuated solenoid outlet valve allowed accurate pressurisation and depressurisation of the vessel to the initial and target pressures required for supersaturation of the solution. In order to prevent significant amounts of chlorine being released into the atmosphere the exhaust chlorine gas from the pressure vessel was passed into a concentrated solution of aqueous NaOH. A diagram of the apparatus is given in figure 3.9 and the standard operating procedure is given in the following section.

3.3.1 Standard Experimental procedure

The apparatus was leak tested prior to every experiment. The apparatus was then purged, first with an inert gas to remove any residual air and moisture, then with chlorine. The chlorine was passed directly from the cylinder into the pressure vessel containing the nucleating liquid and surface, contained in a glass beaker (annealed to remove potential nucleation sites ensuring bubbles are evolved on the designated nucleating surface only). The solution was allowed to equilibrate overnight in the presence of chlorine at a pressure controlled by the regulator on the cylinder and measured using the transducer, the output of which was recorded digitally on a PC. After approximately 24 hours the vessel was decompressed to allow the chlorine in the headspace of the vessel above the solution to escape. This procedure was controlled electronically using a solenoid valve. The solenoid valve was switched open, and the pressure inside the vessel dropped until it reached a specified target value (as recorded by the transducer); at this value the solenoid valve was closed. This depressurisation caused the solution to become supersaturated hence releasing the excess gas from the solution into the headspace. The pressure increase caused by bubble evolution was monitored using a PC via the pressure transducer. LabTech notebook software was used to record the pressure transient as an ASCII file.

Analysis of the pressure vs. time data can yield information about the bubble evolution process and from this the nucleation rate can be determined. However, the actual pressure rise measured contains components which do not arise from bubble formation so must be subtracted before the data can be analysed. A novel method of data analysis that has been developed to determine the nucleation rate as a function of the change in supersaturation over the course of a single experiment is also described in the following section.

3.3.2 Gradient Measurement

As described in section 2.5.1.2 adiabatic expansion causes reheating of the headspace gas that results in a contribution to the measured pressure rise. This effect can be accounted for by carrying out a series of “dummy” experiments. The procedure was the same as described in section 3.3.1, except the pressure vessel was empty so that the subsequent pressure rise was due to the reheating effect only. The reheating was Newtonian (confirmed by the correlation of a series of these experiments), therefore the reheating component was directly subtracted from experimental data [6]. The data are corrected to remove the “adiabatic” component. The nucleation rate is related to the slope of this pressure rise and the supersaturation is calculated from the ratio of final and initial pressures. The details of the novel data analysis technique used to obtain the gradient of the pressure rise as a function of supersaturation is given in section 6.3 of chapter 6.

3.4 Fast Frame video

The method of gas generation used during the fast frame video experiments was the same as that described for the EQCM technique. The electrochemical cell (shown in figure 3.10) was modified to incorporate a planar glass window through which the bubbles forming on the vertical quartz crystal electrode were observed. The video captured 200 images per second, the exposure for each frame being equivalent to 10,000 frames per second shutter speed.

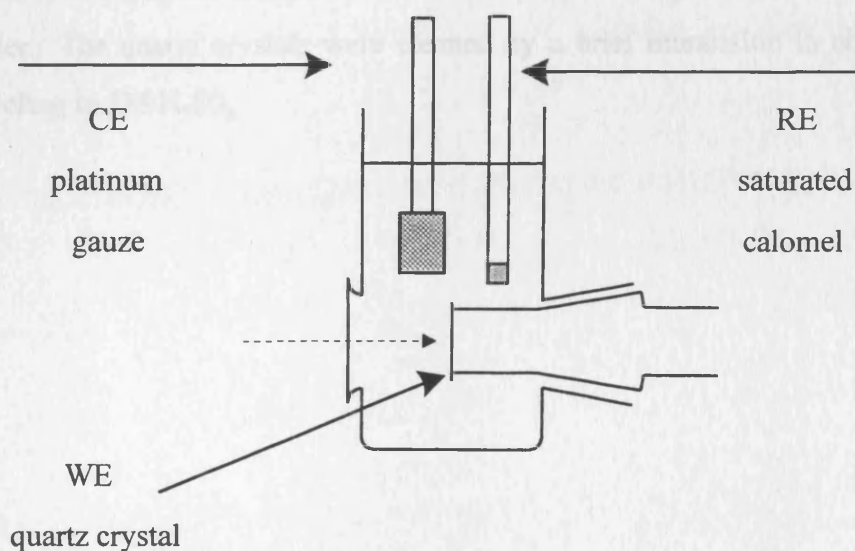


Figure 3.10 Schematic diagram of the electrochemical cell

Both cyclic voltammetry and chronoamperometry were used to evolve bubbles. The current was recorded simultaneously using an X-Y chart recorder. The bubbles recorded using a fast frame video system were measured using a microscope attached to the camera providing x2.6 magnification, which was the maximum permissible with the available light sources (2 halogen lamps). Standard 180-minute duration VHS tapes were used. The tapes were played back on a video interfaced to a PC using Win TV software, allowing individual frames to be saved as black and white bitmap images. The playback feature of the video enabled frames to be captured at 5 ms intervals. Bubble radii were measured from a bitmap image using a pixel-counting method. The absolute values were calculated by comparison with a recorded image of a graticule, or to the known dimensions of the electrode where its outline was visible.

3.5 Chemicals

The electrolytes used to generate gas during EQCM and fast frame video experiments were 0.1M HClO₄ for cathodic hydrogen evolution and 5M NaCl containing 0.01M HCl for anodic chlorine evolution, prepared using Millipore Milli-Q water. 5M NaCl was used in the PRBN experiments. The chlorine used in The PRBN experiments was supplied by MG gases high purity grade. Prior to use, all glassware was first soaked in a concentrated solution of KOH overnight then soaked overnight in 5M HCl followed by thorough rinsing in Milli-Q water. The platinum counter electrode was cleaned using chromic acid and rinsed in Milli-Q water. The quartz crystals were cleaned by a brief immersion in chromic acid followed by cycling in 1M H₂SO₄.

1. Lu, C.; Chanderna, W. A., *Applications of piezoelectric quartz crystal microbalances*; Elsevier: Oxford, 1984.
2. Bruckenstein, S.; Shay, M., *Electrochimica Acta*, **1985**, *30*, 1295.
3. The Southampton Electrochemistry Group, *Instrumental Methods in Electrochemistry*; Ellis Horwood, 1985.
4. Carr, M. W.; Hillman, A. R.; Lubetkin, S. D., *J. Coll. Int. Sci.*, **1995**, *169*, 135-142.
5. Lubetkin, S. D.; Blackwell, M., *J. Coll. Int. Sci.*, **1988**, *126*, 610-615.
6. Carr, M. W., Ph. D. Thesis; University of Bristol, 1993.

4.1 Introduction

This chapter provides a description of a fast frame video (FFV) technique used to monitor the electrochemical evolution of individual bubbles from three different electrode materials: gold, platinum and a mixed ruthenium and titanium oxide (RTO). The methodology is described in detail, including an explanation of the experimental parameters that can be obtained from this technique and how they are applied to the study of bubble evolution. Each surface comprises an electrode of area 0.23 cm^2 coated onto a quartz wafer substrate as used for EQCM analysis. The results are discussed as they are presented throughout the chapter with overall conclusions drawn at the end.

The use of direct observation of bubbles by high-speed photographic or video methods is an established technique that provides immediate and accurate access to the bubble radius during bubble growth from a supersaturated solution [1-9]. Experimental conditions for electrolytic bubble growth used by other researchers vary, a common approach used is the verification of the theoretical growth mechanism by the monitoring of individual bubbles. Individual bubbles are produced either by manufacturing individual nucleation sites by chemical etching of a silicon wafer [1], using highly polished microelectrodes [2,3,4] or mechanically scratching a highly polished surface [5]. Where multiple sites are present on a larger electrode, more complex growth mechanisms have been identified; an example is the coalescence of both oxygen and hydrogen bubbles on transparent nickel and tin oxide electrodes [6]. A comprehensive study of hydrogen, oxygen, chlorine and carbon dioxide bubbles grown on platinum, nickel, copper and iron microelectrodes of different dimensions under a range of current densities identified that the surface material can effect parameters such as coalescence behaviour and the number of nucleation sites [7]. However, this work was restricted to the behaviour of one or two nucleation sites. In most cases, there is agreement between the observed growth kinetics and the theoretical diffusion-controlled spherical phase growth as determined by Scriven [8]. An exception is a more efficient mechanism for bubble growth where the bubble diameter exceeds the diameter of the microelectrode such that all subsequent gas generated is injected directly into the growing bubble, a so-called “direct injection” growth mechanism [9].

It has been found by studying the mass transfer of dissolved gas during electrolytic evolution of various gases that only a fraction of the dissolved gas is transformed into bubbles adhered to the electrode, meaning that the efficiency of gas evolution is significantly less than 100% [10]. The “direct injection” mechanism occurs where the bubble masks the electrode, inhibiting further generation of gas and so retarding the supply of daughter phase to the growing bubble [3,9]. The concentration of gas in the solution is depleted as the bubble interface advances, consuming the gas dissolved in the electrolyte, hence reducing the level of supersaturation. The large concentration gradient for dissolved gas produced between the electrode and the base of the bubble causes the gas evolved at the electrode to be injected into the bubble directly. This is an efficient growth mechanism in terms of the volume of gas produced compared to the increasing bubble diameter, as there is little loss of gas due to diffusion into the bulk electrolyte.

It is plausible that the same mechanism could proceed on a macro electrode where the presence of a large number of tightly-packed, close neighbouring bubbles surrounding a growing bubble effectively obscures it, and the electrode, from the surrounding electrolyte, thereby depleting the local concentration of dissolved gas and inhibiting diffusion of gas from regions of higher supersaturation. For a bubble at the centre of such a cluster, conditions may approximate the “direct injection” growth mechanism, leading to areas of low supersaturation on the electrode surface. This concept of localised supersaturation, which differs compared to the bulk value at the electrode interface, could greatly affect the mass transport of gas to specific areas of the electrode and hence the growth mechanism of certain bubbles.

4.1.1 Objectives

The aim of this study is to determine the behaviour of individual bubbles growing simultaneously at various sites on three different macro electrodes: gold, platinum and RTO, at different current densities. Where different growth mechanisms are viable, these are identified, for example the “direct injection” growth mechanism [9] and very rapid emission of small bubbles previously seen at microelectrodes [7]. Comparison is made between the surfaces, concentrating on the physical properties of the bubbles forming at the naturally occurring nucleation sites, and the interaction between bubbles at adjacent sites to determine the surface properties that give rise to different modes of behaviour, and how this differs from the ideal behaviour predicted from theory. It is established that coalescence determines the detachment parameters, however it is not known to what extent coalescence can be controlled.

In this study, bubbles have been evolved at a similar range of current densities on the different surfaces in order to address this issue.

The focus of the study is on the influence of the nucleation site in terms of its dimension and level of activity on the subsequent development of the bubbles. The dimension of the macro electrodes enables simultaneous measurement of several nucleation sites to determine the level of interaction between bubbles formed at them. The concept of a distribution of nucleation site energetics is introduced to elucidate the frequently observed, but unexplained, random behaviour of nucleation sites. Two model surfaces have been chosen. Gold and platinum differ in their electrocatalytic activity for hydrogen evolution, but both are homogeneous in terms of electrode composition. The behaviour of bubbles forming at an electrocatalytic platinum electrode and non-electrocatalytic gold electrode are compared. The properties of these electrodes as “model surfaces” for different gas evolution regimes are characterised by defining the types of nucleation site that are active, and the variation of activity as a function of current density.

A surface whose electrocatalytic behaviour has been refined over several decades is RTO. Evolution of chlorine at RTO is an industrially relevant system and the development of the RTO electrode has been aimed at reducing running costs associated with chlor-alkali manufacture, but the behaviour of chlorine bubbles at the electrode is surprisingly a relatively unexplored area. The RTO surface is inhomogeneous in terms of distribution of electrocatalytic activity and due to its high surface area has potentially a larger variety and number of available nucleation sites. The features defining chlorine bubble formation at RTO can be compared with gas evolution on the two different model surfaces to determine which aspects of the RTO electrode are dominant in defining its performance as a catalytic surface for bubble evolution.

The results presented in this chapter are a representative sample of a large number of experiments carried out on a variety of different electrode materials. The electrodes were all coated onto a quartz substrate suitable for EQCM analysis in order to allow comparison of behaviour as monitored by the two techniques. In order to clarify the processes occurring during bubble evolution and allow meaningful comparison of results, specific systems were selected that allowed continuity of the operating conditions and apparent surface area, but a diversity of electrocatalytic activities and surface morphology. By definition, the FFV

technique requires analysis of data collected in a pictorial format. A large number of the figures presented in this chapter are “freeze-frame” video images of the electrode. Each is a static image of the complex process occurring at the electrode and is included in the text to clarify the description of the conditions at the electrode surface, therefore it is not intended that the reader attempts to interpret these figures in isolation. The information contained in each bitmap figure is quantified by the use of column diagrams to show the frequency, magnitude and growth mechanism of bubbles. These data are used as a basis for discussion and comparison of bubble evolution from the different systems being studied.

4.2 Theoretical aspects of bubble evolution

4.2.1 Bubble growth

For hydrogen forming at a platinum microelectrode, three different growth mechanisms for individual bubbles have been identified during the lifetime of a single bubble. The functionality of radius with time was seen to differ depending on the time (t) elapsed from nucleation [9]. Growth occurs initially by the expansion of the bubble; the pressure inside a small bubble is high compared to the background pressure, due to the high surface curvature. When $0 < t/\text{ms} < 10$, the increase in radius is linearly proportional to time ($r \propto t$). During this stage of growth, the bubble grows by desorption of the previously generated gas present in the supersaturated solution. Initially expansion is slow, but it quickly accelerates until the solution becomes depleted and the supply of new molecules to the bubble surface by diffusion becomes the rate limiting process between $10 < t/\text{ms} < 500$. In this regime, the surface area increases linearly with time ($r^2 \propto t$) as shown in equation 4.2. The initial expansion stage is very short compared to that of mass transfer control; therefore, it can be assumed that the entire process is governed by mass transfer [6]. At a microelectrode, as the bubble continues to grow, its radius can exceed the radius of the electrode. Now growth occurs by “direct injection” of the gas into the bubble and the volume increases linearly with time ($r^3 \propto t$).

These different modes can be identified easily by the relationship between radius and time. Plotting the log of radius vs. log of time gives a straight line with a slope of 1, 0.5 and 0.33, respectively, for the cases outlined above. The relationship between radius and time can be expressed in the general form

$$r = at^n \tag{4.1}$$

n is referred to as the “time exponent”. In a supersaturated electrolyte, following the very early stages of growth, typically after 10 ms, bubble growth is determined by the rate of diffusion of dissolved gas to the expanding liquid/gas interface, as outlined above. The specific form of equation 4.1 in this case is known as the Scriven equation [8] and is given below

$$r(t) = 2\beta(Dt)^{1/2} \quad (4.2)$$

β is a constant for given conditions of supersaturation, and D is the diffusion coefficient. By taking logs, equation 4.2 becomes

$$\ln r = 0.5 \ln t + C \quad (4.3)$$

where C is a constant, t is the time elapsed since nucleation. The bubble is assumed to have a finite (non-zero) radius at nucleation, and the real time values are adjusted accordingly, i.e. the time at which nucleation occurs is reset to zero for each consecutive bubble event. For a hydrogen bubble growing at a nucleation site on a polished gold electrode, plotting $\ln r$ vs. $\ln t$ gives a straight line as shown in figure 4.1.

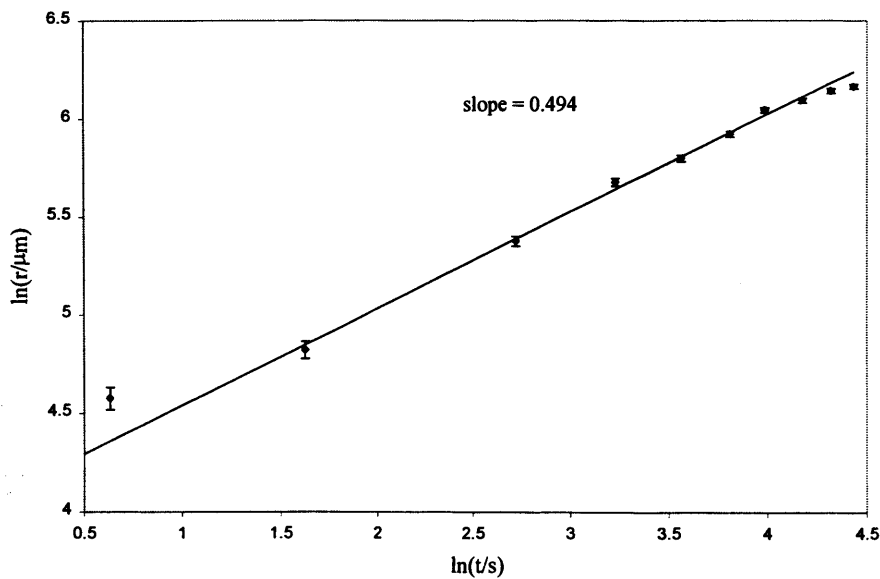


Figure 4.1 $\ln r$ vs. $\ln t$ for a hydrogen bubble growing on a gold electrode. The error bars correspond to the resolution of the bitmap picture from which the radius was measured, $\pm 5.4\mu\text{m}$, the trend line is a least squares fit linear regression.

This plot can be used to determine the growth mechanism described in the previous section: diffusion limited growth will give a slope (the time exponent, n , in equation 4.1) of $1/2$, and direct injection gives a slope of $1/3$. The growth mechanisms of individual bubbles forming a

number of sites on the different electrodes surfaces are presented in sections 4.4 to 4.6.

4.2.2 Bubble nucleation

It has been established from studies on microelectrodes that bubbles form at specific nucleation sites on the electrode surface [3,4] and the nucleation site geometry affects the growth rate, with the activity variations between different sites being greater than the temporal variations occurring at one site [7]. As described in sections 1.3.2 and 2.1.6, bubble formation is favoured at nucleation sites on a solid surface where the activation energy required for nucleation is low. Nucleation sites can be easily identified on a surface by the bubbles produced at them; the most active ones are where bubbles form at the lowest supersaturation (smallest current density). Other nucleation sites on the surface may be dormant, or temporarily de-activated. As the current density (supersaturation) increases, the activity of an existing nucleation site may increase, increasing the rate of nucleation, or the less favourable, dormant nucleation sites may become activated. Both processes increase the rate of gas evolution at the electrode and both types of behaviour are feasible. It is expected that the number of nucleation sites will increase as the current density increases. The relative number of sites available at low supersaturation compared to high supersaturation can be thought of as the distribution of nucleation site energetics, as determined by the nucleation site geometry or chemical composition (such as the presence of an adsorbed impurity on the surface). A narrow range of nucleation site energetics means a very small number of sites are active at low supersaturation, but as soon as the supersaturation level threshold required for nucleation is reached, the majority of sites become active. A wider range of nucleation site energetics results in a gradual increase in the number of active nucleation sites as the supersaturation increases.

4.2.3 Definition of experimental parameters

The growth cycles of consecutive bubbles forming at each site were recorded as a radius vs. time sequence, an example of which is given in figure 4.2. The maximum bubble radius, i.e. the departure radius, is the radius at point III. The detachment frequency is the reciprocal of the time a bubble is resident on the electrode given as the time elapsed between points III and I. The induction time is the time elapsed between the initial generation of current at the start of the experiment at $t=0$ and point I, or the time elapsed between detachment at point III and

subsequent nucleation at point IV. These parameters, along with the time exponent (n) for the growth mechanism will be used throughout the chapter to describe bubble behaviour at the electrode.

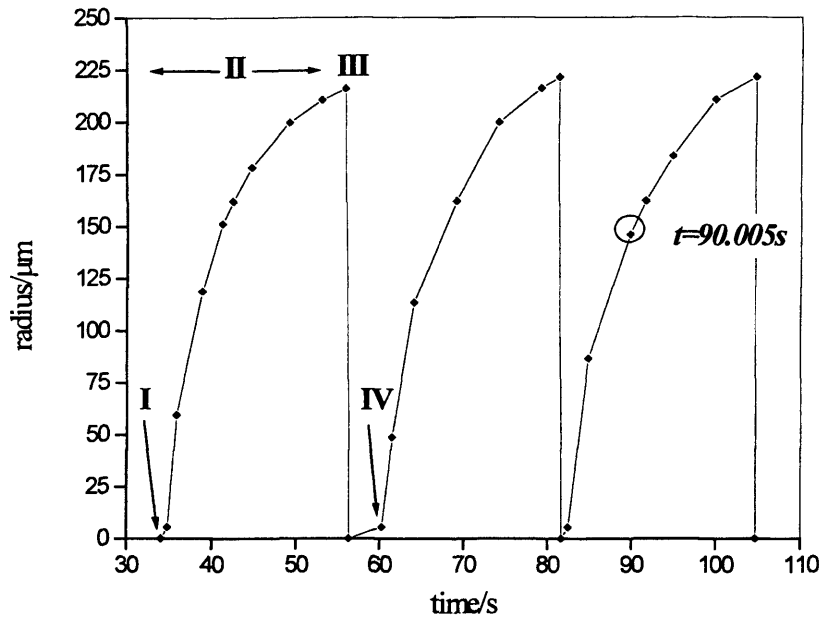


Figure 4.2 Bubble radii vs. time for three consecutive bubbles detaching from a polished gold electrode. Point (I) corresponds to nucleation, the region (II) denotes growth, (III) shows the point of detachment and (IV) the subsequent nucleation of the second bubble growing at the same site. The circled point corresponds to the radius of the bubble highlighted in figure 4.3.

Although the behaviour of bubbles at each nucleation site may be complex, the activity of the nucleation site is a simple concept: prior to the onset of nucleation, it can be assumed that the electrolyte supersaturation adjacent to the electrode has a constant value over the electrode surface. Therefore, the most active sites are the ones at which the first bubbles appear after the generation of a current, i.e. the sites with the shortest induction time. As nucleation site activity decreases, the induction time increases and, theoretically, sites that facilitate nucleation should inhibit detachment, i.e. the residence time of a bubble at an active nucleation site should be longer than that for a bubble at an inactive site.

Another process that can occur at high bubble populations is coalescence, facilitated on surfaces where detachment is slow and bubbles grow to a size where collision with neighbouring bubbles occurs. An anomaly in the normal observed bubble evolution mechanism is the formation of a “bubble pump” seen at some nucleation sites, where a bubble

detaches shortly after nucleation. Together with a very short induction time this produces a vertical “train” of small bubbles leaving the nucleation site. Bitmap images showing examples of these “bubbles trains” are presented in the results section. This type of mechanism has been observed by other researchers [6] but no explanation has been offered for the cause of the rapid detachment.

4.3 Methodology of data analysis from visual observation

In this section, the parameters defined in section 4.2.3 are used to describe bubble behaviour at individual nucleation sites, using an example of hydrogen evolution from 0.1M HClO₄ at a gold electrode (area 0.25 cm²), at a current density of 2.8 mA cm⁻². A highly polished gold electrode was chosen so that only a small number of nucleation sites would be active at all levels of current density. By magnifying the electrode and observing where bubbles appear, the coordinates of the nucleation sites can be determined.

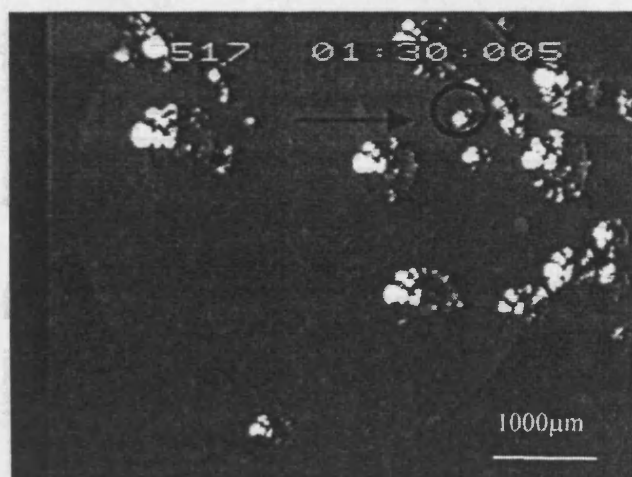


Figure 4.3 Bitmap image of the distinctive keyhole-shaped polished gold electrode (area =0.23cm²) in a vertical orientation, captured from a videotape frame at t=90.005 seconds.

The circled bubble is the third consecutive bubble shown in figure 4.2.

The image in figure 4.3, obtained using the method described in section 3.4 of chapter 3, shows the position of a nucleation site on a gold electrode, which is identified by a bubble growing at the site. The electrode is in a vertical orientation; this configuration was used for each of the electrodes to facilitate a variety of detachment modes. The time display on the picture is a “burnt-in” time recorded onto the videotape simultaneously with the image from the camera.

4.3.1 Induction time

At the lowest current density, 32 nucleation sites were active; the initial induction time for each nucleation site is given in figure 4.4, in which it can be seen that there is a distribution of site activities. The most active sites are those with an initial induction time below 5 seconds and the less active sites have an induction time above 5 seconds.

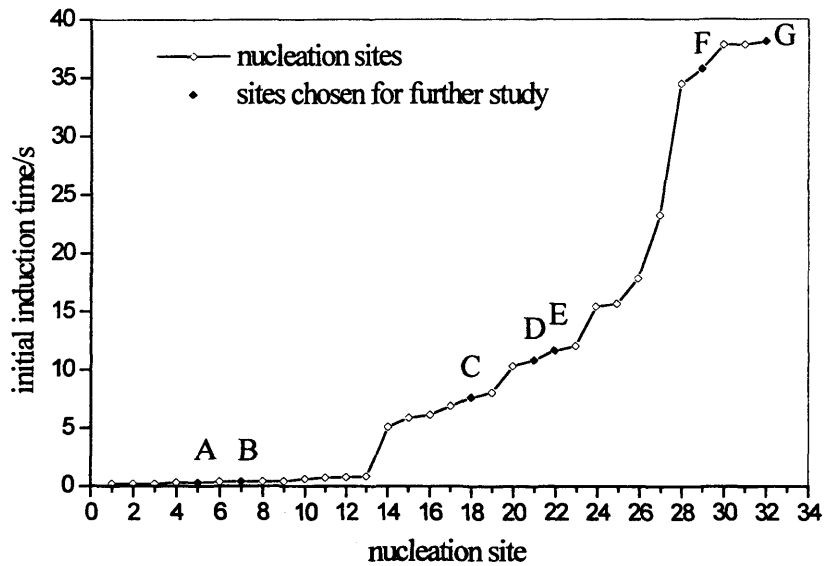


Figure 4.4 Initial induction time, shown in ascending order, for each nucleation site on the gold electrode. The electrolyte was 0.1M HClO₄ and hydrogen was evolved at 2.8 mA cm⁻².

The seven sites labelled (A-G) are studied in further detail in section 4.3.3.

The trend in initial induction time is unrelated to the position of the nucleation sites on the electrode. The issue of a non-uniform distribution of nucleation site activity has been attributed to the non-linear relationship between nucleation rate and supersaturation [11] and is raised again in Chapter 6.

4.3.2 Detachment rate

Assuming that the simple relationship between nucleation activity and detachment rate as outlined in section 4.2.3 is valid, bubble detachment rate is expected to follow the opposite trend as nucleation site activity, increasing as the nucleation activity decreases. In figure 4.5, both parameters are plotted for each nucleation site.

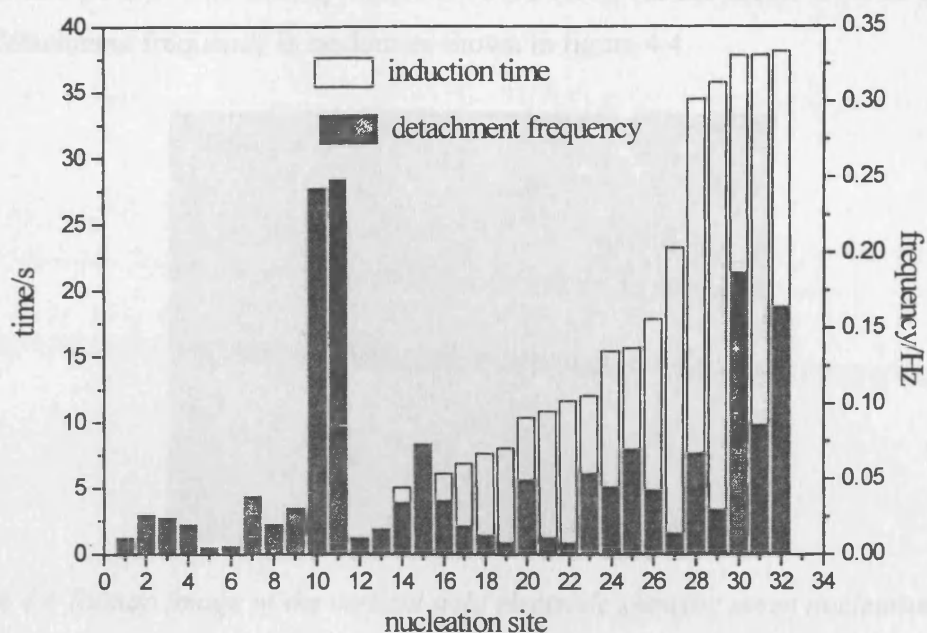


Figure 4.5 Initial induction time (as shown in figure 4.4) and corresponding detachment frequency for each nucleation site active on the gold electrode during hydrogen evolution. The electrolyte was 0.1M HClO₄ and gas was evolved at 2.8 mA cm⁻². The detachment frequency is the reciprocal of the residence time of bubbles at the surface site.

By comparing the two parameters in figure 4.5, it can be seen that the overall trend in detachment frequency is similar to that for the nucleation activity. However, the trends in activity and detachment do not correlate to the same nucleation sites and it can be concluded that the two processes are independent. The relationship between the induction time and detachment rate has become complex due to the detachment mechanism, specifically the role of bubble coalescence; this topic is covered in section 4.2.3.

4.3.3 Specific sites for further study

Of the 32 active sites on the gold electrode, seven were chosen as a representative sample and labelled A-G. The seven sites chosen display a range of activities due to the specific nature of the nucleation site, and a range of detachment frequencies and detachment sizes, depending on their proximity to other bubbles on the electrode. Figure 4.6 shows the position of sites A-G, identified by the bubbles growing at each site. In the frame chosen there is no bubble growing at site F, therefore its position is indicated by a black circle. Table 4.1 below

contains an example of the data collected for five consecutive bubbles at each individual nucleation site (A-G). The activity decreases from A-G, but the distribution of detachment size and detachment frequency is random as shown in figure 4.4.

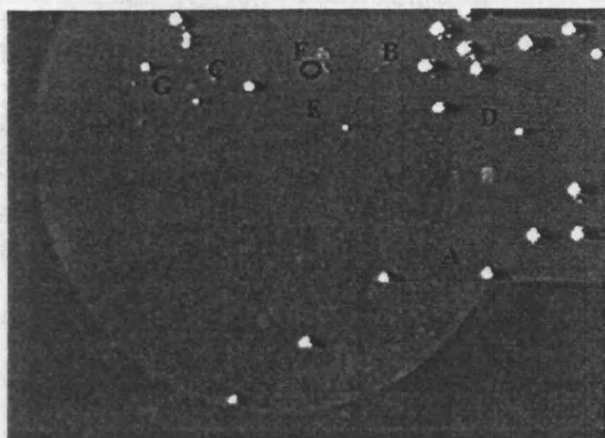


Figure 4.6 Bitmap image of the vertical gold electrode showing seven nucleation sites, labelled A-G. Consecutive bubbles growing at these sites were monitored at different current densities; the results are given in section 4.3.

Nucleation site	Initial induction time/s \pm 0.005	Average detachment radius/ μ m \pm 5.4	Average detachment frequency/Hz
A	0.305	208.5	0.005
B	0.385	216	0.039
C	7.625	469.8	0.012
D	10.825	392.4	0.011
E	11.635	433.8	0.008
F	35.735	293.4	0.030
G	38.095	110.7	0.160

Table 4.1 Statistical data for hydrogen bubbles evolved at nucleation sites A-G on the gold electrode. The electrolyte was 0.1M HClO₄ and gas was evolved at 2.8 mA cm⁻²

There is much smaller variation in activity of consecutive bubbles evolving at individual sites compared to the variation between sites, as shown in figure 4.7. Each column shown in figure 4.7 represents the data for an individual bubble; the groupings identify consecutive growth of individual bubbles at the same nucleation site. The format of this figure is useful for emphasising the behaviour of bubbles at the same site vs. the behaviour of bubbles at different sites and will be used in most subsequent figures.

Figure 4.7 shows the residence time of bubbles at the electrode compared to the induction times. Although the initial induction time gives an indication of site activity, subsequent induction times (time elapsed between detachment and nucleation) are very sensitive to the surrounding conditions and the value of the local supersaturation, which fluctuates as bubbles detach. This causes inconsistencies in consecutive nucleation times at the same site. However, the activity of the site is assumed constant due to the consistency of bubble formation at the site, and other parameters such as detachment size. Generally, the induction time is much shorter than the residence time. This is consistent with a model of bubbles nucleating quickly, and remaining attached to the electrode for a significant time before detaching.

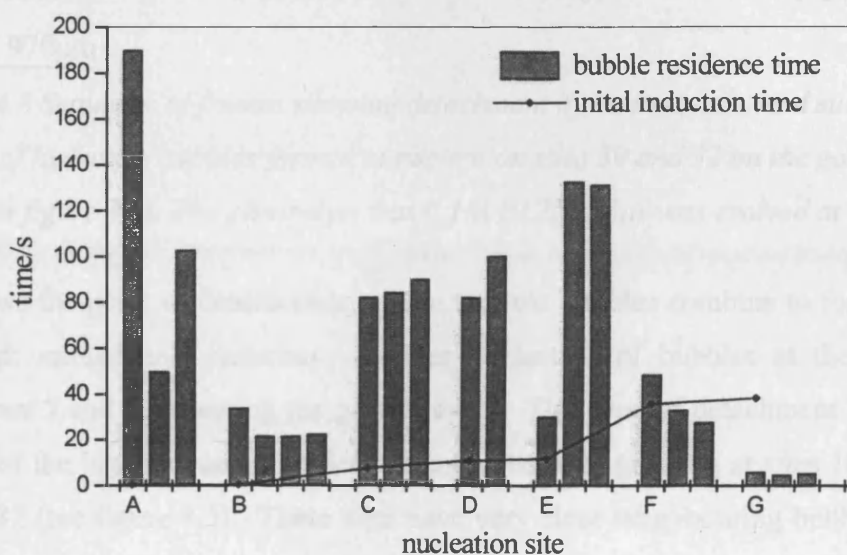


Figure 4.7 Comparison of induction and residence times of bubbles evolved at nucleation sites A-G (as indicated in figure 4.6) on the gold electrode during hydrogen evolution. The electrolyte was 0.1M HClO₄ and gas was evolved at 2.8 mA cm⁻²

4.3.3.1 Detachment mechanism

It is apparent from figure 4.5 that the detachment rates are not dependent solely on the surface conditions at the nucleation site. Detachment occurs primarily by coalescence, as shown in the sequence below for nucleation site G. Frame 1 in figure 4.8 shows two bubbles at nucleation sites 30 and 32 (where site 32 corresponds to site G). Frames 2-6 show the increasing radius of each bubble as it grows at its nucleation site. Between frames 6 and 7,

the two bubble surfaces come into contact.

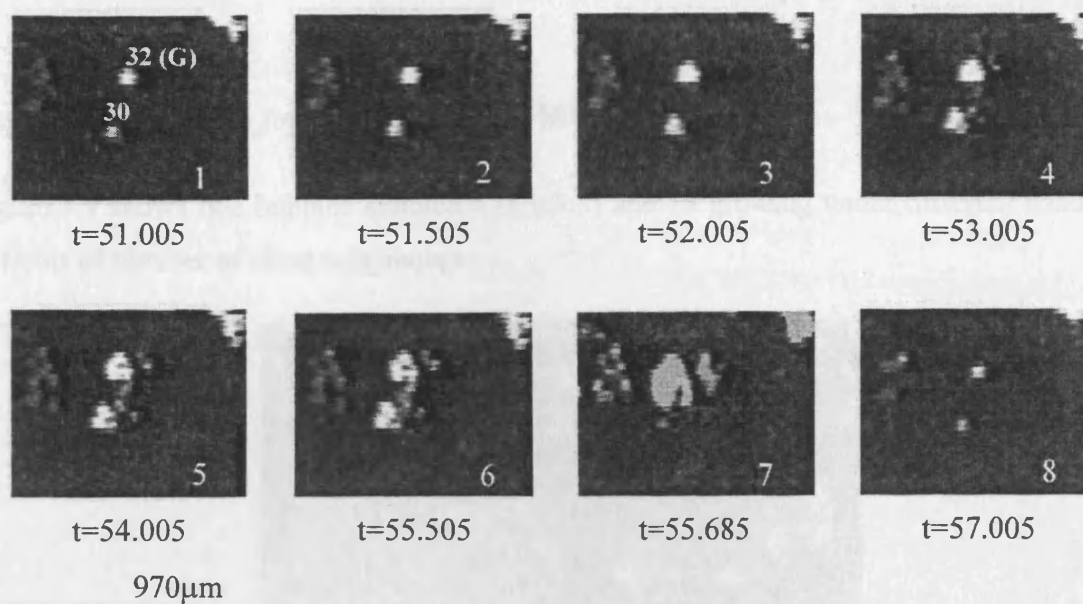


Figure 4.8 Sequence of frames showing detachment by coalescence, and subsequent nucleation of hydrogen bubbles formed at nucleation sites 30 and 32 on the gold electrode (indicated in figure 4.4). The electrolyte was 0.1M HClO₄. Gas was evolved at 2.8 mA cm⁻²

Frame 7 shows the point of coalescence, where the two bubbles combine to form one larger bubble, which immediately detaches. Further nucleation of bubbles at the sites occurs between frames 7 and 8, repeating the growth cycle. This type of detachment mechanism is responsible for the high frequency of detachment of bubbles growing at sites 10 and 11, and sites 30 and 32 (see figure 4.5). These sites have very close neighbouring bubbles, therefore coalescence occurs quickly, when the bubble radius is small. Other types of detachment mechanism are singular detachment due to buoyancy and forced detachment due to the collision with a bubble rising up the face of the electrode.

4.3.3.2 Growth mechanism

The results presented in this section allow for the verification of the growth mechanism for hydrogen bubbles at a gold electrode and establish the conditions where the growth mimics the direct injection model found at microelectrodes. Different growth environments are characterised by the population of active nucleation sites in a given area, i.e. bubble clusters or isolated bubbles as described in section 4.1. As the number of close neighbouring bubbles

in a cluster increases, the local supersaturation in the region of the bubble cluster will decrease.

4.3.3.3 Bubble growth for non-adjacent bubbles

Figure 4.9 shows two bubbles labelled 4 (circled) and 19 growing under different conditions in terms of number of close neighbours.

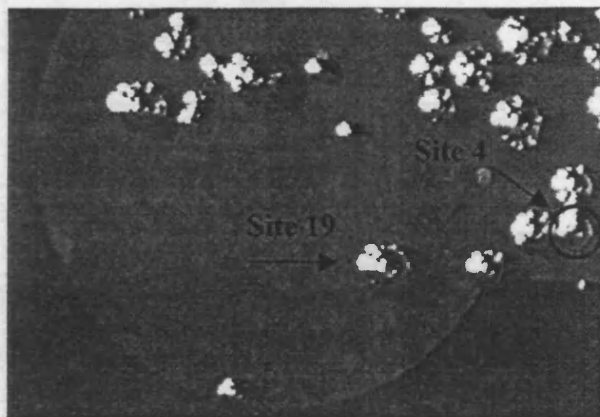


Figure 4.9 Bitmap image of the vertical gold electrode showing hydrogen bubbles growing at nucleation sites 4 and 19. The electrolyte was 0.1M HClO₄. Gas was evolved at 2.8 mA cm⁻². The two nucleation sites differ in terms of the number of close neighbours.

Figure 4.10 shows the raw data for the growth of the two bubbles at nucleation sites 4 and 19, the bubble at site 19 grows to a larger radius before detaching, due to the coalescence of the bubble at site 4 with one of its close neighbours. Figure 4.11 is a plot of $\ln r$ vs. $\ln t$ for the bubbles growing at sites 4 and 19. The data for both bubbles show a good fit to the linear trend line, therefore the growth mechanism is constant throughout the bubble lifetime. The time exponent (n) is given by the slope of each line, according to equation 4.3

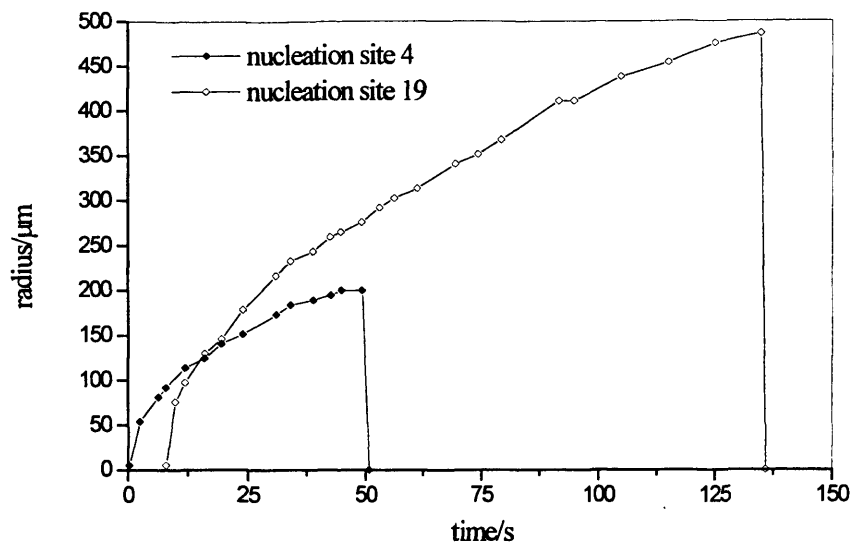


Figure 4.10 Radius vs. time for hydrogen bubbles growing at nucleation sites 4 and 19 on the gold electrode (as shown in figure 4.9). The electrolyte was 0.1M HClO₄. Gas was evolved at 2.8 mA cm⁻².

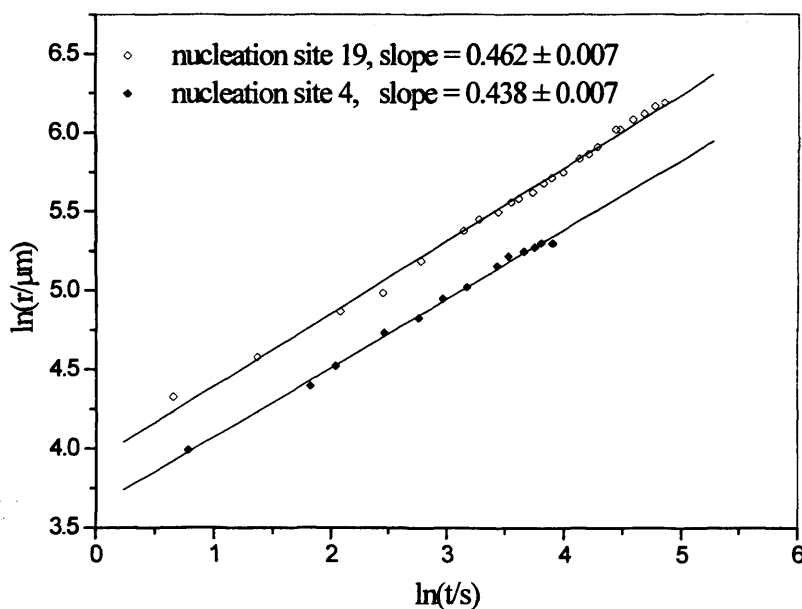


Figure 4.11 Plot of $\ln r$ vs. $\ln t$ for two hydrogen bubbles growing at nucleation sites 4 and 19 on the gold electrode, the values correspond to the raw data shown in figure 4.10, the straight line is a least squares fit linear regression.

The two values of the time exponent, n , are similar and fall between 0.33 and 0.5, therefore, the growth mechanism is definitively neither diffusion or direct injection. However, the value of n for growth of bubbles at site 19 is closer to that expected for diffusion-limited growth

than the value of n measured at site 4. The conditions, in terms of the number of neighbouring bubbles, of the bubbles growing at site 4 approach those where it is reasonable to expect the “direct injection” model found typically at a microelectrode, which could account for the lower value of n measured at this site.

4.3.3.4 Growth at adjacent nucleation sites

In figure 4.10, the detachment radius of the isolated bubble at nucleation site 19 was greater than the bubble growing at the encircled nucleation site 4. Where detachment occurs by coalescence with a neighbouring bubble, it can be assumed that the distance between two nucleation sites will govern the detachment radius and hence the detachment frequency of each bubble growing at the two adjacent sites (assuming a constant growth rate).

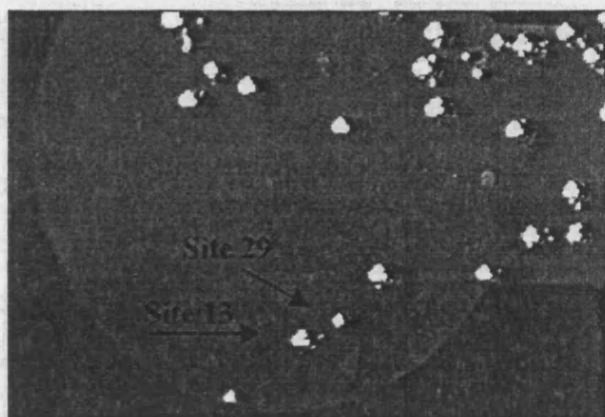


Figure 4.12 Bitmap image of the vertical gold electrode showing hydrogen bubbles growing at two adjacent nucleation sites, 13 and 29. The electrolyte was 0.1M HClO₄. Gas was evolved at 2.8 mA cm⁻². The growth data for each bubble are given in figure 4.13.

Figure 4.12 shows the position of two adjacent nucleation sites (29 and 13) on the gold electrode. The bubble shown at nucleation site 13 is larger because the site was activated first. The shape of the growth curves for the two bubbles in figure 4.13 differs. The initial rapid growth of the bubble at site 29 is not sustained, whereas the growth of the bubble at site 13 is slower but constant over its lifetime, and unchanged by the appearance of its neighbour. The shape of each curve is consistent with the value of the time exponent, n , for each bubble given by the slope of the $\ln r$ vs. $\ln t$ plot in figure 4.14.

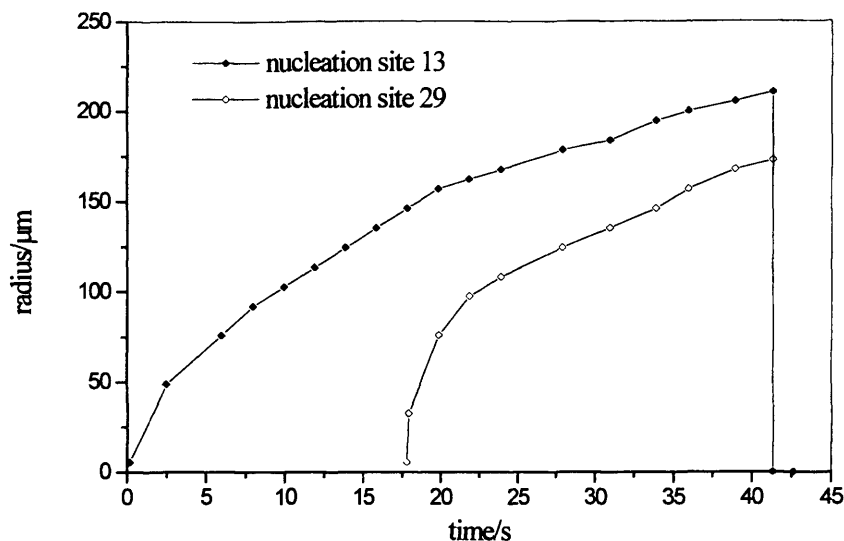


Figure 4.13 Radius vs. time for hydrogen bubbles growing at two adjacent sites 13 and 29 on the gold electrode (as shown in figure 4.11) under the same conditions given above.

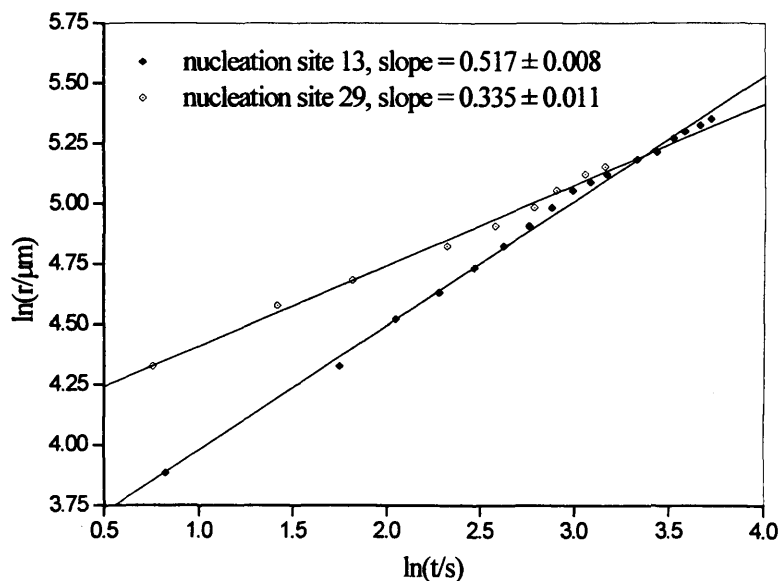


Figure 4.14 Plot of $\ln r$ vs. $\ln t$ for two hydrogen bubbles growing at adjacent nucleation sites 13 and 29 on the gold electrode. The points correspond to the raw data shown in figure 4.12.

The straight lines are a least squares fit linear regressions.

The two adjacent bubbles at sites 13 and 29 coalesce on contact and the resulting large bubble detaches immediately. The bubble at the more active site (13) has a time exponent of 0.52 therefore its growth is diffusion limited. The growth of the second bubble at the less active site has a time exponent of 0.33, and therefore its growth is not determined by the supply of

dissolved gas to its surface. This behaviour mimics the direct injection mechanism, which is possibly a consequence of depletion of the local concentration of dissolved gas caused by the presence of the first bubble.

4.3.4 Summary of methodology

The results presented in the preceding sections have illustrated the methodology used to study the evolution cycle of electrolytically generated bubbles using captured images from the FFV. At the magnification chosen, the position of nucleation sites on the gold electrode surface can be identified by the presence of bubbles growing at them, the radii of which are easily resolved with small error. The time resolution of the frame capture is also sufficient to produce a growth curve (bubble radius vs. time) and hence determine the detachment frequency.

4.3.4.1 Nucleation

Although the induction time varies, the detachment size and frequency are good indications of the behaviour of bubbles at a given nucleation site and therefore these parameters can be used for comparing the effect of different current densities upon the nucleation site activity.

Nucleation sites are located randomly across the surface of a gold electrode, as shown by various bitmap images. There is a distribution of site energetics, demonstrated by a range of nucleation induction times, with some sites only activated at the highest current density. Once formed bubbles tend to be “anchored” to that site during growth up to the point of detachment. Detachment is rate limiting, i.e. residence time of bubbles on the electrode before detachment is much longer than induction time (causing a low detachment frequency).

4.3.4.2 Growth mechanism

The time exponents measured consistently fell within the two limits expected; 0.5 and 0.33. Two growth mechanisms were observed, diffusion limited and “direct injection”, and each are dominant at different nucleation sites, but often growth is intermediate between the two regions. There is no direct correlation between population of nucleation sites and the growth mechanism. However, the presence of one or more neighbouring bubbles was seen to be an influence, possibly due to the local depletion of supersaturation levels. Detachment arising from coalescence with a neighbouring bubble is the dominant mechanism. The inability of

the bubbles to detach prior to coalescence leads to large bubble sizes and is consistent with a high three-phase contact angle, indicating a high surface tension: the force that opposes buoyancy and thereby inhibits detachment.

4.4 Hydrogen evolution on gold

The results shown in this section were recorded at the electrode shown in figure 4.6. Hydrogen gas was evolved at three different current densities: 2.8, 16, 44 mA cm⁻². These represent a small section of a range of current densities at which bubble events were measured. The higher limit (44 mA cm⁻²) is the threshold for measuring individual bubble events under the conditions defined by the recording equipment. At current densities below 2.8 mA cm⁻² there was virtually no activity at any of the nucleation sites. Bubble behaviour at each of the three current densities is treated separately in the following sections. Assuming a resolution of ± one pixel, the smallest determined radius of a hydrogen bubble evolved at a gold electrode was 5.4µm, a magnification of 92.59 pixels/mm.

4.4.1 Results for low current density

At a current density of 2.8 mA cm⁻², the typical nucleation site distribution is shown in figure 4.15. There is a large region on the surface where there are no active sites. The data acquired for successive hydrogen evolution under the conditions given above are displayed in table 4.2. For clarity, the results are also shown in figures 4.16 and 4.17.



Figure 4.15 Bitmap image of the vertical gold electrode showing distribution of nucleation sites over the surface. The electrolyte was 0.1M HClO₄. Gas was evolved at 2.8 mAcm⁻²

Figures 4.16 and 4.17 summarise the data collected for nucleation sites A-G. The behaviour

at these sites was consistent and reproducible, activity in terms of frequency and bubble radius was constant, and all the sites remained active during the course of the experiment. The majority of bubbles remained anchored to their nucleation site throughout growth. The exceptions occurred at 2 different sites where, during one growth cycle, the absence of any close neighbours allowed the bubbles to grow to a very large size before detaching. During the later stages of growth, bubbles that were nucleated at these sites rolled slowly up the electrode before detaching. The dotted lines in figure 4.16 show the expected value of the time exponent for diffusion (0.5) and direct injection (0.33) limited growth. It is shown that for sites A-G the time exponent is predominantly 0.5, indicating diffusion-controlled growth was dominant. Figure 4.17 shows that bubble radii fall between 200 and 550 μm the variation in radius between each site is much greater than the variation in subsequent detachment sizes at the same site.

Site	Bubble number	Residence time/sec $\pm 0.005\text{s}$	Detachment radius/ $\mu\text{m} \pm 5.4\mu\text{m}$	Time exponent	Time exponent error/ $\pm 1\sigma$
A	1	189.8	410.4	0.400	0.003
	2	49.76	183.6	0.404	0.014
	3	102.68	318.6	0.432	0.007
B	1	33.69	205.2	0.465	0.026
	2	21.47	216	0.432	0.027
	3	21.36	221.4	0.478	0.007
	4	22.21	221.4	0.478	0.007
C	1	82.19	448.2	0.500	0.009
	2	84.22	475.2	0.494	0.010
	3	89.97	486	0.484	0.011
D	1	82.11	329.4	0.456	0.007
	2	100.08	329.4	0.434	0.017
E	1	29.74	237.6	0.468	0.009
	2	132.56	513	0.462	0.009
	3	131.2	550.8	0.470	0.012
F	1	48.33	302.4	0.480	0.003
	2	32.89	286.2	0.495	0.007
	3	27.47	291.6	0.504	0.027
G	1	5.64	124.2	0.474	0.022
	2	4.56	118.8	0.505	0.009
	3	5.2	118.8	0.459	0.030

Table 4.2 Parameters obtained for individual hydrogen bubbles evolved at nucleation sites A-G on the gold electrode. The electrolyte was 0.1M HClO_4 , and the gas evolved at 2.8 mA cm^{-2} .

The bubble detachment mechanism was primarily coalescence followed by immediate detachment. This mechanism produces stable and reproducible site activity (see site B), it also directly affects the detachment size because, for very close neighbours coalescence occurs swiftly after nucleation, when the two bubbles are small, termed a “coalescence pair” (as observed at site G).

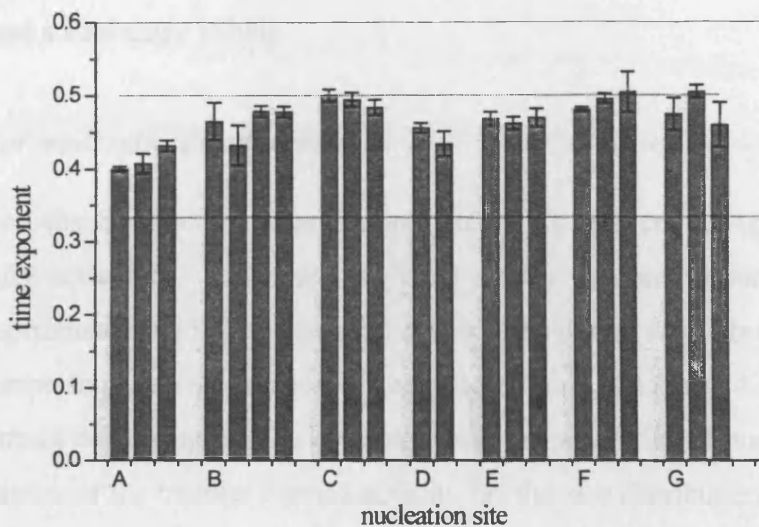


Figure 4.16 Time exponent (shown in table 4.2) for individual hydrogen bubbles at sites A-G on the gold electrode. The electrolyte was 0.1M HClO₄. Gas was evolved at 2.8 mAcm⁻²

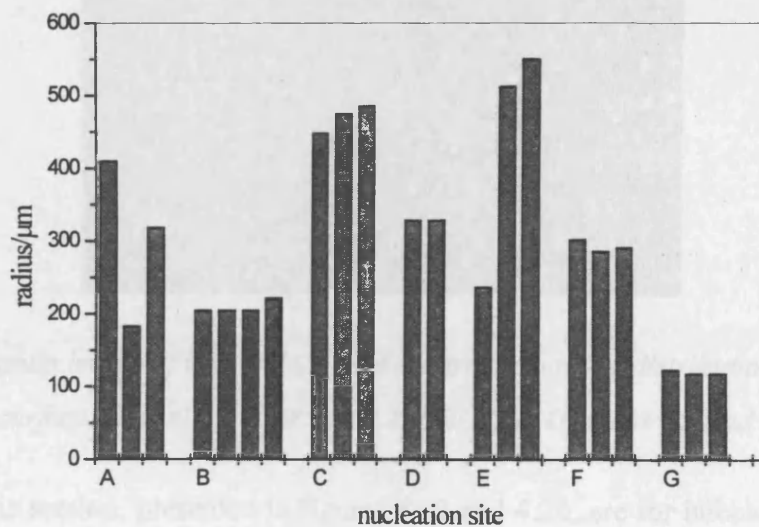


Figure 4.17 Detachment radius for individual hydrogen bubbles growing at sites A-G on the gold electrode. The electrolyte was 0.1M HClO₄. Gas was evolved at 2.8 mA cm⁻².

Less common events were “scavenger” type coalescence during which a large bubble remained attached to the electrode upon coalescence with a smaller neighbour. Unless the

larger bubble detached, it continued to scavenge subsequent bubbles forming at the same neighbouring site. Once the scavenging bubble had detached, both sites resumed their original growth regimes. The factor that determined whether “scavenging” or “detachment” coalescence occurred, appeared to be the ratio of the two bubble radii, although no data were collected for these type of events. Other detachment mechanisms that were observed were the isolated detachment of individual bubbles, and forced detachment arising from the collision of a rising bubble and a stationary bubble.

4.4.2 Results for moderate current density

Figure 4.18 shows the distribution of nucleation sites at 16 mA cm^{-2} . Approximately 100 sites were initially activated. The new sites were mostly clustered around existing sites, although only approximately 75 sites remained active. The others were obscured by resident bubbles. By comparing the two images of the gold (figures 4.15 and 4.18) the effect of increasing the current density appears to have increased the population of nucleation sites, but not the characteristics of the bubbles formed at them, i.e. the size distribution is similar to that seen at the lower current density.



Figure 4.18 Bitmap image of the vertical gold electrode showing distribution of nucleation sites over the surface. The electrolyte was 0.1 M HClO_4 . Gas was evolved at 16 mA cm^{-2}

The results in this section, presented in figures 4.19 and 4.20, are for bubbles evolved at the nucleation sites A-G and are presented in the same format as that shown in section 4.3.1.1. At this intermediate value of current density, most bubbles remained attached to the electrode at the point of nucleation during growth, and coalescence remained the primary method of detachment, although due to the increase in the number of nucleation sites, collision between rising and stationary bubbles was more frequent. In some instances of this dynamic collision

followed by coalescence, the behaviour of subsequent bubbles at the disrupted site was seen to change. A “bubble pump” type mechanism was observed where the bubble detached shortly after nucleation. However these “pumps” were unstable and had short periods of activity at 16 mA cm^{-2} . The activity of site D was seen to change from the formation of “adhere and grow” type bubbles to a “bubble pump” during the course of an experiment, although this switch in mechanism could not be attributed to the type of detachment event.

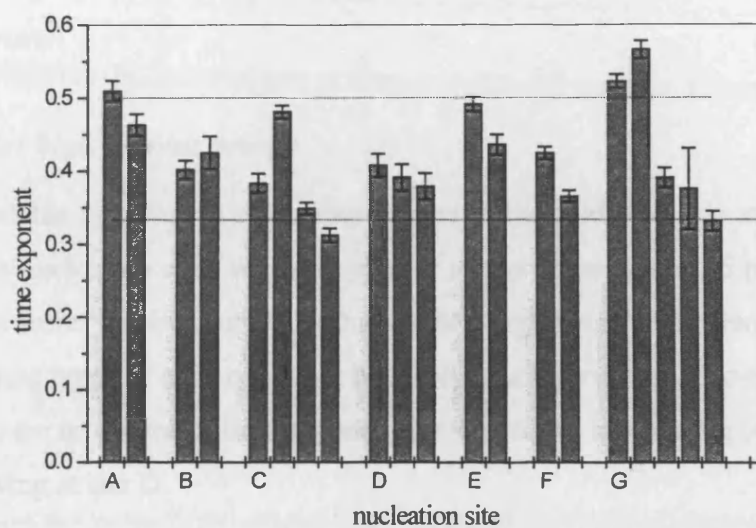


Figure 4.19 Time exponent for individual hydrogen bubbles at sites A-G on the gold electrode. The electrolyte was 0.1 M HClO_4 . Gas was evolved at 16 mA cm^{-2}

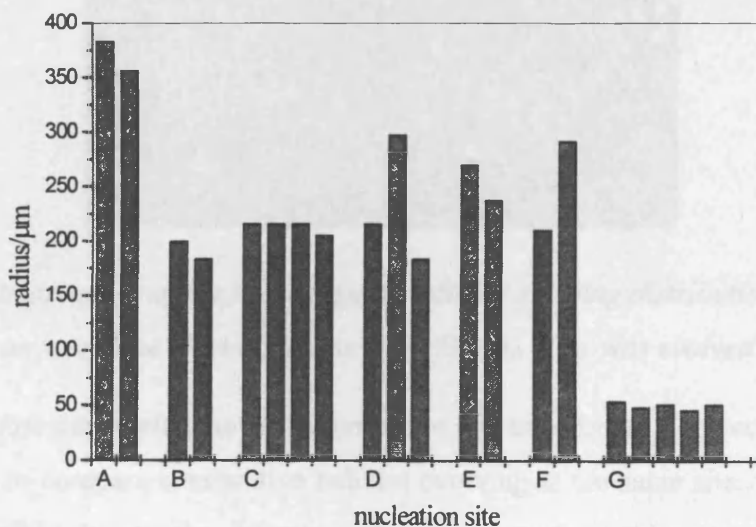


Figure 4.20 Detachment radius for individual hydrogen bubbles growing at sites A-G on the gold electrode. The electrolyte was 0.1 M HClO_4 . Gas was evolved at 16 mA cm^{-2}

The activity at individual sites was less consistent than for the lower current density. Figure 4.19 shows that the time exponent varies not only between different sites but also for different bubbles growing at the same site, with the trend being towards “direct injection” controlled growth for subsequent bubble events at most sites. This change in mechanism occurred over the course of one experiment. A possible explanation is that the level of supersaturation decreases over time, limiting the supply of dissolved gas diffusing to the bubble interface. Detachment size as shown in figure 4.20 is unaffected and remains constant with subsequent detachment events.

4.4.3 Results for high current density

Figure 4.21 shows the distribution of nucleation sites on the gold electrode at 44 mA cm^{-2} . The number of active nucleation sites was very similar to that measured at 16 mA cm^{-2} , however, more of the sites were “bubble pumps”. Due to their high detachment frequency, the growth mechanism of these types of sites could not be resolved at the rate of video-frame capture. For this reason, there are no values of time exponent for the growth mechanism (see figure 4.22) for the bubbles growing at site D.



Figure 4.21 Bitmap image of the vertical gold electrode showing distribution of nucleation sites over the surface. The electrolyte was 0.1M HClO_4 . Gas was evolved at 44 mA cm^{-2} .

The activity at most sites varied during the course of one experiment. The complex behaviour made it difficult to compare consecutive bubbles evolving at the same site. Some sites were deactivated, possibly due to the influence of highly active neighbours reducing the local supersaturation below the threshold required for nucleation. Other sites were physically blocked by the growth of neighbouring bubbles; this inconsistent behaviour is reflected in the data shown in figures 4.22 and 4.23, where only a small number of consecutive bubble events have been recorded at each site. The data shown for sites E and F are average values for the

most common type of bubbles formed at those sites and the data for sites D are average values representing the consistent behaviour of the “bubble pump” type site.

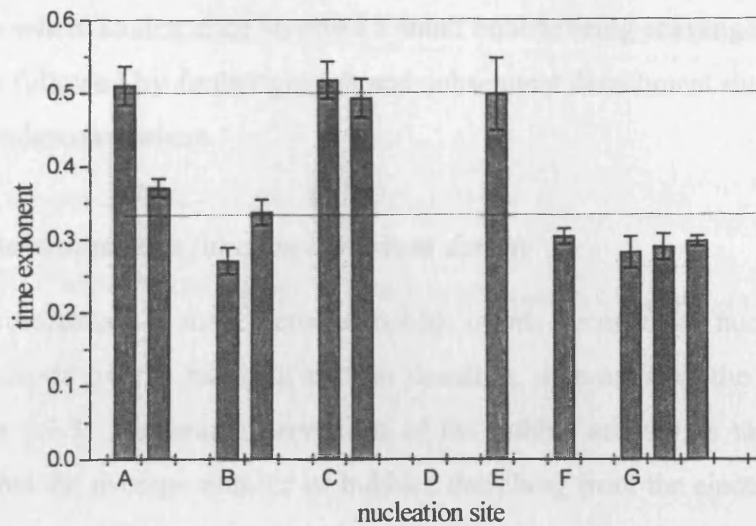


Figure 4.22 Time exponent for individual hydrogen bubbles at sites A-G on the gold electrode. The electrolyte was 0.1M HClO₄. Gas was evolved at 44 mAcm⁻² (there are no data for site D due to the rapid bubble detachment rate).

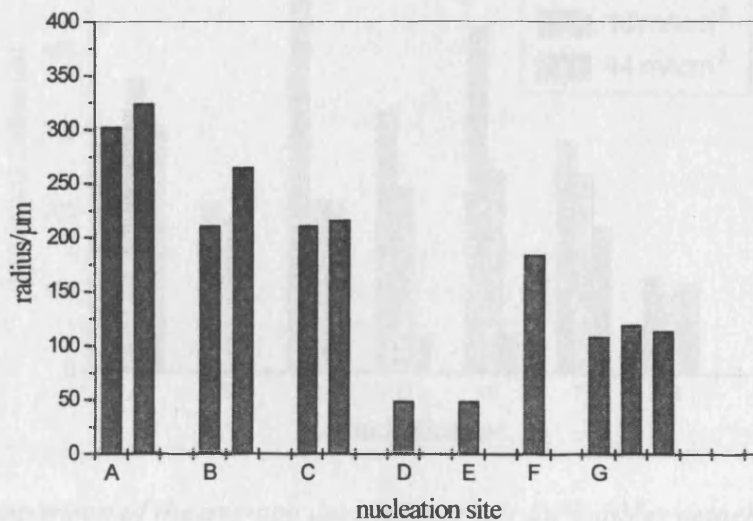


Figure 4.23 Detachment radius for individual hydrogen bubbles growing at sites A-G on the gold electrode. The electrolyte was 0.1M HClO₄. Gas was evolved at 44 mAcm⁻²

Figure 4.22 shows the time exponent for consecutive bubbles to be close to 0.33 at some sites, where the growth mechanism is predominantly “direct injection”, consistent with a surface where high nucleation activity produces a large number of bubbles that rapidly deplete the concentration of dissolved gas during growth. However, at other sites the growth mechanism

remains diffusion controlled, which is consistent with changes in local supersaturation across the surface. Figure 4.23 shows there is little variation in the detachment radius at each nucleation site. Detachment was predominantly due to coalescence with a neighbouring bubble. In cases where coalescence involved a small bubble being scavenged by a larger one, coalescence was followed by further growth and subsequent detachment due to buoyancy, or from a second coalescence event.

4.4.4 Bubble behaviour as a function of current density

In this section, comparison is made between bubble events occurring at nucleation sites A-G on the gold electrode over a range of current densities, summarising the results shown in sections 4.3.1 to 4.3.3. General observations of the bubble activity as the current density increases were that the average number of bubbles detaching from the electrode per unit area per unit time increases. The average bubble radius, residence time (reciprocal of detachment frequency) and time exponent for growth of bubbles at nucleation sites are shown in figures 4.24 to 4.26.

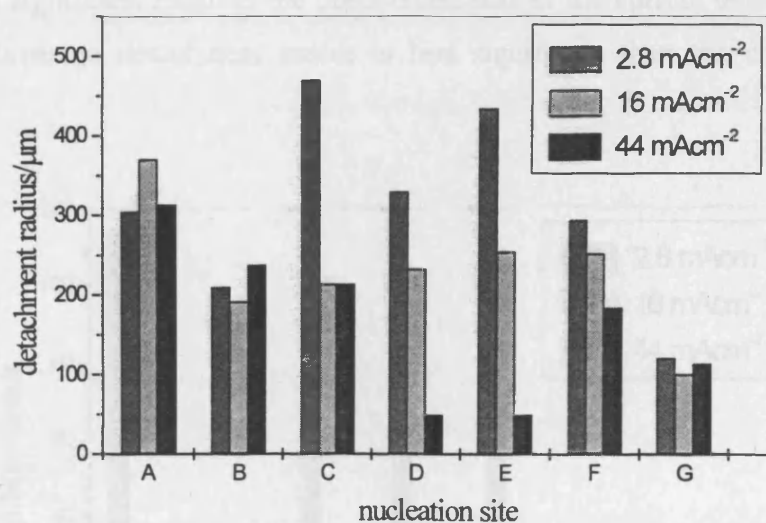


Figure 4.24 Comparison of the average detachment radii for bubbles detaching at sites A-G on the gold electrode at different current densities

Figure 4.24 shows little change in detachment size for sites A, B and G and a trend towards a decreasing detachment size at sites C, D, E and F. The detachment radius of the bubbles growing at sites A, B and G remains virtually unchanged, due to bubbles growing at these sites coalescing with the same neighbouring bubbles. The significant drop in detachment sizes of bubbles at sites D and E deviates from the general trend, and two different processes

were responsible. The average bubble detachment radius at the two sites fell sharply from 329 μm to 48 μm at site D and 433 μm to 48 μm at site E. The regime at site E was affected at the highest current density by the activation of a new nucleation site in close proximity to it, the two bubbles forming a coalescence pair significantly reducing the detachment size of the bubbles from site E. The change in behaviour of bubbles forming at site D was due to a change in the mechanism from the dominant evolution mechanism described above to a “bubble pump” mechanism, where the detachment radius is very small because virtually no growth occurs at the nucleation site prior to detachment.

In figure 4.25 the same trend can be seen for the residence time of bubbles at all of the sites, i.e. residence time decreases as current density is increased. However, there is a more significant decrease in the average residence times for bubbles at all nucleation sites during the first current increase from 2.8 mA cm⁻² to 16 mA cm⁻² which can be attributed to the large increase in the number of active nucleation sites increasing the incidences of collisions and coalescence. A further increase in the current density from 16 mA cm⁻² to 44 mA cm⁻² changes the activity at the existing nucleation sites, but does not activate a significant number of new sites. A significant result is the observation that as the current density increases, the change in the average detachment radius is less significant than the change in average residence time.

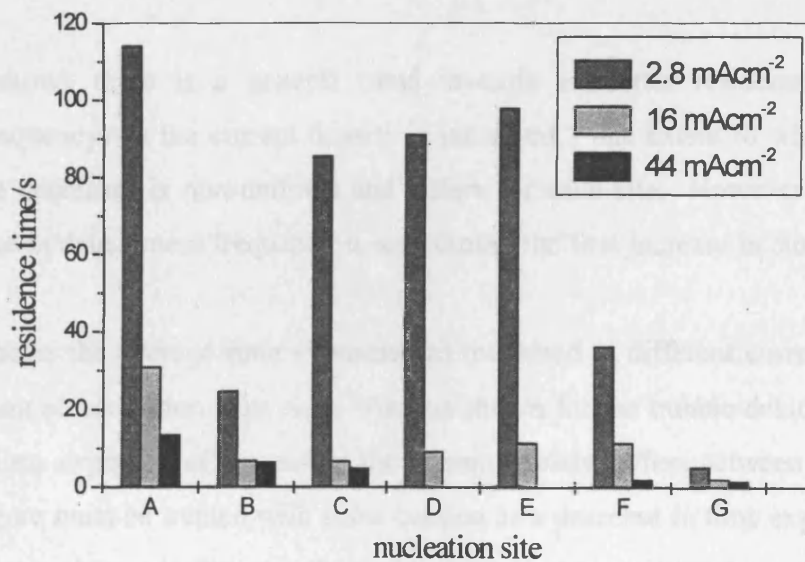


Figure 4.25 Comparison of the average residence time of bubbles during growth at sites A-G on the gold electrode at different current densities

Assuming a uniform growth rate across the electrode, for a given current density, the smaller bubbles will have, by necessity, shorter residence times. Therefore direct comparison cannot be made between the residence times at different nucleation sites. Normalising each detachment radius to unity and correcting the residence time accordingly allows direct comparison of the effect of current density on average residence times in figure 4.26 below.

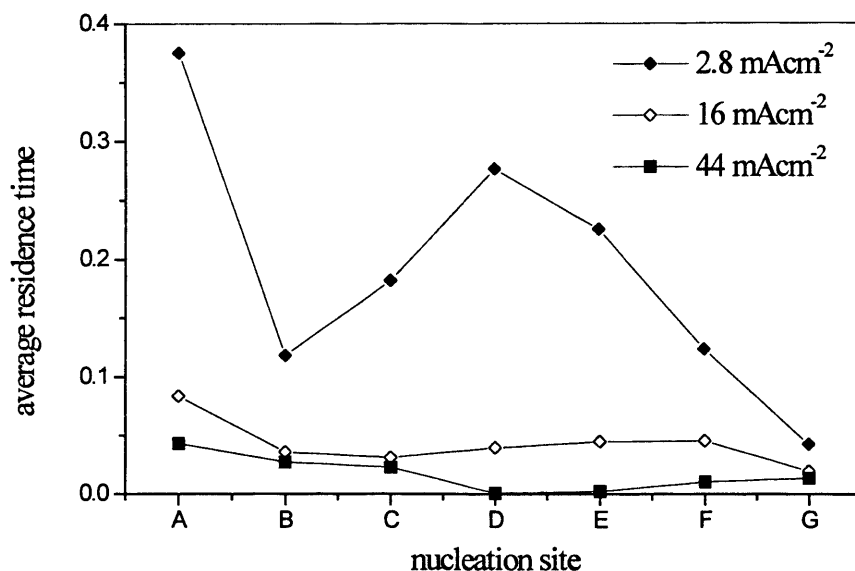


Figure 4.26 Average residence time of bubbles at nucleation sites A-G. The data has been corrected for the variation in detachment size by normalising the detachment size to unity

Figure 4.26 shows there is a general trend towards a shorter residence time (greater detachment frequency) as the current density is increased. The extent to which the average residence time decreases is non-uniform and differs for each site. However, for all sites, a greater increase in detachment frequency is seen during the first increase in current density.

Figure 4.27 shows the average time exponent (n) measured at different current densities for bubbles growing at nucleation sites A-G. As was shown for the bubble detachment size, the effect on the time exponent of increasing the current density differs between each site. The data in this figure must be treated with some caution as a decrease in time exponent from 0.5 to 0.33 signifies a change in the growth mechanism. However, it can be concluded that the averaged values indicate that the growth mechanism at sites A and E is predominantly diffusion controlled. The shift in mechanism at site C from predominantly diffusion controlled to predominantly “direct injection” type of growth mechanism, which is then reversed, is due to variations in the conditions on the electrode in terms of the number of

bubbles adjacent to the site. Generally the other sites progress from a predominantly diffusion controlled mechanism to one of “direct injection” as current density is increased.

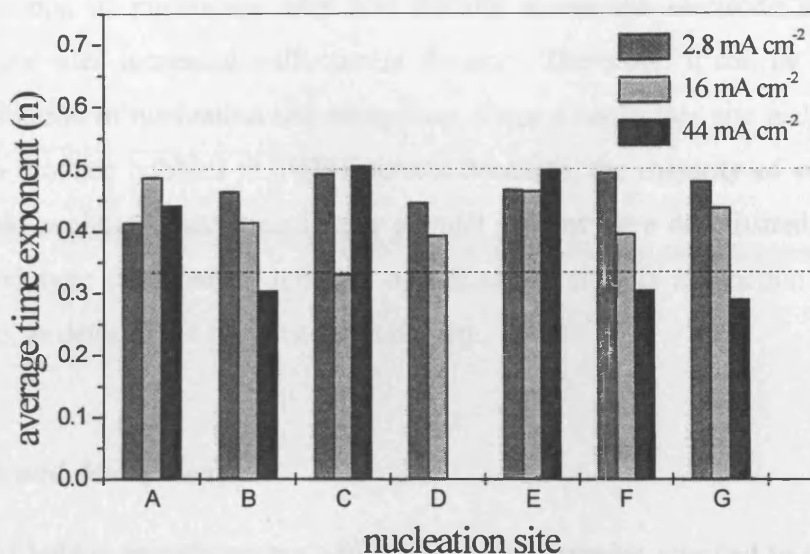


Figure 4.27 Comparison of the average time exponent (n) for bubble growth at nucleation sites A-G on the gold electrode at different current densities. The dotted lines show the values expected for diffusion controlled growth (0.5) and direct injection (0.33)

4.4.5 Conclusions

Both the number of nucleation sites and the bubble detachment frequency at existing sites increase as the average detachment size decreases. For example, at sites A-G, the average residence times were 65s, 11s and 4s and the average detachment radius was 309 μ m, 230 μ m and 165 μ m at current densities of 2.8, 16 and 44 mA cm⁻² respectively, although at any given time the area of the electrode masked by resident bubbles is greater at higher current density. The bubble growth mechanism is mainly diffusion controlled at low current densities, and non-diffusion controlled (approximating the direct injection mechanism) at higher current densities. However, the value of the time exponent is often intermediate between the two values expected for the different mechanisms, making it difficult to determine whether one is dominant.

4.4.5.1 Nucleation

The dominant evolution mechanism for bubble formation on a polished gold electrode is one where the induction time, prior to nucleation, was found to be rapid compared to the residence time. The position of nucleation sites was random across the electrode surface and the number of active sites increased with current density. Therefore, it can be concluded that there is a distribution of nucleation site energetics. Once a nucleation site had become active it continued to produce bubbles at higher current densities, the majority of which displayed the same bubble evolution mechanism; only a small percent were deactivated. In summary, the number and type (and hence activity) of nucleation sites is a function of the overall supersaturation, as determined by the current density.

4.4.5.2 Growth and detachment

The majority of bubble growth occurs whilst the bubble remains attached to the electrode at the nucleation site. The growth mechanism is independent of the bubble's growth environment in terms of its number of close neighbouring bubbles, but can be influenced by the presence of one or more large pre-existing bubbles. The growth mechanism is sensitive to fluctuations in local supersaturation, although not in the way predicted by the approximation to the "direct injection" mechanism caused by the formation of bubble clusters. Consequently, the time exponent is a useful parameter for highlighting the inhomogeneity of the concentration of dissolved gas across the surface. However, the growth mechanism cannot be predicted simply from the control of macroscopic properties, such as the current density or the position of a bubble on the surface.

The detachment mechanism is independent of the current density, with the exception of "bubble pumps", and is primarily due to the coalescence of two neighbouring bubbles, the distance between them governing the detachment radius. Although the average detachment radius decreases as a function of increasing current density, the trend at individual sites is a function of the proximity of neighbouring bubbles. The detachment frequency is more notably affected by the increase in current density; it increases significantly between the lowest and the moderate values of current density, with a less significant increase beyond that. This shows the frequency of detachment to be more sensitive to current density than the detachment size. In conclusion, it can be assumed that the overall growth rate increases with current density.

The exception to the moderate trend in current density arises from two sources, the formation of "bubble pumps" and coalescence pairs. The formation of a "coalescence pair" is caused by the activation of a very close neighbouring nucleation site that is explained by the concept of variations in localised supersaturation, producing "pockets" of high or low activity on the surface. The reason for the switch in mechanism to a "bubble pump" is unclear, although for some sites it is seen to occur after collision with a rising bubble. This would suggest that a Harvey nucleus is left behind at or near the nucleation site facilitating growth and detachment by removing the nucleation step. Alternatively it could arise from the formation of an extremely close "coalescence pair", the individual components of which cannot be resolved. A third process that was seen to cause a sudden change in the average detachment radius, was the deactivation of some nucleation sites at high current densities. This could be caused by a critical decrease in the local supersaturation. This process altered relative positions of neighbouring bubbles, new coalescence pairs were formed and the behaviour of the bubble nucleation sites involved modified.

4.5 Hydrogen evolution on platinum

As described in section 4.1.1, platinum was chosen as a "model" electrocatalytic surface. Hydrogen bubbles were evolved over a similar range of current densities as was used to generate hydrogen on the polished gold electrodes. The same three values (2.8, 16 and 44 mA cm⁻²) were chosen to highlight the behaviour of individual bubbles, but due to the electrocatalytic activity, a lower value of electrode potential was applied to the electrode. During hydrogen evolution the chemical composition of the platinum surface differs greatly from the gold, as hydrogen adsorption at the surface is more extensive. The electrolyte was 0.1 M HClO₄, the potential (vs. SCE) was held at a steady value to maintain a constant current density. The number of surface features is greater due to the coarser surface polishing (5 μm) applied to the quartz substrate used for the platinum electrode. Assuming a resolution of ± one pixel, the smallest determined radius of a hydrogen bubble evolved at the platinum electrode was 5.8 μm, a magnification of 86.28 pixels/mm. The results presented below are a representative sample of a number of different experiments; however, the same electrode has been used at different current densities, to allow direct comparison of bubble formation at specific nucleation sites. The sites chosen for further study at the platinum electrode are labelled A-H. However, it is not intended that direct comparison be made between similarly

labelled nucleation sites on the gold and platinum electrodes.

4.5.1 Specific nucleation sites for further study

The methodology described in section 4.3 was applied wherever possible to the analysis of hydrogen bubble evolution at the platinum electrode, to allow meaningful comparison of bubble behaviour at the gold and platinum surfaces. Figure 4.28 shows the platinum electrode during hydrogen evolution at the highest current density; the nucleation sites chosen for further study are circled. The dark lines shown on the left hand side of the electrode in figure 4.28 (indicated by the white arrows) are small scratches made by contact of the electrode with a glass pipette. Although caused unintentionally, the scratches are “artificial” nucleation sites, and the activity of bubbles formed on the scratches provides information about the nature of nucleation sites on the rest of the surface (see section 4.5.6.1).

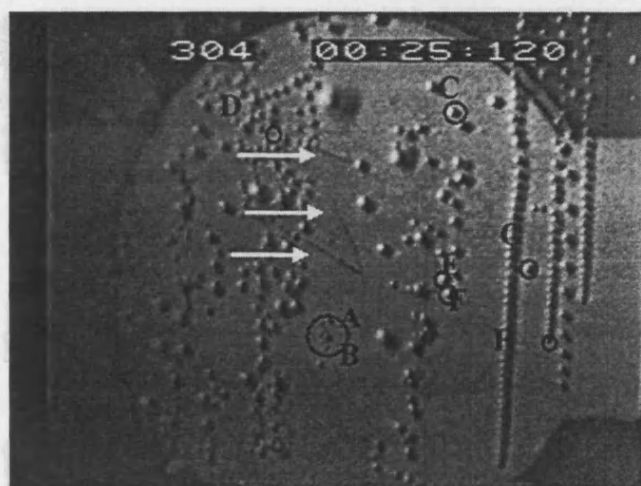


Figure 4.28 Bitmap image of the vertical platinum electrode showing the position on the electrode of sites A-H. The image shows hydrogen bubbles evolved using 0.1M HClO₄, at 44 mA cm⁻².

Comparison of figures 4.28 and 4.37, both of the same electrode surface, highlights the dominance of bubble pump type nucleation sites, in preference to bubbles that adhere to the electrode during growth. Most of the bubbles pictured in figure 4.28 do not indicate nucleation sites, because the bubbles are rising up the face of the electrode. This complicates the process of identifying individual nucleation sites. It was observed that for the platinum electrode the behaviour of bubbles at individual sites was a more complex function of current density than for the gold electrode.

Due to these difficulties, it was unfeasible to comprehensively monitor the activity of a fixed number of nucleation sites at all current densities, as shown for sites A-G on the gold electrode. A solution to this problem was to study specific nucleation sites that were representative of the activity at the surface for each current density. Some of the sites chosen were not active at all current densities. These factors are indicative of the different evolution mechanism dominating the formation of hydrogen bubbles at the platinum electrode, compared to the less electrocatalytic gold electrode.

4.5.2 Results for a low current density

Figure 4.29 shows the typical distribution of nucleation sites on a platinum electrode at a current density of 2.8 mA cm^{-2} . The bubbles seen vertically above the circled sites in figure 4.29 indicate bubbles rising up the face of the electrode, not nucleation sites. There are approximately 10 active sites, a smaller number than observed for the gold electrode (figure 4.15) and large regions of the surface are inactive.

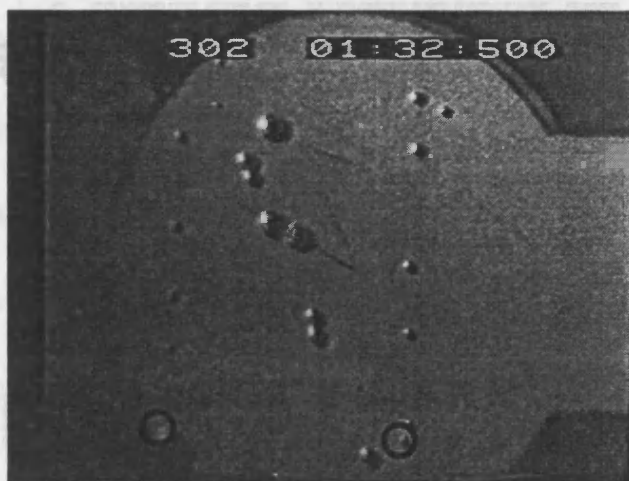


Figure 4.29 Bitmap image of the vertical platinum electrode showing the distribution of nucleation sites over the surface. The circled sites are "bubble pumps". The electrolyte was 0.1 M HClO_4 ; hydrogen gas was evolved at 2.8 mA cm^{-2} .

The data acquired for successive hydrogen bubbles evolved at nucleation sites A-D on the platinum electrode at 2.8 mA cm^{-2} are displayed in figures 4.30, 4.31 and 4.32. The format of these figures is the same as that described in section 4.3. Figure 4.30 gives the detachment radius of successive bubbles, which falls between 100 and 225 μm , the variation in detachment radius at individual nucleation sites is small compared with the variation between sites.

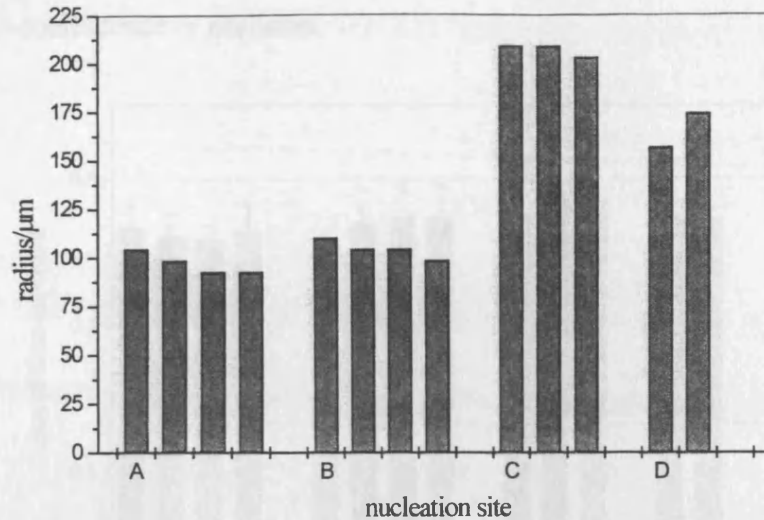


Figure 4.30 Detachment radius for individual hydrogen bubbles growing at sites A-D on the platinum electrode. The electrolyte was 0.1M HClO₄. Gas was evolved at 2.8 mA cm⁻²

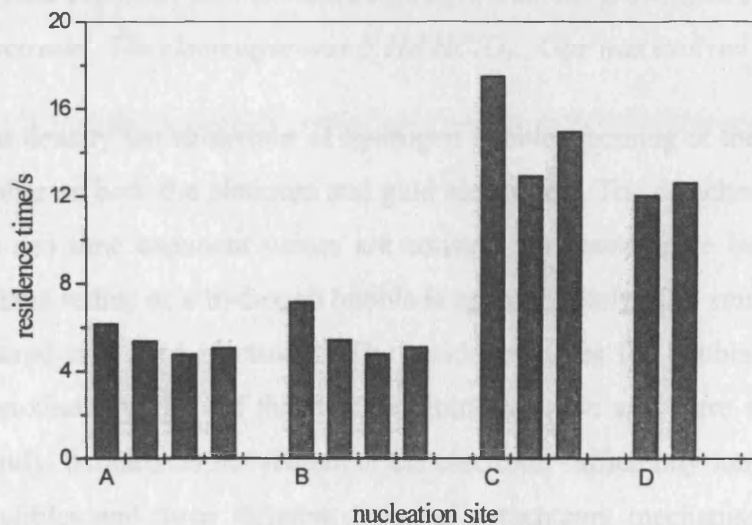


Figure 4.31 Bubble residence time for individual hydrogen bubbles growing at sites A-D on the platinum electrode. The electrolyte was 0.1M HClO₄. Gas was evolved at 2.8 mA cm⁻².

The dominant mechanism for all of the nucleation sites is one where the bubbles remain at the nucleation site during growth, and the growth is diffusion limited as shown in figure 4.32. The bubble residence time prior to detachment (see figure 4.31) is included for each current density, as the time exponent value (see figure 4.32) was unattainable for the “bubble pump” sites where virtually no bubble growth occurs at the nucleation site. Bubbles at sites A and B grow in close proximity forming a “coalescence pair”: hence the short residence times. The dominant detachment mechanism of bubbles forming at site B is forced collision with bubbles

rising from below, whereas the bubbles at site D detach under buoyancy as an individual bubbles without coalescence or collision.

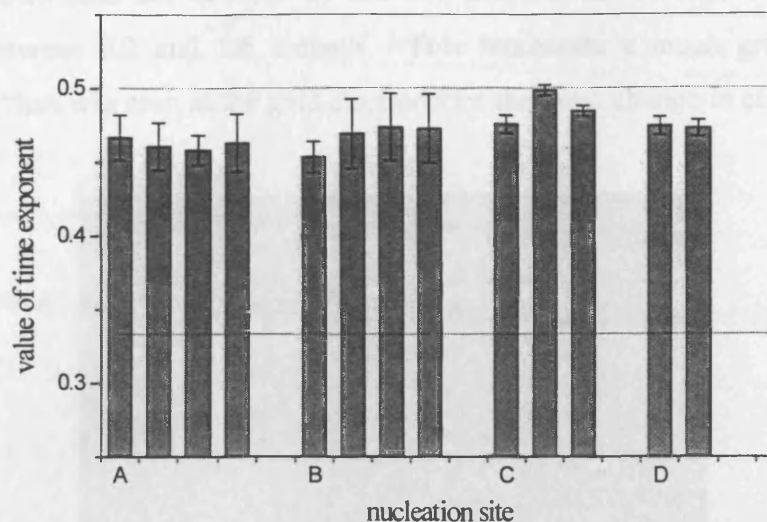


Figure 4.32 Time exponent for individual hydrogen bubbles growing at sites A-D on the platinum electrode. The electrolyte was 0.1M HClO₄. Gas was evolved at 2.8 mA cm⁻²

At a low current density the behaviour of hydrogen bubbles forming at the active nucleation sites is very similar on both the platinum and gold electrodes. The detachment radius, bubble residence times and time exponent values are constant for consecutive bubble events. The average detachment radius of a hydrogen bubble is approximately 50% smaller on a platinum electrode compared to a gold electrode. The residence times for bubbles on the platinum surface are approximately 10% of those at the gold electrode and there are only 10 active sites. Significantly, bubbles do not remain at the electrode sufficiently long to coalesce with neighbouring bubbles and three different types of detachment mechanism were observed; detachment due to buoyancy, collision and the "bubble pump" mechanism.

4.5.3 Results for a moderate current density

Figure 4.33 shows the typical nucleation site distribution on a platinum electrode for hydrogen evolution at 16 mA cm⁻². The number of sites has increased to approximately 35. However, there remain large regions on the surface where there are no active sites. The circled areas consist of "bubble pump" sites: in some areas these are clustered together, in other areas the sites are isolated. As described in section 4.5.1 the bubbles seen vertically above the circled sites are rising up the face of the electrode. The data acquired for successive hydrogen bubbles evolved at nucleation sites A-H (see figure 4.28) are given in figures 4.34-4.36.

Sites E-H were inactive at the lower current densities. The activity at site D was inconsistent at 16 mA cm^{-2} and no representative data could be collected. Figures 4.34 and 4.35 show the average detachment radii fall between 40 and $100 \mu\text{m}$, and the average residence time has decreased to between 0.2 and 1.6 seconds. This represents a much greater increase in detachment rate than was seen at the gold electrode for the same change in current density.

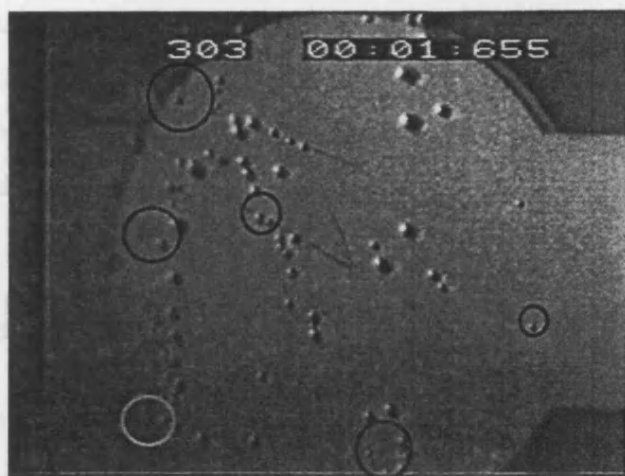


Figure 4.33 Bitmap image of hydrogen bubbles evolved on the vertical platinum electrode using 0.1 M HClO_4 , at a current density of 16 mA cm^{-2} .

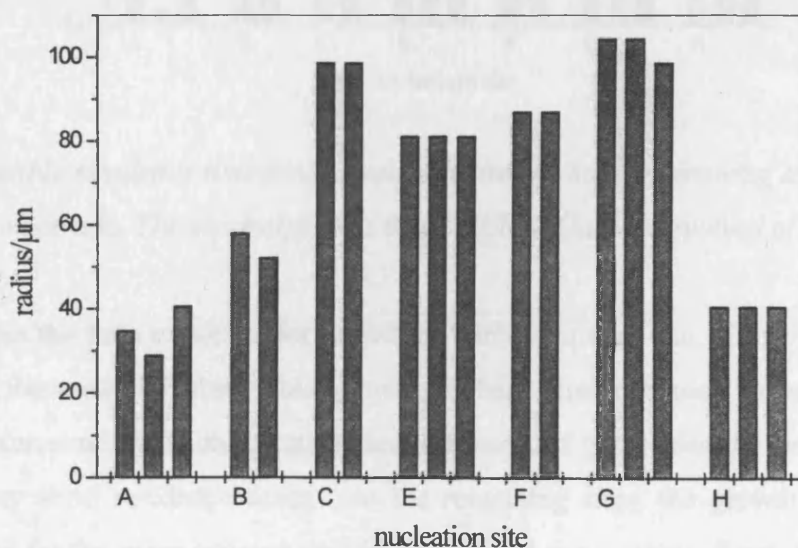


Figure 4.34 Detachment radius for individual hydrogen bubbles growing at sites A-H on the platinum electrode. The electrolyte was 0.1 M HClO_4 . Gas was evolved at 16 mA cm^{-2} .

The behaviour at sites A, B and C remains consistent, despite a significant change in their growth environments. Two new nucleation sites are activated at “satellite” positions around sites A and B forming a cluster. Bubbles in the new cluster coalesce to form two medium sized bubbles that detach from sites A and B at regular intervals. Site C retains its activity where bubbles maintain the “adhere and grow” type mechanism. However, the detachment mechanism becomes one of forced detachment due to collision with a rising bubble. Of the new sites, E and F are a coalescence pair and similar in behaviour to A and B, whereas bubbles at site G display an “adhere and grow” type mechanism, similar to site C. Site H is a “bubble pump” and the very regular bubble evolution cycle of bubbles formed at it (in terms of detachment size and rate) is characteristic behaviour of this type of site.

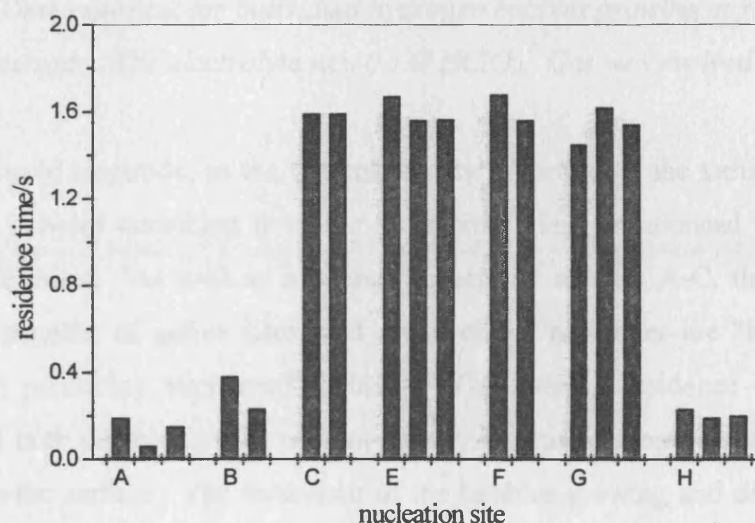


Figure 4.35 Bubble residence time for individual hydrogen bubbles growing at sites A-H on the platinum electrode. The electrolyte was 0.1M HClO₄. Gas was evolved at 16 mA cm⁻².

Figure 4.36 gives the time exponent for growth of bubbles at each site. There are no data for sites A and B, because the observable growth at these sites occurred by coalescence and scavenging of surrounding bubbles rather than diffusion of gas across the bubble interface, resulting in very short residence times. At the remaining sites, the growth mechanism is diffusion limited for the more isolated sites (C and G) and approaching direct injection for the coalescence pair (E and F). It is apparent that the detachment radius and residence time cannot be used in isolation to predict the growth mechanism. However, figures 4.34 and 4.35 clearly show the parameters grouped into two sets; bubbles growing at sites A, B and H, have different characteristics to bubbles growing at sites C, E, F and G.

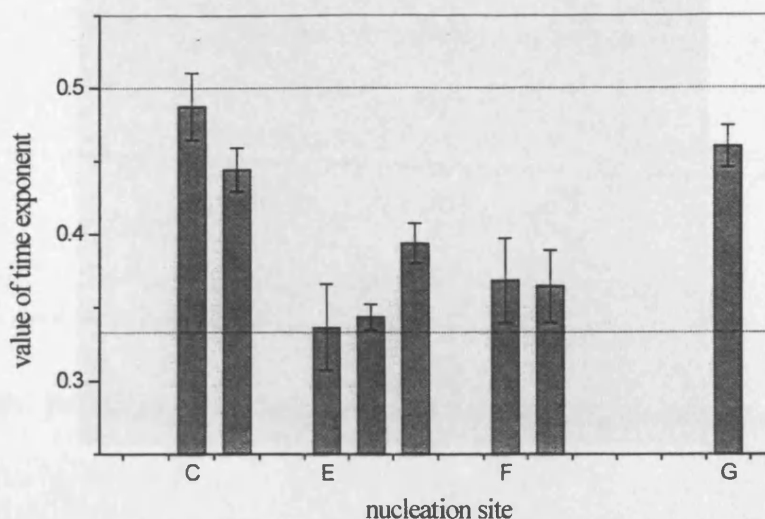


Figure 4.36 Time exponent for individual hydrogen bubbles growing at sites A-G on the platinum electrode. The electrolyte was 0.1M HClO₄. Gas was evolved at 16 mA cm⁻²

As seen for the gold electrode, as the current density is increased, the variation in behaviour for consecutive bubbles detaching from the same site is less pronounced than the variation between different sites. As well as a change in activity at sites A-C, there is a four-fold increase in the number of active sites, and many of the new sites are “bubble pumps” or clusters of sites producing very small bubbles. The average residence time and average detachment size both decrease as the current density increases. Some bubbles are formed at the scratches on the surface. The behaviour of the bubbles growing and detaching from this area has no marked difference, in terms of detachment size and frequency from any other area on the electrode despite the difference in magnitude of the nucleation site. Due to the rapid evolution cycle of bubbles formed at all the sites it is difficult to establish whether there is consistent activity of an individual site or whether some intermittent deactivation occurs.

4.5.4 Results for a high current density

The activity of hydrogen bubbles at the highest current density (44 mA cm⁻²) is more complex than was seen for lower current densities and significantly different from the behaviour of hydrogen bubbles on the gold electrode. Figure 4.37 shows the initial distribution of nucleation sites very soon after the application of current to clearly indicate the most active sites on the platinum electrode.

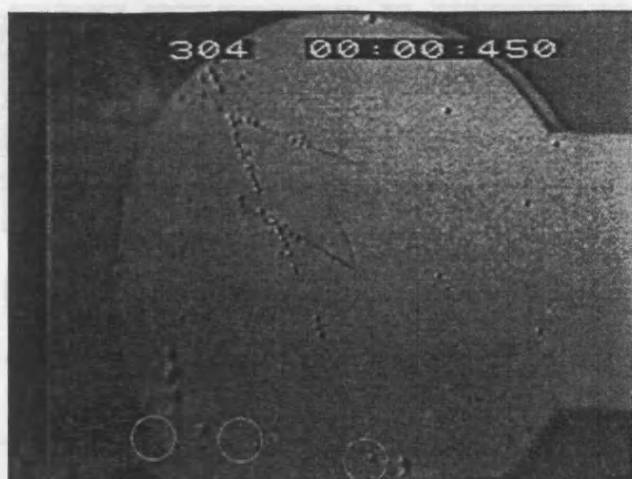


Figure 4.37 Bitmap image of the vertical platinum electrode showing the position of nucleation sites on the surface. The image shows hydrogen bubbles evolved using 0.1M HClO_4 , at the highest current density used, 44 mA cm^{-2}

The circled areas indicate clusters of “bubble pumps” with high detachment frequencies. The figure shows a line of small bubbles at nucleation sites that lie diagonally across the two parallel scratches. This line highlights an array of highly active sites, with very short induction times. Bubbles have nucleated at these sites in preference to the visible scratches. As nucleation sites were distributed randomly across the electrode at the lower current densities, the appearance of a line of nucleation sites is an anomaly. Therefore, it is feasible that the nucleation sites have been formed by a very fine scratch on the electrode, with a few microns diameter not visible at this magnification. The lower activation energy required to form bubbles at the smaller scratch indicates that the larger surface feature is not a preferential nucleation site and therefore effectively inactive at higher current densities.

Comparison of figure 4.37 with figure 4.28 (showing detached bubbles) highlights the difficulty in obtaining data for individual bubbles. Typically, the bubbles stream off the electrode in single lines as seen at site H, or in wide bands, shown on the left side of figure 4.28. The method of detachment is primarily by collision with rising bubbles on the left side of the electrode. However, the behaviour at site H remains very consistent, the detachment size is very small, and growth of the bubbles occurs after they have detached as they rise up the face of the electrode.

There is a cluster of sites around sites A and B, where a complex mechanism of coalescence causes the irregular detachment of small bubbles.

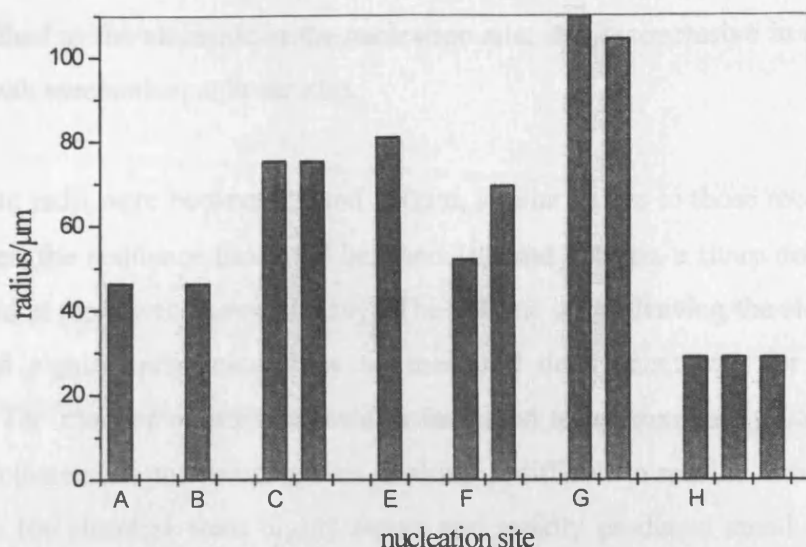


Figure 4.38 Detachment radius for individual hydrogen bubbles growing at sites A-H on the platinum electrode. The electrolyte was 0.1M HClO₄. Gas was evolved at 44 mAcm⁻²

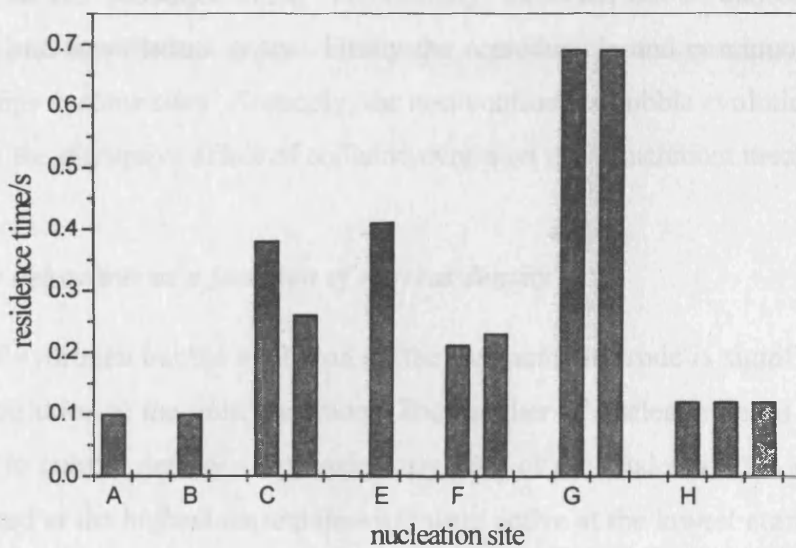


Figure 4.39 Bubble residence time for individual hydrogen bubbles growing at sites A-H on the platinum electrode. The electrolyte was 0.1M HClO₄. Gas was evolved at 44 mAcm⁻².

The bubbles forming at site G retain the “adhere and grow” type mechanism. The detachment mechanism of bubbles at sites C, E and F is due to collision with moving bubbles. The activity of bubbles forming at sites A, B and H remains unchanged from that seen at 16 mA cm⁻²: “bubble pump” type activity and other complex growth patterns such as scavenging and coalescence of bubble clusters means there are no data for the time exponent for bubbles

growing at these sites. The data shown are for the sites where growth occurs whilst the bubble is attached to the electrode at the nucleation site; it is inconclusive in determining the dominant growth mechanism at those sites.

The detachment radii were between 20 and 100 μm , similar values to those recorded at 16 mA cm^{-2} . However, the residence times fall between 100 and 700 ms, a sharp decrease from the values recorded at the lower current density. The volume of gas leaving the electrode per unit time increased significantly, caused by an increased detachment rate for the same size distribution. The number of active sites also increased to approximately 65, with the new sites forming clusters around existing sites, making it difficult to resolve individual bubbles. The new sites (or clusters) were highly active and rapidly produced small bubbles, which coalesced several times before detaching, often scavenging surrounding bubbles, and so modifying the behaviour of the existing sites significantly. The “bubble pump” sites were very stable and any deactivation was temporary, with the normal activity resumed very quickly. The number of collisions between stationary and rising bubbles increased, obviously a factor in the shorter residence times. In summary, the behaviour of bubbles at the surface was separated into two distinct types. Firstly the reproducible and continuous behaviour of the bubble pumps at some sites. Secondly, the non-continuous bubble evolution cycle at other sites caused by the disruptive effect of collision events on the detachment mechanism.

4.5.5 Bubble behaviour as a function of current density

The activity of hydrogen bubble evolution on the platinum electrode is significantly different to hydrogen evolution at the gold electrode. The number of nucleation sites differs, as does their response to current density. Approximately 16% of the total available sites (defined as number activated at the highest current density) were active at the lowest current density, and approximately 50% active at the moderate current density. Due to the faster bubble detachment rates, the platinum electrode is a more dynamic surface compared to gold in terms of the rate of fluctuation of the surface conditions. Bubbles detach at a smaller size, meaning at any given time there is a smaller volume of gas bubbles attached to the platinum electrode. This is an important indicator of the efficiency of the electrode in terms of bubble evolution and will be addressed again in Chapter 5.

Figures 4.40-4.42 show the average detachment radii and residence times of nucleation sites A-H (as shown in figure 4.28) at the platinum electrode at the three different current densities.

Comparison can be made between the activity of bubbles at nucleation sites A, B and C at 3 different current densities. Both parameters show a trend of decreasing magnitude as the current density is increased.

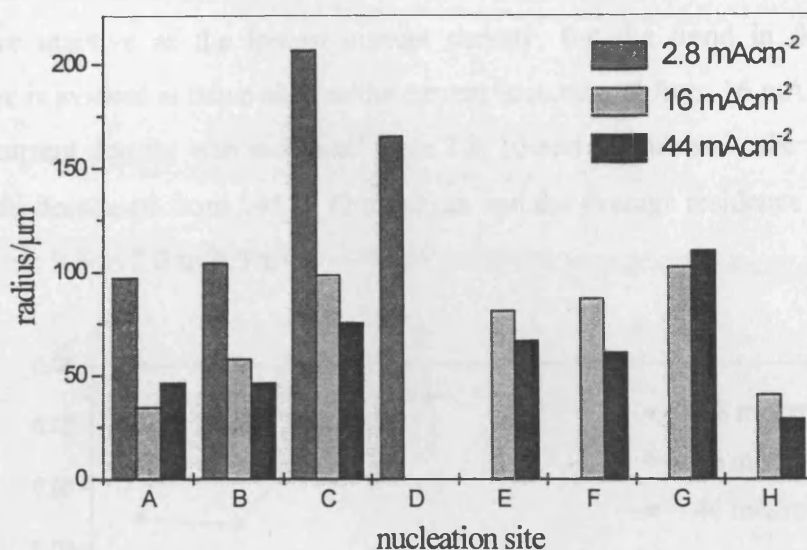


Figure 4.40 Average bubble radius for individual hydrogen bubbles detaching at sites A-H on the platinum electrode shown in figure 4.2.8 at different current densities.

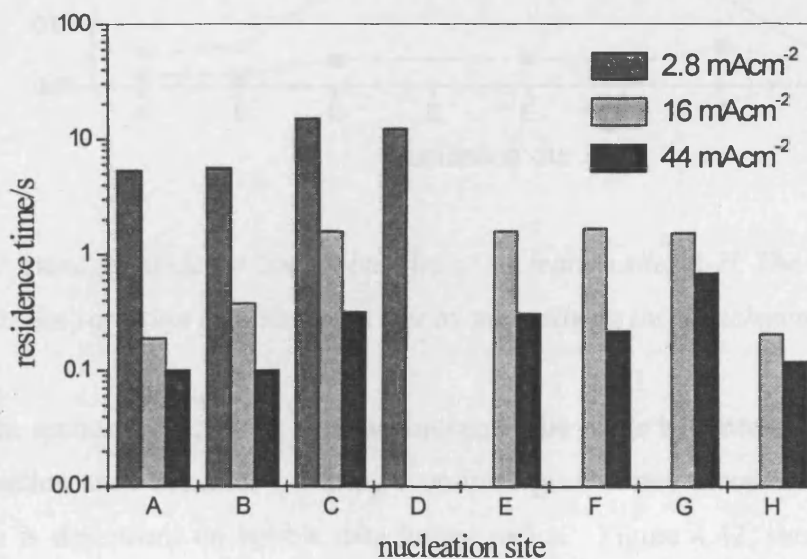


Figure 4.41 Average bubble residence time for individual hydrogen bubbles detaching at sites A-H on the platinum electrode shown in figure 4.2.8 at different current densities.

The logarithmic scale used for the residence time in figure 4.41 emphasises that the decrease in magnitude of this parameter is more significant than the decrease in magnitude of the average detachment radius. For example, increasing the current density from 2.8 mA cm⁻² to

16 mA cm⁻² causes a 2-fold decrease in detachment radius at site C, and a corresponding 20 fold decrease in residence time.

There are no data for site D at the higher current densities because the site was deactivated. Sites E-H were inactive at the lowest current density, but the trend in detachment rate described above is evident at these sites as the current is increased from 16 mA cm⁻² to 44 mA cm⁻². As the current density was increased from 2.8, 16 and 44 mA cm⁻², the average bubble detachment radii decreased from 143 to 72 to 62 μm and the average residence time decreased significantly from 9.6 to 1.0 to 0.3 s.

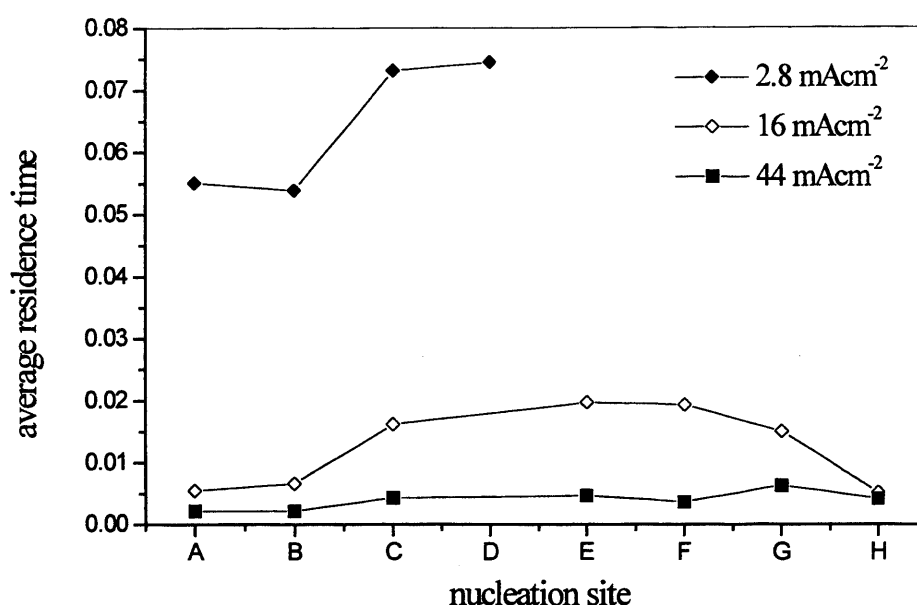


Figure 4.42 Average residence time of bubbles at nucleation sites A-H. The data has been corrected for the variation in detachment size by normalising the detachment size to unity.

As described in section 4.3.4, direct comparison cannot be made between residence times at different nucleation sites because, assuming a uniform growth rate across the electrode, the residence time is dependent on bubble detachment radius. Figure 4.42, showing residence times for normalised detachment radii, is equivalent to figure 4.20 for the gold electrode. The average residence time is seen to decrease as current density is increased; the extent to which this occurs differs between each nucleation site. However, at sites A, B and C, the initial decrease from 2.8 mA cm⁻² and 16 mA cm⁻² is much greater than the subsequent decrease from 16 mA cm⁻² and 44 mA cm⁻².

4.5.6 *Conclusions*

Several mechanisms for bubble evolution were observed on the platinum electrode, each strongly correlated to the nucleation site characteristics from which bubbles were formed. The dominance of a particular evolution mechanism, and hence type of nucleation site, shifted with the change in current density. This observation highlights the complex relationship between nucleation activity and supersaturation at the platinum electrode. The behaviour of consecutive bubbles nucleating at individual sites was not always consistent for a given current density. An exception was the “bubble pump” sites, whose bubble evolution regimes were very stable. The dominant growth mechanism and method of detachment varied both between sites and as a function of current density at individual sites. The mechanism at the most active sites observed at the lowest current density (A-D) was one in which the bubbles nucleated quickly, and in which growth was diffusion limited and occurred whilst the bubble was attached to the electrode at the nucleation site; this is termed an “adhere and grow” type mechanism.

4.5.6.1 *Nucleation*

Nucleation at all sites was rapid compared to the residence time. The number of nucleation sites on the surface increased gradually as a function of current density, which would suggest a wide range of nucleation activities. However, many of the high activity sites that produced bubbles at low supersaturation were inactive at the higher current densities. The sites active at the higher current densities were predominantly bubble pumps and coalescence pairs, very efficient sites, in terms of the higher bubble detachment rates, producing large numbers of small bubbles. The position of nucleation sites changed from random isolated sites to clusters as the current density increased, leaving significant regions of the surface inactive. The visible scratches on the surface were effective nucleation sites at the lowest supersaturation but deactivated at higher current densities. The behaviour of the smaller scratches was reversed, as they were preferential nucleation sites at higher supersaturation, which suggests that the dimensions of a nucleation site are a factor in its activity. Because of the small average detachment size, bubbles covered only a small percentage of the surface. This phenomenon of small bubbles detaching from bubble clusters was a defining feature of the platinum electrode. In contrast, the gold electrode produced larger bubbles from nucleation sites distributed randomly across the electrode surface.

4.5.6.2 *Growth and detachment*

The growth environment of bubbles in terms of the number of close neighbours changed markedly due to the formation of clusters. This modification to existing sites, as the energy input increased, increased the efficiency of the detachment mechanism at some sites and caused others to be deactivated. There was some evidence of a “switching” mechanism on the surface, where a certain type of nucleation sites was activated or “switched on” once a threshold in the supersaturation had been surpassed. The behaviour at nucleation site H is typical of this mechanism. The area of the electrode where site H is situated was inactive at the lowest current density. The site “switched on”, evolving bubbles in a rapid bubble pump type mechanism, as the current density increased and its activity then remained constant, independent of further increases in current density.

Due to the high number of “bubble pump” sites on the surface whose detachment rate and size were beyond the resolution of the recording equipment in terms of the frame capture rate and magnification, it was difficult to collect data for the time exponent variable and analyse the growth mechanism. Typically nucleation sites displayed the “adhere and grow” type mechanism at the lowest current density (for example sites A-D) where the growth was diffusion-controlled. Sites E and F, that were only activated at higher current densities, grew in very close proximity to each other as a “coalescence pair”, where the growth mechanism was observed as approximating the direct injection mechanism. Generally, the time exponent was not useful as a diagnostic variable under the experimental conditions used to measure the formation of hydrogen bubbles at the platinum surface.

Several detachment mechanisms were observed and the dependence of each on the current density varied. The number of collision events resulting in the forced detachment of a stationary bubble increased as the number of rising bubbles increased, so the dominance of this detachment mechanism increased with current density. Detachment occurred by either the coalescence of two close neighbouring bubbles (as for sites A and B), buoyancy forces overcoming surface tension (seen at site C), or by collision between stationary and rising bubbles (as seen for site D). The decrease in detachment size is less significant for bubbles growing at nucleation sites where the detachment mechanism is by coalescence with a close neighbour (as seen for sites E and F) or from a “bubble pump” (as seen for site H).

Summarising these factors, a “two-site” model may be appropriate for describing the activity at the surface. In this model the active nucleation sites, dominant at lower current densities,

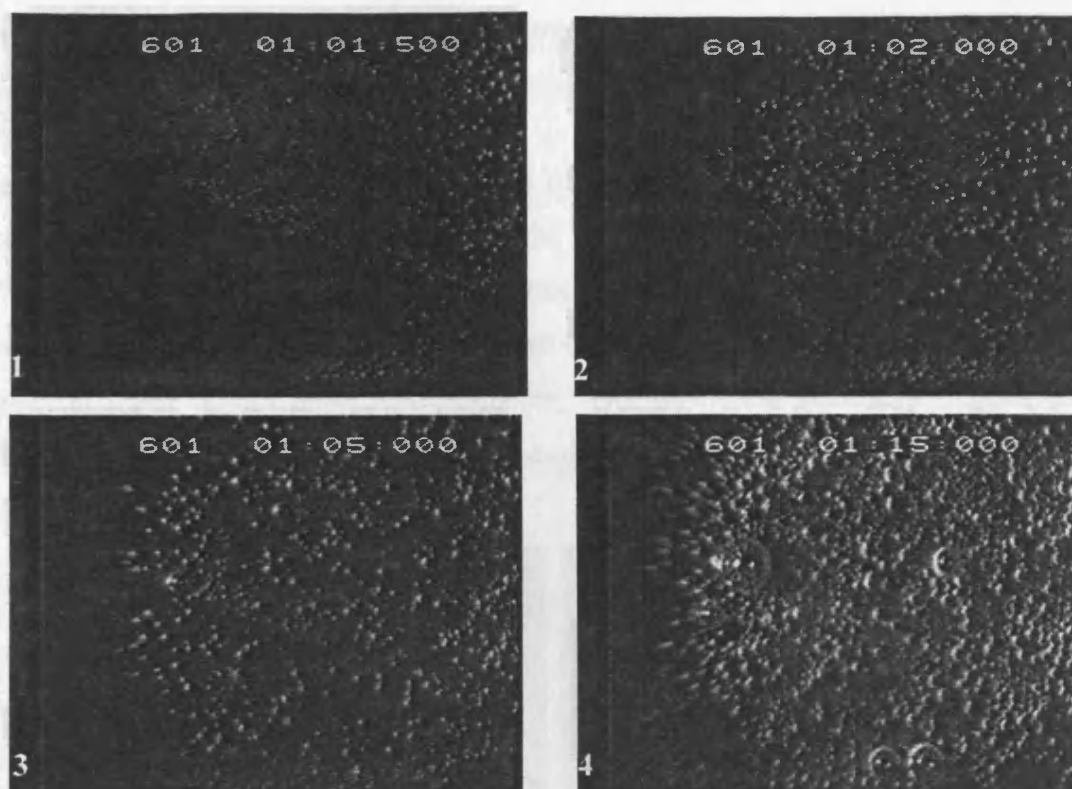
are predominantly of the “adhere and grow” type, with the activity switching to predominantly “bubble pump” type sites with faster evolution kinetics at higher current densities. This effect, produced by two broadly different types of nucleation site, can be observed using other techniques and will be discussed in more depth in chapter 6.

4.6 Chlorine evolution on RTO

The electrode comprised a polished quartz electrode substrate coated with gold and further coated with a thin layer of RTO, according to the method described in section 3.2.3 (which approximates the manufacturing process used industrially). During the preparation of the RTO surface, the electrode is fired at a high temperature, causing the surface to crack, forming deep narrow fissures. This causes the number of surface features on the RTO electrode to be greatly enhanced compared to the platinum or gold electrodes, as shown in figure 3.6. Analogous to the platinum/hydrogen system, the RTO surface is highly electrocatalytic for chlorine evolution, and there is extensive adsorption of chlorine at the surface although this is not discussed at a molecular level here.

4.6.1 *Distribution of nucleation sites*

The electrode was placed in a vertical orientation and chlorine bubbles were evolved from acidified 5M NaCl, which is a comparable composition to the electrolyte used in chlor-alkali cells. Figure 4.44 shows four frames of an RTO electrode captured during a cyclic voltammetry experiment. Chlorine bubbles were generated by cycling the electrode potential between 0 and 1.6 V vs. SCE, at 20 mV s⁻¹. The measured current density was 57 mA cm⁻², 60 mA cm⁻², 88.5 mA cm⁻² and 179 mA cm⁻² (frames 1 to 4). The magnification was 121.4 pixels/mm; assuming a resolution of ± one pixel, the smallest determined radius of a chlorine bubble evolved at the electrode was 4.1 μm. Bubble radii on the surface were in the range of 4.1 μm to 270 μm, although the majority were less than 60 μm. There is very high surface area coverage by bubbles, masking a large percentage of the electrode. There is a marked absence of “bubble pump” type evolution, as the majority of bubbles shown in figure 4.44 adhered to the electrode.



1000 μm

Figure 4.44 Chlorine bubbles evolved from acidified 5M NaCl on a RTO electrode. Each frame shows bubbles evolved at different current densities, increasing from 57 mA cm^{-2} to 179 mA cm^{-2} in frames 1 to 4.

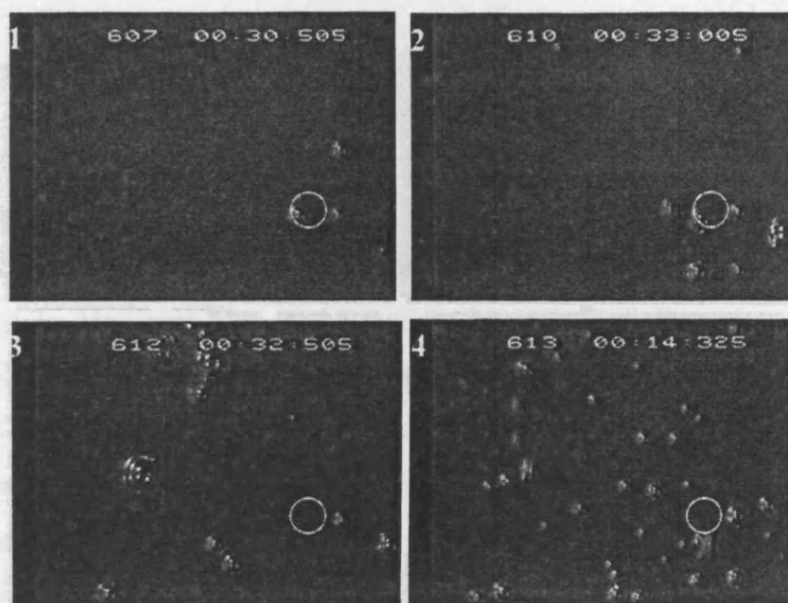
Figure 4.44 shows that the nucleation sites on the RTO electrode are relatively evenly distributed, which contrasts with the gold and especially platinum electrodes at which the nucleation sites formed in clusters. The conditions of supersaturation are different during cyclic voltammetry. Therefore, in order to correlate the behaviour of chlorine bubbles with the behaviour of hydrogen bubbles on the gold and platinum surfaces, individual chlorine bubbles were studied under conditions of constant current. Hence the effect of the electrode composition on the bubble evolution process was compared for equivalent operating conditions.

4.6.2 Chlorine evolution as a function of current density

Due to the high level of bubble activity at the surface and the poor resolution of individual bubble radii in figure 4.44, chlorine bubbles were evolved at lower current densities to allow resolution of individual events. The magnification was increased to 171.2 pixels/mm, enabling approximately 40% of the electrode surface to be studied during one experiment.

Assuming a resolution of \pm one pixel, the smallest determined radius of a chlorine bubble evolved at the electrode was $2.9 \mu\text{m}$.

Data were collected for a 9.8 mm^2 section of the RTO electrode. This was assumed a representative sample of the surface due to the even distribution of nucleation sites. Figure 4.45 shows the distribution of bubbles growing on one section of the electrode at different current densities. All the bubbles shown are stationary, with the exception of the blurred bubbles in frame 4 indicating rising bubbles. Not all of the stationary bubbles indicate nucleation sites as would be expected, this phenomenon is explained in section 4.5.3.



1000 μm

Figure 4.45 Chlorine bubbles growing on the RTO electrode at the four different current densities, 18, 22.4, 32 and 56 mA cm^{-2} in frames 1 to 4 respectively. The electrolyte was acidified 5M NaCl

The studies for hydrogen evolution at both the gold and platinum electrodes focused on the behaviour of bubbles evolving at individual sites as a function of current density. Wherever possible the same methodology was applied to the study of chlorine bubbles evolving at RTO. However, at the lowest threshold required for bubble nucleation, approximately 18 mA cm^{-2} , there was very limited activity on the electrode, with eight bubble growth sites active in the selected area, only one of which (shown circled in figure 4.45) was consistently active as the current density was increased. This behaviour was typical of other sites across the surface and consequently it was not possible to monitor the same individual nucleation sites as a

function of current density. The results presented in these sections provide a qualitative description of events at the electrode, summarising the data collected for all the active sites. Individual bubble events are used to provide examples but are not the focus of the study, as was the case for the hydrogen/gold and hydrogen/platinum systems.

Bubble behaviour was monitored over a range of current density values, four of which (18, 22.4, 32 and 56 mA cm⁻²) were chosen to highlight the different modes of behaviour of individual bubbles. A current density of 56 mA cm⁻² was chosen as the upper limit because as it was increased above this value, the coverage of the electrode with bubbles increased to such an extent as to make the identification of individual nucleation sites difficult.

4.6.3 *Nucleation*

The evolution of chlorine bubbles on the RTO surface is a very dynamic phenomenon caused by the random activity of nucleation sites. At the lowest current density required to produce bubbles, very few sites are active but this number increases gradually with current density as shown in table 4.3. However, due to the random behaviour of these sites, they are not all simultaneously active and this suggests there is a large distribution of nucleation site activities. The same regions of the electrode remain active and produce bubbles, but not necessarily consecutively from the same point on the surface. For example, as the current density is changed, the point of nucleation can move up to 100 μm from the original site. As the current density is increased beyond the range quoted above, the number of nucleation sites continues to increase, and the activity becomes increasingly random, with individual sites being deactivated and reactivated throughout the course of one experiment. The four frames in figure 4.44 show how the number of bubbles on the electrode increases rapidly with increasing supersaturation. At the lower values of current density, the even distribution of the sites meant many are isolated and bubble pairs only form at the higher values of current density, upwards from 32 mA cm⁻². There are no “bubble pump” type of nucleation sites observed at any value of current density.

The very large number of active nucleation sites with a range of activities, is feasible due to the irregular surface morphology of the RTO electrode. Preferential nucleation occurs on a small number of sites at very low current densities, but the behaviour changes at higher current densities, upon which active nucleation sites cover the entire electrode and nucleation can occur at any point on the surface, making the concept of specific nucleation sites

meaningless. This is very different to the two-site model proposed for a platinum electrode, where a fixed number of active sites were present at lower current densities and the lower activity sites were switched on as the current density reached the required value. The RTO surface produces a multi-site model where the nucleation sites are more sensitive to changes in current density and individual sites are gradually activated as the current density increases. A much higher current density is required to activate all the sites. This is possibly due to long induction times and suggests nucleation is the rate-limiting step. The nucleation rate of the low activity sites was higher than for the high activity sites.

4.6.4 Growth and Detachment

The time exponent was measured for individual bubbles at sites distributed across the electrode, and the values varied between values of 0.5 and 0.33, the thresholds expected for diffusion limited and direct injection growth mechanisms. These were the only mechanisms available for bubble growth as there were no occurrences of growth by a scavenging mechanism. The average values of the time exponent for two nucleation sites at which consecutive bubbles formed regularly at all values of current density are shown in figure 4.46 below. The figure shows there is no significant trend at either site A or B as the current density is increased, and neither the direct injection mechanism or diffusion limited growth is the dominant mechanism as the value of the time exponent is intermediate between the two threshold values of 0.33 and 0.5.

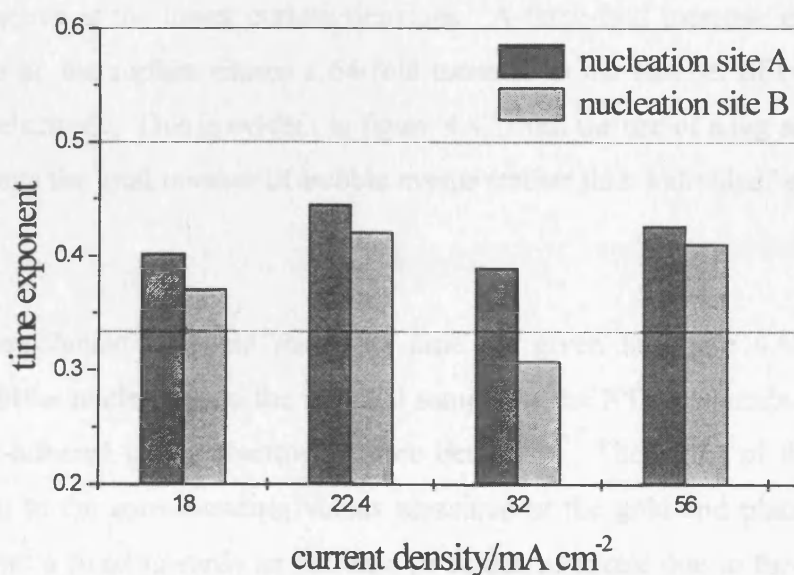


Figure 4.46 Average values of the growth time exponent for chlorine bubbles evolved from two consistently active nucleation sites on the RTO electrode at different current densities

Due to the absence of “bubble pump” type nucleation sites, the majority of growth occurred whilst bubbles were attached to the electrode. However, for many bubbles the growth site was in a different location to the point where nucleation occurred. This occurred by a process where bubbles detached and started to rise up the face of the electrode before re-adhering to the surface to continue growth. The extent to which this occurred at different current densities on the selected 9 mm² area of the RTO electrode, including the number of nucleation sites is given in table 4.3 and figure 4.47.

Current density mA cm ⁻²	Number of active nucleation sites	Number of rising bubbles per minute		
		Passing across the face of the electrode	Adhering to the electrode	Colliding with stationary bubbles
18.0	8	7	2	3
22.4	10	37	6	12
32.0	18	130	4	32
56.0	25	450	12	138

Table 4.3 Data for nucleation site activity for chlorine bubble evolution with varying current density for the 9 mm² section of the RTO electrode shown in figure 4.45.

In figure 4.47 it can be seen that the number of bubbles generated at the electrode, i.e. the overall bubble detachment rate, increases as the current density increases. Assuming the increase in the number of nucleation sites is reflected over the whole of the electrode surface, it is evident that the nucleation rate of the lower activity sites is greater than that of the high activity sites, active at the lower current densities. A three-fold increase in the number of nucleation sites on the surface causes a 64-fold increase in the number of bubbles rising up the face of the electrode. This is evident in figure 4.47 from the use of a log scale, where each column represents the total number of bubble events (rather than individual events as used in earlier figures).

The average detachment size and residence time are given in figure 4.48. The sample includes all bubbles nucleating on the selected sample of the RTO electrode and the passing bubbles that re-adhered to the electrode before detaching. The range of these values was small compared to the corresponding values measured at the gold and platinum electrodes. The figure shows a trend towards an increase in detachment rate due to the shorter average residence time and smaller average detachment radius. The exception is the larger average detachment radius at 32 mA cm⁻², compared to the value at 22.4 mA cm⁻². As shown in frame

3 in figure 4.45 this can be attributed to the presence on the electrode of a small number of sites producing large bubbles.

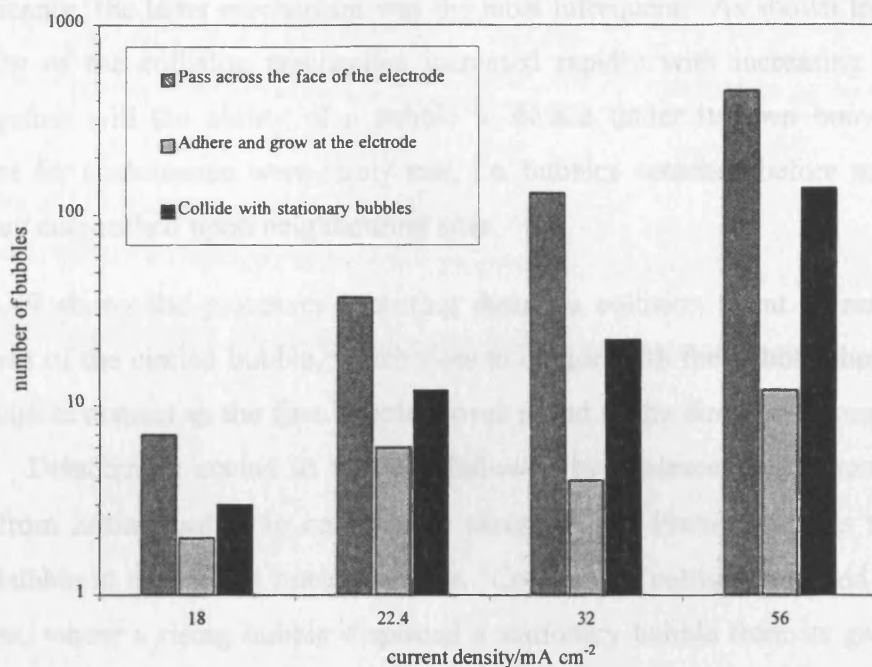


Figure 4.47 Data for nucleation site activity for chlorine bubble evolution with varying current density for the 9 mm² section of the RTO electrode shown in figure 4.45.

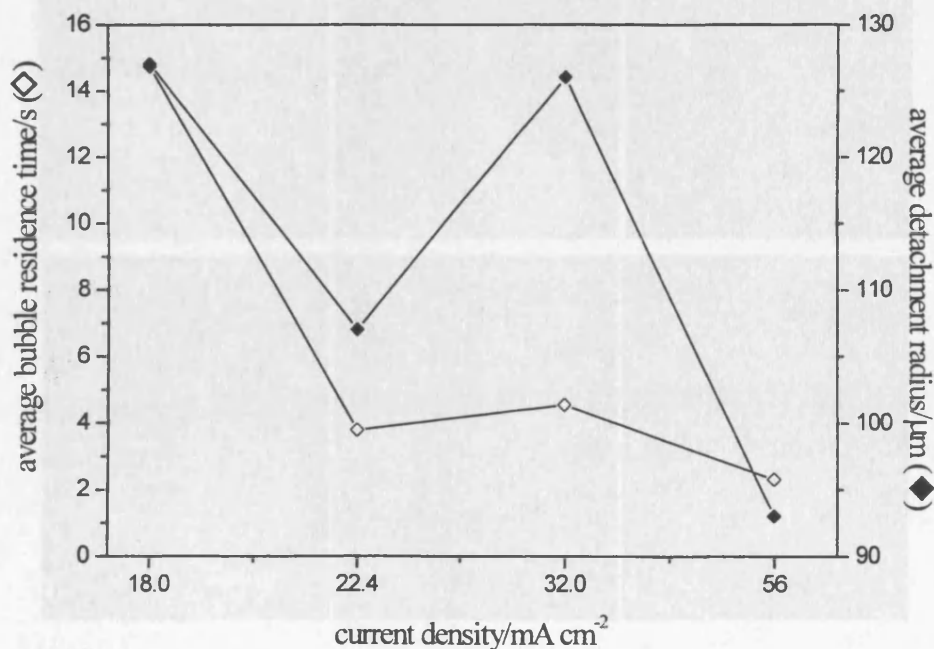


Figure 4.48 Data for the average detachment radius and residence time for chlorine bubbles with varying current density for the 9 mm² section of the RTO electrode shown in figure 4.45.

Three different bubble detachment mechanisms were observed on the electrode: detachment

by the domination of buoyancy forces over surface tension, detachment due to collision of passing bubbles with stationary ones, and coalescence of two neighbouring bubbles. In terms of significance, the latter mechanism was the most infrequent. As shown in figure 4.47, the probability of the collision mechanism increased rapidly with increasing current density. This, together with the ability of a bubble to detach under its own buoyancy meant the conditions for coalescence were rarely met, i.e. bubbles detached before growing to a size where they encroached upon neighbouring sites.

Figure 4.49 shows the processes occurring during a collision event. Frame 1 shows the detachment of the circled bubble, which rises to collide with the bubble above it in frame 2, they remain in contact as the first bubble moves round in the direction given by the arrow in frame 3. Detachment occurs in frame 4 followed by coalescence in frame 5. The whole process from initial contact to coalescence takes 90 μ s. Frame 6 shows the formation of another bubble at the circled nucleation site. Commonly, collisions caused a “billiard ball” type event, where a rising bubble displaced a stationary bubble from its growth site. Both bubbles continued to rise separately without coalescing.

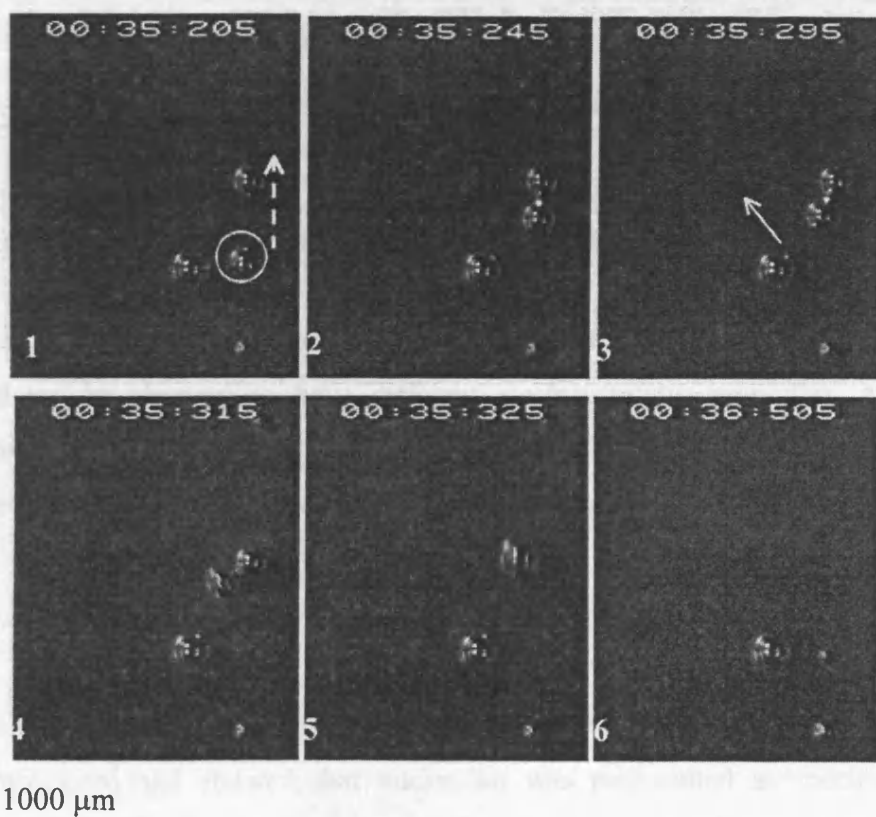


Figure 4.49 Coalescence of two chlorine bubbles on the RTO electrode at a current density of 18 mA cm^{-2} .

4.6.5 Chlorine evolution on RTO; conclusions

The most significant observation of the behaviour of chlorine bubbles on the RTO electrode is in the nucleation activity and detachment mechanism. At the lowest current density, there was a significant resistance to nucleation with only a small number of sites possessing the required energy to overcome the barrier to nucleation. This is significant in light of the large number of sites that subsequently became active at higher current densities. There was very little continuity of nucleation sites, and bubbles showed little preference for specific sites at the higher current densities, suggesting that the levels of supersaturation were high enough for nucleation to occur at any point on the electrode. This is consistent with the fact that the RTO surface has been developed to optimise the electrocatalytic activity across the surface.

At high levels of supersaturation, a high percentage of the electrode was masked from the electrolyte by bubbles resident on the electrode, as the number of nucleation sites increased. The new sites were more highly active and detachment was further facilitated. These factors suggest that there was a low three phase contact angle and low surface tension. The mechanism of rising bubbles becoming re-adhered to the electrode suggests an electrostatic interaction between the bubble and the electrode. This is a plausible explanation for the resistance to coalescence due to the rigid surface of the charged bubbles.

4.7 Conclusions: Bubble evolution at different electrode surfaces

The object of the study was to characterise the behaviour of hydrogen evolution at gold and platinum electrodes deemed to have different electrocatalytic properties, and apply the observations to the interpretation of bubble formation at an RTO electrode in order to characterise the RTO electrode in terms of its ability to evolve bubbles.

4.7.1 Nucleation

The study of individual bubbles at the gold electrode was successful. Consecutive events could be monitored and showed that nucleation was preferential at specific sites. The population density of nucleation sites differed between electrodes. The number of sites active at the lowest threshold of supersaturation required to form bubbles provides an insight into the distribution of nucleation site energetics on the surface. It has been shown, using the platinum

electrode as an example, that a suitable nucleation site can be of any dimension over at least one order of magnitude, from sub-micron to several microns diameter.

The surface roughness increased for the samples used here, from gold to platinum to RTO, therefore it is plausible that the gold electrode would provide the highest barrier to nucleation with only a small number of sites attaining the suitable energetics to evolve bubbles at very low supersaturation. In fact it was impossible to activate an individual nucleation site on the gold electrode. As soon as the supersaturation threshold had been attained for one site, several others were activated, and subsequent nucleation was rapid. This behaviour was less evident on the platinum and RTO electrodes, where the surface roughness and therefore number of potential nucleation sites was greater. It can be concluded that all the surfaces displayed a range of nucleation activities, with the widest range on the RTO electrode and the narrowest range on the platinum electrode. It should be noted that porous electrodes are only effective if all the pores are flooded. This may also have been a factor in the wider distribution of nucleation sites on the RTO electrode as the current density was increased. The relative distribution of gas and electrolyte in the surface features of the RTO electrode is explored in chapter 5.

There were two distinct types of nucleation sites on the platinum electrode and nucleation was rapid at both; at lower supersaturations the behaviour was similar to that on the gold electrode, and at higher supersaturations the mechanism switched to predominantly “bubble pump” type evolution. Nucleation was rapid under all conditions, and the continuity of site activity meant that larger areas of the electrode were free from bubbles. As only a small percentage of the surface was covered by bubbles, it is possible there were large variations in the local supersaturation across the surface, although it is inconclusive whether these variations cause the formations of clusters or vice versa.

The nucleation activity at the RTO electrode was different from that observed at the gold and platinum electrodes. The presence of specific nucleation sites (where preferential bubble evolution occurred over a range of activities) was less evident. Nucleation was slow compared to detachment at most sites, and it was observed that individual sites were not sufficient to overcome the barrier to nucleation for consecutive bubbles, making their behaviour unstable. Assuming nucleation is the rate-limiting step, the fluctuation in local supersaturation has a more significant effect, causing the instability in individual site activity. Bubbles formed at many different sites distributed evenly across the surface, which led to a

high coverage of bubbles and enhanced the mixing of the electrolyte in the region of the electrode.

4.7.2 Growth

The growth mechanism of individual bubbles can be measured by evaluating the time exponent of growth. Conditions on the electrode were investigated where a direct injection growth mechanism would be feasible. This occurs where the concentration of dissolved gas in the electrolyte is depleted, preventing diffusion-controlled growth. The time exponent was measured for hydrogen bubbles growing on the gold electrode. However problems were encountered in the application of this method to the other electrodes. The rapid detachment frequencies of the bubble pump sites and scavenging growth mechanisms on the platinum electrode meant that virtually no growth occurred whilst the bubble was attached to the electrode and therefore the time exponent could not be measured. On the RTO electrode there was no consistent behaviour of bubbles at individual sites, therefore the surface properties were in constant change, and a value of time exponent measured for a single bubble could not be correlated to a specific growth environment.

The growth mechanism for hydrogen bubbles on the gold electrode was found to be independent of the bubble's growth environment in terms of its number of close neighbouring bubbles, which made it difficult to identify circumstances where the "direct injection" could occur. The variation in growth mechanism highlighted the variation in local supersaturation levels across the electrode surface and it can be concluded that the growth mechanism cannot be predicted simply from the control of macroscopic properties such as the current density or the position of a bubble on the surface.

4.7.3 Detachment

For the gold and platinum electrodes a large range of detachment sizes and detachment rates were observed for individual nucleation sites. A much smaller range was observed on the RTO electrode, where a larger number of nucleation sites were active. The detachment mechanism differed greatly. It was predominantly due to coalescence on the gold and platinum electrodes, where the distance of closest neighbour determines detachment size. On RTO electrodes, detachment was due to either collision or buoyancy. Detachment of individual bubbles from RTO was facilitated compared to the gold and platinum electrodes.

This, combined with the inhibition of nucleation, suggests that the three phase contact angle was much smaller for the chlorine/RTO system.

The gold and platinum electrodes displayed different characteristics in terms of nucleation, growth and detachment behaviour, caused by a combination of differences in electrocatalytic activity and surface morphology. The defining features of bubble evolution on the RTO surface can be summarised by a large number of single detachment events, replenishing the solution quickly and therefore enhancing mass transport. Despite the inhibition of nucleation, the volume of the gas masking the electrode at any given time was high. The population of nucleation sites per unit area was much higher than observed for platinum and gold, and the wide range of nucleation site activities meant that there were no areas of the electrode devoid of nucleation sites. The degree of surface coverage of bubbles is an important parameter in the performance of an industrial RTO electrode during chlorine manufacture. A large number of bubbles resident on the surface inhibit further oxidation of chloride ions. It is interesting to note that the electrocatalytic optimisation of the RTO electrode promotes nucleation but not detachment.

4.8 Future work

This chapter has described a preliminary study to test the FFV methodology for a macroscopic electrode. Studying individual bubbles provides a useful insight into the effect of different surface properties, such as surface roughness and chemical composition, on the overall bubble evolution mechanism. The nucleation activity, number, and position of nucleation sites on the surface determined the overall mechanism. Future work in this area would need to address the random behaviour of nucleation sites. Specifically, it would be interesting to establish the physical characteristics and dimensions of a "bubble pump" nucleation site, and the conditions that cause the formation of a "coalescence pair", as these type of sites are very efficient at removing bubbles from the electrode.

A possible, but ambitious technique to achieve, is the preparation of a single crystal gold electrode on which a single nucleation site or array of sites could be etched. This technique could be used to identify the geometry or conditions required to produce a bubble pump, or to measure the effect of current density on an isolated site. The effect of nearest neighbours could be determined by systematically changing the distance between neighbouring sites in

the array. It is impossible to create optically flat RTO, but the size of the "mud flats" comprising the surface structure could be modified to determine if they directly influence the number of active nucleation sites. The electrostatic interaction between chlorine bubbles and the RTO electrode was an important process in the overall evolution mechanism. Its significance could be determined thorough the evolution of different gases at an RTO electrode.

1. Volanschi, A.; Nijman, J. G. H.; Olthuis, W.; Bergveld, P., *Sensors and materials*, **1997**, *9*, 223-240.
2. Kristof, P.; Pritzker, M., *Journal of Applied Electrochemistry*, **1997**, *27*, 255-265.
3. Carr, M. W.; Harris, L. A.; Hillman, A. R., *J. Electroanal. Chem.*, **1994**, *367*, 251-254.
4. Westerheide, D. E.; Westwater, J. W., *A. I. Ch. E. Journal*, **1961**, *7*, 357-362.
5. Khurana, A. K.; Chen, H.; Wall, C. G., *Chem. Eng. Comm*, **1998**, *165*, 199-215.
6. Sides, P. J., "Phenomena and effects of electrolytic gas evolution" in *Modern Aspects of Electrochemistry*; White, R. E., Bockris, J. O'M., Conway, B. E., Ed.; Plenum: New York, 1986; Vol. 18; pp 303-354.
7. Glas, J. P.; Westwater, J. W., *Int. J. Heat Mass Trans.*, **1964**, *7*, 1427-1443.
8. Scriven, L. E., *Chem. Eng. Sci.*, **1959**, *10*, 1-13.
9. Brandon, N. P.; Kelsall, G. H., *J. Appl. Electrochem.*, **1985**, *15*, 475-484.
10. Vogt, H., *Electrochimica Acta*, **1984**, *29*, 175-180.
11. Carr, M. W.; Hillman, A. R.; Lubetkin, S. D., *J. Coll. Int. Sci.*, **1995**, *169*, 135-142.

5.1 Introduction

This Chapter describes the development of the experimental and theoretical aspects of electrochemical quartz crystal microbalance (EQCM) analysis of bubble evolution. The use of Fourier analysis of EQCM data is a novel approach to the measurement of bubble evolution kinetics. Previous work in the area has been on a preliminary basis. The first report of the use of the EQCM technique for the detection of gas bubble evolution was for H₂ evolution from aqueous acid at a gold electrode [1]. This was extended to the process of chlorine evolution at platinum [2]. In both studies the focus was not the effect of individual bubble events, but the overall trends in the EQCM frequency response as gas was evolved at the electrode. The technique was further developed by the use of Fourier analysis of the EQCM frequency response for hydrogen evolution at a nickel electrode [3]. This was a preliminary study based on a method that had previously been used for the analysis of fluctuations in electrode potential caused by hydrogen evolution at a corroding iron electrode [4]. It established the validity of the Fourier analysis for the interpretation of the complex fluctuations in mass caused by bubble evolution.

The results presented in this chapter are a representative sample of the extensive development work carried out in order to refine the FFT analysis technique. For clarity and comprehensiveness, some of the preliminary work will be included as examples to illustrate the methodology. Subsequently the application of the technique to bubble evolution kinetics for gas evolved at three different electrode surfaces is described. The systems of interest are hydrogen evolution from perchloric acid at gold and platinum electrodes, and chlorine evolution from aqueous sodium chloride at a platinum electrode coated with an electroactive layer of mixed ruthenium and titanium oxides. The platinum and so-called unpolished gold electrodes have a 5 μm finish and the polished gold electrodes have a 1 μm finish. The RTO electrode is fabricated from a crystal with a 5 μm finish; however, the surface is covered with deep cracks. The experimental design is as described in chapter 3, section 3.2.

Bubbles were evolved from two aqueous electrolytes in a standard three-electrode cell configuration; the counter electrode was platinum gauze and the reference electrode was a saturated calomel electrode (SCE). All values of electrode potential, E , quoted in this

chapter are referenced to an SCE. *In-situ* EQCM frequency measurements were recorded for bubbles evolved at each electrode with the quartz crystal mounted in various orientations. The frequency measurements were correlated with visual observations of the surface, in which bubble numbers and sizes were estimated.

5.1.1 Principle of EQCM frequency response analysis

The EQCM enables the simultaneous measurement of two parameters, resonant frequency and current. As described in section 2.2, changes in density or viscosity occurring within a 300 nm thick modulation layer adjacent to the electrode cause a change, denoted (Δf), in the resonant oscillation frequency (f_0) of the 10 MHz quartz crystal, onto which the electrode was coated. The formation of a gas bubble causes a displacement of the denser electrolyte, effectively reducing the mass of the electrolyte coupled to the quartz crystal electrode as explained in section 2.3. The oscillation frequency increases, producing a positive value of Δf , *i.e.* the less heavily loaded crystal oscillates at a higher frequency. Upon the detachment of a bubble, the denser electrolyte immediately displaces the gas bubble causing an immediate decrease in the resonant frequency.

The parameter referred to as coupled mass is actually the areal density of the electrolyte in the immediate vicinity of the electrode. For density changes that occur uniformly across the surface, changes in frequency on a scale of several Hz can be expressed as a “mass” change in nanograms according to equation 2.56. The parameter Δf cannot be transformed into an absolute value of coupled mass although it is convenient to visualise the changes in density occurring extensively over the electrode during bubble evolution as mass changes (Δm). By convention, changes in the oscillation frequency of the quartz crystal occurring due to bubble formation are commonly expressed in Hz and this nomenclature has been adopted. The two terms, frequency and coupled mass, are used interchangeably throughout this chapter (on the understanding of the relationship described above). The coupled mass changes that occur at the electrode because of bubble formation in the modulation layer are analogous to the fluctuations in voltage or current that one would expect from the presence of an insulating sphere placed on the electrode [5,6].

5.2 Objectives

As described above, previous analysis of the EQCM response produced during bubble evolution was preliminary and qualitative, this is especially true of the use of Fourier transformation. Although FFT spectra have been presented for hydrogen bubble evolution, no attempt was made to identify the bubble evolution mechanism. By applying the methods of data analysis described in chapters 2 and 3, the EQCM is now used to show that the orientation of the electrode and surface characteristics (such as roughness) determine the behaviour of bubbles formed at the electrode surface during electrochemical gas evolution. Bubble behaviour changes as a function of the supersaturation. Therefore the aim is to identify and categorize features of an EQCM frequency response measured during bubble evolution at different current densities.

As described in chapter 2, section 2.3.2, Fourier analysis provides the frequency at which features in the EQCM coupled mass response occur, by converting the data from the time domain to the frequency domain, ultimately leading to a mechanism for bubble evolution. The aim is to apply the FFT technique to systems in which the bubble behaviour is far too complex to be analysed using direct visual observation. Also, Fourier transformation is used as a diagnostic tool to identify the bubble evolution mechanism as a function of both current density and electrode surface properties. Under no experimental conditions could the number of active nucleation sites on the electrode be controlled or limited; the results presented in this chapter represent a wide range of activities recorded using the EQCM. However, the visual observations made during EQCM experiments were consistent with observations recorded using the FFV technique presented in Chapter 4.

Electrocatalysts provide a low energy pathway for the gas evolution reaction, and their electrocatalytic activity is determined by both their morphology and their electrochemical properties. For example, both the chlorine evolution reaction and the hydrogen evolution reaction occur via the formation of an adsorbed intermediate. Although this leads to bubble nucleation, little is known about the correlation between the two processes. A major economic concern is that bubbles adhered to an electrode block that site to further electrochemical reaction. The degree to which this problem occurs is dependent on the local composition of the electrode i.e. the surface tension that affects the contact angle between the bubble and the electrode. If the surface tension is high, due to adsorbed impurities, then

bubble detachment is inhibited. The microscopic structure of the electrode determines the nucleation activity. Some surface structures provide sites where nucleation is facilitated or at which the nucleation step is even by-passed. The distribution of nucleation sites across the surface is closely related to the level of local supersaturation, i.e. small clusters of isolated bubbles may give rise to large fluctuations in current density across the surface. In summary, a catalytic surface (in terms of bubble evolution) is one where bubbles are nucleated at a large number of distributed evenly sites across the electrode. Growth is rapid and bubbles detach at a small uniform size without significant coalescence occurring whilst the bubbles are attached to the surface.

It is an issue of major industrial relevance to identify surface properties that catalyse bubble activity. The global aim is the development of electrocatalytic materials that simultaneously improve the efficiency of the bubble evolution mechanism. It is the intention to demonstrate that the EQCM is a technique capable of providing detailed information relating to specific bubble activity at an electrode. Also, it will be shown that the surface of a quartz crystal electrode can be modified sufficiently to replicate the surface properties of an industrially relevant electrode surface such as RTO. Finally, it will be demonstrated that FFT analysis of EQCM data enables the technique to be applied to complex bubble behaviour and may be extended to the analysis of bubbles generated under conditions comparable to those of an industrial chlor-alkali cell.

5.3 EQCM Data Analysis

Each of the parameters (current, potential and frequency) is recorded as a voltage in the form of an ASCII file. The EQCM signal is recorded as a voltage and converted back to a frequency value, using calibration constants. The resonant frequency of the crystal (f_0) is not measured directly, but relative to a reference crystal whose resonant frequency (f_{ref}) is constant throughout the experiment. For convenience, the reference crystal is chosen so that its frequency is a few kHz higher than the working crystal. f_{exp} is the measured frequency difference expressed as

$$f_{exp} = f_{ref} - f_0 \quad (5.1)$$

This method allows for greater sensitivity in recording the changes in resonant frequency that occur in the working crystal, because changes in f_0 in the region of a few Hz are measured at a frequency value (f_{exp}) of several kHz magnitude, instead of 10 MHz. According to equation 5.1, an increase in f_0 , (caused by a decrease in coupled mass) decreases the value of f_{exp} causing a negative value of Δf_{exp} (and vice versa). During experiments the f_{exp} output is offset to zero, prior to gas evolution, therefore values of $\Delta f_{exp} \equiv -\Delta f_0$.

5.3.1 Surface Structure

The macroscopic structure of the electrode, as defined by the surface roughness and the morphology of the surface features, influences the bubbles nucleating on the surface. SEM analysis can provide an image of the geometric features but, as an *ex-situ* technique, it is unsuitable for determining the surface tension (or wetting properties) of the electrode, specifically the extent to which any pores or cracks in the surface are flooded by the electrolyte. Exposing one face of a quartz crystal to a liquid decreases its resonant frequency and dampens the oscillation as explained in section 2.2.5. The extent to which this occurs depends on the real surface area exposed to the liquid, a property that can be determined by comparing the resonant frequency of the crystal when exposed to air, with the frequency when one side is immersed in an aqueous electrolyte. This is the basis of a very simple technique to establish the real surface area of an electrode by measuring the effect on the resonant frequency of exposing one side of the electrode to a solution [7]. For optically flat 10 MHz quartz crystal electrodes of 13 mm diameter and 0.2 mm thickness, the difference between the resonant frequency in air and in water ($\Delta f_{liq\ layer}$) is 7 kHz at 25°C and is given by

$$\Delta f_{liq\ layer} = f_{exp(liq)} - f_{exp(air)} \quad (5.2)$$

$f_{exp(liq)}$ and $f_{exp(air)}$ are the two corresponding values of f_{exp} measured whilst the crystal is exposed to a solution and air. Comparing the value $\Delta f_{liq\ layer}$ for electrodes of the same diameter provides insight into the real surface area of each surface. Therefore, $\Delta f_{liq\ layer}$ is a measure of the surface roughness.

5.3.2 *Model of coupled mass response due to bubble evolution*

As described in section 2.3 of chapter 2, a simple model of the feature produced in the EQCM coupled mass response by the formation of a single bubble on the electrode surface, is a sawtooth wave. In this section, that simple model is expanded upon to show the expected shape of the coupled mass response for more complex bubble behaviour, where individual and multiple nucleation sites are active, producing a variety of bubble evolution regimes. Bubbles will form at a site where there is the lowest energy barrier to nucleation. This is expected to be in a cavity. However, the presence of impurities adsorbed at a site on the electrode could be preferential for nucleation. Figure 5.1 shows three different models of the EQCM frequency response for individual bubbles at a single nucleation site at which nucleation, detachment and growth, respectively, are the rate limiting processes.

Considering the cycle of bubble evolution from a single nucleation site on the electrode, the expected coupled mass signal can be modelled using a periodic waveform. Assuming the size of the mass jump due to nucleation to be small compared to that caused by detachment, then the mass changes can be predicted with a simple sawtooth wave. Where the energy barrier to nucleation is high, due to either the structure of the site (see section 1.4.3) or a low contact angle due to high wetting by the solution, it is unlikely that this type of site will show constant activity, i.e. there is a significant induction period between the detachment of one bubble and the nucleation of the next, and nucleation is expected to be the rate-limiting step in the overall bubble evolution mechanism. However, detachment is expected to be rapid therefore the bubble residence time is short, as shown in model A. Model B of figure 5.1 relates to bubbles evolving at a site where nucleation kinetics are rapid, therefore the induction time is very short. The frequency of detachment is a function of the ease of which a bubble detaches from the surface, a process that is inhibited at hydrophobic surfaces. Where nucleation or detachment is facilitated, a third factor, the growth rate determines the detachment rate of bubbles, i.e. a slow growth rate decreases the detachment rate as shown by model C. From previous accounts, the expected magnitude of the coupled mass increase for the detachment of a single bubble is between 2 and 10 Hz [8].

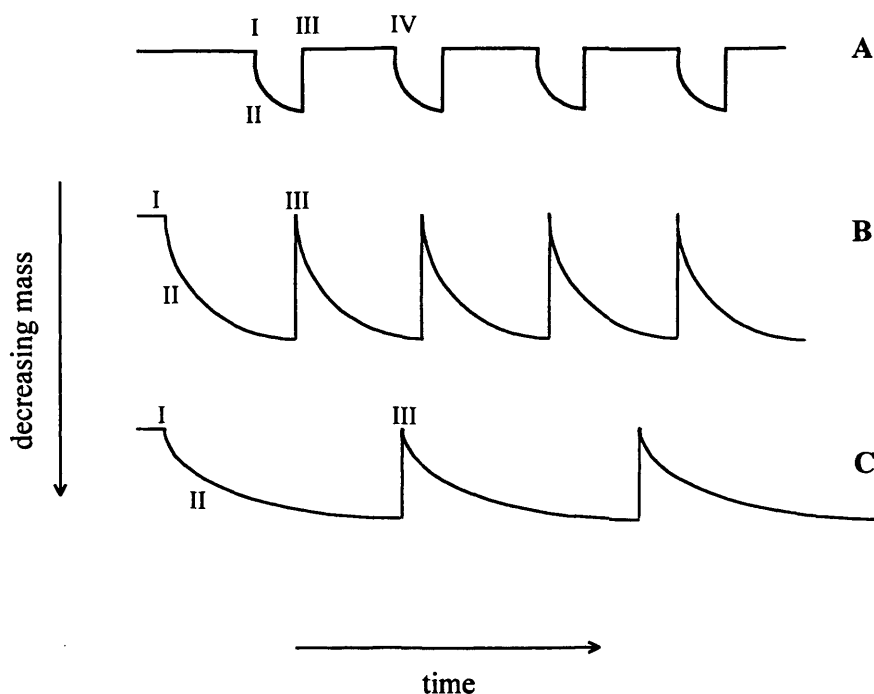


Figure 5.1 Models of EQCM coupled mass response where the rate-limiting process is either nucleation (A), detachment (B), or nucleation and detachment are rapid but growth is slow (C). Point I indicates nucleation, the region shown by II shows growth, detachment occurs at point III and the region between III and IV shown in model (A) is the induction time, which is negligible in models (B) and (C).

It was shown in chapter 4 that the simple model of the bubble evolution regime was not valid at vertical electrodes, where there is concurrent nucleation site activity causing interaction and coalescence between bubbles at neighbouring nucleation sites.

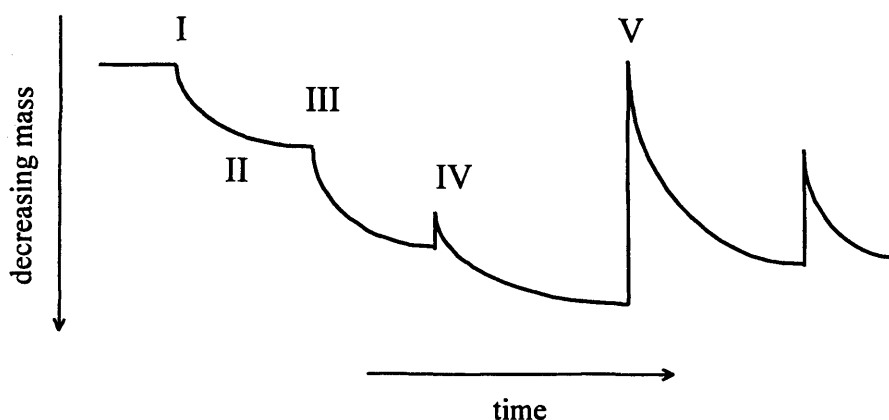


Figure 5.2 Model of EQCM coupled mass response for coalescence of two bubbles where detachment is rate limiting. Points I and III indicate individual nucleation events for two bubbles, the region II shows growth. The two bubbles coalesce at point IV, and detachment of the new larger bubble occurs at point V.

Figure 5.2 depicts the coupled mass transient expected for a coalescence event. For horizontal electrodes, detachment does not always immediately follow coalescence; this complicates the expected coupled mass response. The model in figure 5.2 is no longer a simple sawtooth wave and the detachment rate as identified by the discontinuity in the sawtooth wave is ambiguous because the point of nucleation is not easily identified.

5.3.3 *Data analysis in the time domain*

Three electrochemical methods were used to generate hydrogen gas bubbles at gold and platinum electrodes and chlorine at RTO electrodes; cyclic voltammetry, chronoamperometry and chronopotentiometry. The region of electrode potential where gas evolution occurs can be identified using cyclic voltammetry. Bubbles are evolved under conditions of steadily increasing current, therefore, the bubble activity changes over the course of one scan. Thus little information can be gained by studying the individual detachment events. However, by measuring the overall coupled mass changes and comparing the electrode prior to nucleation and once gas bubbles have been evolved, it is possible to establish the degree to which bubbles remain resident on each electrode. This is an important parameter through which the overall detachment kinetics for different surfaces can be compared.

The chronoamperometric and chronopotentiometric techniques allow an in-depth analysis of individual bubble events, by measuring the magnitude and frequency of bubble activity as a function of supersaturation. Several features of the coupled mass response can be identified. Firstly, the slope of the coupled mass response at short times provides information on the number of bubbles formed and hence the number of active nucleation sites. If there is a long induction time, caused by slow nucleation or very few active nucleation sites, there will be a small number of bubbles on the electrode. This is represented by a shallow coupled mass gradient ($d\Delta f/dt$). At longer times, the slope of the coupled mass response provides information on the growth and detachment rate of bubbles at the surface. If detachment is the rate-limiting step then the gradient will be steep, as bubbles that are resident on the electrode continue to grow. However, if detachment is rapid then the gradient is shallow, as bubbles detach before significant growth takes place.

Secondly, the size and frequency of the discontinuities in the coupled mass response provide information on the activity of the surface in terms of a bubble's ability to detach from it. An active surface is one from which bubbles detach rapidly at a small size. Contrastingly, at an inactive surface, bubbles grow to a larger size and detach infrequently. Coalescence not followed immediately by detachment is the limiting case of this type of behaviour. Nucleation is favoured over detachment, neighbouring bubbles coalesce, and continue to grow therefore increasing the volume of gas resident on the electrode. The size distribution of the discontinuities in the EQCM frequency response that occur upon detachment indicate the degree of uniformity of activity across the surface. These parameters can be compared for different electrode surfaces and correlated with the physical and chemical properties, so defining the mechanism of bubble evolution at any given surface.

5.3.4 *Fast Fourier Transform (FFT)*

As described in chapter 2, Fourier transformation is a method of EQCM data analysis that allows immediate characterisation of the electrode by providing a comparison of the magnitude and frequency of detachment events on the electrode surface. The transform is calculated for coupled mass response data collected in the time domain. A representative sample of the data is chosen and truncated, so the number of data points is equal to 2^n . The first peak on the spectrum arises from the mean value of all the data points. Therefore, the mean value of the data is adjusted to zero, in order to simplify the frequency spectrum. The truncated data can be summed to increase the resolution of the peaks on the frequency spectrum. Different regions of the spectrum can be identified as relating to distinct physical processes occurring at the surface. The peaks appearing in the frequency range between 0 and 1 Hz arise from the majority of the discontinuities in the coupled mass response due to detachment and coalescence events. The rates of the bubble evolution cycles are taken to be the fundamental frequencies of the peaks appearing in this part of the frequency spectrum. The peaks in the higher frequency regions arise from the harmonics of the low frequency events; small changes in this region can be disregarded as they only change the "cosmetic appearance" of the raw data and provide little additional mechanistic insight.

Figure 5.3 shows the FFT spectra produced from the models of the coupled mass response given in section 5.3.2. The peaks on the frequency spectrum correspond to the fundamental frequency f_1 and the harmonics that comprise the sawtooth wave as defined in equation 2.61.

The important feature of the spectra is that the magnitude of the harmonics decays according to the equation $y = 1/x$.

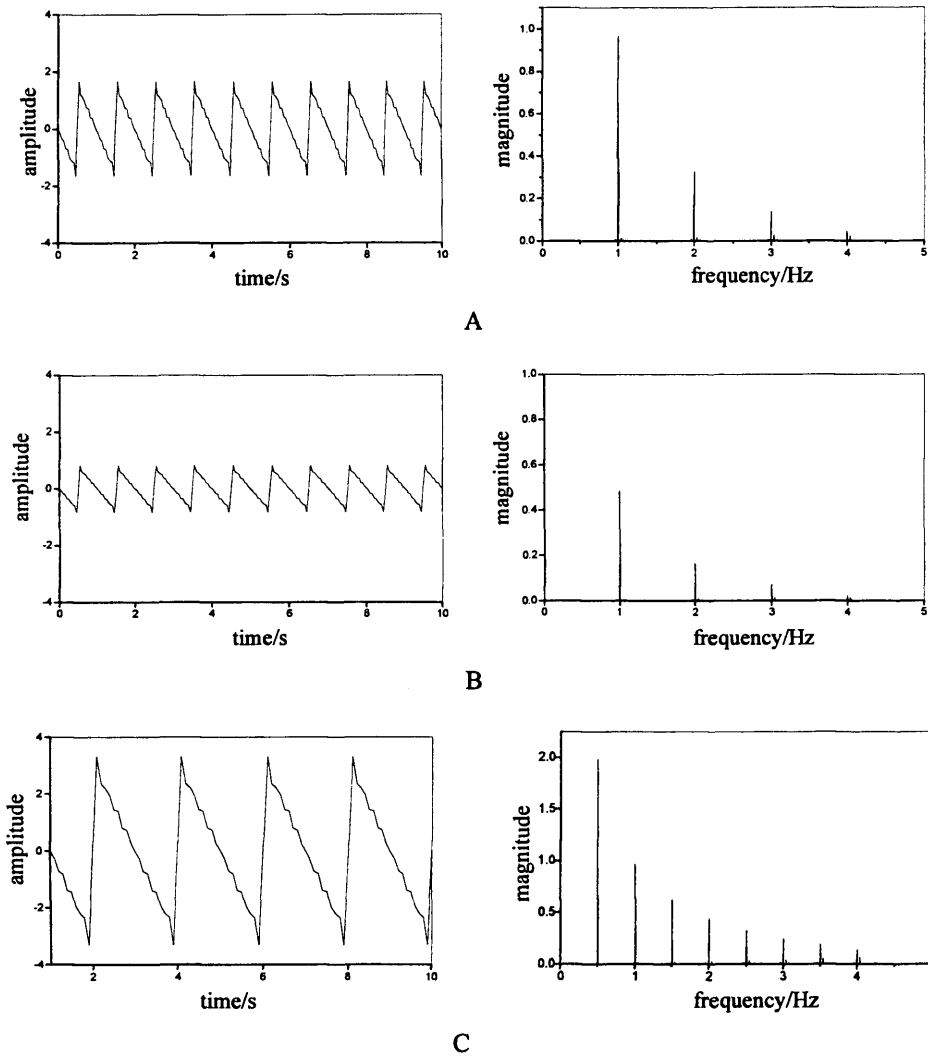


Figure 5.3 Sawtooth wave models of the EQCM frequency signal, showing arbitrary units and corresponding frequency spectra for rapid bubble evolution; A) $V = \pi/2$, $f_0 = 1\text{Hz}$. B) $V = \pi/4$, $f_0 = 1\text{Hz}$ C) $V = \pi$, $f_0 = 0.5\text{Hz}$

The spectra in figure 5.4 demonstrate the effect of increasing the kinetics of bubble evolution. If the detachment rate increases at a constant detachment size the peaks on the frequency spectra are shifted to a higher frequency (A). If the detachment size decreases at a constant detachment rate, the peaks remain at the same frequency but decrease in magnitude (B). If the detachment rate increases at a constant growth rate bubbles detach at a smaller size and the peaks on the frequency spectrum decrease in magnitude, whilst increasing in frequency (C). These changes are summarised in figure 5.4 below.

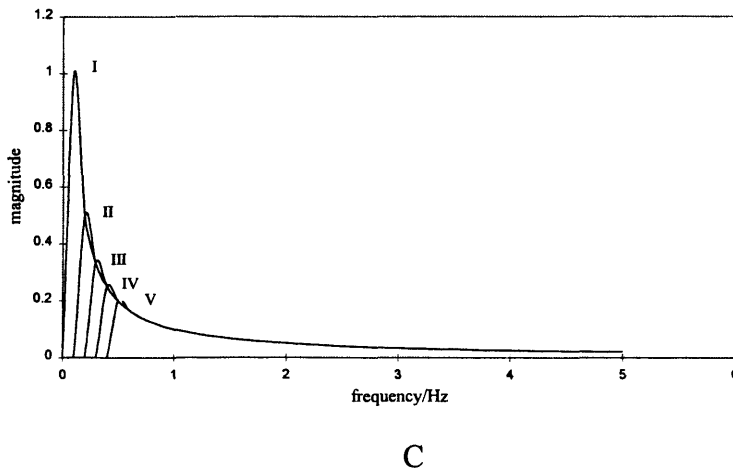
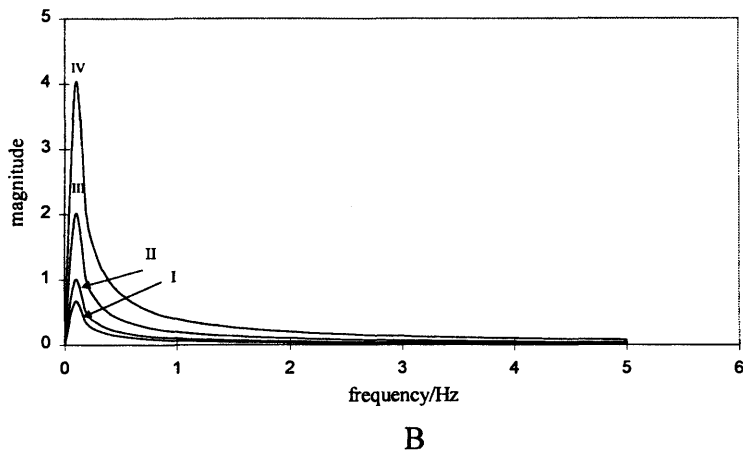
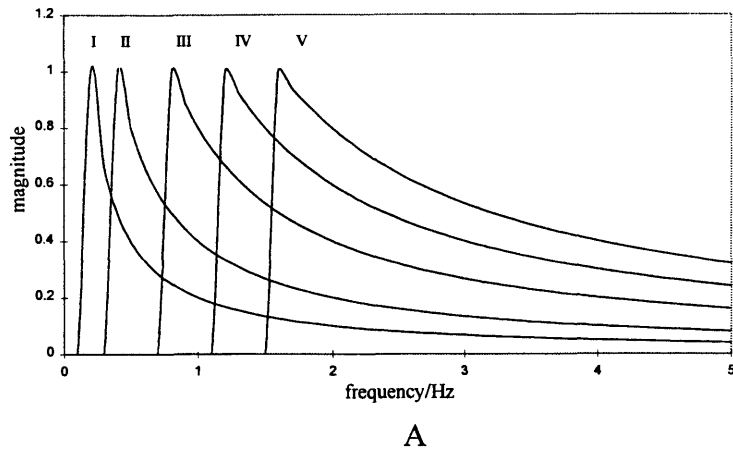


Figure 5.4 Trends in FFT spectra showing the effect of; A) increasing the growth rate at constant detachment size I-V; B) increasing growth rate at constant detachment rate I-IV; C) increasing the detachment rate at constant growth rate I-V.

Figures 5.3 and 5.4 demonstrate the characteristic changes occurring in the coupled mass response resulting from a change in the kinetics of bubble evolution. It is this aspect of the FFT that, in principle, enables the rate constant to be determined: peak size is related to the size of the bubble on detachment, and the frequency value at which the peaks occur provides a rate constant for the activity of that particular site. A shift along the frequency axis represents an increase in the rate of detachment, whereas a shift in peak height represents a change in detachment size. The change in activity as a function of physical and chemical parameters provides mechanistic insight. The extension of this theory to experimental data is complicated by the behaviour of bubbles at a real surface. If a number of sites are active at the surface, a distribution of site activities and bubble evolution mechanisms could arise. The deconvolution of these types of spectra and extraction of kinetic information is presented with the experimental EQCM data. Instead of picking individual peaks, the relative sizes of the distribution of peaks provides insight into the mechanism of bubble activity on the electrode. The theory behind this technique is given in section 2.3.2 and examples are used to illustrate this idea in the next section.

5.3.5 *Summary*

The novel methods of data analysis described in the previous sections promise a means to identify the characteristics of bubble behaviour observed in an EQCM frequency response during gas evolution and the properties of the electrode that influence it. It is expected that the behaviour of bubbles at a real surface will be convoluted and therefore produce complex coupled mass responses. However, characteristics of the coupled mass response, such as the magnitude and frequency of the sawtooth wave, can be identified for simple experimental systems where a small number of bubbles are generated. Further experimental data collected for different systems can then be correlated to the more complex behaviour of bubbles observed at a variety of surfaces.

5.4 **Bubble evolution using cyclic voltammetry**

5.4.1 *Single voltammetry scan*

Figure 5.5 is an example of the EQCM frequency response recorded for the evolution of hydrogen bubbles at an unpolished gold electrode. The measured parameter, $f_{exp(liq)}$ (shown as Δf in all figures) is given in equation 5.2 and is equivalent to $-\Delta f_0$. The onset of nucleation

as Δf in all figures) is given in equation 5.2 and is equivalent to $-\Delta f_0$. The onset of nucleation is indicated by point I. This is followed by a steady, rapid decrease in the value of the coupled mass as bubbles grow at the surface (region II), starting at approximately -0.55V . Detachment events occur in the electrode potential region between -0.7 and -0.8V (vs. SCE). A major detachment event occurs at point III, highlighted by the matching discontinuities in both i and Δf . The maximum current is 1.14 mA , corresponding to a current density of 4.56 mA cm^{-2} , a relatively low value, similar to the level of activity presented in section 4.3.1 of the video analysis chapter.

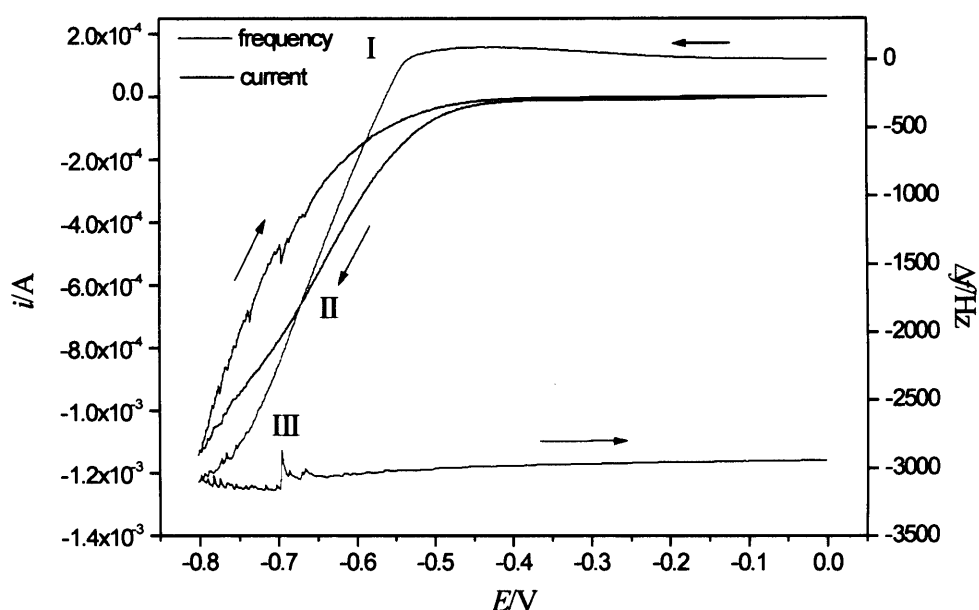


Figure 5.5 Hydrogen bubble evolution from 0.1 M HClO_4 , on a horizontal upward facing gold electrode, (area = 0.25 cm^2). The scan rate = 20 mV s^{-1} in the direction of the arrows. The two lines relate to the simultaneously measured responses of current (in black) and coupled mass (in red). Point I corresponds to the onset of nucleation, region II denotes multiple bubble growth and III indicates a detachment event.

There is significant hysteresis displayed in both the current and Δf responses, due to the majority of the bubbles that are generated remaining attached to the electrode. The current on the reverse section of the scan is significantly smaller, due to the effective smaller electrode surface area, in turn resulting from the presence of insulating gas bubbles at the electrode. The sudden increase in the current observed at point III arises from the instantaneous increase in electroactive surface area that corresponds to bubble detachment

Δf has decreased by 3 kHz, indicating a large volume of gas resident on the electrode surface, effectively decoupling approximately 40% of the previously coupled liquid from the crystal.

5.4.2 *Electrode surface properties*

The overall coupled mass change is a useful parameter in determining the amount of bubbles resident on an electrode. Table 5.1 provides a comparison of the coupled mass ($\Delta f_{\text{bubble layer}}$), of different electrodes at the end of the first scan in each cyclic voltammetry experiment and indicates the amount of gas resident on the electrode. The more efficient electrodes are ones where bubbles detach easily, and therefore the value of $\Delta f_{\text{bubble layer}}$ is small. The values for $\Delta f_{\text{liq layer}}$ in table 5.1 are in the region of 7 kHz, as expected for an unpolished gold electrode, and are a function of the real surface area (as determined by the surface roughness) or surface wetting properties. The exceptionally high values for RTO may be attributed to the higher viscosity of the electrolyte and larger surface area. The values quoted for the different gold and platinum electrodes are typical. However, the values given for RTO are representative, but values of $\Delta f_{\text{liq layer}}$ differed greatly for different electrodes prepared using the same method. i_{max} is the maximum current recorded during each experiment.

Pure gold is hydrophilic [9], but impurities on the surface increase the surface tension, thereby reducing the wettability of the surface. Therefore, the hydrophobicity of the surface is expected to increase with electrode “age”, as contaminants introduced onto the surface during bubble evolution throughout the electrode’s lifetime cause a decrease in the surface area exposed to the electrolyte and the value of $\Delta f_{\text{liq layer}}$ to decrease. This effect can be used as an indicator of the presence of surface contamination, which has a significant effect on bubble behaviour, shown in the following section. Taking account of the three parameters in table 5.1, an image of the conditions of the electrode surface that influence the coupled mass response can be constructed. For example, a small value of $\Delta f_{\text{liq layer}}$, coupled with a small value of i_{max} and a large value of $\Delta f_{\text{bubble layer}}$ suggest that the real surface area is small (or the surface tension is high) and there is significant bubble residence on the surface.

Electrode	Frequency difference due to coupling of the liquid layer $\Delta f_{\text{liq layer}} / \text{kHz}$	Decrease in frequency due to bubble layer $\Delta f_{\text{bubble layer}} / \text{kHz}$	Maximum current/mA
Au (A)	4.221	0.556	-13.2
Au (B)	4.040	0.667	-11.2
Au (C)	4.427	0.089	-14.1
Au (D)	4.330	0.402	-8.8
Au (E)	6.813	0.644	-2.5
Au (F)	5.108	2.946	-1.1
Platinum	8.102	+0.040	-12.0
RTO (G)	13.151	+0.193	+8.7
RTO (H)	22.403	-0.182	+25.3

Table 5.1 Statistics for different electrodes. The positive value of $\Delta f_{\text{bubble layer}}$ for the RTO and platinum electrode indicates an increase in the coupled mass.

5.4.3 Multiple voltammetry scans

Figure 5.5 is an example of the information that can be obtained from qualitative analysis of the EQCM frequency response. In this section, comparison is made between cyclic voltammetry experiments at different electrode surfaces, accounting for properties such as the surface roughness and the electrode wettability. The orientation of the electrode is indicated on the figure legend. The hydrogen was evolved at platinum and gold electrodes using 0.1M HClO₄. Chlorine was generated at the RTO electrodes using acidified 5 M NaCl. The potential was scanned in the direction indicated by the short arrows. Figures 5.6 to 5.10 show several consecutive scans, and the dashed arrow shows the overall trend in the coupled mass. Region (1) indicates the resonant frequency of the electrode prior to nucleation, region (2) indicates the onset of nucleation as the coupled mass decreases due to the decrease in the density of the liquid coupled to the electrode as the electrolyte is displaced by gas bubbles. Region (3) indicates the onset of bubble detachment, where the discontinuities in the EQCM frequency response of all the scans are caused by the detachment of bubbles. Typically, bubbles are nucleated during the first scan, and the new bubbles displace a volume of liquid,

detachment of bubbles. Typically, bubbles are nucleated during the first scan, and the new bubbles displace a volume of liquid, thereby decreasing Δf_{exp} . Fluctuations in Δf_{exp} arise as bubbles detach; this generally only occurs at high overpotentials (region 3).

5.4.3.1 Hydrogen evolution at gold

Figure 5.6 shows the EQCM frequency response as hydrogen gas is evolved during cyclic voltammetry at two horizontal polished gold electrodes (labelled A and B). The International Crystal Manufacturing (ICM) Company manufactured all of the gold electrodes to the same specifications and therefore any differences in the macro surface roughness of each electrode are expected to be minimal. The only difference between them is the extent of impurity accumulation on the surface, possibly introduced by the electrolyte. Electrode B is “aged” in terms of the amount of gas evolved at the surface as compared to the recently cleaned surface, A. The same data are shown for hydrogen evolved under the same conditions at two vertical polished gold electrodes, figure 5.7C and D where electrode D is “aged” compared to electrode C. Due to the complex nature of the figures, colours are used to identify each scan in the sequence, as described in figure 5.6.

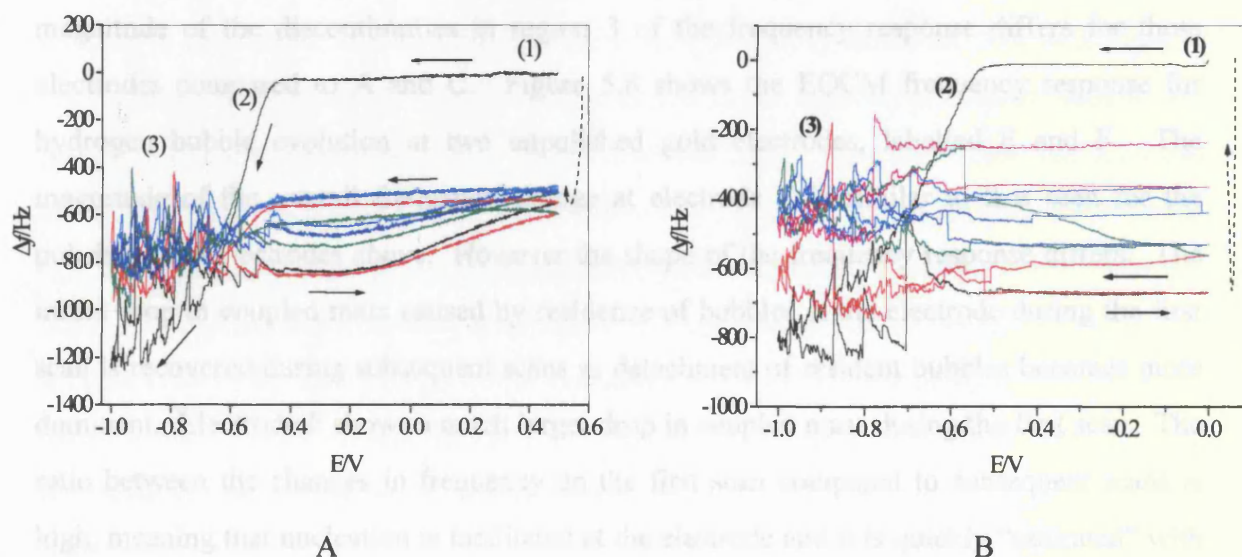


Figure 5.6 EQCM frequency responses for hydrogen bubbles evolved from 0.1 M HClO_4 , scan rate 20 mV s^{-1} at a clean horizontal polished gold electrode (A) and a horizontal polished gold electrode with surface impurities (B). Colours represent cycle numbers; 1=black, 2=red, 3=green, 4=blue, 5=cyan, 6=magenta.

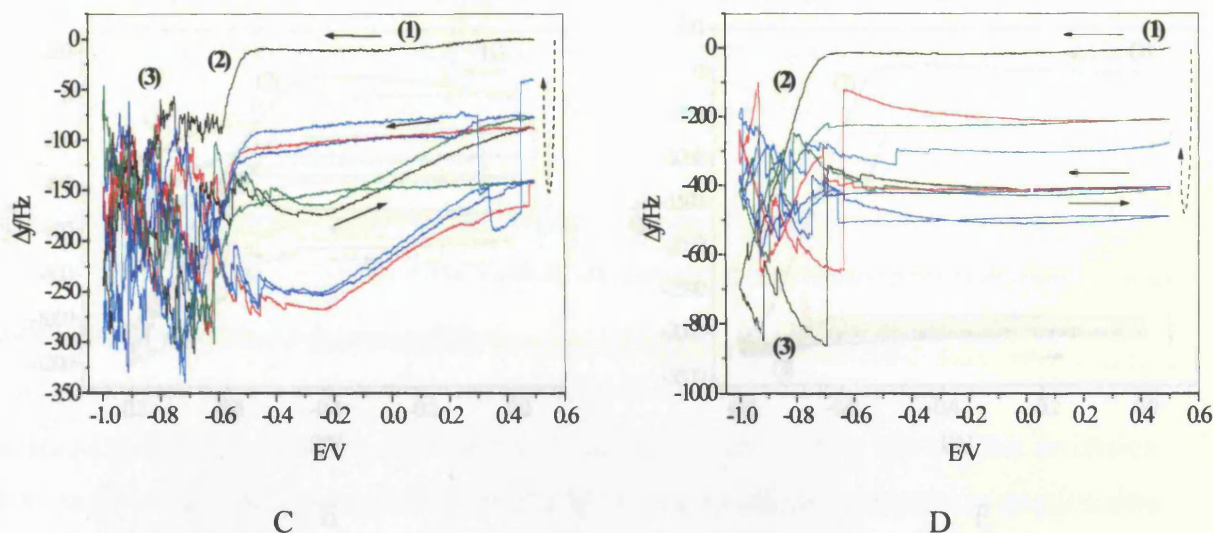


Figure 5.7 EQCM frequency responses for hydrogen bubbles evolved from 0.1 M HClO_4 scan rate 20 mV s^{-1} at a clean vertical polished gold electrode (C) and vertical polished gold electrode with surface impurities (D). Colour sequence as for figure 5.6.

Figures 5.6 and 5.7 clearly show discontinuities in the coupled mass response in the form of a sawtooth wave. The characteristics of the frequency response and the overall mass change for electrodes A and C (indicated by the dashed arrows) are very similar, although the absolute mass changes are smaller at the vertical electrode. Similarly there is a close correlation between the frequency responses for electrodes B and D. The extent and magnitude of the discontinuities in region 3 of the frequency response differs for these electrodes compared to A and C. Figure 5.8 shows the EQCM frequency response for hydrogen bubble evolution at two unpolished gold electrodes, labelled E and F. The magnitude of the overall frequency change at electrode E is similar to that seen for the polished gold electrodes above. However the shape of the frequency response differs. The initial drop in coupled mass caused by residence of bubbles at the electrode during the first scan is recovered during subsequent scans as detachment of resident bubbles becomes more dominant. Electrode F shows a much larger drop in coupled mass during the first scan. The ratio between the changes in frequency on the first scan compared to subsequent scans is high, meaning that nucleation is facilitated at the electrode and it is quickly “saturated” with bubbles and further detachment is inhibited. This effect was commonly seen at “aged” unpolished gold electrodes, where the difference between the behaviour of electrodes with different surface composition was more marked than differences seen when electrodes with the same surface composition were placed in a different orientation.

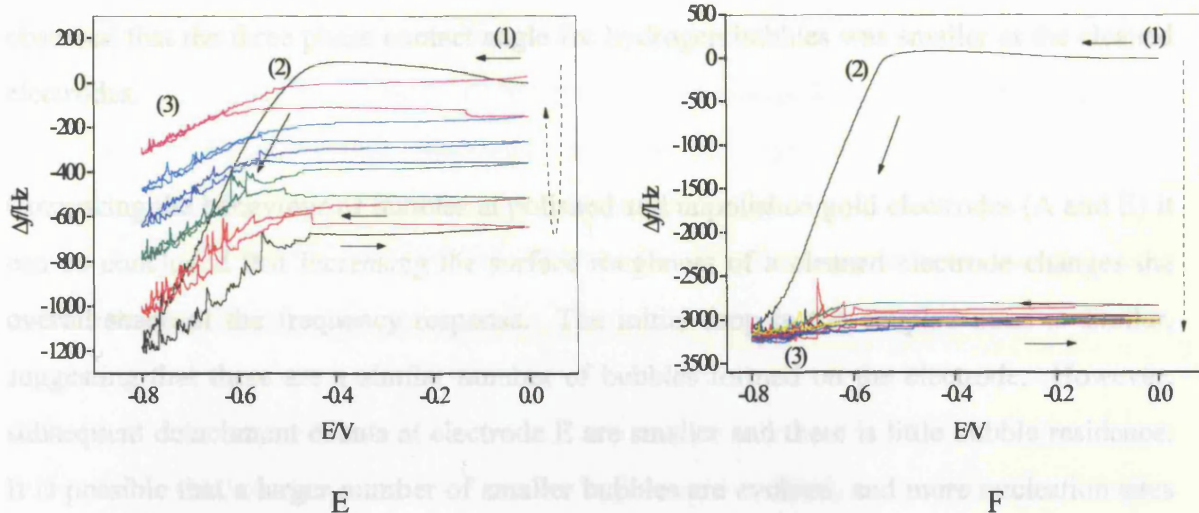


Figure 5.8 EQCM frequency responses for hydrogen bubbles evolved from 0.1 M HClO_4 , scan rate 20 mV s^{-1} at a clean horizontal unpolished gold electrodes (E) and a horizontal unpolished gold electrode with surface impurities (F). Colour sequence as for figure 5.6.

In conclusion, the overall mechanism of bubble evolution is one where hydrogen bubbles nucleate easily at all the surfaces studied, as there is significant coverage of all electrodes with bubbles after the first scan. However, the detachment rate is dependent on the conditions at the surface, even though detachment events occur in the same region of electrode potential. The level of activity is higher at clean electrodes, indicated by the increase in the number of fluctuations in the EQCM frequency response. The magnitude of the fluctuations is generally smaller, suggesting a larger number of smaller bubbles are generated at the cleaned electrodes. As the electrode “ages”, the detachment rate decreases and bubbles grow to a larger size. This behaviour is typical of gold electrodes and suggests that the chemical composition of the surface is modified during the evolution of hydrogen bubbles. The bubble evolution mechanism is very similar for the electrodes in both a horizontal and vertical orientation, with deviations in the mechanism being more apparent at surfaces with higher surface tension, i.e. “aged” electrodes. The major factor in the behaviour of bubbles during cyclic voltammetry of gold electrodes appears to be the surface conditions.

At polished electrodes, individual detachment events give rise to frequency changes that are large compared to the overall frequency change. This is caused by fewer detachment events of a larger magnitude. As the surface tension increases at “aged” electrodes bubble detachment is inhibited further and the detachment rate decreases. This is consistent with

visual observations of bubbles at the surface made during similar experiments. It was also observed that the three phase contact angle for hydrogen bubbles was smaller at the cleaned electrodes.

The overall magnitude of the coupled mass change is very small, and dominated by the size of the bubble detachment events, which themselves are small, since

Comparing the behaviour of bubbles at polished and unpolished gold electrodes (A and E) it can be concluded that increasing the surface roughness of a cleaned electrode changes the overall shape of the frequency response. The initial drop in the coupled mass is similar, suggesting that there are a similar number of bubbles formed on the electrode. However, subsequent detachment events at electrode E are smaller and there is little bubble residence. It is possible that a larger number of smaller bubbles are evolved, and more nucleation sites are available because they are not masked by large bubbles adhered to the electrode. At the “aged” unpolished electrode, F, there is a significant decrease in the coupled mass that is sustained throughout the experiment, meaning that a larger number of bubbles are formed at the electrode. The observations for both of the unpolished gold electrodes are in agreement with the hypothesis that increasing the surface roughness of a gold electrode increases the number of nucleation sites.

5.4.3.2 Hydrogen evolution at platinum

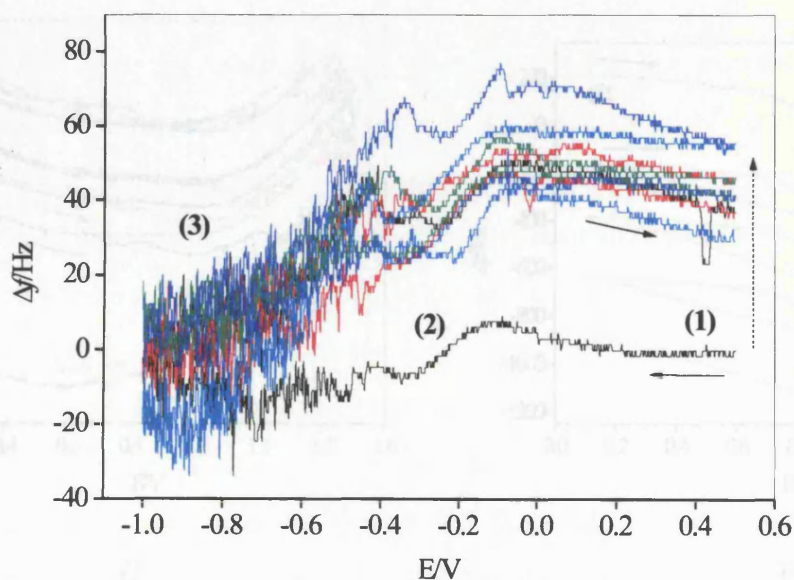


Figure 5.9 EQCM frequency responses for hydrogen bubbles evolved from 0.1 M HClO_4 , scan rate 20 mV s^{-1} , at a clean horizontal platinum electrode.

Figure 5.9 shows the EQCM frequency response for hydrogen evolution at a horizontal platinum electrode. The characteristics differ markedly from those seen for the gold electrodes. The overall magnitude of the coupled mass change is very small, and dominated by the size of the bubble detachment events which, although themselves are small, cause fluctuations which account for the majority of the change in coupled mass response observed during the scan. Bubble detachment events are rapid, and the value of the coupled mass response returns to approximately zero Hz during bubble evolution. This indicates that there is no significant growth at the electrode, also accounting for the very high detachment rate. This surface is very efficient in terms of bubble evolution, as there is virtually no gas resident on the electrode: as bubbles are evolved, they detach immediately. This is consistent with observations of “bubble pump” type nucleation sites on different vertical platinum electrodes made using a fast frame video, where the majority of growth occurred after the bubbles had detached from the electrode, undetected in the modulation layer and therefore inaccessible to measurement by EQCM. This behaviour is typical of hydrogen evolution at platinum and, unlike the gold electrodes, the behaviour of bubbles did not differ markedly as a function of either electrode age or orientation.

5.4.3.3 Chlorine evolution at RTO

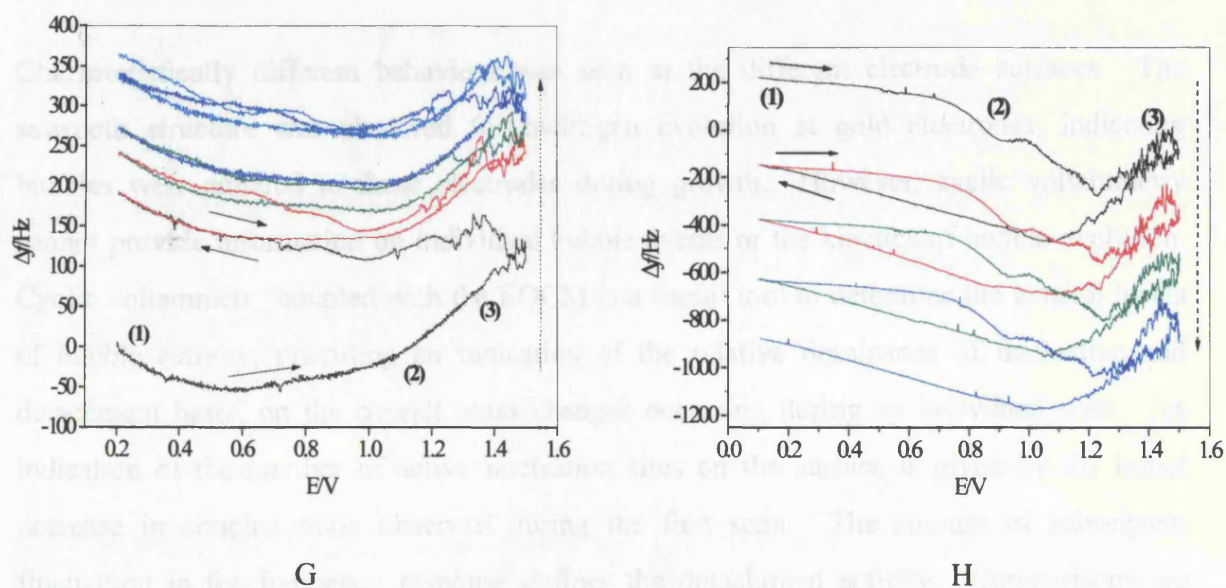


Figure 5.10 EQCM frequency response for chlorine bubbles evolved from 5M NaCl + 0.01 M HCl, scan rate 20 mV s⁻¹, at two clean horizontal RTO electrodes (G) and (H).

Figure 5.10 shows the EQCM frequency response as chlorine gas is evolved at two RTO electrodes during cyclic voltammetry. The frequency response observed at electrode G differs from gold and platinum. There is a moderate change in the coupled mass, but it increases steadily during consecutive scans. The detachment events are small and do not produce a saw tooth wave formation in the frequency response. They are also less frequent than seen at the platinum electrode. Because of the overall rise in coupled mass it can be assumed that there is virtually no residual gas on the electrode at the end of the experiment. This is consistent with visual observations, and it was confirmed that a deposition process did not cause the increase. The structure of the RTO is also very different, characterised by deep pores and channels. It is possible that these pores are not flooded immediately upon contact with the electrolyte, but the solution gradually floods the pores during bubble evolution, which would cause the coupled mass to increase as the gas trapped in the pores is replaced by solution. The detachment events observed for electrode (H) are similar in frequency and magnitude to those seen for electrode (G). However, the overall mass change is in the opposite direction. The surface properties are similar for the two electrodes and they were fabricated using the same methods. However, electrode (H) is slightly “aged” compared to electrode (G). It is possible that the pores in electrode H have become flooded and therefore the overall coupled mass decreases as bubbles form at the surface.

5.4.4 Conclusions

Characteristically different behaviour was seen at the different electrode surfaces. The sawtooth structure was observed for hydrogen evolution at gold electrodes, indicating bubbles were adhered to these electrodes during growth. However, cyclic voltammetry cannot provide information on individual bubble events or the kinetics of bubble evolution. Cyclic voltammetry coupled with the EQCM is a useful tool to determine the general levels of bubble activity, providing an indication of the relative dominance of nucleation and detachment based on the overall mass changes occurring during an individual scan. An indication of the number of active nucleation sites on the surface is given by the initial decrease in coupled mass observed during the first scan. The amount of subsequent fluctuation in the frequency response defines the detachment activity. Comparisons are easily drawn between the behaviour of bubbles at different surfaces and these can be correlated to the different properties of the surface that influence bubble activity as measured

by the parameters $\Delta f_{bubble\ layer}$ and $\Delta f_{liq\ layer}$. For example, the values of $\Delta f_{liq\ layer}$ are consistently smaller, and the average size of the jumps in the frequency response on detachment and value of $\Delta f_{bubble\ layer}$ larger, for the “aged” electrodes. All the observations are consistent with a non-wetting surface with high surface tension.

Visual observation of bubble evolution was difficult *in-situ*, but was used for bubbles evolved under the same experimental conditions. It was noted that where there was a high coverage of the electrode with bubbles (often seen at the “aged” electrodes), coalescence events were not necessarily followed immediately by detachment. The large resulting bubbles would remain attached at the electrode and continue to grow until a further coalescence event occurred that would result in the majority of the bubbles on the electrode being removed in one very large detachment event. It is possible that this mechanism was responsible for some of the very large detachment events recorded at electrodes B and D.

5.5 Time domain and Fourier analysis of EQCM data

As detailed in chapter 4 and demonstrated in figure 5.2, the nucleation, growth and detachment model may oversimplify the real mechanism of bubble evolution at some electrodes where coalescence is possible. If the resonant frequency changes shown in figure 5.2 are consistent with a mechanism where there is little detachment, the sawtooth structure must be attributed to coalescence as well as detachment. In order to elucidate the behaviour depicted at all the electrodes the structure of the EQCM frequency transients must be studied in detail, characterising the exact shape and magnitude of the peaks. This is done by measuring the resonant frequency response as a function of time at different potentials within the region of bubble evolution. Fourier analysis is used to acquire the frequency at which these features appear.

5.5.1 Acquisition rate

It was shown in the previous section that the rate of bubble evolution varies according to the dominant mechanism. Detachment of larger bubbles is slow, whereas smaller bubbles detach at a faster rate. It is a logical step to increase the data acquisition rate in order to

increase the resolution of the sawtooth waves produced in the EQCM frequency response and therefore identify the frequency and magnitude of bubble events more clearly

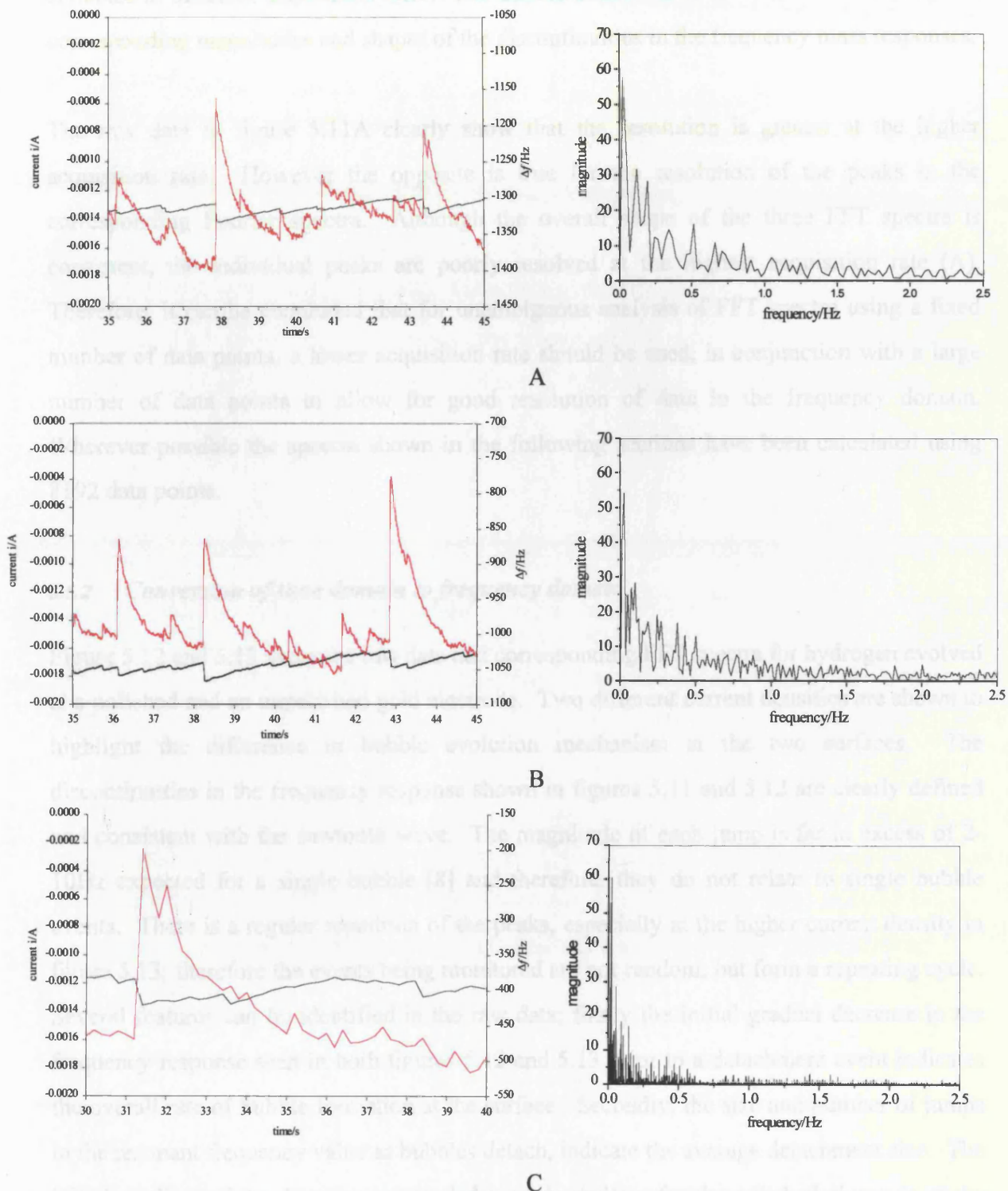


Figure 5.11 Left-hand panels: EQCM frequency response (in red) and simultaneous current response (in black) for hydrogen evolution at different acquisition rates (A) 100 Hz, (B) 50 Hz and (C) 5 Hz at an unpolished gold electrode from 0.1 M HClO₄. Right-hand panels: The corresponding FFT spectra of the raw data from the left-hand panels.

Figure 5.11A-C shows the evolution of hydrogen bubbles at a horizontal upward facing platinum electrode, where the gas is evolved at similar current densities and the data collected at different acquisition rates. The bubble behaviour is similar, as reflected by the corresponding magnitudes and shapes of the discontinuities in the frequency mass responses.

The raw data in figure 5.11A clearly show that the resolution is greater at the higher acquisition rate. However the opposite is true for the resolution of the peaks in the corresponding Fourier spectra. Although the overall shape of the three FFT spectra is consistent, the individual peaks are poorly resolved at the highest acquisition rate (A). Therefore, it can be concluded that for unambiguous analysis of FFT spectra using a fixed number of data points, a lower acquisition rate should be used, in conjunction with a large number of data points to allow for good resolution of data in the frequency domain. Wherever possible the spectra shown in the following sections have been calculated using 8192 data points.

5.5.2 Conversion of time domain to frequency domain

Figure 5.12 and 5.13 show the raw data and corresponding FFT spectra for hydrogen evolved at a polished and an unpolished gold electrode. Two different current densities are shown to highlight the difference in bubble evolution mechanism at the two surfaces. The discontinuities in the frequency response shown in figures 5.11 and 5.12 are clearly defined and consistent with the sawtooth wave. The magnitude of each jump is far in excess of 2-10Hz expected for a single bubble [8] and therefore, they do not relate to single bubble events. There is a regular repetition of the peaks, especially at the higher current density in figure 5.13; therefore the events being monitored are not random, but form a repeating cycle. Several features can be identified in the raw data; firstly the initial gradual decrease in the frequency response seen in both figures 5.12 and 5.13 prior to a detachment event indicates the overall rate of bubble formation at the surface. Secondly, the size and number of jumps in the resonant frequency value as bubbles detach, indicate the average detachment size. The initial gradient of the decrease in coupled mass is shallow for the polished electrode at the lowest current density (figure 5.12a) and increases at the higher current density (figure 5.12b).

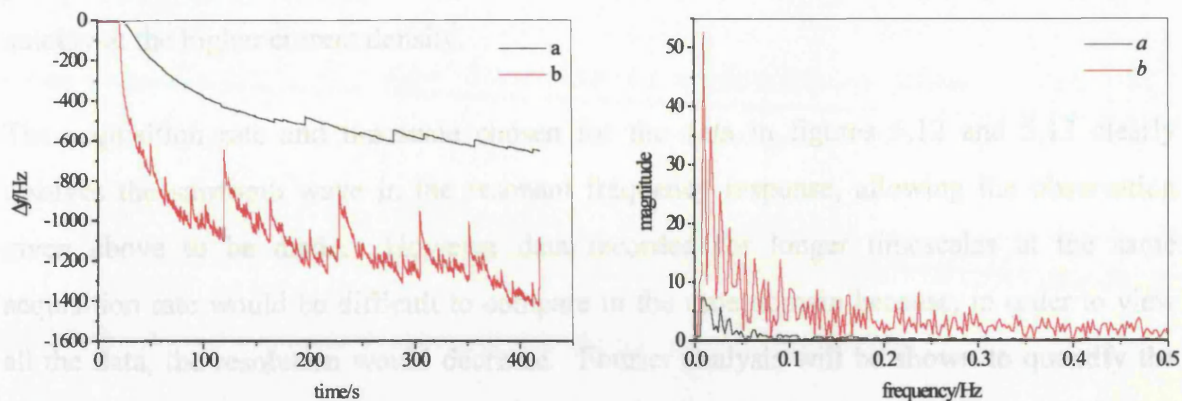
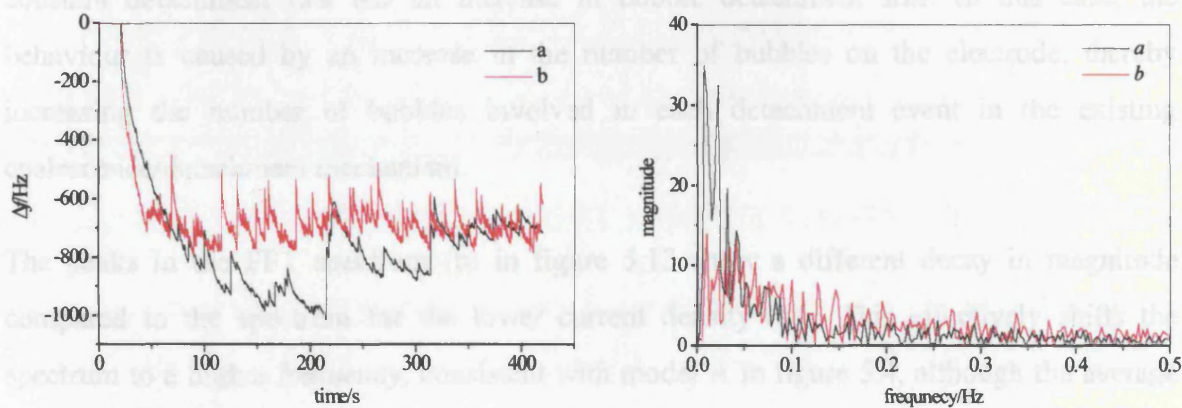


Figure 5.12 EQCM frequency response for hydrogen bubble evolution at horizontal polished gold electrode 0.1 M HClO_4 . The potential was stepped from 0 to -0.7 V (a) and -1 V (b) vs. SCE. Current density was approx. 0.8 mA cm^{-2} (a) and 6 mA cm^{-2} (b) respectively.



A

B

Figure 5.13 EQCM frequency response for hydrogen bubble evolution at horizontal unpolished gold electrode 0.1 M HClO_4 . The potential was stepped from 0 to -0.7 V (a) and -1 V (b) vs. SCE. Current density was approx. 4.4 mA cm^{-2} (a) and 12.2 mA cm^{-2} (b) respectively.

The shallow gradient indicates that there is a longer induction time for bubble nucleation or that a smaller number of nucleation sites are active. The larger jumps in resonant frequency at the higher current density are consistent with a larger number of bubbles on the electrode and therefore it can be concluded that the number of active nucleation sites increases with current density at the polished electrode. There is little difference in the initial gradient for the decrease in coupled mass at the unpolished electrode at different current densities. This suggests that all available nucleation sites are activated quickly, and the increase in current simply increases the activity at those sites. This is confirmed by the fact that the sizes of the jumps in resonant frequency are similar at both current densities, but the “steady state”

pattern, where there is very little general decrease in the coupled mass, is achieved more quickly at the higher current density.

The acquisition rate and timescale chosen for the data in figures 5.12 and 5.13 clearly resolves the sawtooth wave in the resonant frequency response, allowing the observation given above to be made. However data recorded for longer timescales at the same acquisition rate would be difficult to compare in the time domain because, in order to view all the data, the resolution would decrease. Fourier analysis will be shown to quantify the fluctuations in the EQCM frequency response and thereby enable unambiguous characterisation and comparison of these fluctuations for the different electrodes. The FFT spectrum (b) in figure 5.12 shows an increase in magnitude at all frequencies compared to the spectrum for (a). This behaviour is consistent with model B in figure 5.4, showing a constant detachment rate but an increase in bubble detachment size. In this case, the behaviour is caused by an increase in the number of bubbles on the electrode, thereby increasing the number of bubbles involved in each detachment event in the existing coalescence/detachment mechanism.

The peaks in the FFT spectrum (b) in figure 5.13 show a different decay in magnitude compared to the spectrum for the lower current density (a). This effectively shifts the spectrum to a higher frequency, consistent with model A in figure 5.4, although the average magnitude has increased. The smaller magnitude of the low frequency detachment events is due to a smaller volume of gas resident on the electrode. In summary the rate of detachment at the existing nucleation sites is increased but no new nucleation sites are activated.

5.5.3 Appearance of EQCM frequency response features in FFT spectra

It was shown in section 5.4.3 that discontinuities in the resonant frequency response for hydrogen evolution at gold electrodes were characterised by a sawtooth wave. However, this behaviour was not seen at the platinum and RTO electrodes, due to the detachment of bubbles prior to significant growth at the electrode. It has also been suggested that not all of the discontinuities arise from detachment events; coalescence of bubbles that remain attached to the electrode may be a significant contributing factor. This sawtooth behaviour was further characterised by using visual observation of the electrode during the EQCM experiment.

5.5.3.1 Change in mechanism

It was found that two very distinct characteristics were produced in the EQCM frequency response by different modes of bubble behaviour; each is shown in figure 5.14.

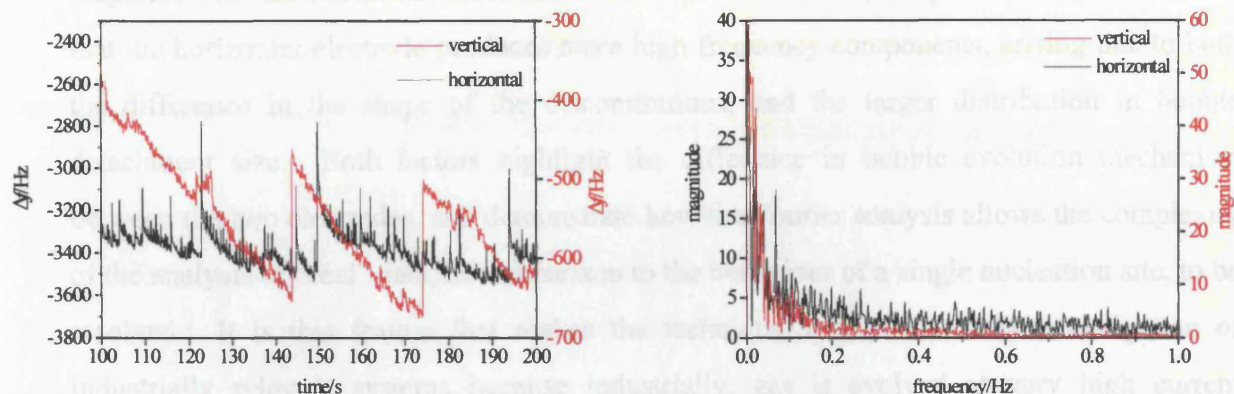


Figure 5.14 EQCM frequency response and corresponding FFT spectra for hydrogen evolution from 0.1 M HClO₄ at different unpolished gold electrodes with a high surface tension, horizontal (shown in black) and vertical (shown in red).

The current density was 8 mA cm⁻² and 6 mA cm⁻² respectively.

The data in figure 5.14 for hydrogen bubble evolution at the vertical unpolished gold electrode depicts a simple nucleation, growth, coalescence and detachment cycle. Contrastingly, the data for hydrogen bubble evolution at the horizontal unpolished gold electrode depicts a more complex bubble evolution cycle of nucleation, growth, coalescence, further growth and nucleation followed by a combined coalescence/detachment event. This was confirmed by visual observation. The major characteristic of this cycle is the very steep decrease in coupled mass following each large discontinuity, arising as large areas of the electrode are “swept clean” by the detachment of large bubbles. Following this is the rapid nucleation and growth of new bubbles. The smaller magnitude of the jumps and the shallower decrease in coupled mass following each jump seen at the vertical electrode indicates that the average detachment size is smaller and there is not significant growth following each detachment event. This suggests that the detachment events were isolated and involved a smaller number of bubbles, and therefore the distribution of bubbles on the electrode was not altered significantly during a single detachment event.

Small samples of the raw coupled mass data are shown in figure 5.14 in order to resolve individual discontinuities. The corresponding FFT spectra were calculated from a much

larger range of data. The two spectra are shown on separate scales in order to directly compare their overall shapes. By matching the magnitude of the peaks at approximately 0.03 Hz (as shown for the raw data), it can be seen that the magnitude of the peaks in the FFT spectrum recorded at the vertical electrode decays sharply, whereas the decay in peak magnitude for the horizontal electrode is more gradual. Comparing the two spectra shows that the horizontal electrode produces more high frequency components, arising due to both the difference in the shape of the discontinuities, and the larger distribution in bubble detachment size. Both factors highlight the difference in bubble evolution mechanism between the two electrodes, and demonstrate how the Fourier analysis allows the complexity of the analysis of “real” data, in comparison to the behaviour of a single nucleation site, to be resolved. It is this feature that makes the technique applicable to the investigation of industrially relevant systems because industrially, gas is evolved at very high current densities where the electrodes are designed to produce large number of nucleation sites, giving rise to complex patterns of behaviour.

Figure 5.15 also shows characteristically different bubble behaviour, but this time for the same electrode in different orientations for which the change in mechanism is due to the difference in the force balance governing detachment, and is not a function of the chemical composition of the surface. There are similarities between figures 5.14 and 5.15 and both show that there is a larger distribution in detachment size at the horizontal electrode. However the mechanism at the cleaned unpolished horizontal electrode (shown in figure 5.15) is one where there are a large number of detachment events, and significantly less coalescence than observed for the electrode with high surface tension (shown in figure 5.14). This is reflected in the smaller peak magnitude on the FFT spectra. The mechanism at the vertical electrode is virtually identical for both electrodes; the simple nucleation, growth, coalescence and detachment cycle is retained. The magnitudes of the low frequency peaks on the two spectra have been matched as before, and comparing them it can be seen that, whilst the spectra for the horizontal electrode again show larger peaks at higher frequencies the difference is less significant, especially at frequencies, in excess of 0.5 Hz. This is due to a similar shape of both the coupled mass responses and the absence of the major coalescence events.

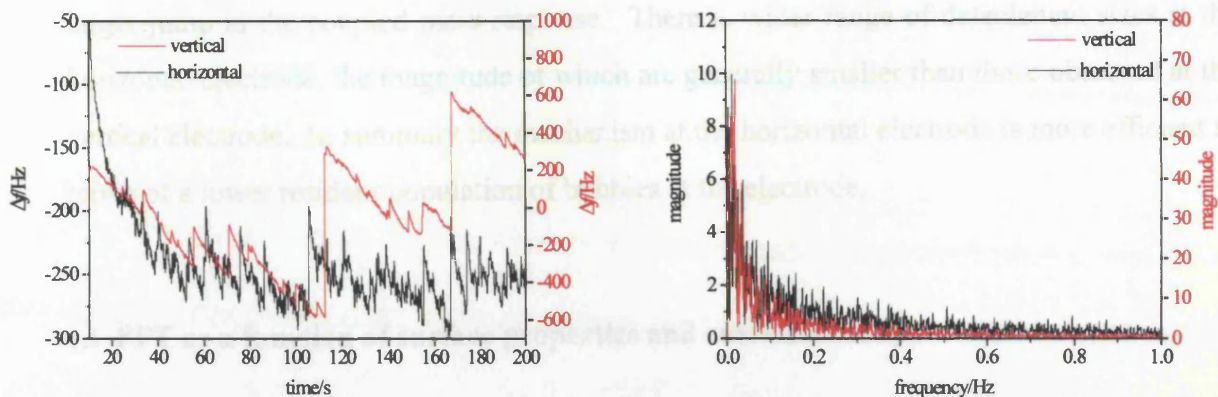


Figure 5.15 EQCM frequency response and corresponding FFT spectra for hydrogen evolution from 0.1 M HClO_4 at a clean unpolished gold electrode in a horizontal (shown in black) and vertical (shown in red) orientation. The current density is 9.92 mA cm^{-2} and 9.6 mA cm^{-2} respectively.

5.5.3.2 Change in activity

Figure 5.16, shows the coupled mass response and corresponding FFT spectra for hydrogen evolution where the mechanism is independent of the orientation of the electrode, possibly due the lower surface tension, which facilitates bubble detachment from the horizontal electrode. However there is a change in activity, reflected by a much closer correlation between the two FFT spectra.

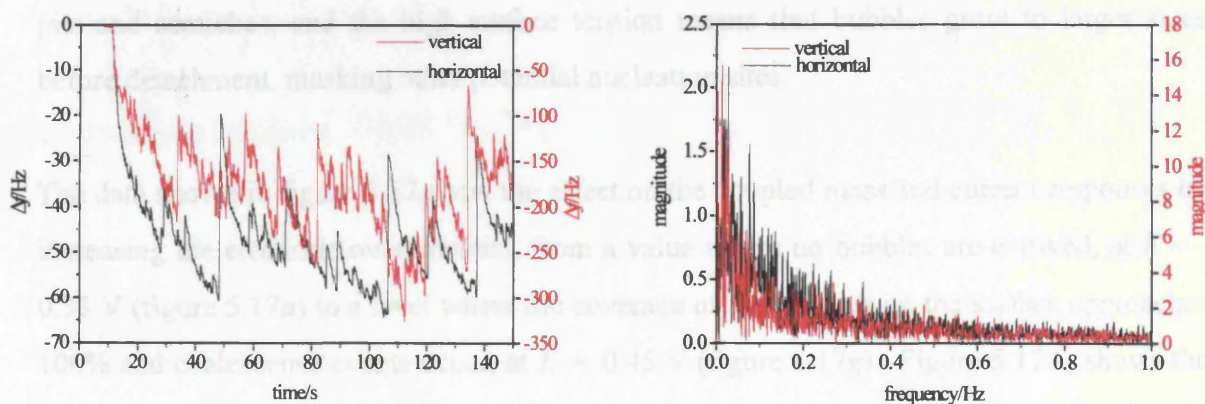


Figure 5.16 EQCM frequency response and corresponding FFT spectra for hydrogen evolution at 12 mA cm^{-2} from 0.1 M HClO_4 at a clean polished gold electrode in a horizontal (shown in black) and vertical (shown in red) orientation

The increased activity at the vertical electrode means that bubble detachment events cause a larger jump in the coupled mass response. There is wider range of detachment sizes at the horizontal electrode, the magnitude of which are generally smaller than those observed at the vertical electrode. In summary the mechanism at the horizontal electrode is more efficient in terms of a lower resident population of bubbles at the electrode.

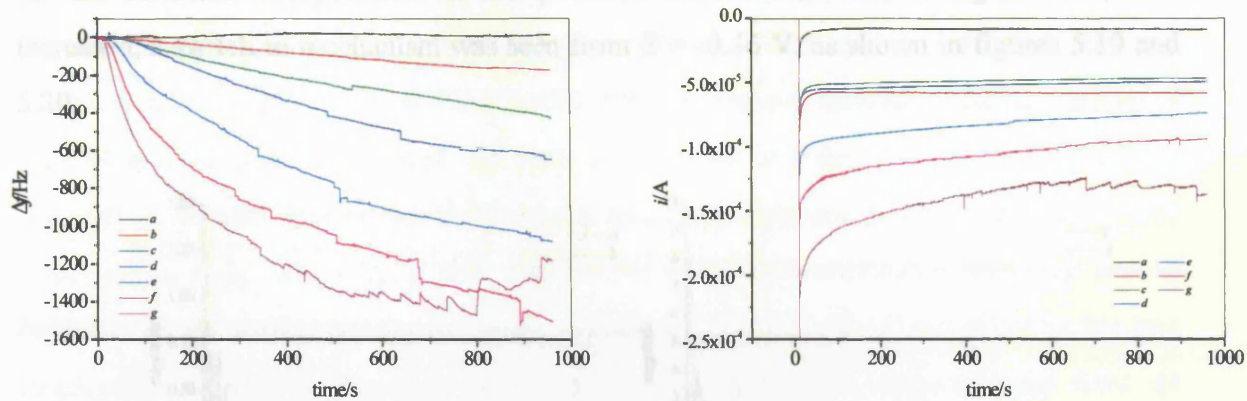
5.6 FFT as a function of surface properties and current density

In this section, the FFT analysis of bubble evolution at gold, platinum and RTO electrodes is presented and the functionality of bubble behaviour with two parameters, current density and electrode orientation, is examined. Increasing the supersaturation of the electrolyte may cause more nucleation sites to be activated or an increase the growth rate of existing bubbles. By changing the orientation of the electrode between horizontal (upward-facing) and vertical, the force balance between buoyancy and surface tension that governs bubble detachment is altered. Also bubbles rising up the vertical face of the electrode may disrupt the growth of resident bubbles, a process that cannot occur at a horizontal electrode.

5.6.1 *Low surface activity: Hydrogen evolution at polished gold*

A polished gold electrode with high surface tension was chosen in order to minimise the number of potential nucleation sites. The highly polished surface has only a small number of pits and scratches, and the high surface tension means that bubbles grow to larger sizes before detachment, masking other potential nucleation sites.

The data shown in figure 5.17 show the effect on the coupled mass and current responses by increasing the electrode overpotential, from a value where no bubbles are evolved, at $E = -0.35$ V (figure 5.17a) to a level where the coverage of the bubbles on the surface approaches 100% and coalescence events occur, at $E = -0.45$ V (figure 5.17g). Figure 5.17A, shows the coupled mass decreasing steadily at each potential, as bubbles nucleate at the surface but do not detach. The gradient ($d\Delta f/dt$) increases with current density and there is also an increase in the value of Δf (equivalent to $\Delta f_{bubble\ layer}$) at the end of each experiment. This indicates that the number of active nucleation sites, and therefore the overall rate of nucleation, increases with current density.



A

B

Figure 5.17 EQCM frequency response (A), and corresponding current (B) for hydrogen evolution from 0.1 M HClO_4 at a polished vertical electrode (area = 0.25 cm^2) with a high surface tension where the electrode potential for each curve is given by a = -0.35 V, b = -0.40 V, c = -0.41 V, d = -0.42 V, e = -0.43 V, f = -0.44 V, g = -0.45 V.

Visual observations of the surface confirmed that the number of active nucleation sites increased rapidly with electrode overpotential. For example: no nucleation sites were active when $E = -0.35 \text{ V}$, 5 nucleation sites were active at $E = -0.4 \text{ V}$, 6 sites are active at $E = -0.41 \text{ V}$, 10 sites are active by $E = -0.43 \text{ V}$ and 100% of the surface was covered at $E = -0.45$. The rate of detachment was not seen to increase significantly, and bubble detachment did not occur until a current density of 6 mA cm^{-2} (during the later stages of experiment g). However, the rate of coalescence increased steadily, causing the small discontinuities in the resonant frequency seen in figure 5.17A.

The change in gradient ($d\Delta f/dt$), i.e. the nucleation activity, is not reflected in the FFT spectra (figure 5.18). The coupled mass data are adjusted so that the mean value is zero before the FFT is calculated, and therefore only the frequency of the discontinuities is shown in the spectra. As expected from the raw data shown in figure 5.17, all of the corresponding FFT spectra have the same shape as there is no increase in the frequency of the coalescence events. However, the size of the jumps in the resonant frequency response caused by a coalescence event does increase at higher current densities, and this is shown by a general increase in magnitude of the FFT spectra in figure 5.18.

As the electrode overpotential at the polished electrode (shown in figure 5.17) was increased, a switch in mechanism was seen from $E = -0.46$ V, as shown in figures 5.19 and 5.20.

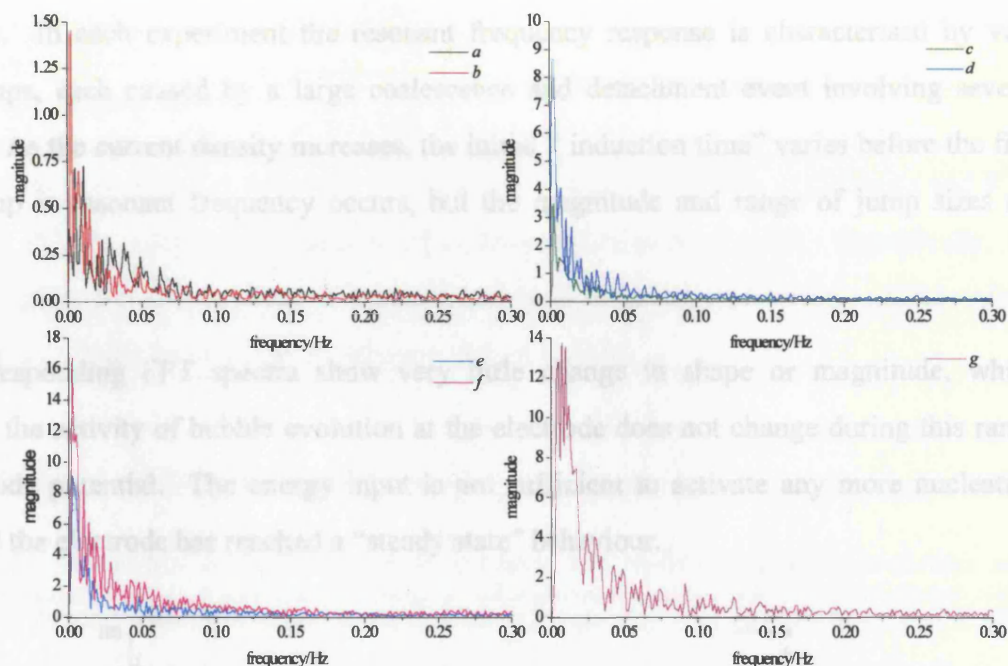


Figure 5.18 FFT spectra of the EQCM frequency responses shown in figure 5.17. Where a-g are the corresponding electrode potentials defined in figure 5.17.

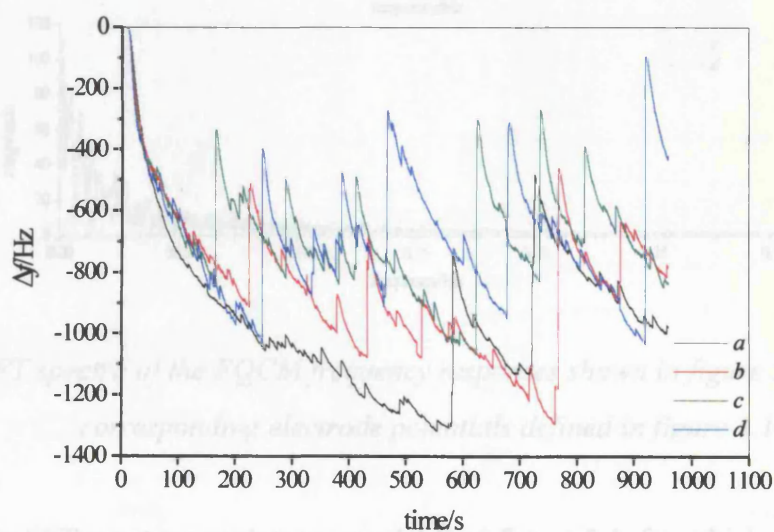


Figure 5.19 EQCM coupled mass response for hydrogen evolution from 0.1 M HClO_4 at a polished vertical electrode with a high surface tension where the electrode potential for each curve is given by a = -0.46 V, b = -0.47 V, c = -0.48 V, d = -0.49 V.

Figure 5.19 shows the EQCM frequency response recorded at the higher overpotentials, the measured current density was between 0.5 and 2 mA cm⁻². The initial gradient (dΔf/dt) and overall trend in coupled mass is the same for experiments *a-d*, because a similar number of nucleation sites were active and the same coalescence and detachment mechanism was dominant. In each experiment the resonant frequency response is characterised by very large jumps, each caused by a large coalescence and detachment event involving several bubbles. As the current density increases, the initial “induction time” varies before the first large jump in resonant frequency occurs, but the magnitude and range of jump sizes are similar.

The corresponding FFT spectra show very little change in shape or magnitude, which confirms the activity of bubble evolution at the electrode does not change during this range of electrode potential. The energy input is not sufficient to activate any more nucleation sites, and the electrode has reached a “steady state” behaviour.

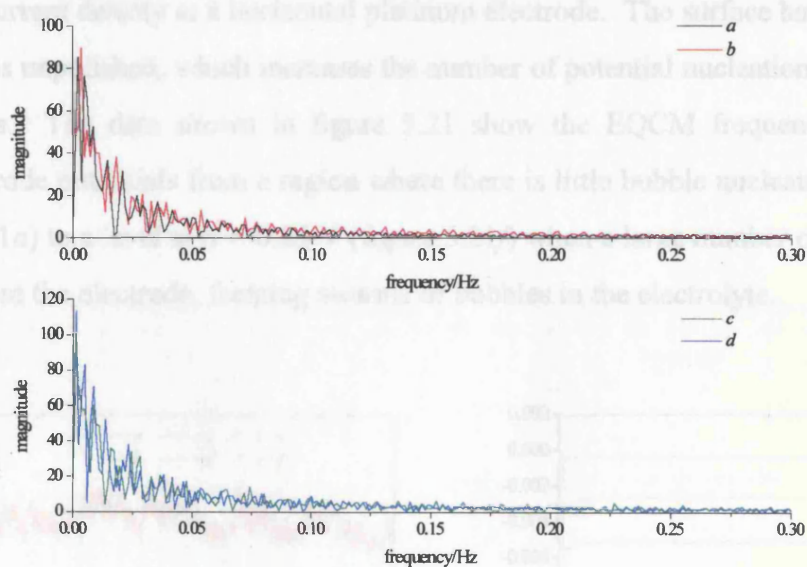


Figure 5.20 FFT spectra of the EQCM frequency responses shown in figure 5.19, where *a-g* are the corresponding electrode potentials defined in figure 5.18.

The trend in the FFT spectra correlates to model B in figure 5.4, for which detachment size increases at a constant detachment rate, i.e. the peaks remain at the same frequency but increase in magnitude. The high surface tension of the electrode inhibits bubble detachment and due to the presence of adhered bubbles masking potential nucleation sites on the surface, further nucleation can only occur following a large coalescence and detachment event. The

steep gradient of the coupled mass response that follows each discontinuity means that subsequent nucleation and growth are rapid and therefore bubble detachment is the rate-limiting step in the bubble evolution mechanism at this surface, a generally inefficient mechanism for bubble evolution.

5.6.2 High surface activity

It was shown in section 5.4.3 that the mechanism of bubble evolution at platinum and RTO electrodes differs from the mechanism of hydrogen evolution at gold. Specifically, the growth regime and the number of bubbles involved in coalescence events differ, which consequently affects the average detachment size of bubbles.

5.6.2.1 Hydrogen evolution at platinum

Figure 5.21 shows the EQCM frequency response for hydrogen bubble evolution as a function of current density at a horizontal platinum electrode. The surface has a low surface tension, and is unpolished, which increases the number of potential nucleation sites from pits and scratches. The data shown in figure 5.21 show the EQCM frequency response at various electrode potentials from a region where there is little bubble nucleation at $E = -0.35$ V (figure 5.21a) to a level at $E = -0.85$ V (figure 5.21f) when a large number of bubbles were detaching from the electrode, forming swarms of bubbles in the electrolyte.

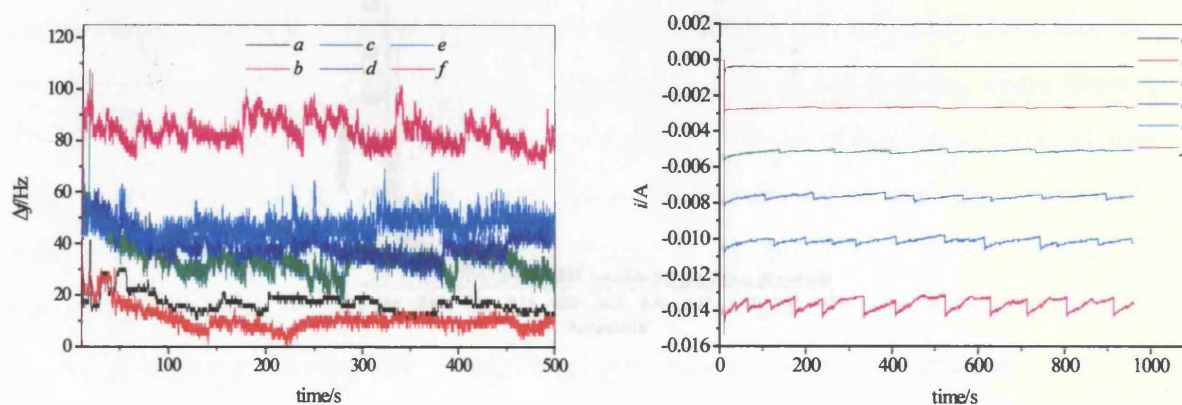


Figure 5.21 EQCM frequency response (A), and corresponding current (B) for hydrogen evolution from 0.1 M HClO₄ at a horizontal platinum electrode (area = 0.25 cm²). Where electrode potential for each curve is given by a = -0.35 V, b = -0.45 V, c = -0.55 V, d = -0.65 V, e = -0.75 V, f = -0.85 V.

The sawtooth wave is less evident in the raw data, and the individual discontinuities in the resonant frequency response cannot be resolved. This is because bubbles detach from the electrode before significant growth has occurred, allowing for a larger number of detachment events, and so increasing the detachment rate. There is not significant coalescence between neighbouring bubbles and therefore the population of bubbles on the electrode does not change significantly due to individual detachment events. The low level of bubble residence means there is no gradual decrease in the coupled mass, and the jumps lie on a linear baseline.

The corresponding FFT spectra in figure 5.22 reflect the changes seen in the resonant frequency response. There is an increase in the magnitude as a function of current density, which is mostly consistent with model B in figure 5.4. This is caused by an increase in the number of bubbles at the electrode whilst the detachment mechanism is unchanged.

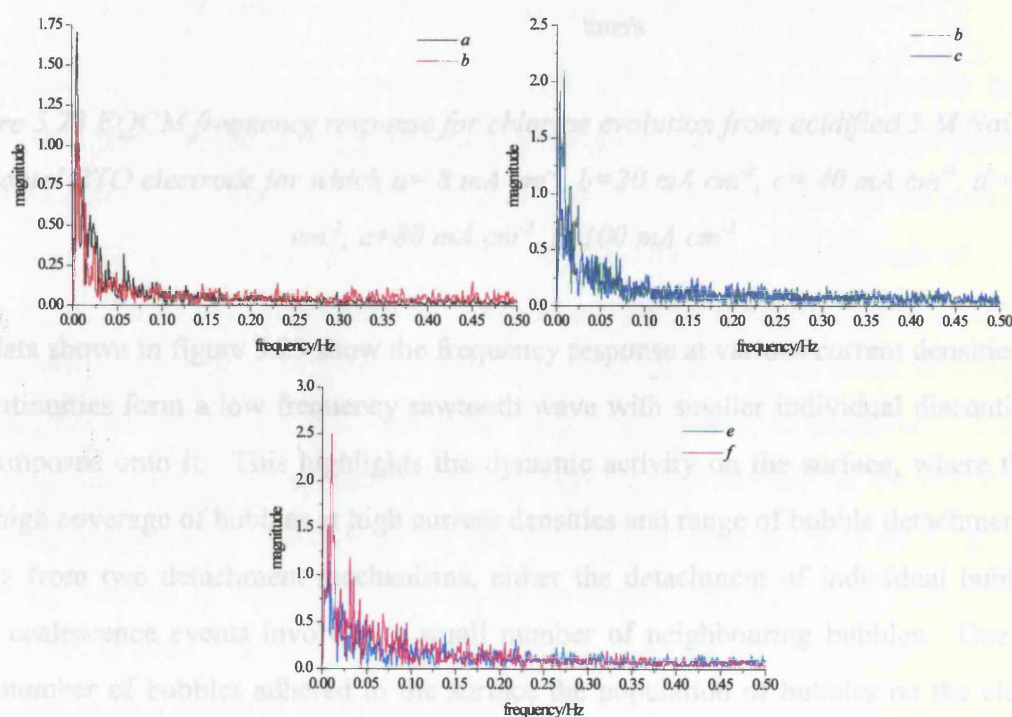


Figure 5.22 FFT spectra of the EQCM frequency response shown in figure 5.21, the spectra are grouped for clarity.

5.6.2.2 Chlorine evolution at RTO

Figure 5.23 shows the EQCM frequency response for chlorine bubble evolution as a function of current density at a horizontal RTO electrode, which has a low surface tension and a large number of deep cracks at the surface, providing potential nucleation sites.

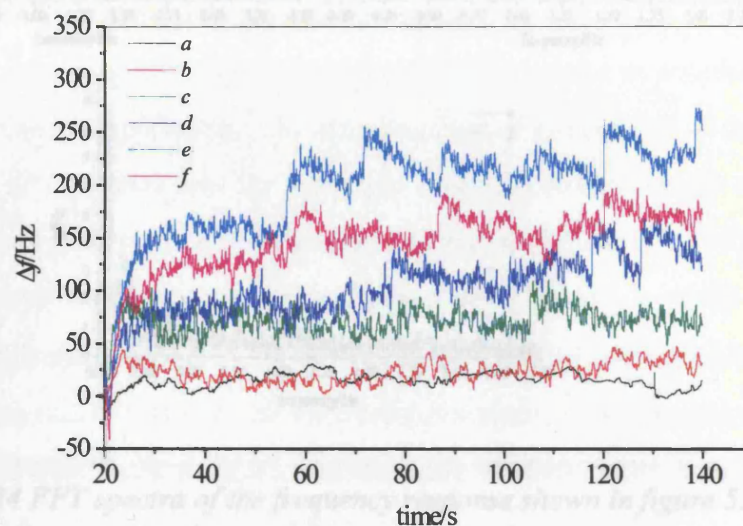


Figure 5.23 EQCM frequency response for chlorine evolution from acidified 5 M NaCl at a horizontal RTO electrode for which $a=8 \text{ mA cm}^{-2}$, $b=20 \text{ mA cm}^{-2}$, $c=40 \text{ mA cm}^{-2}$, $d=60 \text{ mA cm}^{-2}$, $e=80 \text{ mA cm}^{-2}$, $f=100 \text{ mA cm}^{-2}$

The corresponding FFT spectra in figure 5.24 show that, as the current density increases the magnitude of the peaks in the region 0 to 0.25 Hz on the x-axis increases. The magnitude of the peaks in the region 0.25 to 1.5 Hz decreases. This is because the detachment size of individual bubbles increases with increasing current density.

The data shown in figure 5.23 show the frequency response at various current densities. The discontinuities form a low frequency sawtooth wave with smaller individual discontinuities superimposed onto it. This highlights the dynamic activity on the surface, where there is very high coverage of bubbles at high current densities and range of bubble detachment sizes arising from two detachment mechanisms, either the detachment of individual bubbles or small coalescence events involving a small number of neighbouring bubbles. Due to the large number of bubbles adhered to the surface the population of bubbles on the electrode does not change significantly due to individual detachment events. The gradual decrease in coupled mass associated with bubble residence on the electrode is not observed; this has been attributed to the gradual flooding of the porous surface with electrolyte [10].

Different surface properties have been shown to cause different trends in bubble evolution as a function of current density. The results below show the trends in bubble evolution for two similar electrode surfaces where the electrode is placed in a different orientation to facilitate

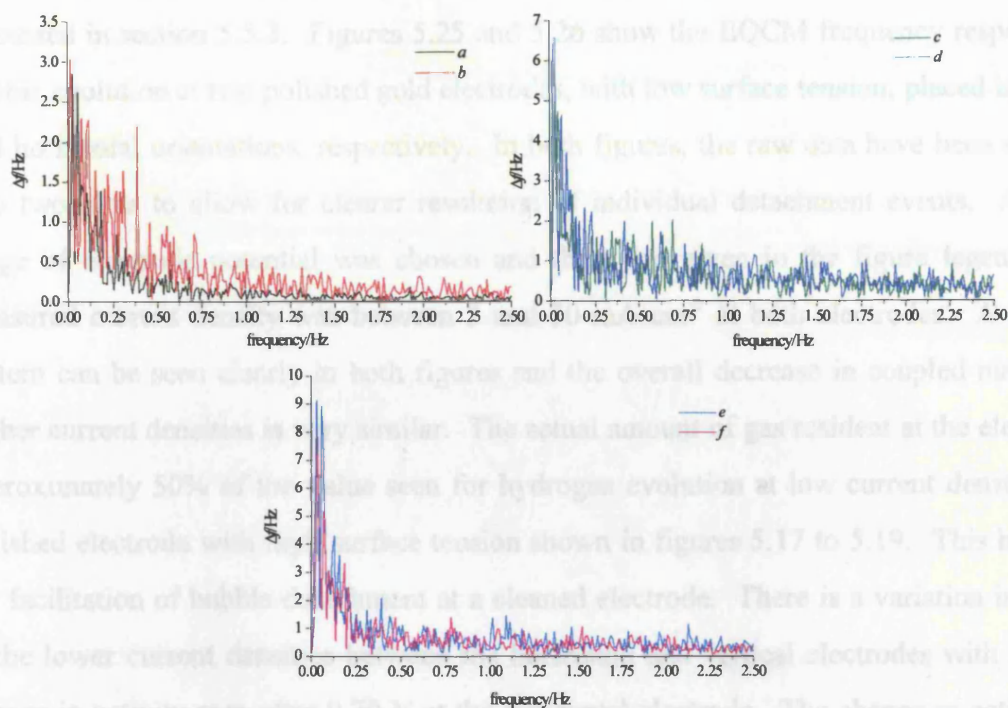


Figure 5.24 FFT spectra of the frequency response shown in figure 5.23.

The corresponding FFT spectra in figure 5.24 show that, as the current density increases there is an increase in the average magnitude and a change in the distribution of peaks along the frequency axis. At higher current densities, whilst the magnitude of the peaks in the region 0 to 0.25 Hz on the frequency spectra increases, the relative magnitude of the peaks in the region 0.25 to 1.5 Hz decreases. This is because the detachment size of individual bubbles does not increase with current density. Although there is an initial increase in the average bubble detachment size, this arises from the increase in magnitude of the low frequency detachment events, caused by coalescence. This can be attributed to the increasing influence of coalescence on the detachment mechanism, arising due to the increasing numbers of bubbles resident on the electrode. Although it was not possible to confirm this visually, it is most likely that increase in the number of bubbles was caused by an increase in the number of active nucleation sites.

5.6.3 Electrode orientation

Different surface properties have been shown to cause different trends in bubble evolution as a function of current density. The results below show the trends in bubble evolution for two similar electrode surfaces where the electrode is placed in a different orientation to facilitate

or inhibit various bubble detachment mechanisms, for example to the role of coalescence as discussed in section 5.5.3. Figures 5.25 and 5.26 show the EQCM frequency responses for bubble evolution at two polished gold electrodes, with low surface tension, placed in vertical and horizontal orientations, respectively. In both figures, the raw data have been separated into two plots to allow for clearer resolution of individual detachment events. A similar range of electrode potential was chosen and these are given in the figure legends. The measured current density was between 3 and 50 mA cm⁻² at both electrodes. A sawtooth pattern can be seen clearly in both figures and the overall decrease in coupled mass at the higher current densities is very similar. The actual amount of gas resident at the electrode is approximately 50% of the value seen for hydrogen evolution at low current densities on a polished electrode with high surface tension shown in figures 5.17 to 5.19. This highlights the facilitation of bubble detachment at a cleaned electrode. There is a variation in activity at the lower current densities between the horizontal and vertical electrodes with a sudden change in activity seen after 0.70 V at the horizontal electrode. The change in activity as a function of current density is much more gradual at the vertical electrode and the level of activity in terms of the number of detachment events is generally higher.

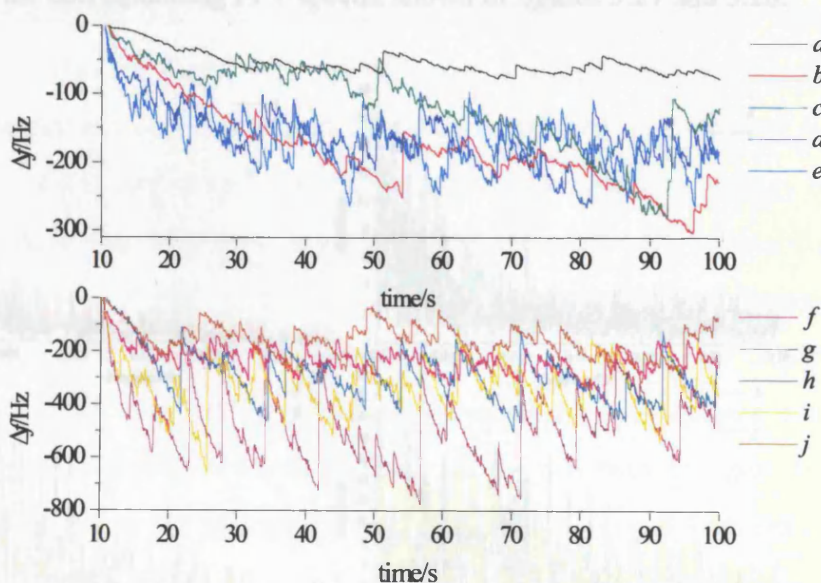


Figure 5.25 EQCM frequency response for hydrogen evolution from 0.1 M HClO₄ at a vertical polished gold electrode for which $a = -0.50$ V, $b = -0.55$ V, $c = -0.60$ V, $d = -65$ V, $e = -0.70$ V, $f = -0.75$ V, $g = -0.80$ V, $h = -0.85$ V, $i = -0.90$ V, $j = -0.95$ V.

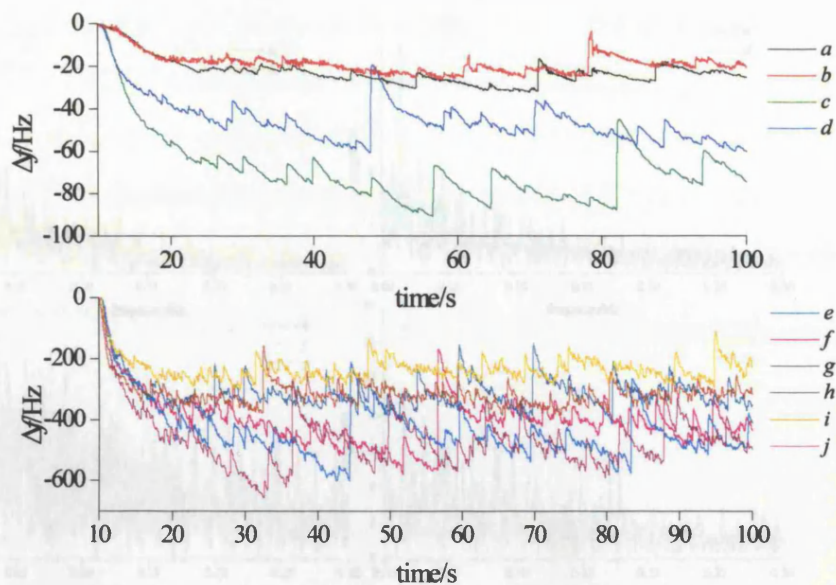


Figure 5.26 EQCM frequency response for hydrogen evolution from 0.1 M HClO_4 at a horizontal polished gold electrode for which, $a = 0.50 \text{ V}$, $b = 0.55 \text{ V}$, $c = 0.60 \text{ V}$, $d = 65 \text{ V}$, $e = 0.70 \text{ V}$, $f = 0.75 \text{ V}$, $g = 0.80 \text{ V}$, $h = 0.85 \text{ V}$, $i = 0.90 \text{ V}$, $j = 0.95 \text{ V}$.

The variation in the activity at the two electrodes and the trends in activity with current density are more apparent in the corresponding FFT spectra shown in figures 5.27 and 5.28.

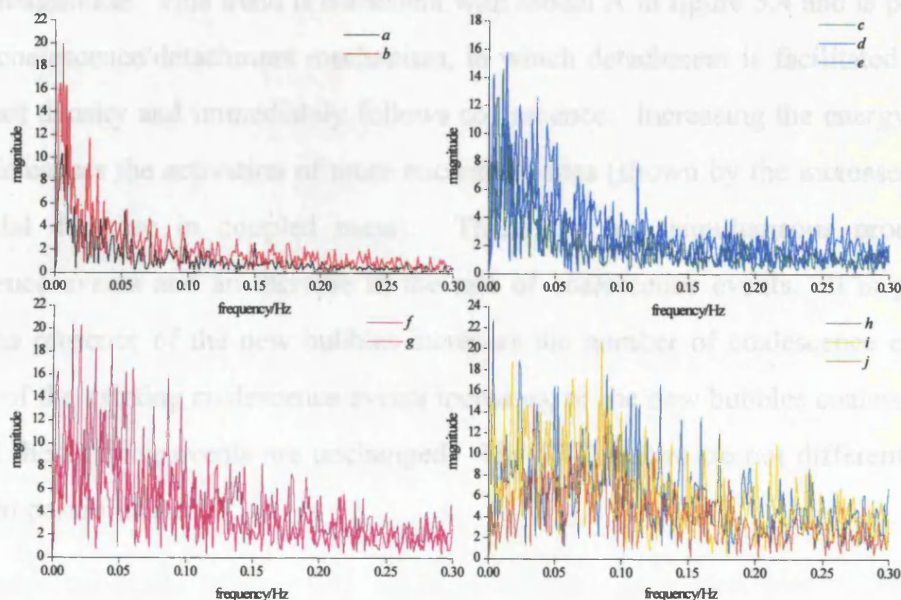


Figure 5.27 FFT spectra of the EQCM frequency responses shown in figure 5.25

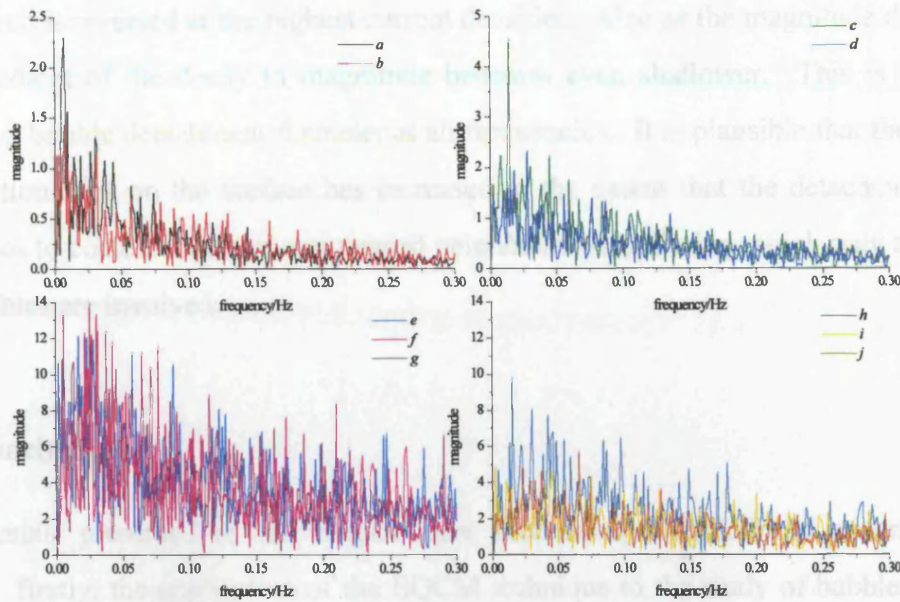


Figure 5.28 FFT spectra of the EQCM frequency responses shown in figure 5.26.

The behaviour at the vertical electrode shown in figure 5.27 shows the predominance of peaks in the frequency spectrum shift along the frequency axis as the current density increases. In addition, the decay in magnitude is shallow, effectively broadening the distribution of detachment frequencies on the FFT spectrum, and gradually increasing the overall magnitude. This trend is consistent with model A in figure 5.4 and is produced by a simple coalescence/detachment mechanism, in which detachment is facilitated at all values of current density and immediately follows coalescence. Increasing the energy input to the electrode causes the activation of more nucleation sites (shown by the increased gradient of the initial decrease in coupled mass). There are two simultaneous processes: more coalescence events and an increase in the rate of coalescence events. It is plausible that either the presence of the new bubbles increases the number of coalescence events, whilst the rate of the existing coalescence events increases, or the new bubbles coalesce at a higher rate and the existing events are unchanged. The FFT spectra cannot differentiate between these two possibilities.

The behaviour at the horizontal electrode, and therefore the analysis of the FFT spectra, is more complex. The distribution of peak sizes i.e. the shape of the spectrum does not change significantly with current density. The absolute value of the magnitude does change with current density, although not according to a simple trend. There is an initial increase

suggesting the number of bubbles involved in the coalescence events increases. However, this trend is reversed at the highest current densities. Also as the magnitude decreases again, the gradient of the decay in magnitude becomes even shallower. This is due to a more uniform bubble detachment diameter at all frequencies. It is plausible that the population of nucleation sites on the surface has increased to the extent that the detachment mechanism switches to coalescence between nearest neighbours only, during which only a small number of bubbles are involved.

5.7 Conclusions

The results presented in this chapter have successfully fulfilled two general aims of the study: firstly, the application of the EQCM technique to the study of bubble evolution as a function of various electrode properties, and secondly, the development of the novel analysis technique of Fourier transformation of EQCM data. It has been shown that EQCM analysis provides an insight into the activities of bubbles at an electrode. The technique does not rely on the interpretation of individual bubbles, and therefore lengthy data analysis is not required. This feature enables the EQCM analysis of bubble evolution systems that are too complex to be studied using a direct observation technique, such as fast frame video. It has been proved that the EQCM is a flexible technique enabling the surface features of an electrode to be modified, by coating it with different materials. Further modification of the experimental design allowed the same electrode surface to be positioned in a variety of orientations. RTO was successfully coated onto a quartz crystal, using the spray-bake method providing an industrially relevant sample characterised by a “mud flat” microstructure containing deep cracks.

The effect of parameters such as surface roughness and morphology, chemical composition and electrode orientation were established. Data analysis methods were developed for EQCM analysis in both the time domain and the frequency domain, and the results from both were compared to models of the EQCM coupled mass response expected for bubble behaviour based on the activity of an individual nucleation site. This chapter has demonstrated the validity of the novel use of FFT analysis of the EQCM coupled mass response as a tool for providing mechanistic insight into the evolution of bubbles at a variety of surfaces. Using this technique it has proved possible to distinguish between different

bubble evolution mechanisms. This allows the characteristics of bubble behaviour to be defined and correlated to the surface properties, an important fundamental step in the application of this technique to complex systems. Several parameters were identified. The initial gradient in the EQCM coupled mass response is related to the overall nucleation rate. The shape of the discontinuities determines the dominant detachment mechanism. Finally, the general level of activity (number of discontinuities) in the coupled mass response provides an insight into the ability of bubbles to detach from the surface.

5.7.1 *Surface properties*

The bubble evolution mechanism was found to be similar on both polished and unpolished gold, nucleation was facilitated at both surfaces, and detachment was primarily through coalescence of neighbouring bubbles. Increasing the surface roughness increased the number of active nucleation sites on the surface. The sawtooth wave structure, upon which the theoretical model was based, arises in the measured resonant frequency response. However, it is not caused by the detachment of individual bubbles, but by the simultaneous action of multiple bubbles and is mainly attributed to a combined coalescence and detachment mechanism. The shape of the sawtooth wave differed, specifically its amplitude and the slope of the decay, depending on the dominant mechanism. Where a large number of bubbles were involved in a multiple coalescence event, rapid nucleation and growth followed a larger sized detachment event, causing a steep decay on the sawtooth wave. This mechanism was prevalent at horizontal electrodes where there was a high population of bubbles on the surface.

The bubble evolution mechanism was characteristically different at the platinum and RTO electrodes. Although coalescence events occurred, they were less significant in the detachment mechanism, as there was only limited bubble growth at the electrode. Consequently the average bubble detachment size was much smaller at these electrodes, and the EQCM frequency response was not characterised by a sawtooth wave. The surface finish for the platinum and unpolished electrodes is very similar, and therefore this change in mechanism cannot be attributed simply to the surface morphology (although this property cannot be ruled out for RTO electrodes). It is possible that the electrocatalytic properties of the electrode influence the detachment size. For example, the fast kinetics of both the

chlorine evolution reaction and the hydrogen evolution reaction may increase the local supersaturation levels at the electrode, enhancing the growth rate of bubbles and activating more nucleation sites. Another factor is the surface tension at the electrode interface, which increases due to adsorbed impurities, inhibiting bubble detachment and thereby lowering activity. A high surface tension was observed at “aged” gold electrodes, possibly caused by the introduction of impurities by the electrolyte. Interestingly, this effect was not observed at the platinum and RTO electrodes. In conclusion the efficiency of the surface in terms of bubble detachment is similar for both platinum and RTO electrodes, and both are more efficient than the gold electrode.

5.7.2 FFT as a diagnostic tool

Fourier analysis of EQCM frequency responses data provides a method of directly comparing spectra, regardless of the underlying processes and timescale of the experiment. The FFT spectrum was shown to be useful in highlighting trends in activity as a function of current density, and in quantifying the distribution of bubble detachment sizes. For example, it is difficult to determine the distribution in detachment sizes by studying the data in the time domain for simple bubble evolution mechanisms, when a small number of nucleation sites are activated at low current density, and virtually impossible at high current densities. Also it is difficult to establish the magnitude of a jump in the frequency response when it is superimposed on a non-linear baseline. In order to resolve individual discontinuities in the frequency response, only a small section of the data can be viewed. This may lead to ambiguous analysis if assumptions are made when only part of the bubble evolution cycle is visible. The FFT spectra were calculated using all of the recorded data points, providing a more accurate analysis of the activity on the surface. Fourier analysis is useful tool to deconvolute the complex resonant frequency response, although this is simplified by correlating the spectra with visual observations.

Comparing the trends in the FFT spectra to the models expected for ideal bubble behaviour, it was established that the most common effect of increasing the current density was an increase the magnitude of detachment events, but not an increase in detachment rate.

5.8 Future Work

One of the technologically orientated aims of this study was to determine whether there is significant residence of chlorine bubbles at the RTO electrode, since the adherence of bubbles to the electrode blocks those sites to further electrochemical reaction. Interestingly, this parameter was hard to define at the RTO surface, due to flooding of the porous surface by the electrolyte. Visual observations confirmed that there was significant coverage of the electrode with bubbles, but this did not hinder bubble detachment, in fact the surface was highly active. The wettability of the electrode may itself be of economic concern, because if there is a significant area of the electrode that is not in contact with the electrolyte then only part of the surface is being utilised for chlorine evolution and further inefficiency is introduced. The EQCM is the ideal apparatus to study this phenomena and more work in the area would enable the two simultaneous processes of pore flooding and bubble evolution to be separated, and establish whether the two processes are related.

Although the quartz crystal electrodes were successfully modified using the spray-bake technique, as an *ex-situ* preparation, significant developmental work was needed to obtain the correct thickness of the oxide layer, in order that its chemical and physical properties were comparable to those of a commercial electrodes, but also without overloading the crystal and preventing it from oscillating. Using the EQCM technique, an RTO electrode surface could be prepared *in-situ* by an electrodeposition or sol-gel technique whilst monitoring the mass being deposited onto the crystal. This would allow the amount of material deposited to be controlled more carefully. Also, the ratio of metal oxides could be varied to extend the study of the effect of surface properties on bubble behaviour. Different deposition techniques could be used to modify the surface morphology.

The EQCM has been shown to be a flexible instrument that allows the physical properties of the experimental set-up to be modified. Changing other physical properties, such as the atmospheric pressure above the electrolyte or the temperature of the cell, would provide control over further parameters upon which the bubble evolution mechanism is known to be dependent. Finally much of the analysis in this chapter has relied upon visual observation to support the resonant frequency and current data. Obviously, for the more complex systems the EQCM technique would be enhanced by its combination with a direct observation technique, and by correlating both sets of data.

1. Carr, M. W.; Hillman, A. R.; Lubetkin, S. D.; Swann, M. J., *J. Electroanal. Chem.*, **1989**, *267*, 313-320.
2. Li, F.; Lubetkin, S. D.; Roberts, D. J.; Hillman, A. R., *J. Chem. Soc. Chem. Comm.*, **1994**, 159-160.
3. Gabrielli, C.; Huet, F.; Keddam, M.; Torresi, R., *J. Electroanal. Chem.*, **1991**, *297*, 515-522.
4. Gabrielli, C.; Huet, F.; Keddam, M., *J. Appl. Electrochem.*, **1985**, *15*, 503-508.
5. Gabrielli, C.; Huet, F., *J. Appl. Electrochem.*, **1994**, *24*, 593-601.
6. Hodgson, D. R., *Electrochimica Acta*, **1996**, *41*, 605-609.
7. Bruckenstein, S.; Shay, M., *Electrochimica Acta*, **1985**, *30*, 1295.
8. Li, F.; Hillman, A. R.; Lubetkin, S. D.; Roberts, D. J., *J. Electroanal. Chem.*, **1992**, *335*, 345-362.
9. Gardner, J. R.; Woods, R., *J. Electroanal. Chem.*, **1977**, *81*, 285-290.
10. Chirkov, Y. U.; Pshenichnikov, A. G., *Electrokhimiya*, **1991**, *26*, 1545-1549.

6.1 Introduction

This chapter describes the development and application of modifications to the Pressure Release Bubble Nucleation (PRBN) technique. PRBN is an established, although relatively unexplored method of measuring the rate of heterogeneous bubble nucleation, induced inside a sealed vessel [1-4]. As explained in section 2.1.6 and given in equation 2.36 of chapter 2, the rate at which gas bubbles evolve in a supersaturated solution is calculated from the rate at which the pressure inside the vessel increases

Previously the technique has been used to measure the nucleation rate of carbon dioxide and chlorine bubbles as a function of surface morphology and contact angle from surfaces such as Pyrex, stainless steel, RTO, and PTFE [1,2,3]. The surface tension was modified by the addition of surfactants to the supersaturated solution [3]. The rate of the pressure rise is directly related to the rate of bubble nucleation and allows comparison with the nucleation rate predicated by classical nucleation theory [4].

It has been shown that the relationship between nucleation rate (J) and supersaturation (σ) is complex at surfaces where there are a range of nucleation site activities. The distribution in activity is due to the variation in nucleation site geometry and energetics. Classical nucleation theory predicts a linear relationship when $\ln J$ is plotted vs. $(\sigma P)^2$ [5]. However, it has been shown that this is only applicable to surfaces that have *one* type of active nucleation site, for example conical pits with identical geometries. Where there is a *distribution* of nucleation sites with different geometries (expected for all physically inhomogeneous surfaces), there will be a *distribution* of nucleation rates. The measured nucleation rate is a sum of the rates at each individual nucleation site. Therefore the relationship between supersaturation and the overall nucleation rate is a function of the independent activity at each type of nucleation site and it has been found that the relationship is non-linear for a variety of surfaces [3,6]. When plotting the rate as a function of supersaturation, the measured nucleation rate is in fact a composite of the rate of nucleation, J , of each type of site at the surface. If the activity of these sites varies significantly, the distribution of rates gives rise to curve when $\ln J$ is plotted vs. the reciprocal of supersaturation, not the straight line predicted by the theory. The deviation from theory has been attributed to the phenomenon of nucleation rate dispersion.

The full experimental procedure and apparatus design of the PRBN is given in section 3.3.1. The basis of the technique is as follows. The PRBN technique comprises a sealed vessel containing the nucleating surface, and a solution in which the gas is dissolved at an elevated pressure. Decompression of the vessel causes the solution to become supersaturated to an extent relative to the ratio of the initial and final pressures of the vessel: bubbles are then nucleated spontaneously at the surface. The vessel is resealed immediately upon decompression, therefore the formation of bubbles increases the pressure inside the vessel. The pressure is measured continuously, allowing the rate of bubble formation to be calculated. The calculated nucleation rate is equal to the overall rate at the surface integrated over time and space, so the method does not allow observation of individual nucleation events.

Some aspects of the PRBN apparatus design and data analysis methods have previously limited its application [3]. Firstly, the method of controlling the supersaturation is imprecise. The initial saturating pressure is controlled using a gas cylinder regulator valve, this allows the solution to be saturated with the gas at a constant pressure. However, the lower target pressure is controlled manually using a needle valve, making it difficult to achieve the same target pressure consistently. This introduces variations in conditions between experiments, making it difficult to compare the bubble nucleation rate at two different surfaces. Secondly, data collection is time-consuming, as the system must equilibrate for 24 hours to supersaturate the solution. Each experiment provides the nucleation rate at one value of supersaturation, as determined by the starting and end pressures in the vessel. Experiments are repeated, varying the supersaturation ratio each time. Considering the complex relationship between nucleation rate and supersaturation and the distribution of nucleation activity at the surface, a large amount of data are required to create a $\ln J$ vs. $(\sigma P)^2$ plot described above.

Another limitation is the fabrication of the nucleation surface. The container inside the vessel holding the solution is made from the nucleating surface. For practical reasons this has consisted of a cylindrical beaker. The drawback of this technique is the limited number of materials that can be used, considering either cost or ease of manufacture. These design issues are addressed in the following section.

6.1.1 Objectives

The objective of this study is to adapt the PRBN technique to increase its applicability

through three advances in the development of a novel data analysis technique and modification of the design of the apparatus. Firstly, in order to apply the technique to the study of different surface materials, a disc, fabricated from the surface to be studied, replaces the cylindrical beaker. The disc is placed at the bottom of an annealed glass beaker, which has a negligible number of nucleation sites; ensuring nucleation occurs predominantly at the upper surface of the disc. Secondly, the accuracy of the pressure parameter is improved by controlling the target pressure using an air actuated solenoid valve. This ensures that the vessel is released immediately as the target pressure is reached, making each experiment reproducible. Thirdly, to overcome the time required to collect a sufficient amount of data to characterise the nucleation activity at the surface, the nucleation rate is calculated as a function of supersaturation for a single experiment. This is possible because the supersaturation of the solution decreases as dissolved gas is removed from the solution as bubbles.

The results shown in this chapter have been obtained using the modified PRBN technique to study the kinetics of bubble nucleation as a function of both physical and chemical parameters. The systems chosen are the nucleation rate of chlorine bubbles from supersaturated brine (5M NaCl) at titanium and RTO surfaces at a temperature of 298K. Each sample of the 2 materials was made into a disc of 4cm diameter. Two different volumes of NaCl were used; 150 ml and 50 ml. Different RTO samples were prepared using the spray bake technique; all the surfaces are characterised by deep crevices. Modification of the composition of the coating i.e. the ratio of RuO₂ to TiO₂ was used to determine the effect of chemical composition on the nucleation rate. The titanium discs were etched in oxalic acid for different durations, increasing the surface roughness gradually from an optically flat surface; this enabled the effect of the roughness of the substrate on nucleation rate to be determined.

These systems have been used to identify whether the proposed novel data analysis and design can provide comparable information on nucleation rate dispersion as identified with the traditional method of data analysis. Successful modification of the PRBN will provide a more efficient method of data analysis that decreases the time required to obtain results and increases the flexibility of the application of the PRBN technique as a diagnostic tool for bubble nucleation studies on a wide variety of materials.

6.2 Principles of PRBN analysis

6.2.1 Nucleation rate measurement

Nucleation is known to be the rate-limiting step for systems with a low contact angle. This is assumed to be valid for both systems under study. Where nucleation is the rate-limiting step, it can be shown [7] that the nucleation rate is linearly related to pressure rise. Assuming the bubbles reaching the surface are of equal radius, containing n moles of gas, then the relationship between the pressure rise and the nucleation rate is given by

$$\frac{dP}{dt} = \frac{RT}{V} nJ(t) \quad (6.1)$$

where V is the volume of the vessel headspace and J is the bubble nucleation rate as defined in equation 6.2.

$$J = A \exp\left(-\frac{16\pi\gamma^3 f(\theta)}{3kT(\sigma P)^2}\right) \quad (6.2)$$

In accordance with equation 6.2, the results are plotted in the form $\ln(dM/dt)$ vs. $(\sigma P)^{-2}$ where M is the rate of gas released in units of $\text{mol m}^{-2} \text{s}^{-1}$ and is calculated from the initial rise in pressure following the decompression of the PRBN vessel. The difference between dM/dt and the nucleation rate J , which has units, $\text{bubbles m}^{-2} \text{s}^{-1}$, results in a difference in the value of the y axis intercept, but not in the overall shape of the plot.

6.2.2 The two site model

As explained in chapter 2, theory predicts that a $\ln J$ vs. $(\sigma P)^{-2}$ plot will yield a straight line. However, it has been found experimentally for the nucleation of CO_2 from H_2O , that the plot gives a curve. This has been attributed to a distribution in nucleation site energetics; each with a particular rate equation and the overall measured nucleation rate is a combination of several different rates. The simplest example of this concept is a surface with two types of nucleation site geometry (or nucleation energetics), where site a is the predominantly active site at the higher supersaturations and site b is predominantly active at lower supersaturations. The $\ln J$ vs. $(\sigma P)^{-2}$ plot expected for this scenario is demonstrated in figure 6.1 below.

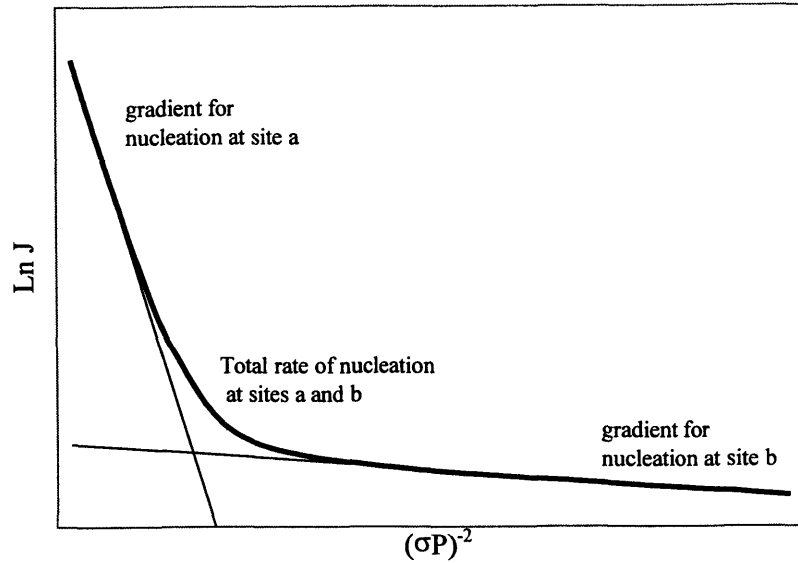


Figure 6.1 Schematic plot of $\ln J$ vs. $(\sigma P)^{-2}$ for a nucleating surface where the nucleation rate for the 2 sites individually is shown by the two linear regions. The total rate at the surface as a function of supersaturation is shown by the composite curve.

Equation 6.2 can be assigned to both linear regions in figure 6.1. The total rate of nucleation at the surface is given by

$$J_{tot} = J_a + J_b \quad (6.3)$$

where J_a and J_b are the rate expression for each type of site, derived from the gradient and intercept of the two linear regions of figure 6.1.

6.2.3 Novel methodology

In order to obtain multiple points on a $\ln J$ vs. $(\sigma P)^{-2}$ plot from each experiment, a novel technique has been developed. As bubbles nucleate, the supersaturation of the solution decreases. The supersaturation ratio is defined by the actual concentration of dissolved gas in the solution relative to the equilibrium concentration, defined by the solubility of the gas in the solutions at a given pressure. The measured pressure rise can be used to calculate the nucleation rate and also to simultaneously calculate the supersaturation of the solution, thereby providing the two parameters for a plot of $\ln J$ vs. $(\sigma P)^{-2}$. The experimental technique used is discussed in section 6.3.

6.3 Data analysis technique

The following sections describe the experimental techniques used to calculate bubble nucleation rate using the PRBN technique.

6.3.1 Calibration

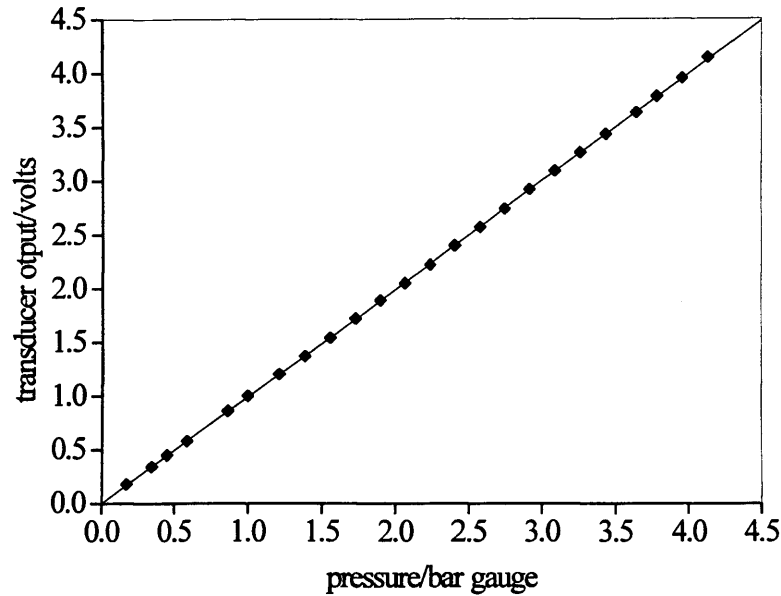


Figure 6.2 Plot of transducer output voltage vs. pressure for the oil filled transducer over a pressure range 0 – 4.5 bar (gauge).

Pressure is measured continuously during each experiment using a transducer, protected from the chlorine atmosphere with a silicone oil-filled tantalum diaphragm. This silicone oil, was used as an incompressible transfer fluid between the diaphragm and the piezoelectric sensor in the transducer. The transducer and diaphragm apparatus were calibrated using a 0 - 150 p.s.i. Budenberg gauge, the results of which are shown in figure 6.2.

6.3.2 Adiabatic Expansion

As described above, the pressure vessel is rapidly decompressed to cause the solution to become supersaturated. During this process the gas in the headspace of the vessel undergoes adiabatic expansion, causing the expanding gas to drop in temperature. When the vessel is resealed, the remaining gas in the headspace above the solution quickly re-equilibrates to the ambient temperature of the vessel. This process of re-heating causes a pressure rise in the

vessel and is a component of the measured pressure response over short times (< 50 seconds). Before the gradient of the pressure rise can be used to calculate bubble nucleation this re-heating component must be accounted for and subtracted from the measured pressure parameter.

Once this component has been accounted for, bubble evolution rates can be measured directly. Experiments were carried out in order to establish the relative contributions of reheating of residual headspace. In order to measure the pressure rise due to reheating, several “dummy” experiments were carried out as described in section 3.1.1. The initial pressures were varied and the target pressure was maintained at 0.05 bar gauge. Figure 6.3 shows eight typical pressure vs. time curves for chlorine, it can be seen that the reheating effect occurs within the first 50 seconds.

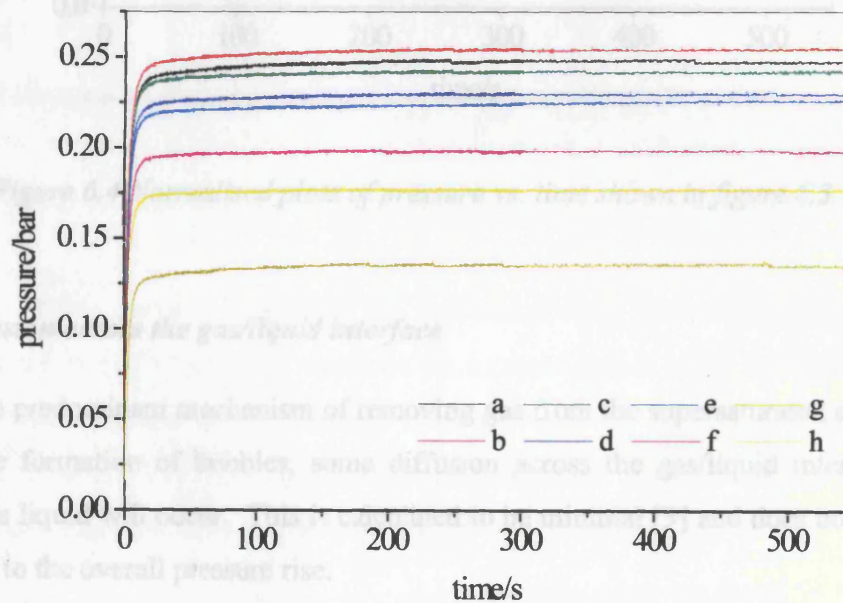


Figure 6.3 Plot of typical pressure vs. time transients arising from adiabatic expansion of chlorine where $t=0$ is the point at which the vessel is resealed after decompression for different values of initial pressure of $a=4.5$, $b=4$, $c=3.5$, $d=3$, $e=2.5$, $f=2$, $g=1.5$, $h=1$ (bar gauge).

Figure 6.4 shows the normalised data, where each point on an individual curve is divided by the final value of pressure measured for that curve, showing all the curves are superimposable. It can be assumed that the reheating is Newtonian, i.e. the temperature of the gas in the headspace increases exponentially irrespective of the degree of cooling. Therefore the appropriate “adiabatic” pressure response can simply be subtracted from the

measured pressure response to account for the re-heating component [3]. The details of the method of measuring the pressure rise gradient are given in section 6.3.4.

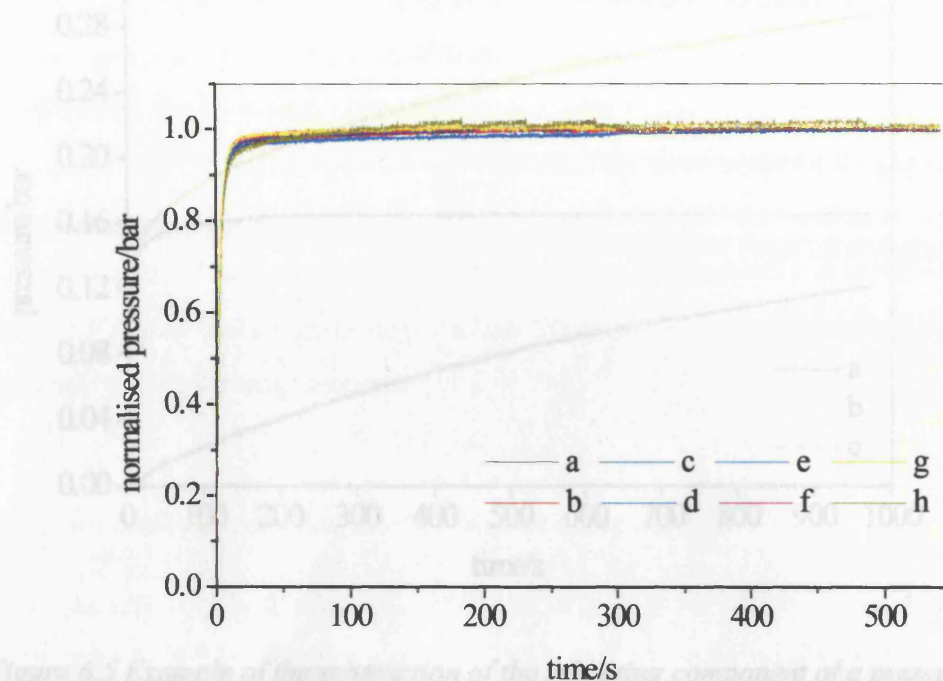


Figure 6.3 Example of the extraction of the re-heating component of a pressure vs. time transient where *a*=measured pressure vs. time transient, *b*=re-heating component and *c*=corrected pressure vs. time transient.

Figure 6.4 Normalised plots of pressure vs. time shown in figure 6.3.

6.3.3 Diffusion across the gas/liquid interface

Although the predominant mechanism of removing gas from the supersaturated solution will occur by the formation of bubbles, some diffusion across the gas/liquid interface at the surface of the liquid will occur. This is calculated to be minimal [3] and does not contribute significantly to the overall pressure rise.

6.3.4 Gradient Measurement

In order to calculate dM/dt , the rate of bubble evolution, from the measured pressure curve, the pressure rise must first be corrected for the re-heating component arising from adiabatic expansion. The actual magnitude of the re-heating curve is chosen so that a continuous curve is produced in the corrected data as shown in figure 6.5.

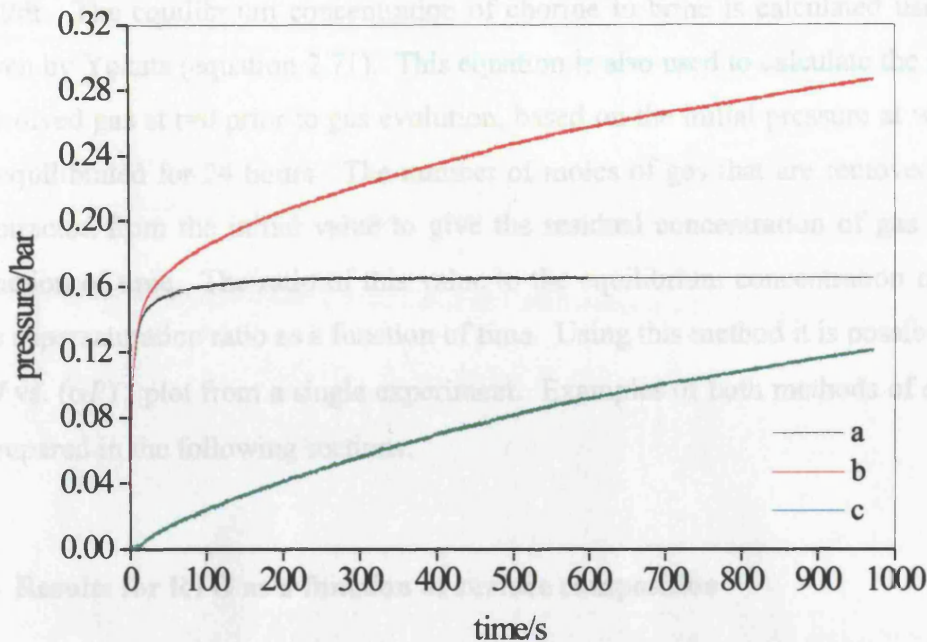


Figure 6.5 Example of the subtraction of the reheating component of a pressure vs. time transient where a=measured pressure vs. time transient, b=reheating component and c=corrected pressure transient. The data show chlorine evolution from titanium, for $\sigma=4.4$.

The gradient of this curve is related to the nucleation rate. The established method of composing a $\ln J$ vs. $(\sigma P)^{-2}$ plot is to calculate the supersaturation of the solution at $t=0$, i.e. immediately following the decompression, from the ratio of initial and target pressures according to equation 2.1. The gradient of the corrected curve is measured by linear regression of the initial pressure increase typically 0 to 100 seconds [6].

The novel data analysis method calculates the extent to which the supersaturation of the solution decreases. This parameter is determined by the concentration of gas dissolved in the solution, relative to the equilibrium concentration, i.e. the solubility of the gas at a given pressure. Both of these values change over the course of an experiment as gas is removed from the solution as bubbles. As the pressure above the solution rises, so does the equilibrium concentration of gas in solution (calculated from the solubility of the gas). The volume of gas leaving the solution is also calculated from the measured increase. Combining these calculations on a spreadsheet allows the rate of pressure rise to be expressed as a function of supersaturation.

The measured data are corrected for the adiabatic effect, and then differentiated to derive dM/dt . The equilibrium concentration of chlorine in brine is calculated using the equation given by Yokata (equation 2.71). This equation is also used to calculate the concentration of dissolved gas at $t=0$ prior to gas evolution, based on the initial pressure at which the system is equilibrated for 24 hours. The number of moles of gas that are removed (as bubbles) is subtracted from the initial value to give the residual concentration of gas in solution as a function of time. The ratio of this value to the equilibrium concentration of chlorine gives the supersaturation ratio as a function of time. Using this method it is possible to compose a $\ln J$ vs. $(\sigma P)^2$ plot from a single experiment. Examples of both methods of data analysis are compared in the following sections.

6.4 Results for RTO as a function of surface composition

In this section, PRBN of chlorine bubble evolution at various RTO surfaces is presented. The samples of RTO differ in the ratio of RuO_2 to TiO_2 in the mixed oxide layer coated onto a titanium substrate. All of the discs were fabricated using the pre-treated titanium substrate. The percentage of RuO_2 present at the surface of the samples is as follows; sample a = 10%, b = 15%, c = 25%, d = 35%, e = 60%, meaning electroactivity increases from sample a to sample e. The bubble nucleation rate is measured as a function of both surface composition and supersaturation.

Figure 6.6 shows pressure vs. time transients measured for chlorine bubble evolution from 5M NaCl at the five different RTO samples, *a-e*, for the same value of supersaturation. The data have not been corrected for the effect of adiabatic expansion, which is clearly seen to be dominant in the first 50 seconds of each experiment; at longer times there is a gradual variation in the rate of pressure rise. The target pressure for each experiment is 0.05 bar gauge, variation in the value of the initial pressure, means that the supersaturation for this set of experiments lies between 4.40 and 4.62.

As mentioned above, the established method of analysis [1,6] is the measurement of the initial pressure vs. time gradient for a single surface at various values of supersaturation. Figure 6.7 shows the corrected pressure vs. time transients for RTO sample *d* as a function of supersaturation. It can be seen that the nucleation rate increases with supersaturation. However, the plot is non-linear for most of the experiments, therefore, the gradient of the region between 0 and 100 seconds was chosen. This is the initial gradient and is therefore

consistent with the established methodology.

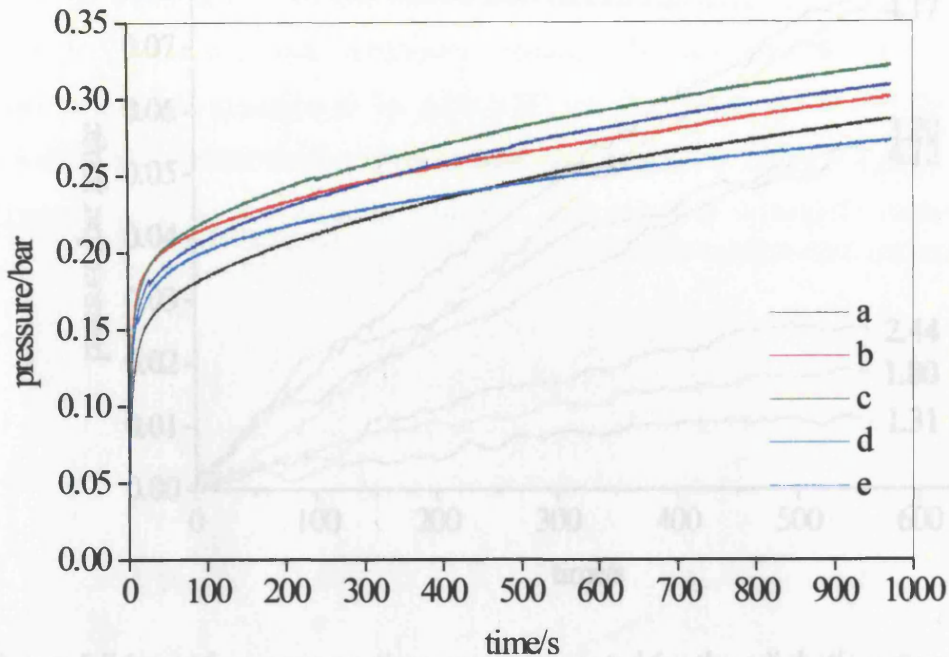


Figure 6.6 Pressure vs. time transients for the $\text{Cl}_2/\text{NaCl}/\text{RTO}$ system for five different surfaces, a-e, where the ratio of RuO_2 to TiO_2 increases from sample a-e. The small variation in supersaturation (σ) for each experiment is given by $a = 4.42$, $b = 4.40$, $c = 4.51$, $d = 4.52$, $e = 4.62$.

Figure 6.6 Pressure vs. time transients for the $\text{Cl}_2/\text{NaCl}/\text{RTO}$ system for five different surfaces, a-e, where the ratio of RuO_2 to TiO_2 increases from sample a-e. The small variation in supersaturation (σ) for each experiment is given by $a = 4.42$, $b = 4.40$, $c = 4.51$, $d = 4.52$, $e = 4.62$.

Plotting the data shown in figure 6.7 as a $\ln(dM/dt)$ vs. $(\sigma P)^{-2}$ plot in figure 6.8, shows that there is a deviation from linearity as predicted by theory and equation 6.2. This is consistent with previous observations using the PRBN technique for chlorine bubble evolution at an RTO surface [3]. Figure 6.8 shows there is a linear region at the higher supersaturations (the left side of the x axis) for all the samples shown. However, where the data are available, this trend does not continue at the lower values of σ , as the curve levels out, where the rate of bubble evolution is enhanced compared to the expected values.

The range of values of supersaturation over which the breakdown in linearity occurs is denoted the transition supersaturation (σ_{trans}). A single value is usually assigned that lies in the mid-point of the range. Due to the scatter and position of the data points on the curve in figure 6.8, it would be difficult to assign a value for σ_{trans} for any of the five RTO samples. However, the actual values shown in the figure compare very well with data collected using a cylindrical RTO beaker [3].

6.6 Results for a single experiment

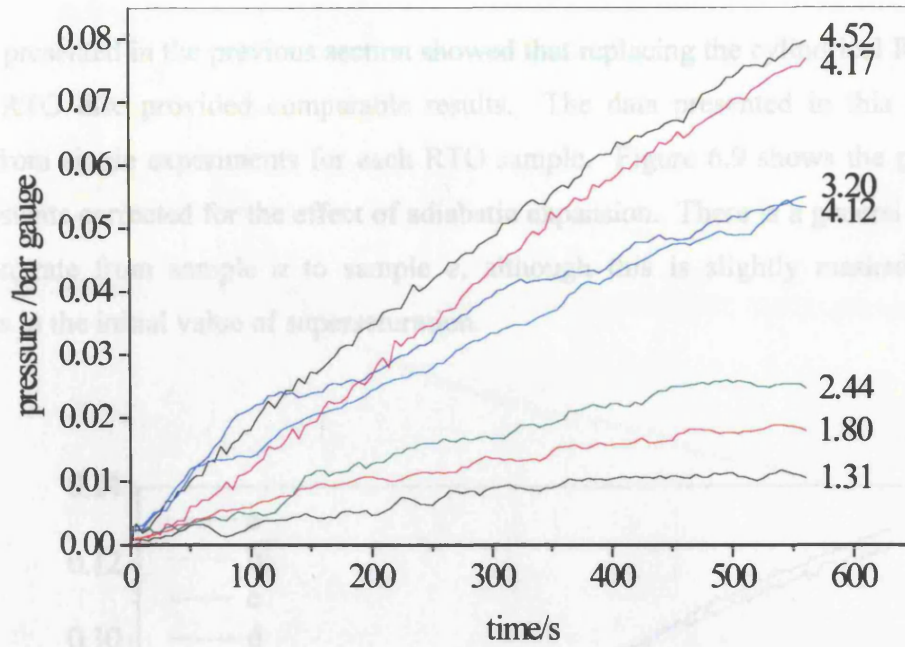


Figure 6.7A set of pressure vs. time curves corrected for the adiabatic component for a $Cl_2/NaCl/RTO$ system (using sample d) showing the increase in gas evolution rate with supersaturation. The supersaturation (σ) is given for each experiment.

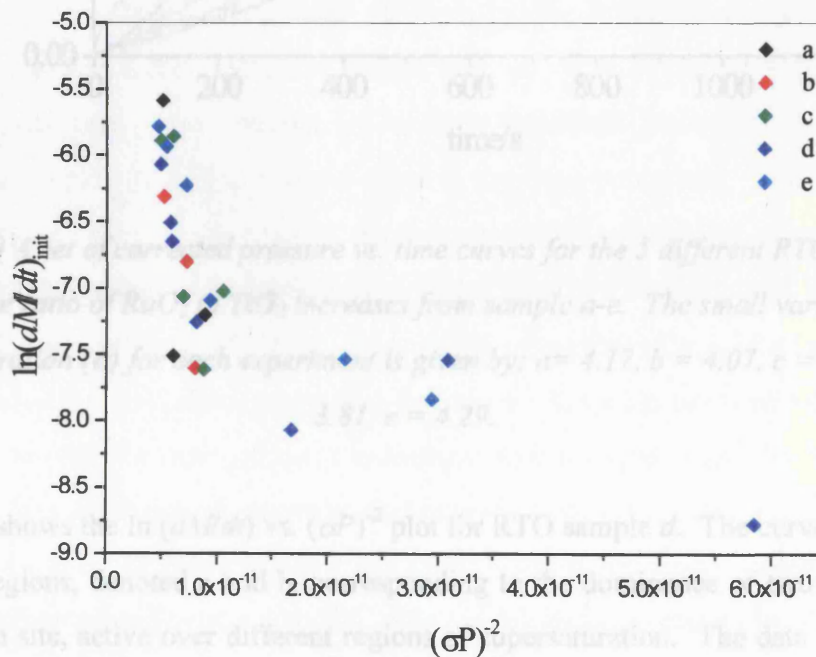


Figure 6.8 Plot of $\ln(dM/dt)$ vs. $(\sigma P)^{-2}$ for the 5 different $Cl_2/NaCl/RTO$ samples a-e.

6.4.1 Results for a single experiment

The data presented in the previous section showed that replacing the cylindrical RTO beaker with an RTO disc provided comparable results. The data presented in this section are derived from single experiments for each RTO sample. Figure 6.9 shows the pressure vs. time transients corrected for the effect of adiabatic expansion. There is a general increase in nucleation rate from sample *a* to sample *e*, although this is slightly masked by minor variations in the initial value of supersaturation.

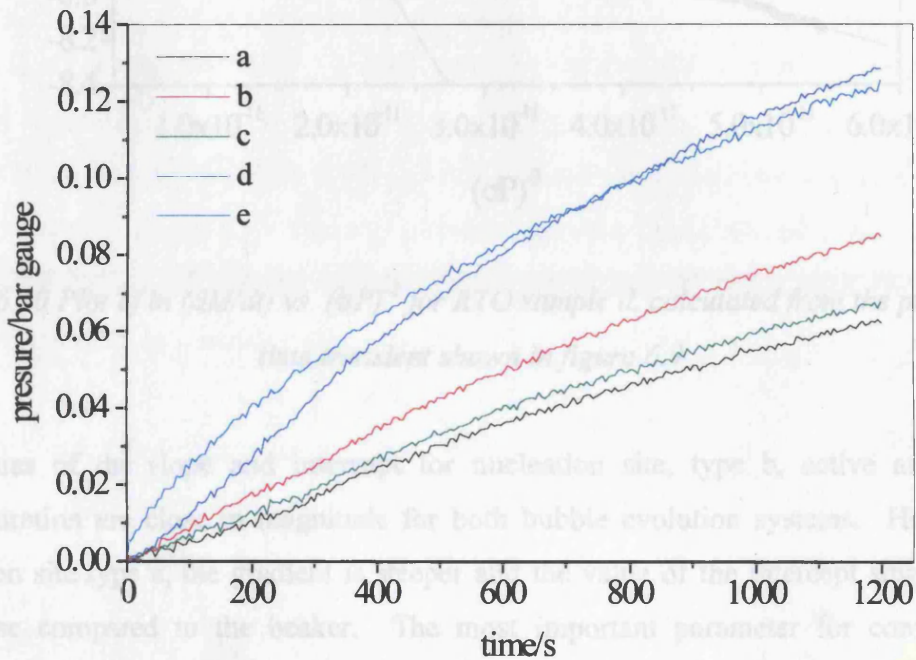


Figure 6.9 A set of corrected pressure vs. time curves for the 5 different RTO samples where the ratio of RuO_2 to TiO_2 increases from sample *a*-*e*. The small variation in supersaturation (σ) for each experiment is given by; $a = 4.17$, $b = 4.07$, $c = 3.72$, $d = 3.81$, $e = 4.29$.

Figure 6.10 shows the $\ln(dM/dt)$ vs. $(\sigma P)^{-2}$ plot for RTO sample *d*. The curve clearly shows two linear regions, denoted *a* and *b*, corresponding to the dominance of two different types of nucleation site, active over different regions of supersaturation. The data are also shown in table 6.1 against data collected by other workers using the established apparatus design and method of analysis methods.

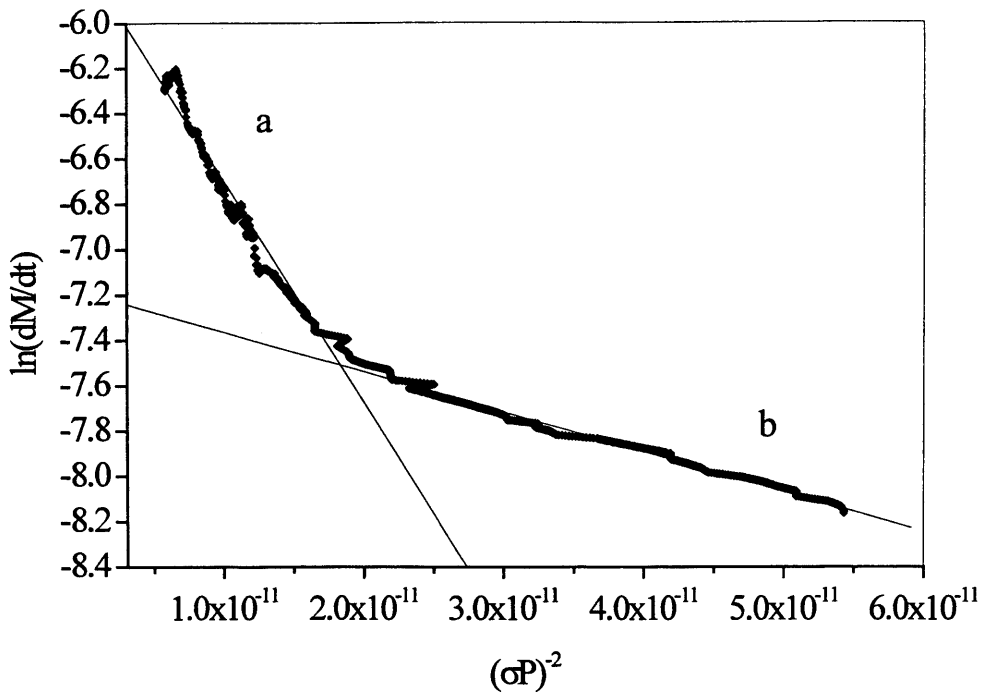


Figure 6.10 Plot of $\ln(dM/dt)$ vs. $(\sigma P)^2$ for RTO sample *d*, calculated from the pressure vs. time transient shown in figure 6.9.

The values of the slope and intercept for nucleation site, type b, active at the lower supersaturation are close in magnitude for both bubble evolution systems. However, for nucleation site type a, the gradient is steeper and the value of the intercept smaller for the RTO disc compared to the beaker. The most important parameter for comparing the efficiency of bubble evolution at the surface is the σ_{trans} parameter. The position of σ_{trans} along the x axis gives an indication of the supersaturation required to activate the dominant nucleation sites, i.e., type a nucleation sites, where there is a large increase in nucleation rate over a small range of supersaturation. Interestingly, the value of σ_{trans} for the RTO beaker is higher than for the RTO disc, suggesting that more energy (in terms of supersaturation) is required to activate the more efficient nucleation sites (of type a) present on the surface of the beaker. It is worth noting, however, that imperfections introduced onto the surface of the RTO beaker during its manufacture make direct comparison of the two systems difficult. Such difficulties arising during manufacturing are minimised using a disc shaped nucleating surface.

Bubble evolution system	Type of nucleation site	Intercept (<i>I</i>)	Slope (<i>S</i>)
RTO disc $\sigma_{\text{trans}} = 2.26$	<i>a</i>	-5.717	-9.798×10^{10}
	<i>b</i>	-7.13	-1.887×10^{10}
RTO beaker [3] $\sigma_{\text{trans}} = 3.93$	<i>a</i>	-4.000	-5.912×10^{11}
	<i>b</i>	-7.341	-5.439×10^{10}

Table 6.1 Data for the $\ln(dM/dt)$ vs. $(\sigma P)^{-2}$ plot shown in figure 6.10 and from [3].

Figure 6.11 shows the $\ln(dM/dt)$ vs. $(\sigma P)^{-2}$ plot for the five RTO discs, calculated for the individual pressure vs. time transients shown in figure 6.9. The plot shows there is a deviation from linearity for each RTO sample, with all curves approximating the two-site model as shown in figure 6.1. There is a general increase in the overall bubble nucleation rate over all values of supersaturation as the percentage of RuO₂ (and therefore the electrocatalytic activity), increases.

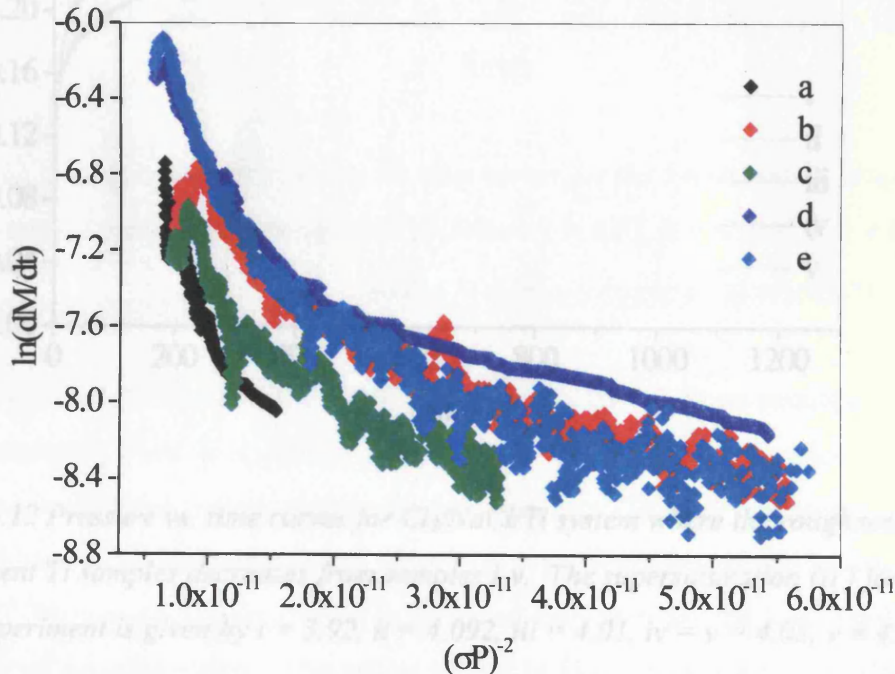


Figure 6.11 Plot of $\ln(dM/dt)$ vs. $(\sigma P)^{-2}$ for the 5 different Cl₂/NaCl/RTO samples a-e (as defined in the text) calculated from the 5 pressure vs. time transients shown in figure 6.9.

Comparing figure 6.11 with figure 6.8, it can be seen that the values on both plots are comparable. However, the larger number of data points in figure 6.11, make it easier to extract accurate values of slope, intercept and σ_{trans} .

6.5 Results for titanium as a function of surface roughness

The RTO samples were prepared by coating the oxide solution onto a titanium substrate, which was etched by soaking in oxalic acid. In this section, chlorine bubble nucleation rate from 5 M NaCl is calculated at five different titanium surfaces, as a function of surface roughness. The discs (4 cm diameter) were polished to a mirror finish prior to etching. The length of time each disc was immersed in oxalic acid is as follows; sample i = eight hours, ii = five hours, iii = three hours = iv = one hour, v = no etching, i.e. mirror polish, meaning the surface roughness decreases from sample i to sample v.

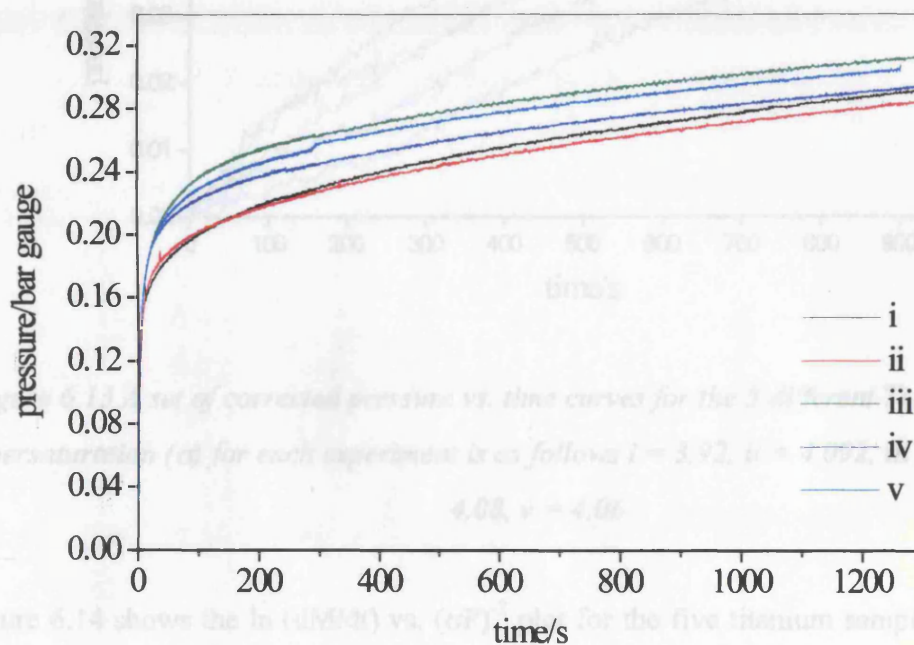


Figure 6.12 Pressure vs. time curves for $Cl_2/NaCl/Ti$ system where the roughness of the 5 different Ti samples decreases from samples i-v. The supersaturation (σ) for each experiment is given by i = 3.92, ii = 4.092, iii = 4.01, iv = v = 4.08, v = 4.06

Figures 6.12 and 6.13 show the pressure vs. time transients for uncorrected data (figure 6.12) and the data corrected for the effect of adiabatic expansion (figure 6.13) for the titanium surfaces. It can be seen that there is a general increase in nucleation rate as the surface

roughness increases. The exception is for sample v, the polished titanium surface. This anomaly is possibly due to the manufacturing process of the discs. Each disc was cut from a titanium sheet, and the edges of the discs were roughly polished to remove sharp protrusions. Both faces of each disc were then highly polished. The oxalic acid etches both the faces and edges of the disc, giving a uniform roughness. It is possible that sample v, which was not immersed in the acid, was left with a greater roughness on the edge of the disc, and this accounts for its nucleation activity.

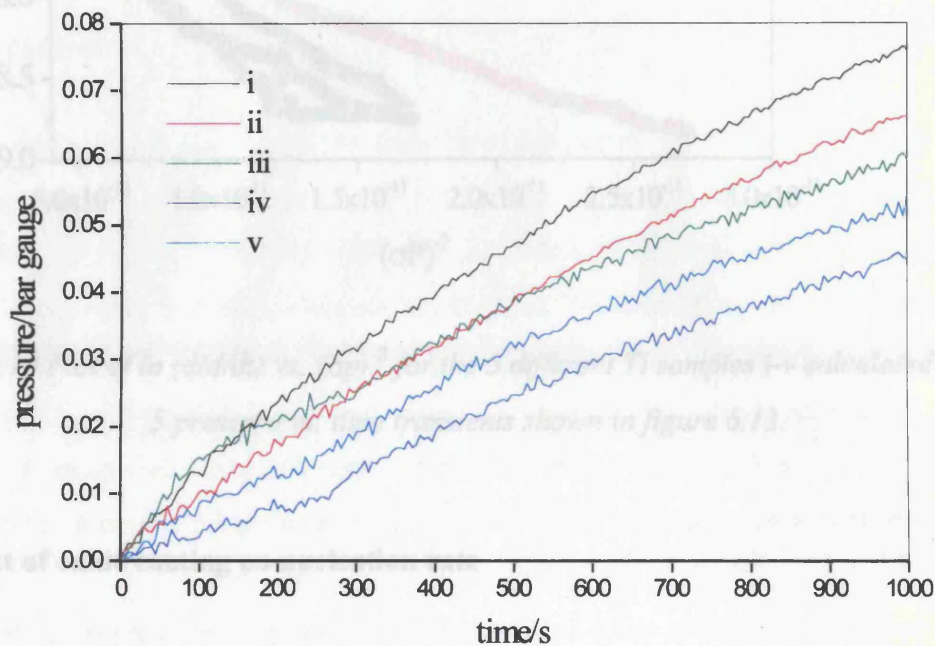


Figure 6.13 A set of corrected pressure vs. time curves for the 5 different Ti samples i-v, the supersaturation (σ) for each experiment is as follows $i = 3.92$, $ii = 4.092$, $iii = 4.01$, $iv = v = 4.08$, $v = 4.06$

Figure 6.14 shows the $\ln(dM/dt)$ vs. $(\sigma P)^{-2}$ plot for the five titanium samples. As seen for the RTO samples, there is deviation from linearity for all of the samples. This can be attributed to multiple nucleation geometries on the surface. There is a general increase in the overall bubble nucleation rate over all values of supersaturation as the surface roughness increases. The nucleation rate appears to be lower than seen for the RTO surfaces for the same value of supersaturation. The values shown in figure 6.14 are comparable with data collected on a cylindrical beaker made from etched titanium (etched for eight hours) [3].

Figure 6.13 Comparison of $\ln(dM/dt)$ for the RTO and titanium samples, where samples 1 to 5 are the 5 data correspond to RTO samples a-e and titanium samples (i-v). Supersaturation = 1.

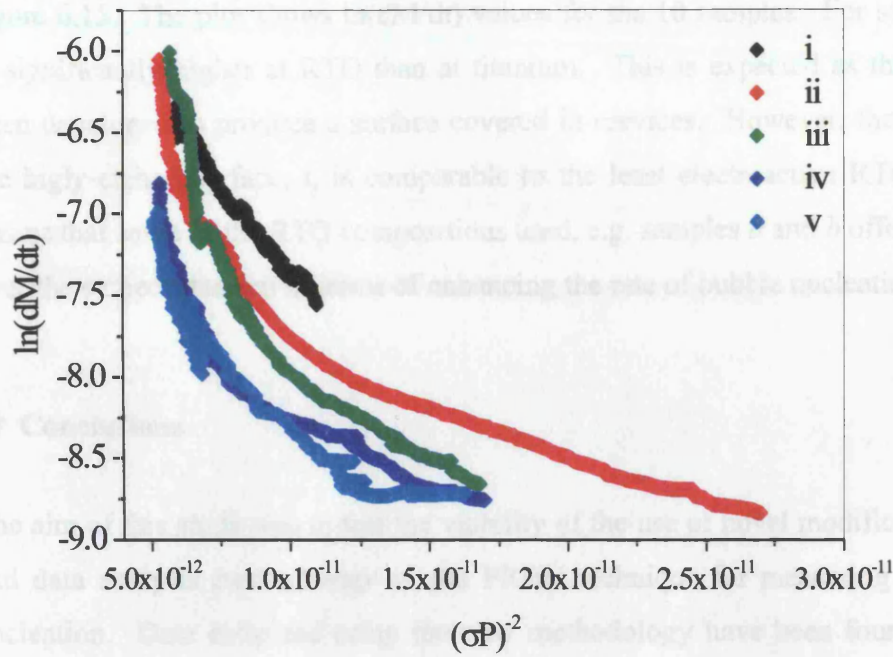


Figure 6.14 Plot of $\ln(dM/dt)$ vs. $(\sigma P)^{-2}$ for the 5 different Ti samples i-v calculated from the 5 pressure vs. time transients shown in figure 6.13.

6.6 Effect of oxide coating on nucleation rate

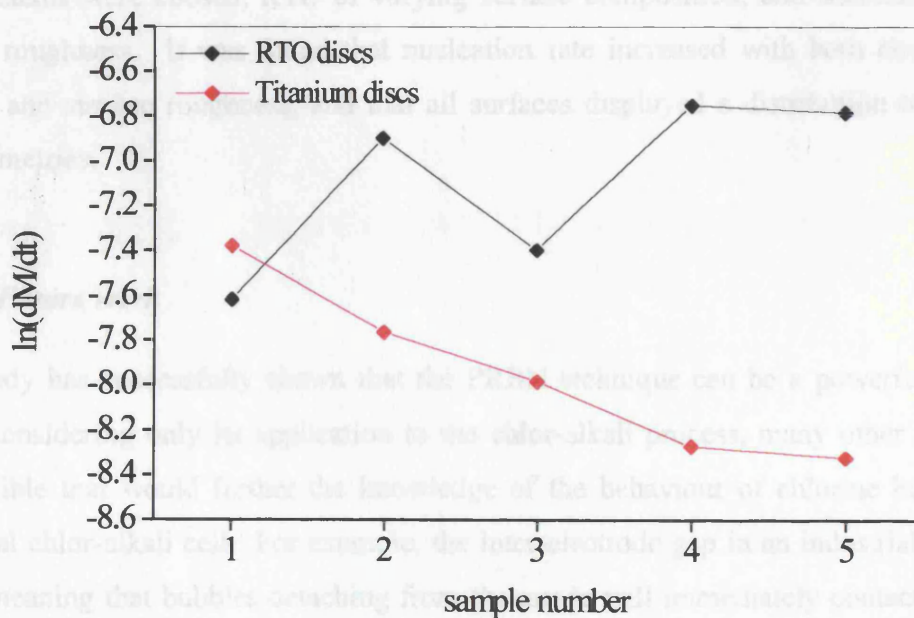


Figure 6.15 Comparison of $\ln(dM/dt)$ for the RTO and titanium samples, where samples 1 to 5 on the x axis correspond to RTO samples a-e and titanium samples i-v. Supersaturation = 3.

The effect on nucleation rate of coating the titanium discs with an RTO layer is seen in figure 6.15. The plot shows $\ln(dM/dt)$ values for the 10 samples. For samples 2-5, the rate is significantly higher at RTO than at titanium. This is expected as the RTO coating has been developed to produce a surface covered in crevices. However, the nucleation rate for the highly-etched surface, *i*, is comparable to the least electroactive RTO surface, *a*. This means that some of the RTO compositions used, e.g. samples *a* and *b* offered little advantage over the etched titanium in terms of enhancing the rate of bubble nucleation.

6.7 Conclusions

The aim of this study was to test the viability of the use of novel modifications to the design and data analysis methodology of the PRBN technique for measuring the rate of bubble nucleation. Data collected using the new methodology have been found to compare well with existing data. The time required establishing the relationship between nucleation rate and supersaturation has been greatly reduced, improving the efficiency of the PRBN technique. Also, by using a disc made from the nucleating material under study, rather than a beaker, a much wider range of materials can be used. This expands the use of the PRBN as a diagnostic technique for the empirical study of bubble nucleation on new materials.

Two systems were chosen, RTO of varying surface composition, and titanium of varying surface roughness. It was found that nucleation rate increased with both electrocatalytic activity and surface roughness, and that all surfaces displayed a distribution of nucleation site geometries.

6.7.1 Future work

This study has successfully shown that the PRBN technique can be a powerful diagnostic tool. Considering only its application to the chlor-alkali process, many other experiments are feasible that would further the knowledge of the behaviour of chlorine bubbles in an industrial chlor-alkali cell. For example, the inter-electrode gap in an industrial cell is very small, meaning that bubbles detaching from the anode will immediately contact and adhere to the Nafion ® membrane that separates the anode and cathode. The PRBN could be used to study the nucleation rate of bubbles at Nafion ® membranes, to determine its function during bubble evolution in the cell. The rates of bubble nucleation in this chapter have been

measured at 298K. Since the vessel is thermostated, it is feasible to increase the temperature of the vessel, to measure nucleation rate as a function of temperature, although it should be noted that due to the corrosive properties of chlorine, some modifications would be needed to protect the vessel from corrosion.

1. Lubetkin, S. D.; Blackwell, M., *J. Coll. Int. Sci.*, 1988, 126, 610-615.
2. Lubetkin, S. D., *J. Appl. Electrochem.*, 1989, 19, 668-676.
3. Carr, M. W., PhD Thesis, University of Bristol, 1993.
4. Lubetkin, S. D., *J. Chem. Soc., Faraday Trans. 1*, 1989, 85(7), 1753-1764.
5. Wilt, P.M., *J. Coll. Int. Sci.*, 1986, 112, 530-538.
6. Carr, M. W.; Hillman, A. R.; Lubetkin, S. D., *J. Coll. Int. Sci.*, 1995, 169, 135-142.
7. Blackwell, M. R., M. Sc. Thesis, University of Bristol, 1986.

The mechanisms of hydrogen bubble evolution at gold and platinum, and chlorine bubble evolution at RTO electrodes have been successfully characterised using three complementary experimental techniques: fast frame video (FFV), electrochemical quartz crystal microbalance (EQCM) and pressure release bubble nucleation (PRBN). These techniques provide an integrated approach to the study of bubble evolution systems that enables the mechanism to be established. Each technique provides a different perspective, through either the study of individual bubble events (FFV) or the nucleation and detachment rate at the surface (PRBN, and EQCM).

The FFV and EQCM techniques were developed using hydrogen evolution at gold electrodes as a model system, comparing the surface roughness and electrode orientation. Through studying this system using the FFV technique, it has been shown that the growth mechanism of hydrogen bubbles on a macroscopic electrode is a function of both the bubbles' growth environment and the current density. In the current density range 3 - 44 mA cm⁻², hydrogen bubble nucleation was found to be rapid at a polished gold electrode. The number of nucleation sites and detachment frequency increased with current density, whereas the average detachment size decreased. The detachment mechanism was predominantly due to coalescence of neighbouring bubbles. The growth mechanism was predominantly diffusion limited, but under some conditions approximated the direct injection mechanism previously observed for microelectrodes. Although it was demonstrated that the value of the time exponent for the growth mechanism was not a practical diagnostic variable, it highlighted the variation in localised levels of supersaturation at the electrode surface.

Novel Fast Fourier transform analysis of EQCM data, measured for the same type of surface, allowed the same conclusions to be drawn. In the same current density range, the bubbles were seen to nucleate rapidly and grow whilst attached to the electrode surface. The detachment frequency increased with current density, with little change in the volume of gas leaving the electrode. In conclusion, the EQCM was shown to be a useful technique for bubble measurements that would be difficult and time-consuming using the direct visual observation technique. Combination of these two techniques will provide a very powerful tool for characterisation of bubble nucleation systems.

FFV studies of the platinum electrodes showed the hydrogen gas evolution mechanism was markedly different from hydrogen evolution at a gold electrode. Hydrogen bubbles nucleated rapidly at platinum electrodes and the number of active nucleation sites increased with current density, despite some sites becoming deactivated. The new sites that were active only at high current densities were characteristically different, forming in clusters and producing very small bubbles that detached rapidly, prior to significant growth at the electrode. These nucleation sites produced vertical streams of departing bubbles and were termed “bubble pumps”. The dimensions of the active nucleation sites ranged over at least one order of magnitude, from sub-micron to several microns in diameter. Detachment occurred by coalescence of neighbouring bubbles as seen for the gold electrode, in addition detachment caused by the collision of stationary and rising bubbles was more significant. The switch in mechanism that was observed for hydrogen bubble evolution at a platinum surface has been highlighted as an example of nucleation rate dispersion, a phenomenon that has been identified for other surfaces using the PRBN technique. It was more difficult to define conclusively the mechanism of hydrogen evolution at platinum using the EQCM technique. The frequency changes accompanying bubble detachment were small compared to the resolution of the apparatus, making FFT analysis difficult. However, it can be concluded that the small frequency changes showed that only a small volume of gas was resident on the platinum electrode during bubble evolution, an observation that is consistent with the FFV results.

Visual observation of chlorine bubble evolution at the vertical RTO electrodes identified that the study of specific nucleation sites is less applicable to this system. Unlike the platinum and gold electrodes, where consecutive bubbles formed at specific nucleation sites, the location of bubbles on the RTO surface was random, with very few consecutive bubble cycles being established. In the current density range 18 - 56 mA cm⁻², the number of active nucleation sites increased with current density and there was a much wider distribution in the number of active nucleation sites as a function of supersaturation. This suggests that nucleation was inhibited at the low values of supersaturation and was the rate-limiting step. The majority of bubble growth occurred whilst the bubbles were attached to the electrode, but not necessarily at the point of nucleation. Detachment occurred due to buoyancy forces or the collision of two bubbles, there was a small decrease in the average detachment size and an increase in the detachment rate with current density. Coalescence of neighbouring bubbles was uncommon and generally not involved in the detachment mechanism.

These observations were confirmed by the EQCM measurements of chlorine bubble evolution at horizontal RTO electrodes. In the current density range 8 - 60 mA cm⁻² the EQCM data are consistent with an increase in the number of nucleation sites. There was a change in mechanism as the current density increased further, with bubble detachment causing large jumps in frequency; this has been attributed to the influence of coalescence on the detachment mechanism. It was not possible to determine the amount of gas resident on the RTO electrode during the EQCM experiments, because of an apparent increase in coupled mass during gas evolution. One likely explanation is that the porous RTO surface becomes flooded with electrolyte during gas evolution.

Having established that nucleation was the rate-limiting step in the evolution of chlorine bubbles at an RTO surface, the nucleation rate was investigated further using the PRBN technique. The results confirmed that the nucleation activity varied as a function of current density and that different types of nucleation sites were activated at different values of supersaturation. Although the values of supersaturation that are generated using the PRBN technique are an order of magnitude lower than those generated during electrocatalytic gas evolution, it is reasonable to assume that the two-site model observed with the PRBN could be extended to a multi-site model over a larger range of supersaturation. Measurements of chlorine evolution from titanium showed that the surface roughness of the titanium substrate contributes significantly to the nucleation activity of the RTO surface.

Several issues have been identified during the development of the three experimental techniques used in this study that could be resolved through further research. The FFV technique provides characterisation of individual nucleation sites by quantifying the behaviour of bubbles forming at them. However, it was not possible to control the activity of the nucleation sites at the surfaces, even when using highly polished electrodes. In addition, the physical features and chemical properties of nucleation sites cannot be identified using FFV; however these are important parameters that give rise to the specific modes of bubble behaviour. Future research would need to address the relationship between the morphology of a nucleation site and the mechanism of the bubble formed at it. One solution would be to systemically vary the macroscopic properties of a surface such as the surface roughness or the contact angle, whilst simultaneously measuring the trends in the bubble behaviour. Alternatively, individual nucleation sites could be generated artificially by etching a single crystal surface, in an attempt to replicate the mechanisms observed at the naturally occurring sites.

This approach could be applied to further EQCM analysis, specifically a study of the volume of gas present on the electrode in the form of adhered bubbles, during bubble evolution, determined by the value of the $\Delta f_{\text{bubble layer}}$ parameter. In this study it has been shown that it is possible to modify the surface of the EQCM quartz crystal and the preliminary studies of the porous RTO electrode suggested that the pores became flooded during chlorine evolution. A more in depth analysis of the phenomenon, achieved by varying the surface structure of the electrode through different metal oxide deposition techniques, would provide an insight into the effect this process has on the bubble evolution mechanism. The novel data analysis methodology developed for the PRBN technique has shown it to be a powerful diagnostic tool for determining the nucleation activity of a solid surface. Any surface that can be manufactured as a small disc can be characterised using this technique. The role of other materials in the behaviour of bubble evolution in an industrial chlor-alkali cell is not well understood. For example, in addition to possible further analysis testing modifications to the anode and cathode materials presently used in chlor-alkali analysis, an interesting future development would be the study of bubble nucleation from the Nafion® membrane.